Dissertation

submitted to the

Combined Faculties of the Natural Sciences and Mathematics

of the Ruperto-Carola-University of Heidelberg. Germany

for the degree of

Doctor of Natural Sciences

Put forward by

Ismael Alejandro Pessa Gutiérrez

born in Rancagua, Región del Libertador Bernardo O'higgins, Chile

Oral examination: July 25, 2022

Study of star formation and resolved stellar populations in nearby galaxies

Referees:

Prof. Dr. Hans-Walter Rix

PD Dr. Simon Glover

Abstract

Observations have revealed a bimodality in galaxy properties such as color and morphology leading to a fundamental classification into passive red galaxies and star-forming blue galaxies, where the latter follow a tight correlation between their stellar mass and their star formation rate (SFR), known as star formation main sequence (SFMS). In this thesis, I use a sample of star-forming galaxies from the multi-wavelength Physics at High Angular resolution in Nearby GalaxieS (PHANGS) survey to study the physics that regulate the formation of stars and keep these galaxies on the SFMS, as well as to investigate how they have assembled their stellar mass, and thus, unveil their evolution through cosmic times. The PHANGS survey allows us to perform these analyses, for the first time, at a spatial resolution of ~ 100 pc, thus, resolving individual star-forming regions and galactic morphological features. I find that correlations between stellar mass surface density (Σ_*), molecular gas surface density ($\Sigma_{\rm mol}$), and SFR surface density ($\Sigma_{\rm SFR}$) hold at these spatial scales, albeit with an increased scatter compared to lower-resolution measurements. The correlation between $\Sigma_{\rm mol}$ and $\Sigma_{\rm SFR}$ is the most homogeneous across different galaxies and galactic environments indicating that the amount of molecular gas is regulating the formation of stars. The interplay between Σ_*, $\Sigma_{\rm mol}$, and $\Sigma_{\rm SFR}$ reveals significant variations across individual galactic environments implying that an additional mechanism(s) not captured by either Σ_* or $\Sigma_{\rm mol}$ is playing a role in setting the level of SFR. Analysis of the age and metallicity distributions of the stars across the galaxies shows negative stellar age and metallicity gradients, consistent with an inside-out growth scenario. A clear dependency of the stellar velocity dispersion on age is present in the galaxies, where younger stellar populations at any given radius have lower velocity dispersion than older stars. Variations of the time-averaged SFR across the galactic disk reveal a diffusion of the galactic structure with lookback time – consistent with the progressive dynamical heating of young stellar populations through interactions with molecular gas and/or non-axisymmetric galactic features. The results presented in this thesis show how local processes shape the evolution of galaxies, driving the formation of stars, and modulating the local star formation histories across the galactic disk of nearby galaxies.

Zusammenfassung

Eine klare Bimodalität in Galaxien-Eigenschaften wie Farbe und Morphologie wird beobachtet, die zu einer grundlegenden Klassifizierung in sogenannte passive rote Galaxien und sternbildende blaue Galaxien führt. Letztere zeigen eine enge Korrelation zwischen ihrer stellaren Masse und ihrer Sternentstehungsrate (SFR) folgen, die als Sternentstehungs-Hauptreihe (SFMS) bekannt ist. In dieser Arbeit verwende ich sternbildend Galaxien aus dem Multi-Wellenlängen Projekt "Physics at High Angular Resolution in Nearby GalaxieS" (PHANGS), um die physikalischen Vorgänge zu untersuchen, die die Sternentstehung regulieren und die diese Galaxien auf der SFMS halten. Desweiteren untersuchen wir, wie diese Galaxien ihre stellare Masse aufgebaut haben, um ihre kosmische Entwicklung zu enthüllen. Die PHANGS-Daten ermöglichen es uns, diese Analysen zum ersten Mal mit einer räumlichen Auflösung von ~ 100 pc durchzuführen und so einzelne Sternentstehungsgebiete und galaktische morphologische Strukturen aufzulösen. Ich stelle fest, dass Korrelationen zwischen der Oberflächendichte der Sternmasse (Σ_*), der Oberflächendichte des molekularen Gases ($\Sigma_{\rm mol}$) und der SFR-Oberflächendichte ($\Sigma_{\rm SFR}$) auf diesen räumlichen Skalen bestehen, wenn auch mit einer größeren Streuung im Vergleich zu Messungen mit geringerer Auflösung. Die Korrelation zwischen $\Sigma_{\rm mol}$ und $\Sigma_{\rm SFR}$ ist über verschiedene Galaxien und galaktische Umgebungen hinweg am homogensten, was darauf hindeutet, dass die Menge an molekularem Gas die Bildung von Sternen reguliert. Das Zusammenspiel von Σ_*, $\Sigma_{\rm mol}$ und $\Sigma_{\rm SFR}$ zeigt signifikante Variationen zwischen den einzelnen galaktischen Umgebungen, was darauf hindeutet, dass zusätzliche Mechanismen, die weder von Σ_* noch von $\Sigma_{\rm mol}$ erfasst werden, eine Rolle bei der Festlegung des SFR-Niveaus spielen. Die Analyse der Alters- und Metallizitätsverteilungen der Sterne in den Galaxien zeigt negative stellare Alters- und Metallizitätsgradienten, die mit einem Inside-out-Wachstumsszenario übereinstimmen. In den Galaxien ist eine klare Abhängigkeit der stellaren Geschwindigkeitsdispersion vom Alter vorhanden, wobei jüngere stellare Populationen bei einem gegebenen Radius eine geringere Geschwindigkeitsdispersion aufweisen als ältere Populationen. Variationen der zeitlich gemittelten SFR über die galaktische Scheibe zeigen eine Diffusion der galaktischen Struktur mit der Rückblickzeit - dies ist konsistent mit der fortschreitenden dynamischen Erwärmung junger stellarer Populationen durch Wechselwirkungen mit molekularem Gas und/oder nicht-achsensymmetrischen galaktischen Strukturen. Die in dieser Arbeit vorgestellten Ergebnisse zeigen, wie lokale Prozesse die Entwicklung von Galaxien beeinflussen, die Sternentstehung vorantreiben, und die lokale Sternentstehungsgeschichte in galaktischen Scheiben naher Galaxien modulieren.

Contents

List of Figures

List of Tables

1 Introduction

"Physicists are made of atoms. A physicist is an attempt by an atom to understand itself"

by Michio Kaku

1.1 Galaxy evolution

Understanding how galaxies form and evolve across cosmic time, along with predicting their future evolution, is one of the most ambitious goals of astronomy, requiring to understand physics from the smallest to the largest scales in the Universe. Galaxies are dynamic entities, constantly evolving both chemically and dynamically. As a result of this evolution, galaxies that we observe in the present-day universe exhibit a wide variety of morphologies, colors, and stellar populations. However, there is not yet a clear picture that connects specific evolutionary phases that a galaxy might have experienced and the properties we observe today. Knowing which and how different mechanisms shaped galaxies through cosmic time is key to ultimately understand how the heterogeneous Universe in which we live formed from the almost perfectly homogeneous beginning revealed by the observations of the cosmic microwave background (Planck Collaboration et al., 2020). Thus, the evolution of galaxies is one of the most critical topics in extragalactic astronomy. This evolution is driven by external and internal processes that shape galaxies and lead to different features.

External processes (e.g., mergers of galaxies) operate on relatively short time scales (about hundreds of Myr, Whitney et al., 2021) and can drastically alter the morphology of a galaxy (e.g., trigger star formation, disrupt its morphology). Mergers can be categorized according to the number of galaxies involved (binary vs. multiple), relative masses of the merging galaxies (minor vs. major), and amount of gas carried by the interacting galaxies. The latter classification is particularly important to understand the impact of the merger on the galactic properties. A merger between two gas-rich galaxies (wet merger) will typically trigger large amounts of star formation, as well as active galactic nucleus (AGN) activity with subsequent AGN feedback. Star formation leads to chemical enrichment of the interstellar medium (ISM), and evolution of the optical colors of the merging galaxies towards bluer wavelengths. On the other hand, a merger between two gas-poor galaxies (dry merger) will

likely have less impact on some of the physical properties of galaxies such as color, although it can still alter the morphology and gravitational potential of the interacting galaxies.

Internal processes (e.g., secular evolution) act more gradually and slowly, on longer time scales, but are particularly important in low-density regions of the universe, where late-type galaxies are relatively more abundant (Khim et al., 2015). Secular evolution is the process by which a galaxy redistributes its mass and angular momentum as a consequence of the formation of a stellar bar and/or spiral arms (Kormendy, 2013).

These different processes (internal and external) give rise to a variaty of morphological types that are illustrated in Fig. 1.1. Elliptical galaxies are shown on the left side of the diagram. They are dynamically supported by random motions, and are thought to originate through mergers of galaxies. Spiral galaxies, opposite to elliptical galaxies, are dominated by a rotationally supported disk, in which spiral arms develope as compression waves that travel through the disk (Lin & Shu, 1964) and cause a piling-up of stars and gas at the crest of the wave, stimulating the formation of stars. Rotating disk are also unstable to the formation of stellar bars (Ostriker & Peebles, 1973; Toomre, 1977), that form when stellar orbits deviate from circular paths into very elongated orbits around the galactic center. A fraction of $20\% - 60\%$ (increasing towards lower redshifts) of galaxies show a bar (Sheth et al., 2008), and they are thought to transport material inwards fueling central star formation or an AGN (Knapen et al., 2002). The central region of galaxies can host a 'classical' bulge or a 'pseudobulge', which encloses high concentrations of stellar mass. Whereas the first share similarities with elliptical galaxies, and it is belived to form through mergers, the second is usually understood as evidence of secular evolution (Kormendy, 1979; Combes & Sanders, 1981; Okamoto, 2013; Conselice, 2014), as it results from the dissipation of angular momentum of the gas. As a consequence, they retain properties of the disk from which they formed such as kinematics dominated by rotation (Kormendy, 1993) and flattening similar to that of their outer disk (Kormendy, 1993; Fathi & Peletier, 2003).

Lenticular galaxies (S0) are galaxies with a bulge and a disk but without any signs of spiral arms. They host no to little star formation, as they lack gas to fuel the formation of stars, although they retain dust in their disks. Several formation mechanisms have been proposed for these galaxies, including spiral galaxies that ran out of gas and lost their spiral arms pattern (Blanton & Moustakas, 2009), mergers of galaxies (Christlein & Zabludoff, 2004), and disk assembly via accretion of gas by elliptical galaxies (Graham, 2013). Finally, irregular galaxies are objects that do not fall anywhere in the Hubble sequence, having no defined shape or distinctive features. They are similar to spiral galaxies, as they show ongoing star formation, although their masses are commonly smaller (Conselice, 2014).

It is worth noting that the shape and structure of galaxies do not simply represent a morphological classification. It is widely known that the physical properties of galaxies strongly correlate with their morphology. The size, surface brightness, and velocity dispersion of elliptical galaxies are correlated through the fundamental plane of elliptical galaxies (Djorgovski & Davis, 1987). Similarly, the rotation velocity and luminosity of spiral galaxies are connected through the Tully-Fisher relation (Tully & Fisher, 1977). More generally, late-type galaxies (LTGs; spiral and irregulars) show bluer colors, higher star formation, a combination of young and old stellar populations, and are on average less massive than early-type galaxies (ETGs, elliptical and lenticular), which show essentially no recent star formation, and are composed exclusively of old stars (e.g., Pannella et al., 2009). I will describe this

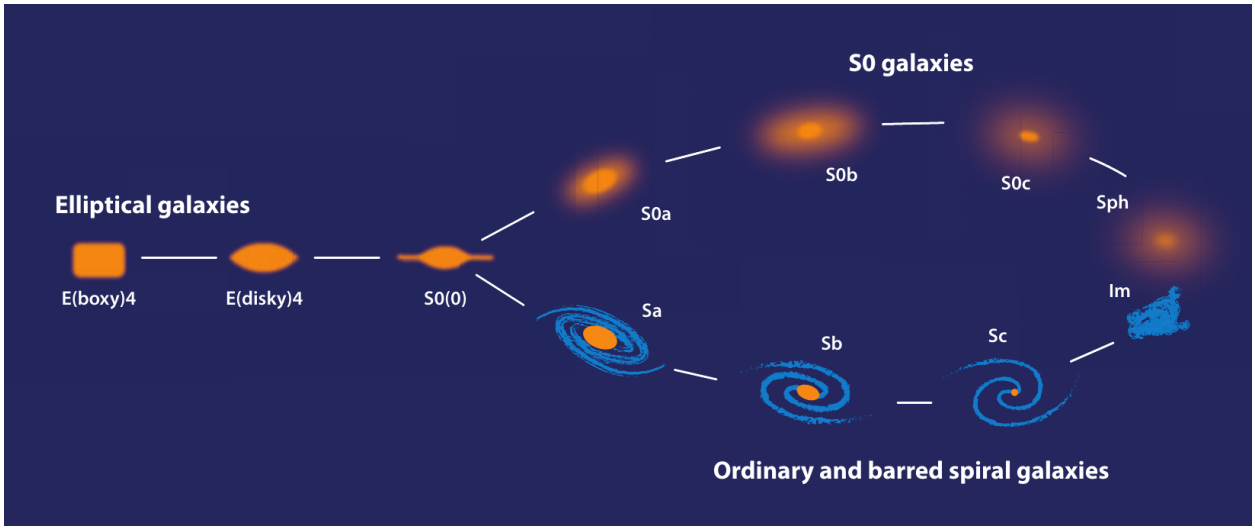

Figure 1.1: Modern version of the Hubble sequence (from Kormendy & Bender, 2012) that shows the sequence for elliptical and lenticulars (S0s) galaxies, as well as the classic Hubble classification for spiral galaxies. The elliptical sequence is determined by the shape of the galaxy, the lenticular sequence is determined by the size of their central bulge, relative to the full galaxy, and the spiral sequence is defined by how tight the spiral configuration is, and the size of the bulge/disk size ratio. The low mass dwarfs spheroidals and irregular galaxies are also shown at the right end of the figure.

early- and late-type bimodality in detail in the next section.

1.2 Bimodality in the galaxy population

Initially, galaxies were exclusively classified in a qualitative fashion, according to their morphological features. Then, de Vaucouleurs (1948) proposed the first quantitative distinction between ETGs and LTGs, by examining their surface brightness profiles, as ETGs typically show centrally cuspy profiles, while disk-dominated LTGs are better described by an exponential profile. This was later generalized by Sérsic (1963), who introduced a parametrization that allows the description of the surface brightness of galaxies with different morphological features, the so-called Sérsic profile, defined as:

$$I(R) = I_e \exp\left[-b_n\left(\frac{R}{R_e}\right)^{1/n} - 1\right] \tag{1.1}$$

where I_e is the intensity at the effective radius R_e that encloses half of the total light, n is the so-called Sérsic index, which controls the degree of curvature of the profile, and b_n is defined in terms of n such that $b_n = 1.9992n - 0.3271$. In this context, the De Vaucouleurs profile is a particular case with $n = 4$ for spheroidal galaxies and bulges. In general, the surface brightness profile of a galaxy is well reproduced by two components: an exponential disk ($n = 1$) and a Sérsic profile with a higher Sérsic index for its inner region. The ratio of stellar mass in these two components (the bulge-to-disk or bulge-to-total ratios) correlates with qualitative Hubble type classification, as shown in Fig. 1.2. LTGs are characterized by

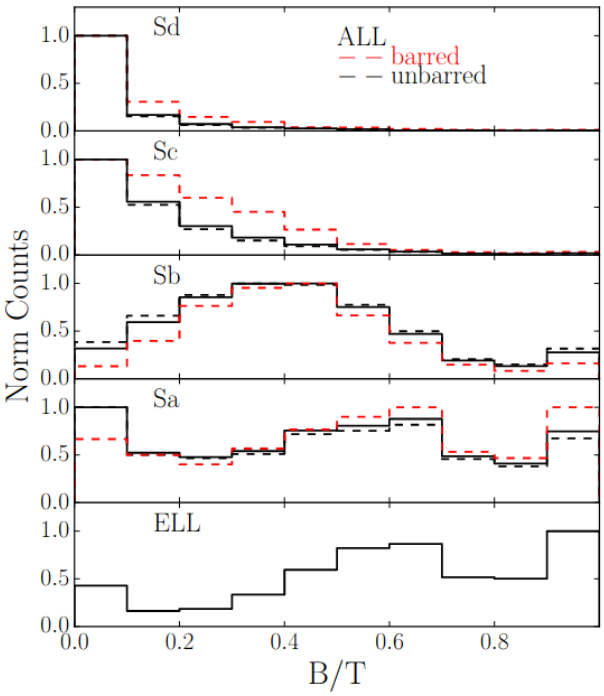

Figure 1.2: Bulge-to-total ratio for a sample of galaxies from the Sloan Digital Sky Survey (SDSS) Data Release 7 (York et al., 2000; Abazajian et al., 2009). Distributions are shown separately for different Hubble types, from late spirals (*top*) to elliptical galaxies (*bottom*). The morphological classification is from the Galaxy Zoo citizen science project (Lintott et al., 2008, 2011). Credits: Morselli et al. (2017).

prominent disks, and hence, lower values of bulge-to-total ratios (B/T) than ETGs. Thus, B/T is a useful metric to characterize the morphology of galaxies quantitatively.

However, the bimodality in the galaxy population is not limited to their morphologies. The color of galaxies represents one of the most extensively studied bimodal distribution seen in galaxy properties, mainly through color-magnitude (or color-mass) diagrams (e.g., Mateus et al., 2006; Brammer et al., 2009; Schawinski et al., 2014), as photometric parameters are easily measured for a large number of galaxies. Figure 1.3 shows the $u-r$ colour - mass diagram for a large sample of galaxies from the SDSS DR7 survey (York et al., 2000). ETGs populate preferentially the top right part of the panel, a.k.a. red sequence, with red colors and higher mass values than LTGs, which populate preferentially the bottom left part of the diagram, a.k.a. blue cloud. Between both sequences lies the green valley. Galaxies in the green valley are interpreted as transitioning from a spiral to an elliptical morphology. It is worth noting that this color bimodality has been found to persist towards higher redshifts (e.g., Wiegert et al., 2004).

Since galaxy colors are a direct sign of their star formation history, a bimodality in their distributions suggests that they have evolved along two different major paths. In this line, Cui et al. (2021) find evidence that connects the origin of the color bimodality to variations in the stellar-to-halo mass ratio due to differences in the halo formation times. However, a careful interpretation of this feature must take into account that the age of the underlying stellar populations is not the only factor determining the color of a galaxy. A large dust

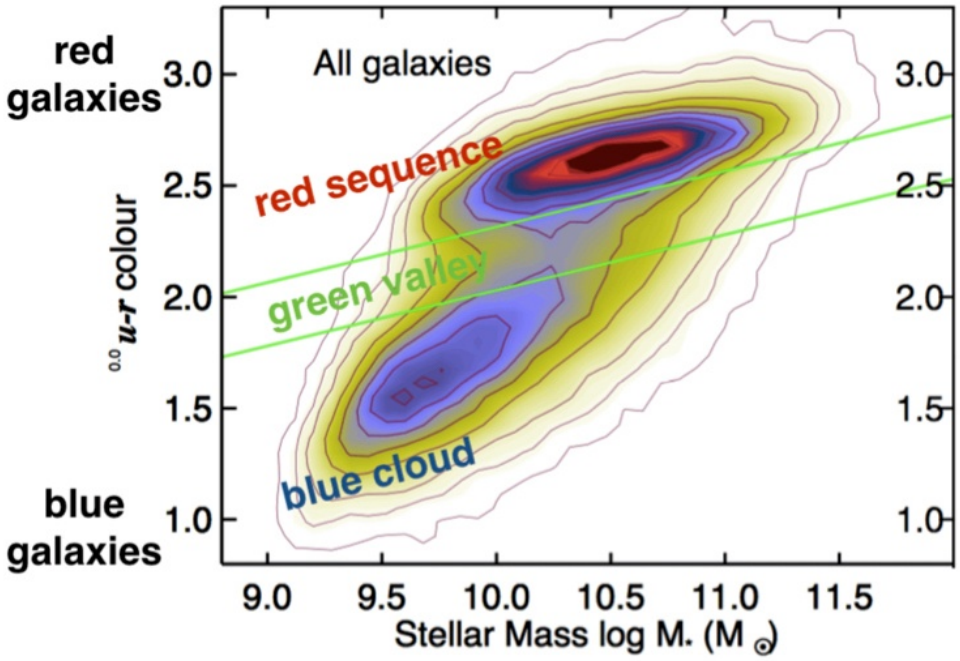

Figure 1.3: The u-r colour-mass diagram for a sample of $\sim$ 25000 galaxies from the SDSS DR7, limited in redshift to $0.02 < z < 0.05$. The morphological classification is from Galaxy Zoo. The green lines delimitate the green valley between the red sequence and the blue cloud. Credits: Schawinski et al. (2014).

content or very high metallicities can mimic the red colors typical of old stellar populations (de Meulenaer et al., 2013). Similarly, AGN activity can ionize the surrounding ISM, which then recombines emitting UV radiation that can mimic the blue colors characteristic of young populations (Satyapal et al., 2018). For this reason, investigating this bimodality in more directly interpretable galactic properties provides relevant insights about its nature.

In particular, star formation rate (SFR) is defined as the quantity of stellar mass (in units of solar masses, $M_\odot$) produced yearly by a galaxy, and it is a primary metric to describe galaxy evolution, as it modulates the star formation history of a galaxy. Figure 1.4 shows how this bimodality persists in the SFR - stellar mass plane while also explicitly showing its connection to morphology through the Sérsic index. Star-forming LTGs lie in a well defined sequence, the so-called *Main Sequence of star forming galaxies* (SFMS; Brinchmann et al., 2004; Noeske et al., 2007; Daddi et al., 2007; Whitaker et al., 2012; Pannella et al., 2015; Pearson et al., 2018; Popesso et al., 2019).

The scatter of the SFMS is found to be constant with $0.2-0.3$ dex over the full stellar mass and redshift range probed so far, and the low-mass slope is consistent with unity (Förster Schreiber & Wuyts, 2020), while a flattening of the relation shows up at the high-mass end ($\log M_* \gtrsim 10.5$). This flattening is stronger at low redshifts, and nearly vanishes towards $z > 2$ (Tomczak et al., 2014, 2016). Different factors can drive quantitative differences in the exact derived slope and normalization of the SFMS, such as (1) method and strictness of star-forming galaxy (SFG) selection, (2) stellar mass range over which the relation is fit, and (3) use of SFR tracers.

Although the overall slope and scatter of this relation does not change drastically with

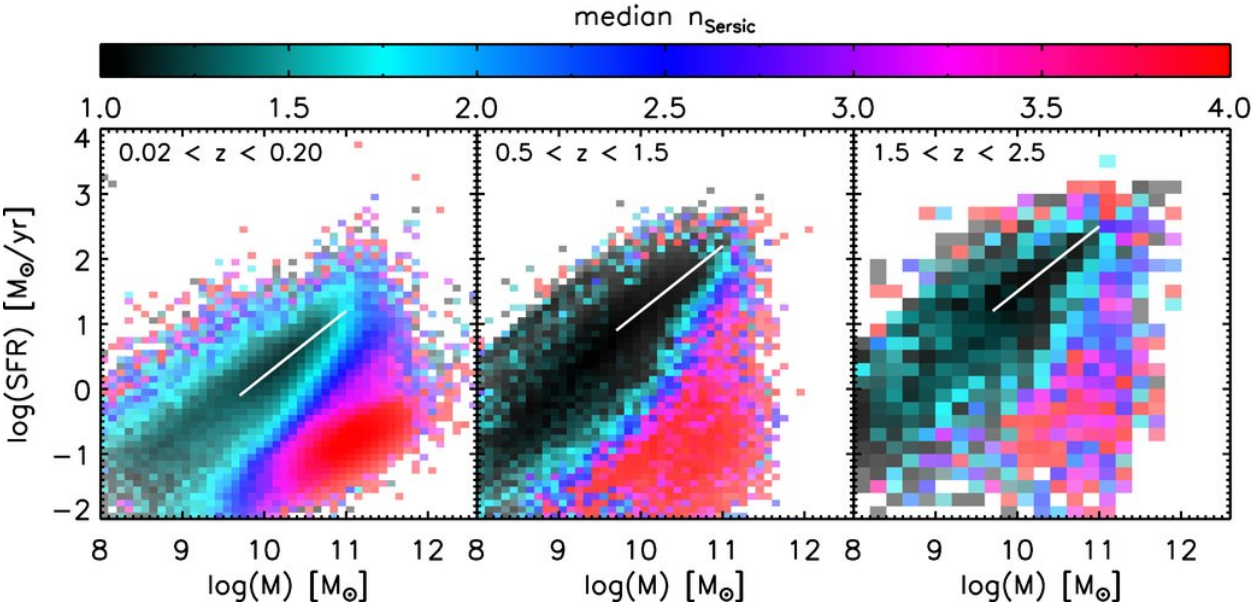

Figure 1.4: The SFR-mass diagram for a sample of galaxies, across different redshift ranges. The color-coding represents the median value of the Sérsic index n of all galaxies in each [SFR, M] bin. A clear bimodality exist between star-forming LTGs, described by an exponential disk ($n \approx 1$), and quiescent ETGs, described by higher n values. The sequence conformed by the LTGs can be well described by a constant slope of 1 and a zero point that increases with lookback time (white line). Credits: Wuyts et al. (2011)

redshift (Popesso et al., 2019), its normalization evolves with cosmic time. In fact, the characteristic specific star formation rate of the SFMS population decreases by a factor ~ 20 from $z = 2$ to $z = 0$ (Schreiber et al., 2015), indicating a decline of the levels of SFR over time, consistent with results from studies of the cosmic evolution of the star formation rate density (SFRD; Madau & Dickinson, 2014). The SFMS of galaxies is considered one of the most useful tools in astrophysics to study the evolution of the star formation activity in galaxies (Oemler et al., 2017), and one of its main implications is that galaxies form the bulk of their stars through steady-state processes rather than violent episodes of star-formation, putting constraints on the star formation history of galaxies. In the SFR - stellar mass plane, elliptical galaxies form a cloud in the bottom-right part of the diagram. Finally, green valley galaxies are particularly important for studying the mechanisms that drive the quenching of galaxies (e.g., Jian et al., 2020; Das et al., 2021), since they are interpreted as being transitioning from star-forming to passive. This thesis focuses primarily on the physics that modulate the star formation processes in star-forming galaxies.

1.3 Star-forming galaxies

Late-type galaxies that lie close to the SFMS are often referred to as star-forming galaxies (SFGs). However, as mentioned in the previous section, the exact selection criteria used for SFGs can influence the slope and normalization of the resulting SFMS. Peng et al. (2010) assume a mass-dependent color selection to choose galaxies exclusively from the blue cloud

(see Fig. 1.3). Daddi et al. (2007) and Pannella et al. (2009) use a two-color BzK selection criterion, Williams et al. (2009) and Whitaker et al. (2012) perform a selection based on rest-frame UVJ data, and Karim et al. (2011) applies a threshold in specific star formation rate (sSFR $\equiv$ SFR / M_*). In the search for a more objective definition of the SFMS, Renzini & Peng (2015) propose a method that does not require an explicit pre-selection of galaxies, fitting the ridgeline in the 3D surface defined by the SFR-mass-number relation.

Star-forming galaxies that lie significantly above the SFMS are referred to as starburst (SB) galaxies. Typically starbursts are disturbed galaxies, and many are observed to be merging systems (Muxlow et al., 2006). Recent works have reported a bimodality within the SFMS (Caputi et al., 2017; Rinaldi et al., 2021), claiming that the classic SFMS is actually composed of two distinguishable components, the starburst sequence, and the main sequence.

Morphologically, star-forming galaxies correspond to spirals and dwarf irregular galaxies. The former cover stellar mass ranges typically of $10^9 M_\odot < M_* < 10^{11} M_\odot$ (Lelli et al., 2016), while the latter have typically masses of $10^5 M_\odot < M_* < 10^9 M_\odot$. (Zhang et al., 2012; Lelli et al., 2016). In this thesis, I will focus on spiral star-forming galaxies. Specifically, studying the physics that regulate the star formation processes and keep them on the SFMS, as well as investigating the assembling of their stellar mass through cosmic times.

1.4 Components of the interstellar medium

Galaxies are not only made of stars; they also contains significant amounts of nebulous matter, heterogeneously distributed throughout interstellar space. The interstellar medium (ISM) is defined as the matter and radiation that exist between stars within a given galaxy. It includes gas (ionized, atomic, and molecular), dust, cosmic rays, and magnetic fields.

1.4.1 Gas

Interstellar gas is the main ingredient to fuel the formation of stars and AGN activity. Its chemical composition is primarily hydrogen, followed by helium with trace amounts of carbon, oxygen, and nitrogen (Herbst, 1995). The gas in the ISM is present in a variety of phases, which are characterized by their temperatures and densities (see Table 1.1).

Phase	State	Density cm^{-3}	Temperature K
Atomic (H I)	Cold	$\simeq 25$	100
	Warm	$\simeq 0.25$	8000
Molecular (H_2)		≥ 1000	≤ 100
Ionized	H II regions	$\simeq 1 - 10^4$	$\simeq 10000$
	Diffuse	$\simeq 0.03$	8000
	Hot	$\simeq 6 \times 10^{-3}$	$\simeq 5 \times 10^5$

Table 1.1: Properties of the gas in the different phases of the interstellar medium. Table adapted from Lequeux (2005).

Atomic gas

Atomic Hydrogen is the most abundant element in the universe; however, it is not directly observable at optical wavelengths. It is usually measured through the H I line at 21 cm, which was initially predicted theoretically by van de Hulst (1946) and then observationally detected in our Galaxy by Ewen & Purcell (1951). It traces both the gas content and kinematics. Indeed, most of our knowledge on the large-scale kinematics of the Milky Way comes from H I line studies (e.g., Burton, 1988). This radiation occurs when the electron flips its spin orientation back to the lower energy configuration. This H I spin-flip transition has a long decay half-life of about 10^7 years. Nevertheless, the large number of hydrogen atoms makes the H I line the strongest thermal line observed in radio astronomy (Dickey, 1991). The surface brightness of H I can be used to trace the underlying gas mass, provided that the medium is optically thin. Its distribution is often used to study the distribution of dark matter in spiral and dwarf galaxies (e.g., Bosma, 1981; de Blok et al., 2008; Das et al., 2020) assuming that it traces the underlying gravitational potential.

The atomic gas in spiral galaxies is organized as a rotating disk, although considerably more extended than the stellar disk (Boomsma et al., 2008), and with the presence of extra-planar gas (Sancisi et al., 2008; Marasco et al., 2019), of which a fraction can be explained by external accretion events (Sancisi et al., 2008). The atomic gas disk does not present a homogeneus distribution, instead, it show holes, which are associated to stellar feedback from recent star formation events (Boomsma et al., 2008; Bagetakos et al., 2011). In other galaxies, the total atomic-to-stellar mass fraction depends on a number of factors. There is plenty of evidence that show that to first order, more massive galaxies host lower atomic-to-stellar mass ratios (Catinella et al., 2010; Popping et al., 2014; Parkash et al., 2018; Hunt et al., 2020), typically ranging from ~ 1 at the lowest mass galaxies ($\log M_* \sim 8$) to ~ 0.01 at the high mass end of the stellar mass distribution ($\log M_* \sim 11$). However, morphology also plays a relevant role to determining the amount of atomic gas. In LTGs , the total atomic gas content increases towards higher stellar masses (Parkash et al., 2018). On the other hand, ETGs harbor smaller atomic gas reservoirs whose mass does not strongly correlates with the total stellar mass of the galaxy (Catinella et al., 2010; Serra et al., 2012; Parkash et al., 2018). Besides morphology, local environment also plays a relevant role in setting the content of atomic gas, as galaxies residing in higher density environments are more likely to have their H I reservoir stripped by interactions with other galaxies (Stevens et al., 2019; Hu et al., 2021).

As shown in Table 1.1, the atomic phase of the ISM is also divided into two sub-phases. The warm neutral medium (WNM) is ubiquitous in our Galaxy and represents the bulk of the H I gas seen in emission-line surveys ($\approx 60\%$; Brinks, 1990). On the other hand, the cold neutral medium (CNM) is distributed as dense clouds where CNM can eventually transit to molecular gas (Wolfire et al., 2003). It represents a minor fraction of the ISM, and it is mostly traced by H I measured in absorption. The CNM phase was first reported by Garwood & Dickey (1989), and then confirmed by Liszt et al. (1993). In nearby galaxies, Dib et al. (2021) recently find that the two sub-phases of the atomic gas can be modeled as two independent power laws, where the CNM dominates the atomic gas budget in the inner regions ($r < 0.5R_{25}$), and the WNM dominates the atomic gas content at larger radii.

Molecular gas

Molecular Hydrogen (H_2) is, by a few orders of magnitude, the most common molecule in our Universe. Since H_2 is a symmetric diatomic molecule, electric dipole driven vibrational transitions are forbidden, and only weak electric quadrupole transitions are allowed, making its detection extremely difficult in emission[1]. Hence, carbon monoxide (CO) is the most used tracer of molecular gas. It is the second most abundant molecule in the ISM, and its low-energy rotational transitions are easily detectable in relatively high-density regions. However, a ratio between CO luminosity and H_2 mass must be assumed to convert CO intensity to total molecular gas mass. Bolatto et al. (2013) suggest a value of 4.35 $M_\odot$ pc^{-2} (K km $s^{-1})^{-1}$ for our Galaxy, although variations with the metallicity of the ISM are expected (Accurso et al., 2017; Hunt et al., 2020). The first large-scale surveys of CO emission were carried out by Scoville & Solomon (1975) and by Burton et al. (1975), covering only a fraction of the Galactic equator accessible from the Northern terrestrial hemisphere. The molecular gas in the inner regions of our Galaxy is well confined to a thin rotating disk, while the gas at large Galactocentric distances often displays flaring and warping structures (Su et al., 2016).

High spatial resolution CO observations in nearby galaxies (e.g., Schinnerer et al., 2019a) show that molecular gas is not homogeneously distributed across the galactic disk. It is mostly found as discrete giant molecular clouds (GMC), with a typical scale-length of about ~ 100 pc (Heyer & Dame, 2015), that are located preferentially in galactic structures such as bars and spiral arms (Pan et al., 2022). Recent studies have also shown that the physical properties of these molecular clouds, such as surface density, velocity dispersion, and pressure, are intimately connected to their location in the galactic disk and the galactic structure in which they are embedded (Colombo et al., 2014; Renaud et al., 2015; Sun et al., 2020b; Meidt et al., 2021; Querejeta et al., 2021).

In nearby LTGs, the amount of molecular gas determined from CO emission scales with their total stellar mass (Boselli et al., 2014). However, the ratio of atomic-to-molecular gas anticorrelate with stellar mass, typically within the range (in log) of -0.5 for massive galaxies, up to 1.5 in low-mass galaxies, being > 0 for most of the stellar mass range (Catinella et al., 2018; Hunt et al., 2020). On the other hand, Davis et al. (2019) find that for a sample of ETGs, the total molecular gas content has little dependency on the total stellar mass. Furthermore, Lisenfeld et al. (2017) find that galaxies transitioning from star-forming to quiescent lie below star-forming galaxies and above quiescent galaxies in the molecular gas mass - stellar mass plane, showing that the content of molecular gas is connected to the quenching of galaxies.

This is not surprising, as it is well known that this phase of the interstellar gas is closely related to the formation of stars, as the latter takes place in GMCs (Kennicutt & Evans, 2012). Stellar feedback from the newly born stars deposits energy into the GMCs, eventually leading to their disruption (e.g., Dobbs et al., 2014; Krumholz et al., 2014), regulating the overall galaxy star formation rate. Indeed, studies in nearby galaxies indicate that GMCs disperse within just 1-5 Myr once massive stars emerge (Chevance et al., 2020a).

[1] H_2 is, however, easily detected in absorption in the far-UV, provided a background target is available (e.g., Takezawa, 1970).

Ionized gas

In hot regions of the ISM, the matter is mostly ionized. In the case of H II regions, the gas is ionized by massive OB-type stars whose energetic (hard UV) radiation is able to heat and ionize their surrounding gas. The ionized bubble surrounding a single star is also known as 'Stromgren sphere', and its radius depends primarily on the ISM's density and the star's temperature. This is why H II regions have long been considered as the optimal probes of massive star formation in galaxies (Kennicutt, 1989). Emission line measurements of H II regions enable the study of the ISM metallicity distribution (Williams et al., 2022a), as well as the processes driving the metal mixing within the ISM (e.g., Ho et al., 2017; Kreckel et al., 2020).

However, not all ionized gas is organized as discrete clouds. A large fraction of the ionizing radiation from massive stars may escape from H II regions in their immediate vicinity and contribute to powering the diffuse ionized gas (DIG; e.g., Vale Asari et al., 2019). Nevertheless, recent studies find that emission from hot, low-mass evolved stars is required to explain some of the spectral features of the DIG emission, pointing to a double-origin scenario of the photons that ionize the DIG (Belfiore et al., 2022). Due to its different origin, this diffuse component does not trace well local star formation activity, and its contribution to the flux of H II regions must be accounted for in order to carefully interpret H II region flux as SFR (Blanc et al., 2009).

The hottest phase of the ionized gas, a.k.a. coronal gas corresponds to low-density gas which has been shock-heated by fast stellar winds and blast waves from novae and supernovae (Slavin & Cox, 1993). Unlike photoionized H II regions, coronal gas is collisionally ionized and, thus, contains very highly ionized species, such as O IV. Therefore, absorption lines from O IV and other ions are currently the most effective way of detecting the hot ionized ISM. When the temperature of the coronal gas exceeds 10^6 K, it can also be detected via X-ray Bremsstrahlung emission.

Finally, since different mechanisms could be responsible for ionizing the ISM (e.g., AGN, starbursts), high-to-low excitation line ratios are often used to identify the ionizing source. Whereas low excitation lines probe H II regions that are photoionized by massive stars, higher excitation lines sample highly ionized gas that requires harder radiation fields (e.g., AGNs). The most common method to quantitatively identify the dominantly ionization source in a given galaxy or galactic region is based on the Baldwin, Phillips, & Terlevich (BPT; 1981) empirical diagnostic diagrams using optical emission line ratios. Figure 1.5 shows modern versions of the BPT diagram using different pairs of line ratios. Different regions within these diagrams separate galaxies where the ionization is predominantly due to star-formation, AGNs, or low-ionization nuclear emission-line region (LINER) emission. The latter are a type of galactic nucleus that show an optical spectra dominated by low ionization species emission lines [(O I), (N II), (S II)], and faint high-ionization emission lines (Márquez et al., 2017), whose dominant ionization mechanism is still amatter of debate (e.g., Yan & Blanton, 2012; Márquez et al., 2017).

1.4.2 Dust

The first convincing evidence for solid dust particles in interstellar space was presented by Trumpler (1930), based on discrepancies between color indices and spectral types (color

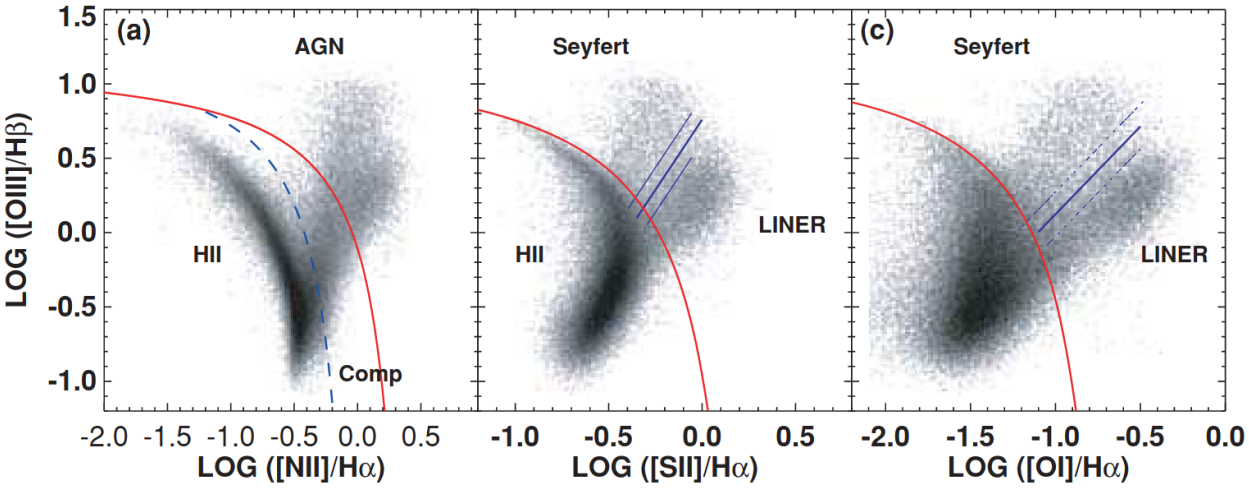

Figure 1.5: BPT diagnostic diagram for SDSS galaxies using different sets of line ratios. The blue dashed line in the left panel shows the AGN-star-formation limit. Galaxies that lie below the dashed line are classified as H II-region-like galaxies. The red solid line marks an upper bound to the star-forming sequence on the three diagrams. Composite galaxies, whose ionization is due to a combination for star formation end either AGN or LINER emission, lie between the red and the blue lines. Galaxies classified as composites in the left diagram lie mostly within the star-forming region in the middle and right panels. Galaxies that lie above the red line are likely dominated by non-star formation ionization. The diagonal blue solid lines mark the Seyfert-LINER limit. Credits: Kewley et al. (2006).

excess) in distant star clusters. Then, Jenkins & Savage (1974) and Bohlin (1975) found evidence that suggested that interstellar dust does not show a homogeneous spatial distribution on the sky, and that it actually follows the inhomogeneous and patchy distribution of the interstellar gas. The most evident manifestation of this interstellar dust is the obscuration and reddening of incoming light from stars. Dust grains are formed primarily within the atmospheres of low-mass (1-4 $M_\odot$) asymptotic giant branch (AGB) stars and are dispersed into the ISM via the strong AGB star winds (Gehrz, 1989). Other sources of dust grains are the ejecta of explosive core-collapse supernova (Dwek et al., 2014) and growth of grains by accretion of gas-phase species in the ISM, ocurring in the CNM and within cold molecular clouds (Zhukovska et al., 2016).

The decrease in the luminosity of a star when seen through a dust cloud is due to two different physical phenomena: the absorption of photons by the material of the grains and the scattering of photons in random directions. The ensemble of these mechanisms is known as extinction (Salim & Narayanan, 2020). On the other hand, the stellar light absorbed at short wavelengths is then re-emitted in the infrared (IR). In the case of our Galaxy, about 30% of its total luminosity corresponds to IR emission from dust (Li & Greenberg, 2003).

The extinction curve represents the wavelength dependence of dust extinction, and it is used to infer the intrinsic stellar spectral energy distribution (SED) from the observed (and extincted) SED. Thus, the extinction curve is the fundamental tool for interpreting the observational SEDs of galaxies (e.g., Takagi et al., 2003).

The extinction A_λ is classically expressed as the ratio of the emerging flux $I(\lambda)$ and the

incident flux $I_0(\lambda)$ such that:

$$I(\lambda) = I_0(\lambda)10^{(A_\lambda/2.5)} = I_0(\lambda)e^{-\tau_\lambda} \tag{1.2}$$

where $\tau_\lambda = 0.921\ A_\lambda$ corresponds to the optical depth, and A_λ is the strength of the extinction expressed in magnitudes. The shape of the extinction curve depends strongly on the physical properties of dust grains (grain size, dust components, etc., see, e.g., Mathis et al., 1977; Mathis, 1990; Nozawa & Fukugita, 2013). Therefore, understanding these properties is of great importance to properly correct an extincted SED.

The physical properties of the dust grains are not exclusively inferred through their extinction of stellar light. Dust emission and polarization measurements (due to the alignment of dust grains with ambient magnetic fields, e.g., Lee et al., 2020) also put constraints on the dust properties. The SED of LTGs are dominated by dust emission at wavelengths larger than $\sim 10\mu$m (Popescu et al., 2011).

There are two main dust populations: 'cold' dust, conformed by large grains with sizes $\gtrsim 250$Å, wich are illuminated by the general interstellar radiation field, and reach equilibrium temperatures of 15 K $\lesssim T \lesssim$ 25 K, emitting strongly at wavelengths $\gtrsim 60\mu$m (Li, 2004b). On the other hand, smaller grains with sizes $\lesssim 250$Å constitute the 'warm' dust. These grains have energy contents comparable to the energy of a single starlight photon, hence, they can be easily heated by individual photons, reaching temperatures higher than their 'steady-state' temperature, to then rapidly cool down to a temperature below their 'steady-state' temperature before the next photon is absorbed. This stochastic heating by absorption of photons results in transient 'temperature spikes', during which the energy absorbed from the photon is re-radiated in the IR, at wavelengths $\lesssim 60\mu$m (Li, 2004b,a).

Orellana et al. (2017) found a tight relation between the total gas cold gas mass (atomic + molecular) and the total dust mass in nearby galaxies, and dust-to-gas ratios (DGR) are typically around $\sim 1\%$, with passive galaxies lying preferentially above this value, and star-forming galaxies below. Further studies on the DGRs revealed a systematic dependency of the DGR on the gas-phase metallicity of the galaxy, where more metal-rich galaxies are associated to higher DGR values, with no significant dependence on stellar mass (De Vis et al., 2019; Li et al., 2019). Recent works use dust-content (characterized by optical attenuation) as tracer of the spatial distribution of interstellar gas (e.g., Barrera-Ballesteros et al., 2020).

Besides modifying the observed SED of a given object, dust also plays an active role in modulating the ISM physical conditions. Dust controls the temperature of the ISM, providing heating through electrons ejected photoelectrically from grains (Tielens, 2005). On the other hand, it also accounts for most of the elements which provide cooling (e.g., Hirashita & Ferrara, 2002; Cazaux & Spaans, 2009). Furthermore, dust is an essential coolant in star formation, inducing fragmentation into low-mass stars (Omukai et al., 2005; Schneider et al., 2006). Additionally, Hydrogen molecules form primarily on the surfaces of dust grains (e.g., Cazaux & Tielens, 2004). Therefore, dust grains are intimately related to the star formation activity in galaxies.

For this thesis, accounting for dust is of utmost importance in order to calculate un-biased SFR values (Calzetti, 2013), and derive the stellar population properties from integrated spectra (de Meulenaer et al., 2013).

1.4.3 Other components of the ISM

Cosmic rays are a significant component of the interstellar medium, sharing an equivalent energy density with the magnetic field and the interstellar gas. They are high-energy charged particles (89% protons, 10% other ions, and 1% simple electrons) produced by supernovae (SNe), traveling nearly at the speed of light. Most galactic cosmic rays have energies between 100 MeV (velocity $\sim 43\%$ of the speed of light) and 10 GeV (velocity $\sim 99.6\%$ of the speed of light) (Cronin et al., 1997). Cosmic rays with energies higher than 10^{14} eV produce cascades of charged particles when entering the earth's atmosphere, also known as 'air-showers' (e.g., Watson, 2011), emitting Cherenkov light, because they travel faster than the light in the medium. Cosmic rays can influence ISM conditions, ionizing the gas through collisions, and dissociating molecules within dense molecular clouds (Galli & Padovani, 2015). Cosmic rays are also an efficient source of heating accross different environments, from the dense gas in molecular clouds (Goldsmith & Langer, 1978), to photodissociation regions (Shaw et al., 2009), because the energy of the electrons produced by the ionization process is in large part converted into heat by inelastic collisions with ISM atoms and molecules (Padovani et al., 2009).

Magnetic fields also constitute an important fraction of the total energy budget of the ISM and significantly contribute to the total pressure that balances the ISM against gravity. Furthermore, magnetic fields have been found to be relevant in several ISM processes, including driving the flow of cosmic rays (Aharonian et al., 2012), and preventing the gravitational cloud collapse in the early stages of star formation (McKee & Ostriker, 2007; Padoan & Nordlund, 2011). Galactic magnetic fields have been measured with a number of techniques, including radio synchrotron emission from accelerated cosmic rays (Beck, 2009), optical polarization due to interstellar dust grain alignment (Andersson et al., 2015), Faraday rotation of background sources (Van Eck et al., 2021), and Zeeman splitting of radio spectral lines (Ching et al., 2022).

The average strength of the total magnetic field in the Milky Way in our stellar vicinity is about 6 μG and increases to 20-40 mG towards the Galactic center region (Beck, 2003) in radio filaments near the Galactic center and dense clouds of cold molecular gas (Wielebinski & Beck, 2005). Finally, although it has been measured, the origin of the Galactic magnetic field remains unclear (Widrow, 2002). Theories typically advocate a field origin that either dates back to the formation of the Galaxy or is created and continually sustained by a Galactic dynamo (Beck et al., 2019).

Observations of synchrotron radiation have also allowed us to investigate the magnetic properties of nearby LTGs (e.g., Fletcher, 2010; Fletcher et al., 2011; Beck, 2015; Beck et al., 2020). In the case of elliptical galaxies, magnetic fields are poorly constrained due to their lack of significant synchrotron emission (Shah & Seta, 2021). Disk galaxies have a two-component magnetic field, a regular field component that is ordered on length scales comparable to the size of the galaxy, and a random turbulent magnetic field of comparable or greater strength (Fletcher et al., 2011). While the strongest ordered fields (10 - 15 μG) are generally found in the interarm regions, the strongest turbulent fields are located preferentially in spiral arms and bars (20 - 30 μG), as well as in central starburst regions (50 - 100 μG) (Beck, 2015).

1.5 Life-cycle of baryons

Baryonic matter is all the matter that we encounter in our everyday life and can perceive and interact with, including any type of atoms. However, the current cosmological paradigm predicts that only $\sim 4.9\%$ of the energy content in the Universe is in the form of baryonic matter (Planck Collaboration et al., 2020). The remianing energy is distributed primarly among dark energy ($\sim 69\%$) and dark matter ($\sim 26\%$). Other components such as neutrinos and photons constitute a very small fraction of the total energy budget ($< 10^{-2}\%$).

A nearly complete census of the baryons is available in the low redshift Universe ($z < 0.3$) (e.g., Shull et al., 2012; Tumlinson et al., 2017; Nicastro et al., 2018). The large majority ($\sim 82\%$) of the cosmic baryons are in the intergalatic medium (IGM, e.g., Shull et al., 2012), highly ionized ($T \sim 10^5 - 10^7$ K), and organized in a filamentary structure also known as the 'cosmic web'.

The remaining $\sim 18\%$ of the baryons at $z \approx 0$ are gravitationally bound to galaxies, groups and clusters, constituting the 'collapsed phase' of the baryonic matter (Shull et al., 2012). Stars are included in this phase, comprising a total of 7% of the total baryon density (Nicastro et al., 2018). The cold gas (H I and H_2) comprises nearly 1% at $z = 0$, $\sim 85\%$ of which is in the form of atomic Hydrogen. Hot haloes of gas surrounding galaxies are known as circumgalactic medium (CGM, e.g., Wisotzki et al., 2018), and they contain about 5% of the total cosmic baryon budget. Other sub-phases that account for a minor contribution of the total baryon budget are the diffuse-ionized medium (e.g., Werk et al., 2014), supermassive black holes (Kormendy & Ho, 2013), and dust (Sandstrom et al., 2013). It has been largely known that the relative proportion between the different phases of the baryonic matter is not constant over cosmic time. The gradual assembly of the large-scale structure of our Universe drives the physical conditions in which baryons lie (Davé et al., 2001; Walter et al., 2020), and thus, their temperature, density and ionization state.

Similarly, at smaller spatial scales, the interstellar medium is far from being a static entity. Interstellar gas that orbits in a galaxy disk can change significantly its physical properties during its path around the galaxy center. A particular parcel of gas may be molecular Hydrogen first, then finds itself close to a newly born massive star and becomes part of an H II region. The star may then explode as a supernova, heating the gas up to temperatures of millions of degrees. Finally, the gas may cool back down and become neutral, before it collects into a dense region that gravity gathers into a giant molecular cloud (Goldsmith et al., 2007). Furthermore, the interstellar medium is not a closed system. Gas from the CGM constantly falls on galaxies supplying gas to the interstellar medium, potentially fueling star formation activity (Tumlinson et al., 2017). On the other hand, the gas collapses to form new stars, locking interstellar matter into stars. As stars evolve, the fraction of their mass returned to the ISM will depend on their mass; massive stars return a large fraction of their mass, while low-mass stars return much less. On average, roughly one-third of the matter in stars is returned to the interstellar medium (e.g., Leitner & Kravtsov, 2011). Feedback mechanisms, such as SNe explosions or AGN feedback can also drive interstellar mass out of the galaxy (Biernacki & Teyssier, 2018). Thus, the total amount of mass of the interstellar medium is modulated by the gain of mass from the IGM and CGM, and the lost of mass caused by star formation and feedback mechanisms.

Fig. 1.6 shows a schematic representation of how the different components of baryonic

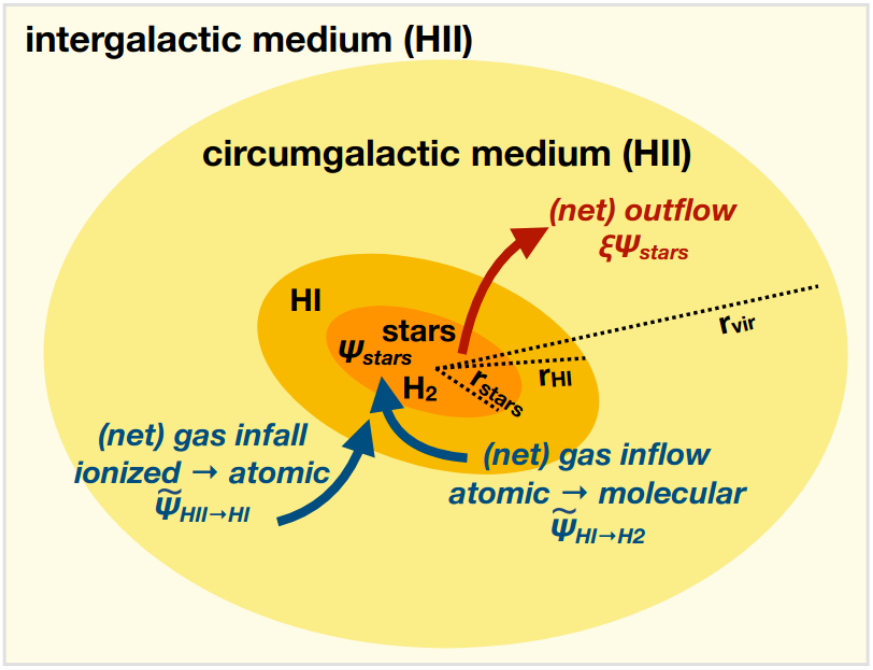

Figure 1.6: Schematic of the different baryonic components that are present within the dark matter halo of a galaxy, delimited by its virial radius $r_{\rm vir}$. The inner region ($r < r_{\rm stars}$), contains the vast majority of stars and molecular gas, and stars form here at a rate $\psi_{\rm stars}$. This region is surrounded by a reservoir of atomic gas (H I), with $r < r_{\rm HI}$, that in turn, is surrounded by primarily ionized gas (H II) that constitutes the CGM, and the IGM at larger distances. Blue arrows indicate the (net) infall of ionized gas to the H I reservoir ($\psi_{HII \rightarrow HI}$) as well as the (net) inflow of atomic gas to the molecular gas (H_2) reservoir ($\psi_{HI \rightarrow H2}$). The red arrow indicates the material expelled as outflows towards the outer regions of the halo, potentially reaching the IGM, here assumed to be proportional to $\psi_{\rm stars}$. Credits: Walter et al. (2020).

matter are distributed within the dark matter halo of a galaxy. The inner regions contain the vast majority of stars, molecular gas, and on-going star formation. In this region, stars form from giant molecular clouds with a typical timescale of order 10^7 yr (Schinnerer et al., 2019a; Chevance et al., 2020a), which are eventually dissipated by the feedback from massive stars (e.g. stellar winds). Molecular gas is also expected to form out of atomic gas in the galactic disk on a similar timescale (Clark et al., 2012; Walch et al., 2015). Since the gas-phase formation of H_2 is extremely inefficient under typical ISM conditions (Klessen & Glover, 2016), most of the H_2 in the ISM forms instead on the surface of dust grains (Gould et al., 1963). The inner region is surrounded by a reservoir of atomic gas (H I). At even larger radius, the gas is predominantly ionized, constituting the CGM and the IGM. The process, by which baryonic matter moves through these different phases is known as the baryon cycle. Fig. 1.7 shows the sequential evolution of the different phases of the baryons in the ISM, from molecular gas clouds to star formation, the dissipation of the neutral gas reservoir, and its subsequent re-formation.

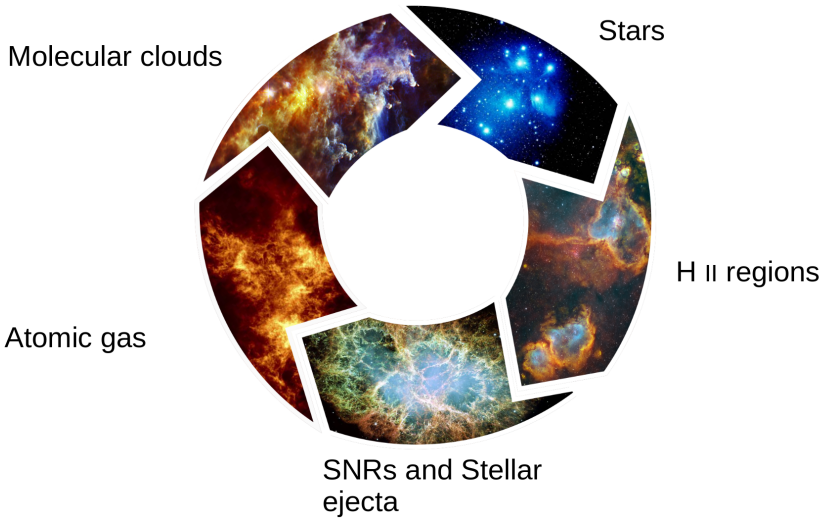

Figure 1.7: Schematic representation of the life-cycle of baryons in the interstellar medium. Molecular gas collapses and forms stars. The UV-photons emitted by newly born massive stars ionize their surrounding ISM, creating H II regions. As stars evolve, they inject mass and energy to the ISM through stellar feedback such as stellar winds and SNe. This material eventually cools and transforms into neutral atomic gas, that eventually transitions into molecular gas on the surface of dust grains, restarting the cycle. Credits: Francesco Santoro

1.6 Resolved star-forming scaling relations

The star formation rate is a primary metric to describe the evolution of a galaxy through cosmic times. However, what are the main physical processes that set the SFR of a galaxy, and drive its evolution is not yet completely clear. In Sec. 1.2, I introduced the SFMS of galaxies, which correlates the total mass of a star-forming galaxy with its total SFR. The existence of this relation implies that the formation of stars is a process regulated by small- and/or large-scale mechanisms that are directly or indirectly reflected in this correlation. Similar to the SFMS, the Kennicutt-Schmidt relation offers an alternative perspective on the mechanisms regulating the formation of stars in a galaxy. It correlates total SFR with total amount of gas and is consistent with a power-law of order unity (Schmidt, 1959; Kennicutt, 1998; Wyder et al., 2009; Genzel et al., 2010; Tacconi et al., 2010; Genzel et al., 2012).

However, since star formation is a local process that occurs in specific regions within galaxies, the physics that regulates the formation of stars are expected to operate on small scales, comparable to the size of the star-forming regions. This does not exclude additional large-scale mechanisms (e.g. galactic potential and sub-structure; Whitaker et al., 2015). Indeed, Sánchez et al. (2013) find that individual H II regions identified in the CALIFA (Sánchez et al., 2012) dataset show a correlation between their star-formation rate surface density ($\Sigma_{\rm SFR}$), and stellar mass surface density (Σ_*), analogous to the global SFMS. Although the spatial scales sampled by CALIFA are in the range of $\sim 0.5-1.5$ kpc, much larger than individual H II regions (~ 100 pc, see e.g., Ye, 1992; Bolatto et al., 2008; Freeman et al., 2017; Sun et al., 2018), this result implies that the mechanisms setting the SFMS are actually operating on sub-galactic scales.

Later, Cano-Díaz et al. (2016) presented this sub-galactic scale version of the SFMS as the

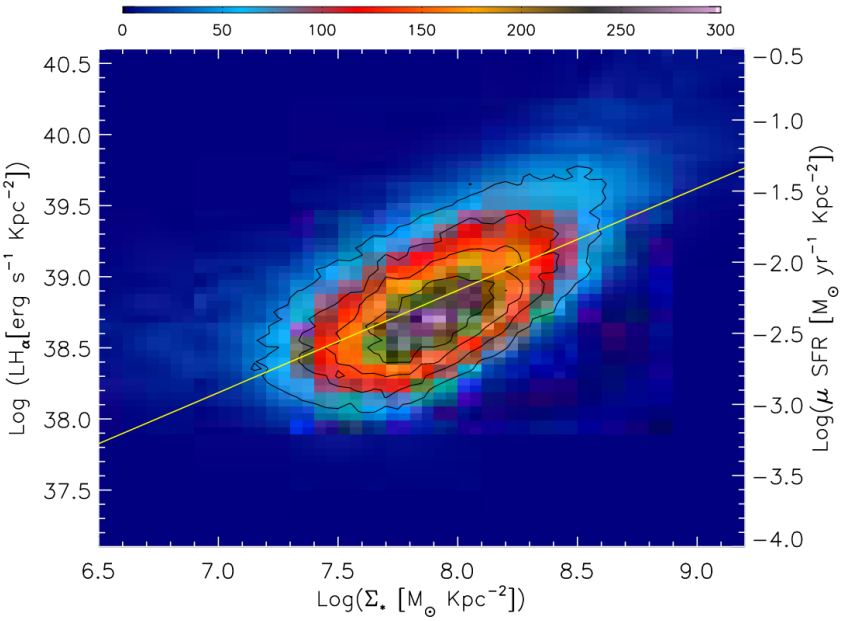

Figure 1.8: Spatially resolved SFMS relation for the CALIFA sample. Colors scale with the number density of datapoints in each [Σ_*, $\Sigma_{\rm SFR}$] bin. Contours enclose the 80%, 60%, 40% and 20% of the total amount of data in the plot. The yellow line marks the best-fitting power law to the data. Credits: Cano-Díaz et al. (2016)

spatially resolved star formation main sequence (rSFMS), with an slope of 0.72 ± 0.04, showed in Fig. 1.8. A possible interpretation of this relation is that SFR is regulated by the interplay between local hydrostatic pressure of the disk and feedback mechanisms (Ostriker et al., 2010; Ostriker & Shetty, 2011). Several subsequent works have studied this spatially resolved relation, finding a scatter of $\sim 0.2-0.3$ dex, and sub-linear slopes (see, e.g., Abdurro'uf & Akiyama, 2017; Hsieh et al., 2017; Liu et al., 2018; Medling et al., 2018; Lin et al., 2019; Ellison et al., 2020a; Morselli et al., 2020; Sánchez et al., 2021)

However, the key ingredient to form stars is cold gas. Hence, it is not surprising that also the Kennicutt-Schmidt relation is preserved towards smaller spatial scales, with a similar slope, and a scatter even lower than that found for the rSFMS ($\sigma \sim 0.2$ dex, e.g., Bigiel et al., 2008; Leroy et al., 2013; Dey et al., 2019; Lin et al., 2019), a.k.a. the resolved Kennicutt-Schmidt relation (rKS). Such a relation implies that the SFR of a given star-forming region depends primarily on the amount of molecular gas available to form stars. A vertical offset in this relation can be interpreted as variations in the star formation efficiency (SFE) at a fixed molecular gas surface density, that could be driven by, e.g., variations in the physical properties of molecular gas clouds (Sun et al., 2020a). A linear slope implies a constant depletion time (defined as $\tau = \Sigma_{\rm mol}/\Sigma_{\rm SFR}$), and a sub-linear slope leads to a depletion time that increases with gas surface density (Shetty et al., 2014).

Finally, the spatially resolved correlation between stellar mass and molecular gas mass surface densities is known as the (resolved) molecular gas main sequence (rMGMS). It was firstly introduced by Lin et al. (2019), although a correlation between these two quantities had been reported earlier (Wong et al., 2013). Its existence implies that either stellar mass dominates the local gravitational potential of the disks, or that the spatial distribution of

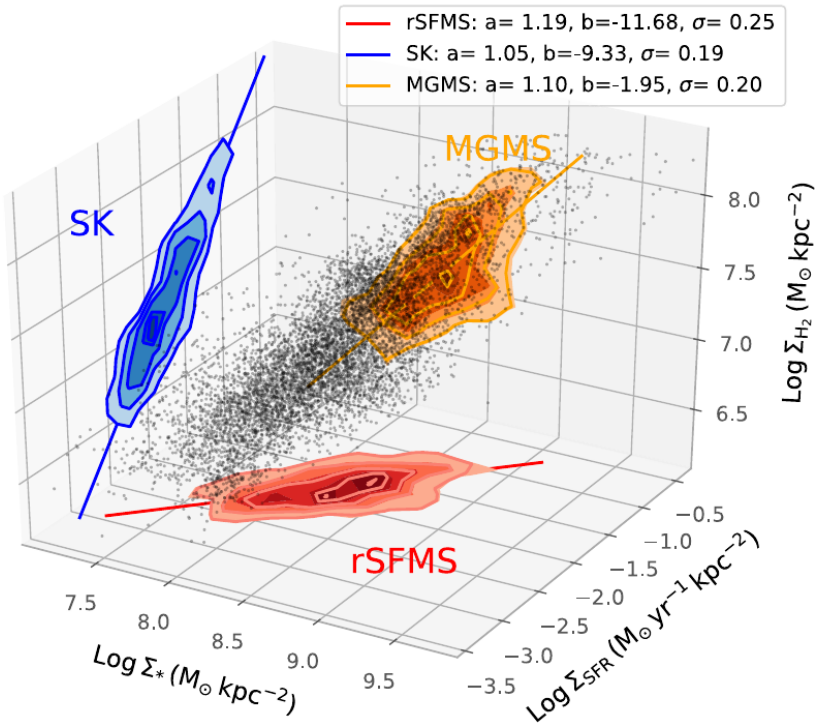

Figure 1.9: The 3D distribution between Σ_*, $\Sigma_{\rm mol}$, and $\Sigma_{\rm SFR}$ computed for 5383 spaxels (black points) identified as star-forming regions in star-forming galaxies from the ALMaQUEST sample. The contours show the relations that result from the projection of the 3D space on the 2D planes (red: rSFMS; blue: rKS; orange: rMGMS). The contour levels show the 20%, 40%, 60%, 80%, and 90% of the density peaks. The best-fit slope (a), intercept (b) and scatter (σ) are indicated in the legend. Credits: Lin et al. (2019)

both, stars and gas, is defined the same gravitational potential set by the underlying total mass (Lin et al., 2019).

These three scaling relations (rSFMS, rMGMS, and rKS) represent a powerful tool to understand the mechanisms controlling star formation at small spatial scales, and recent works often study the interplay between these three quantities (Σ_*, $\Sigma_{\rm mol}$, and $\Sigma_{\rm SFR}$) to shed light on what are the physics regulating the formation of stars (see e.g., Lin et al., 2019; Morselli et al., 2020; Ellison et al., 2020a; Sánchez et al., 2021).

In particular, Lin et al. (2019), using data from the ALMaQUEST survey (spatial resolution ~ 1 kpc; Lin et al., 2020), find that Σ_*, $\Sigma_{\rm mol}$, and $\Sigma_{\rm SFR}$ are strongly correlated, and form a 3D linear (in log) relation, in which the three scaling relations are just 2D projections of this 3D space. Figure 1.9 shows the 3D space conformed by these three quantities. The study of these three correlations suggests that the rSFMS (and its higher scatter, compared to the other relations) can be naturally explained by the combination of the rMGMS and the rKS. A similar conclusion was reached by Morselli et al. (2020), using data from the DustPedia archive (Davies et al., 2017), probing spatial scales of ~ 500 pc, and more recently, by Baker et al. (2022), using data from the ALMaQUEST survey.

The universality and the origin of the scatter of these relations have been a matter of discussion in recent literature. Ellison et al. (2020b) used data from the ALMaQUEST survey

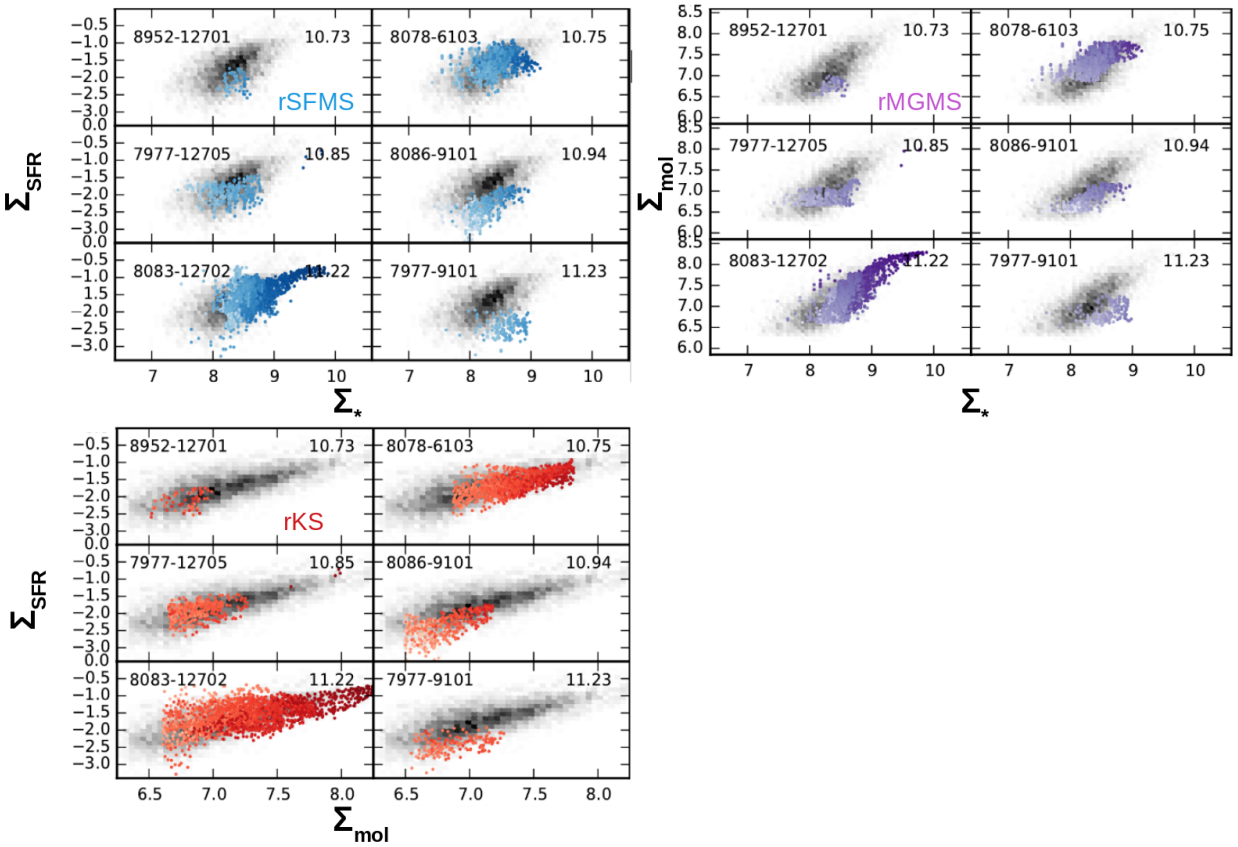

Figure 1.10: rSFMS (blue), rKS (red), and rMGMS (violet) for a fraction of individual galaxies from the ALMaQUEST sample. Significant galaxy-to-galaxy variations exist for the three relations, with individual galaxies lying above or below the overall relations, considering all galaxies (background relation in gray). The color of each dot scales with galactocentric radius, with darker colors representing smaller radius (i.e., inner regions). The total log M_* of each galaxy is indicated on the top right corner of each panel. Credits: Figure adapted from Ellison et al. (2020a)

and concluded that the scatter of the rSFMS is driven by variations in the star formation efficiency, rather than by gas fraction, i.e., regions that form more stars at a fixed Σ_* do so because they transform molecular gas into stars more efficiently, rather than hosting larger gas reservoirs. Sánchez et al. (2021) find, however, that the correlation between the scatter on the rSFMS and changes in SFE (i.e. scatter in the rKS), and more generally, the correlation between the residuals of these three correlations are a pure consequence of the noise in the observed datasets, without physical meaning. Nevertheless, Ellison et al. (2020a) find significant galaxy-to-galaxy variations in these three spatially resolved correlations, which suggest that indeed, there might be additional physical variables driving the scatter of these relations. These galaxy-to-galaxy variations are shown in Fig. 1.10. For the three relations, some galaxies lie preferentially above or below of the overall (all galaxies) relation, and these variations correlate to some degree with global galactic properties such as total stellar mass, specific star formation rate, and Sersic index. Thus, whether the scatter of these relations is dominated by random uncertainties, or there are indeed additional physics introducing systematic differences, and hence, regulating the formation of stars, is yet an open question.

Finally, the spatial scale at which these relations are probed is a relevant quantity that can strongly influence the inferred relations. This is because the physical properties of a star-forming cloud evolve rapidly, within timescales of a few Myr (see e.g., Chevance et al., 2020a). They start as clouds formed primarily out of cold molecular gas. Eventually, first stars are formed, but the surrounding gas and dust obscure their light. When this gas and dust is disrupted and dispersed by stellar feedback, the light emitted by gas ionized by the newly born massive stars is able to escape and reach us (Chevance et al., 2020a). Thus, the same star-forming cloud transits from being dominated by cold molecular gas, to being dominated by ionized gas, which is used as the SFR tracer. At a spatial scale of ∼kpc, each spatial resolution element contains a number of individual star-forming clouds, in different stages of the star-forming process, that are averaged to a representative number of $\Sigma_{\rm mol}$, or $\Sigma_{\rm SFR}$. However, at smaller spatial scales, each spatial resolution element can potentially be dominated by a single star-forming cloud in a specific evolutionary stage of the star-forming process (Schruba et al., 2010; Feldmann et al., 2011; Kruijssen & Longmore, 2014; Kruijssen et al., 2018). Furthermore, at a spatial scale comparable to the size of molecular clouds, the SFR is not homogeneously distributed across the galactic disk, but its distribution is strongly determined by the galactic structure (Schinnerer et al., 2019a; Pan et al., 2022). Moreover, the methodology adopted to account for pixels with SFR values below the detection threshold can significantly impact the measurement (e.g., de los Reyes & Kennicutt, 2019).

In this thesis, I use these spatially resolved scaling relations to study what mechanisms set the level of SFR in a given region of the galactic disk. I will quantify how much these relations vary, not only from one galaxy to another, but also from one galactic environment (disk, spiral arms, bars, centers, and rings) to another, exploring as well the potential origin of these variations. Further, I will assess the impact of spatial resolution on the measurements, to link measurements done in nearby galaxies to those obtained in our own Galaxy.

1.7 Spatially resolved stellar populations in nearby galaxies

The study of stellar populations is critical to shed light on the time evolution of a given galaxy or galactic region. The properties of these populations are directly connected to the process by which a galaxy has assembled its stellar mass. A stellar population can be defined as an ensemble of stars that were born from the same molecular cloud, hence, sharing the same age, chemical composition, and average kinematic properties (Lequeux, 2005). Their stellar mass distribution at birth is described by the initial mass function (IMF) (e.g., Chabrier, 2003). The time evolution of the stellar populations in a galaxy (or galactic region) is encoded in its star formation history (SFH) and its chemical evolution history (ChEH) (de Boer et al., 2012). While the former describes how much mass has been transformed into stars as a function of time, the latter describes how the chemical elements were formed in stars and progressively enriched the ISM of the galaxy. The study of the SFH and the ChEH through the determination of the properties of its stellar populations is known as the fossil record method (Tinsley, 1968).

There are essentially two different ways to implement the fossil record method; parametric, in which one adopts a specific functional form for the SFH or the ChEH (see e.g., Zibetti et al., 2017); and non-parametric, in which the SFH (or ChEH) are defined as single burst of star-formation, where each burst is represented by a single stellar population (SSP) model

with known properties (i.e., age, metallicity). Both approaches present different advantages and limitations. While the parametric method is unable to reproduce in detail the full spectral features of the observed spectra, it provides as an output the parameters that modulate the shape of the SFH (or ChEH), which are more easily interpretable. On the other hand, the flexibility of the non-parametric approach permits to reproduce observed spectral features with more detail, but the interpretation of its results is not straightforward (Sánchez, 2020).

However, it is important to keep in mind that the fossil record method has its limitations, the most important being that it relies heavily on the assumed IMF, stellar evolution isochrones, and stellar libraries (Walcher et al., 2011; Martins, 2021). Furthermore, different codes used to determine the SFH from the observed spectrum might also lead to systematic differences in the result (e.g., San Roman et al., 2019). Nonetheless, despite its limitations, this method has proven to be an extremely powerful tool to unveil the assembly history of galaxies (e.g., Wilkinson et al., 2015; López Fernández et al., 2018; Zhuang et al., 2019; Neumann et al., 2020)

Studying how galaxies progressively assembled their stellar mass as a function of cosmic time is key to understanding how galaxies form and evolve. High-resolution imaging has allowed constraining the assembly histories of galaxies, carrying out morphological and structural studies (e.g., Kormendy, 1993; Kormendy & Kennicutt, 2004; Weinzirl et al., 2011). However, Integral Field Spectroscopy (IFS or IFU) surveys, such as CALIFA (Sánchez et al., 2012), MaNGA (Bundy et al., 2015) and SAMI (Croom et al., 2012), have taken these morphological studies to the next level, enabling the extraction of spectra from different regions of a galaxy simultaneously, with typical spatial resolutions of ~ 1 kpc, and thus, allowing the study of stellar populations and ionized gas properties of different galaxy components, unveiling their assembling process. In the following, we will summarize what we have learned from the study of the SFH (and ChEH) of nearby galaxies in a spatially resolved manner.

1.7.1 Radial structure in the distribution of stellar populations

The way in which stellar populations are distributed in a galaxy is intimately related to the galaxy's assemblying process (e.g., González Delgado et al., 2016). Hence, one of the most studied features in this kind of analysis is the radial structure of stellar population properties. Sánchez-Blázquez et al. (2014) find that age and metallicity gradients in LTGs from the CALIFA dataset are shallow and negative, without a strong correlation with galaxy mass or morphological type. González Delgado et al. (2014b) report similar results, and interpret the negative age gradients as evidence for inside-out growth of galaxies (Mo et al., 1998). The inside-out growth of galaxies was first reported using the fossil record method in spatially resolved data by Pérez et al. (2013), and has been subsequently confirmed by several studies (see e.g., González Delgado et al., 2016; Zheng et al., 2017; García-Benito et al., 2017; López Fernández et al., 2018), although Goddard et al. (2017) find a positive age gradient for early-type galaxies, suggesting an outside-in formation process for these galaxies. Figure 1.11 shows the lookback time at which inner regions (half-light radius; HLR ≤ 0.5) and outer regions ($1.5 \leq$HLR≤ 2.0) assembled the bulk of their current stellar mass, as a function of total stellar mass, local stellar mass surface density, and Hubble type, measured by García-Benito et al. (2017).

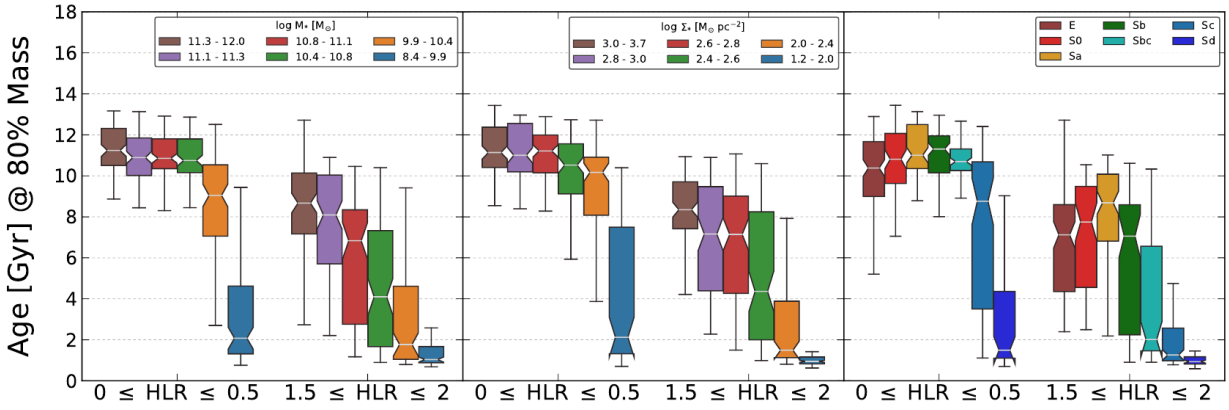

Figure 1.11: Lookback time at which inner regions (HLR $\leq$ 0.5) and outer regions (1.5 $\leq$HLR$\leq$ 2.0) assembled the bulk of their current stellar mass, as a function of total stellar mass, local stellar mass surface density, and Hubble type (from left to right). The innermost regions of galaxies assemble their mass earlier than regions located in the outer parts, at any given stellar mass, stellar mass surface density, and Hubble type. Credits: García-Benito et al. (2017)

González Delgado et al. (2014b) also find steeper age gradients in massive disk galaxies with prominent bulges and negative stellar mass surface density profiles across the full sample, that steepens with total stellar mass. Finally, their findings suggest that while the SFH of disks is intimately connected to the local stellar mass surface density, the SFH of bulges is mostly determined by the total galaxy mass. A similar conclusion was reached for bulges by Breda et al. (2020); however, they report a large scatter in the relation between total mass and age gradient in the bulge, which could be due to additional processes modulating the SFH of bulges (e.g., negative and positive AGN feedback, bar-driven gas inflows).

Wilkinson et al. (2015) and Parikh et al. (2021) used the MaNGA dataset to investigate radial trends as a function of morphological type, and find that, on average, ETGs have flat age and negative metallicity gradients, while LTGs have negative age and metallicity gradients, with more massive LTG showing steeper gradients. Figure 1.12 shows the age and metallicity radial trends across different stellar mass bins for ETGs and LTGs, measured by Parikh et al. (2021). These differences between ETGs and LTGs are consistent with the findings reported in Ibarra-Medel et al. (2016), where the authors study the assembly history of the stellar mass of galaxies from the MaNGA sample, and find that spiral galaxies show a significantly more pronounced inside-out formation mode, compared to ETGs (i.e. a more obvious difference between the formation times of inner and outer regions). Theoretically, an inside-out formation process is expected when the stars are distributed in a rotating disk; since the specific angular momentum increases outwards, the inner parts should form earlier than the outer parts (Larson, 1976; Brook et al., 2006, 2012). However, for low-mass galaxies ($\lesssim 5 \times 10^9 M_\odot$), Ibarra-Medel et al. (2016) find a large diversity in their radial assembly history.

Ibarra-Medel et al. (2016) also find that more massive galaxies assembled their stellar mass earlier in cosmic history than less massive galaxies, a phenomenon established before, on the basis of spatially unresolved data (downsizing; see e.g., Cowie et al., 1996; Heavens et al., 2004; Pérez-González et al., 2008). Pérez et al. (2013), using data from the CALIFA

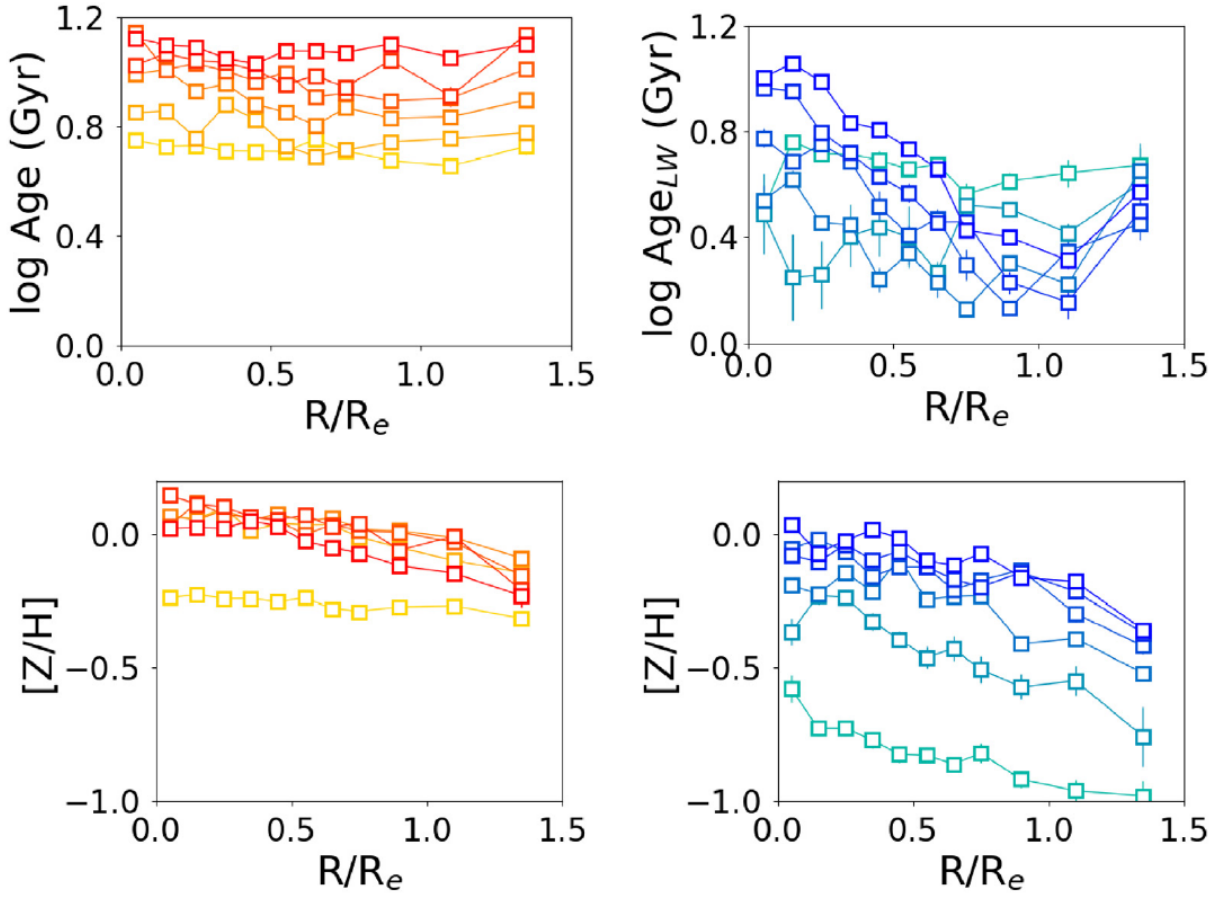

Figure 1.12: Mean stellar ages (top) and metallicities (bottom) as a function of galactocentric distances for ETGs (left) and LTGs (right). The colours represent different mass bins, scaling from $\log M/M_\odot \sim 9.3$ (yellow) to $\log M/M_\odot \sim 11.2$ (red) for ETGs, and from $\log M/M_\odot \sim 8.9$ (green) to $\log M/M_\odot \sim 10.9$ (blue) for LTGs. While ETGs have on average flat age and negative metallicity gradients, LTGs have negative age and metallicity gradients. Credits: Figure adapted from Parikh et al. (2021)

sample, reported for the first time that the signal of downsizing is spatially preserved, with both inner and outer regions growing faster for more massive galaxies.

Finally, Zhuang et al. (2019) studied the origin of the metallicity gradients in galaxies from the CALIFA sample, and find that they arise from the local stellar mass surface density - metallicity relation (González Delgado et al., 2014a), concluding that the spatial distribution of stellar populations within a galaxy is primarily the result of the in-situ local star formation history, rather than being shaped by radial migration. Also, they find that low mass and late type galaxies show more commonly positive metallicity gradients, as opposed to most of the galaxies in the sample, consistent with stellar feedback more efficiently modifying the baryon cycle in the central regions of these galaxies.

1.7.2 Scaling relations of stellar populations properties

What can we learn from these spatially resolved studies of the SFH of nearby galaxies, beyond the radial structure of stellar populations? Zibetti et al. (2017) studied the stellar mass surface density–age distribution in CALIFA galaxies, and find that the global bimodality between old and young/star-forming galaxies, discussed earlier in Sec. 1.2, is mirrored locally in the bimodal age distribution of individual regions. This local bimodality is mainly driven by regions in early-type and late-type galaxies primarily populating the old and the young peak, respectively. However, the age bimodality applies also internally within spiral galaxies, with bulges and interarm regions clustering at older ages than spiral arms. Figure 1.13 shows the spatially resolved bimodality in the stellar mass surface density–log (age) plane, across different Hubble types.

The relation between local stellar mass surface density and local stellar metallicity has also been explored (González Delgado et al., 2014a; Neumann et al., 2021). In particular, Neumann et al. (2021) reports a significant correlation between these two quantities for galaxies of all types and masses. Furthermore, they find that the scatter of this relation correlates with galactocentric distance, which suggests that something else, besides stellar mass surface density, promotes chemical enrichment in the outer parts of galaxies, such as gas accretion, outflows, or radial migration.

1.7.3 Inner structure of galaxies at high spatial resolution

Several works have explored in detail the stellar populations within central structures of nearby galaxies, in the context of the TIMER project (Time Inference with MUSE in Extragalactic Rings; Gadotti et al., 2019), at spatial resolutions of the order of ~ 100 pc. Rosado-Belza et al. (2020) find that kinematic differences caused by different stellar populations can be identified in the central regions of nearby galaxies, by measuring higher velocity dispersion values in the young stellar populations of nuclear rings than in the old ones. Neumann et al. (2020) find that different stellar populations are characterized by different orbital motions within bars. Specifically, intermediate-age stars ($\sim 2-6$ Gyr) are trapped on more elongated orbits shaping a thinner part of the bar, while older stars (> 8 Gyr) are trapped on less elongated orbits shaping a rounder and thicker part of the bar. These measurements are consistent with expectations from chemodynamical simulations of barred galaxies (see e.g., Wozniak, 2007). Bittner et al. (2020) and Bittner et al. (2021) explore the distribution

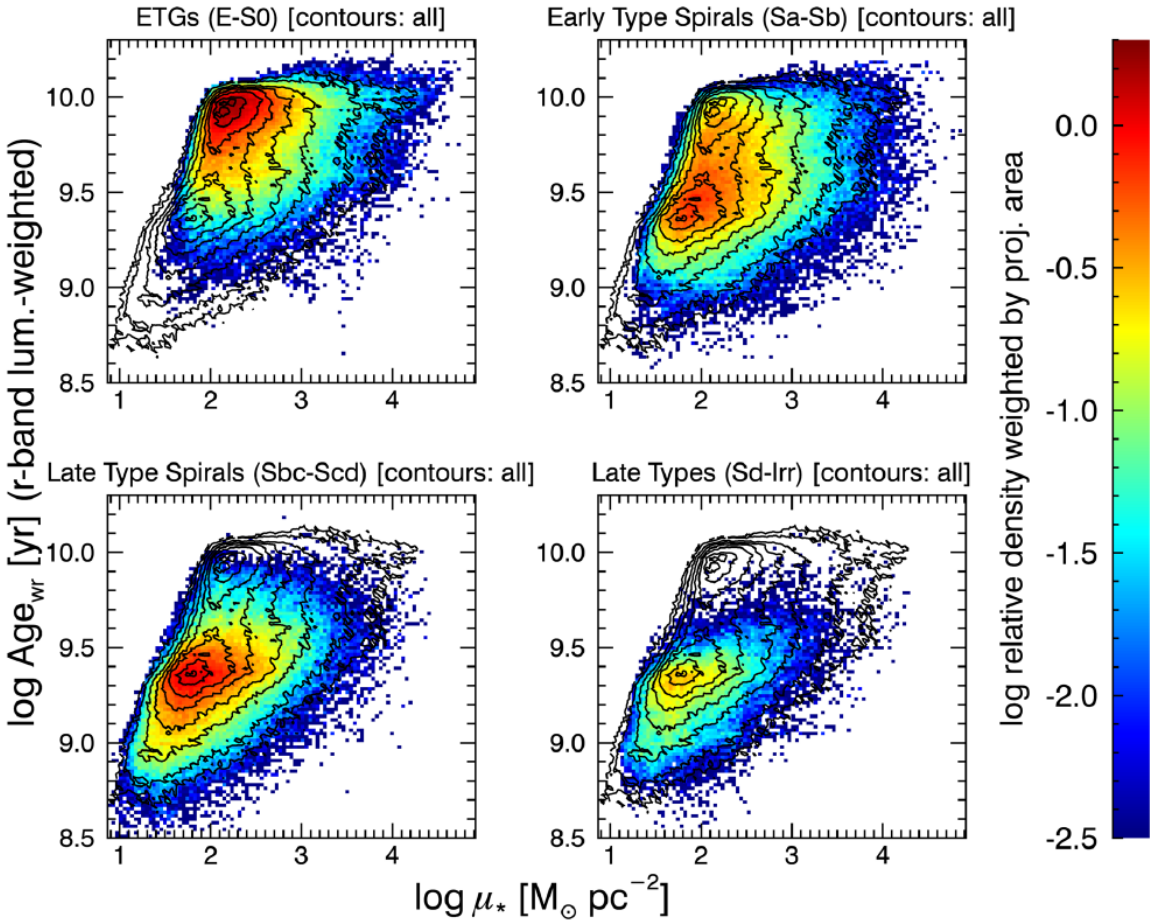

Figure 1.13: Distribution of regions belonging to galaxies of different morphological classes, in the log (age)–log (stellar mass surface density) plane. Contours mark densities that are 0.9, 0.75, 0.5, 0.35, 0.20, 0.1, 0.03 and 0.01 times the maximum density of the overall distribution, i.e., considering all galaxies in the sample. Colors indicate the number density of pixels within each [log(μ_*), log (age)] bin, for galaxies of specific Hubble types, indicated above each panel. Credits: Zibetti et al. (2017)

of stellar populations in the inner structures of galaxies, finding that mass-weighted age and metallicity gradients are slightly shallower along the bar than in the disk, likely due to orbital mixing in the bar, and that inner nuclear rings are the star-forming outer edge of nuclear disks, which are formed by the gas transported towards the galaxy center by the bar.

1.7.4 What comes next in the study of resolved stellar populations?

Recent studies have aimed at resolving the SFH across the galactic structure, and characterized how different regions within galaxies have assembled their stellar mass (Peterken et al., 2019, 2020), by 'time-slicing' galaxies in different age bins. However, the limited spatial resolutions of large IFU surveys place limitations on this kind of study. In this thesis, I will present what we can learn from the spatially resolved SFHs of a sample of LTGs, measured at spatial scales where galactic structure is clearly resolved. Therefore, we can address questions such as, how galactic structure modulates the SFH and the ChEH, or what other local mechanisms drive the growth of galaxies at these spatial scales, contributing to progress in this field.

1.8 PHANGS survey

The work carried out in this thesis is being done in the framework of the Physics at High Angular resolution in Nearby Galaxies (PHANGS[2]; Schinnerer et al., 2019b; Leroy et al., 2021a) project, which aims to sample the different stages of the star formation and feedback cycle, and connecting these measurements to galaxy-scale properties and processes. These goals are addressed through a set of multiwavelength programs that span the spectrum from the far-UV to radio in a sample of local galaxies that is representative of where stars form in the z = 0 Universe. The galaxies from the PHANGS sample have measured distances typically lower than 20 Mpc, to resolve typical star-forming region scales of 50-100 pc. They are relatively face-on, with inclinations mostly lower than 60°, to limit the effect of extinction and make identifying individual clouds easier, and they sample the SFMS of galaxies across nearly two orders of magnitud, in the range of $9.18 \lesssim \log M_* \lesssim 11.15$.

The main observational campaigns conducted within PHANGS are the PHANGS-ALMA Large Program (PI: E. Schinnerer; Leroy et al., 2021a), which maps the CO $J = 2 \rightarrow 1$ emission, hereafter CO(2-1), for 90 ALMA-accessible star-forming galaxies. A sub-sample of 38 of these galaxies have also been observed as part of the PHANGS-HST (PI: J. Lee; Lee et al., 2022) Treasury program, whose UV-optical imaging enables the study of young star clusters and stellar associations. Finally, 19 of these galaxies comprise the sample of the PHANGS-MUSE Large Program (PI: E. Schinnerer; Emsellem et al., 2022), where the VLT/MUSE instrument is used to measure the properties of ionized gas and stellar populations at a resolution matched to ALMA. Star-forming galaxies within the PHANGS sample are also diverse in terms of internal structure, including strongly barred and unbarred galaxies, grand-design spirals, flocculent spiral, and irregular galaxies withouth any obvious morphological feature. Figure 1.14 shows how these galaxies populate the SFMS, spanning a dynamical range of ~ 2 dex in total stellar mass.

[2] http://phangs.org/

In addition to the three main pillars, there exist other complementary programs that include high-resolution far-UV imaging with AstroSAT (PI: E. Rosolowsky), ground-based narrowband Hα data using the MPG 2.2 m/WFI and Du Pont/DirectCCD instruments (PIs: G. Blanc, I.-T. Ho; A. Razza et al. in preparation), H I imaging using the Very Large Array (VLA) and MeerKAT (PI: D. Utomo), Keck Cosmic Web Imager (KCWI) spectroscopy (PI: K. Sandstrom), Canada-France-Hawaii Telescope SITELLE [O II] imaging (PI: A. Hughes), and Russian 6m Fabry-Perot Interferometre spectroscopy (PI: E. Egorov). Finally, the 19 galaxies with available ALMA, MUSE and HST data have also been awarded a James Webb Space Telescope (JWST) Treasury programme (PI: J. Lee), enabling the measurement of the timescales and efficiencies of the earliest phases of star formation and stellar feedback, and the study of the dust grain properties as function of local ISM conditions.

The work presented in this thesis is primarily based on data from the PHANGS-MUSE and PHANGS-ALMA surveys, and in the following sections, I will describe these programs in detail, placing them in context with other large surveys which are relevant to the field.

1.8.1 PHANGS-ALMA

ALMA has allowed us to observe molecular line emission in nearby galaxies at a resolution of ~ 1" and with sensitivity better than previous molecular gas surveys with unprecedented observing efficacy (Wootten & Thompson, 2009). This faster survey speed enables PHANGS-ALMA surveying a large and representative sample of local galaxies at a spatial resolution of ~ 100pc, comparable to the size of individual giant molecular clouds ($M_{mol} > 10^5 M\odot$; e.g., Solomon et al., 1987; Bolatto et al., 2008; Freeman et al., 2017; Rosolowsky et al., 2021). These characteristics make PHANGS-ALMA an ideal sample to measure the demographics, kinematics, and spatial distribution of molecular gas (clouds) in nearby galaxies. Specifically, the main science goal for which PHANGS-ALMA was designed can be summarized as follows:

- Study the physical properties of molecular clouds, and measure how these properties depend on galaxy-scale characteristics of the host galaxy, as well as the location of the cloud within a galaxy.
- Measure how the efficiency with which these clouds form stars, and how this efficiency depends on properties of the molecular cloud, such as density, or dynamical state.
- Quantify the transition between the different phases of the star-forming cycle, going from quiescent non-star-forming clouds, to the stage in which they are disrupted by the feedback from newly born stars.
- Link the self-regulation of the large-scale structure of galactic galaxy disks, to the cloud-scale physical mechanisms where the self-regulation is thought to emerge. This is, investigating the relation between the different mechanisms playing a role in the pressure balance within the galactic disk across different spatial scales.
- Characterize the kinematics and structure of molecular gas in galaxies, which is not captured by low-resolution studies.

Previous surveys have mapped the CO emission in the Local Group of galaxies at high spatial resolution, including the Magellanic Clouds (Wong et al., 2011), M31 (Nieten et al.,

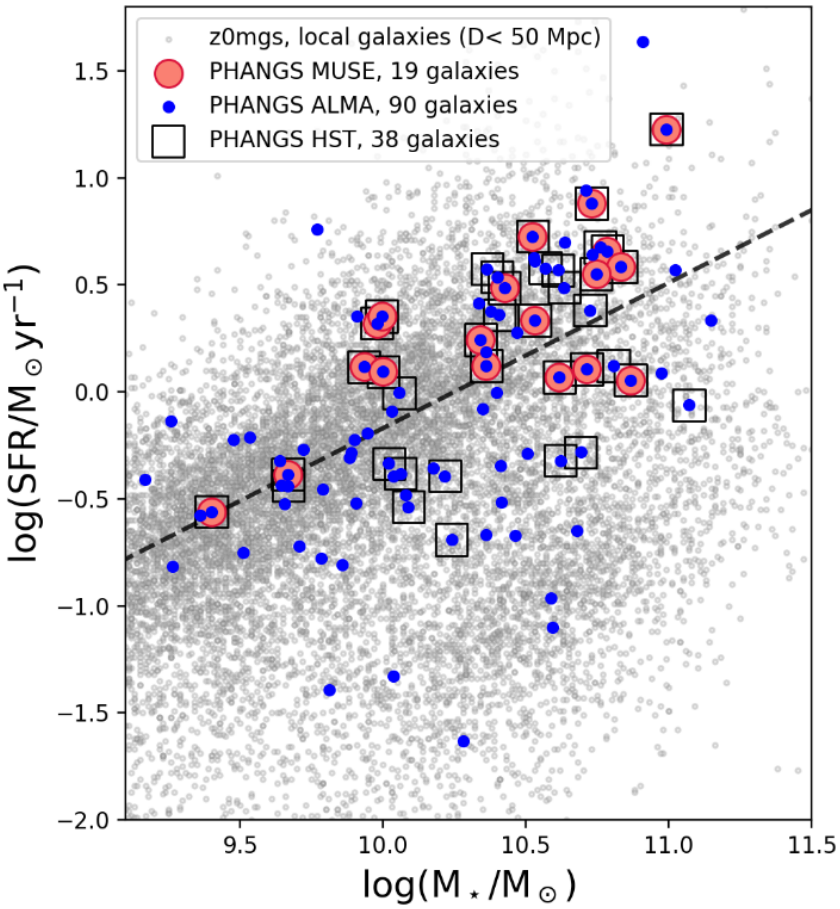

Figure 1.14: PHANGS sample compared with the population of local galaxies from z0MGS (Leroy et al., 2019, small grey dots). The blue circles represent the galaxies from the PHANGS-ALMA sample, the open black square represent the galaxies from the PHANGS-HST sample, and the filled red circles are galaxies from the PHANGS-MUSE survey. The black dashed line shows the best fit to the SFMS, as determined by Leroy et al. (2019). Credits: Emsellem et al. (2022)

2006; Rosolowsky et al., 2007), M33 (Rosolowsky et al., 2007; Onodera et al., 2012; Druard et al., 2014), as well as other dwarf galaxies (Leroy et al., 2006). However, the low number of galaxies within the Local Group, together with the poor coverage of the parameter space (e.g., M_*, SFR, etc.), and the lack of diversity in terms of morphology and galactic structure render the Local Group not a representative sample to study star formation at $z = 0$.

Additionally, before ALMA, mapping the CO emission at a resolution comparable to the size of GMCs in a single normal star-forming galaxy represented a major time investment. In this regard, the CANON survey (Koda & Nearby Galaxies CO Survey Group, 2009) took an important step toward the cloud-scale mapping of a sample of spiral galaxies beyond the Local Group, providing important evidence for variations in molecular gas properties as a function of galactic environment. A subsequent relevant survey was the PdBI Arcsecond Whirlpool Survey (PAWS; Pety et al., 2013; Schinnerer et al., 2013), which mapped M51 at a resolution of ~ 40pc, and revealed significant differences in the distribution of the molecular gas, compared to galaxies from the Local Group (Hughes et al., 2013). Furthermore, PAWS studies also showed how high-resolution mapping could shed light on the evolution and timescales of individual star-forming regions (Schinnerer et al., 2013; Meidt et al., 2015; Schinnerer et al., 2017). Despite these efforts, the limited sample size of high spatial resolution CO observations in nearby galaxies has been a major drawback in the search for a representative view of the molecular gas properties in the local Universe.

On the other hand, there are surveys of molecular gas in nearby galaxies that have mapped a larger number of galaxies, with a lower ($\sim$kpc) spatial resolution, e.g., STING (Rahman et al., 2011), HERACLES (Leroy et al., 2009), NRO COMING (Sorai et al., 2019). Although these surveys have demonstrated a close link between molecular gas and star formation (e.g., Schruba et al., 2011), they are not able to distinguish individual molecular clouds, and thus, offer limited insight into the physical state of molecular gas. Moreover, in low-resolution observations, the CO emission from GMCs is diluted with nearby non-CO emitting regions, producing an apparent relatively smooth distribution, which does not reflect the intrinsic distribution of CO emission in galaxies, strongly clumped on scales much smaller than 1kpc (e.g., Pan et al., 2022).

Thus, PHANGS-ALMA is the first cloud-scale resolution molecular gas survey of a representative sample of nearby star-forming galaxies. These data offer an unprecedented view of the physics that govern giant molecular gas clouds and star-forming regions, and hence, shape the growth of galaxies in the local Universe. An exhaustive description of the PHANGS-ALMA survey, and the associated science data-products can be found in Leroy et al. (2021a) and Leroy et al. (2021b), respectively.

1.8.2 PHANGS-MUSE

PHANGS-MUSE provides the first integral field spectrograph view of star formation across different local environments, allowing detailed studies of the demographics and characteristics of individual H II regions and other ionized nebulae. Furthermore, PHANGS-MUSE allows the study of gas and stellar kinematics, and provides constraints on the star formation history and chemical evolution history of galaxies. Figure 1.15 summarizes some of the key outputs that can be extracted from the MUSE mosaics, and how this data set complements the PHANGS-ALMA and PHANGS-HST surveys.

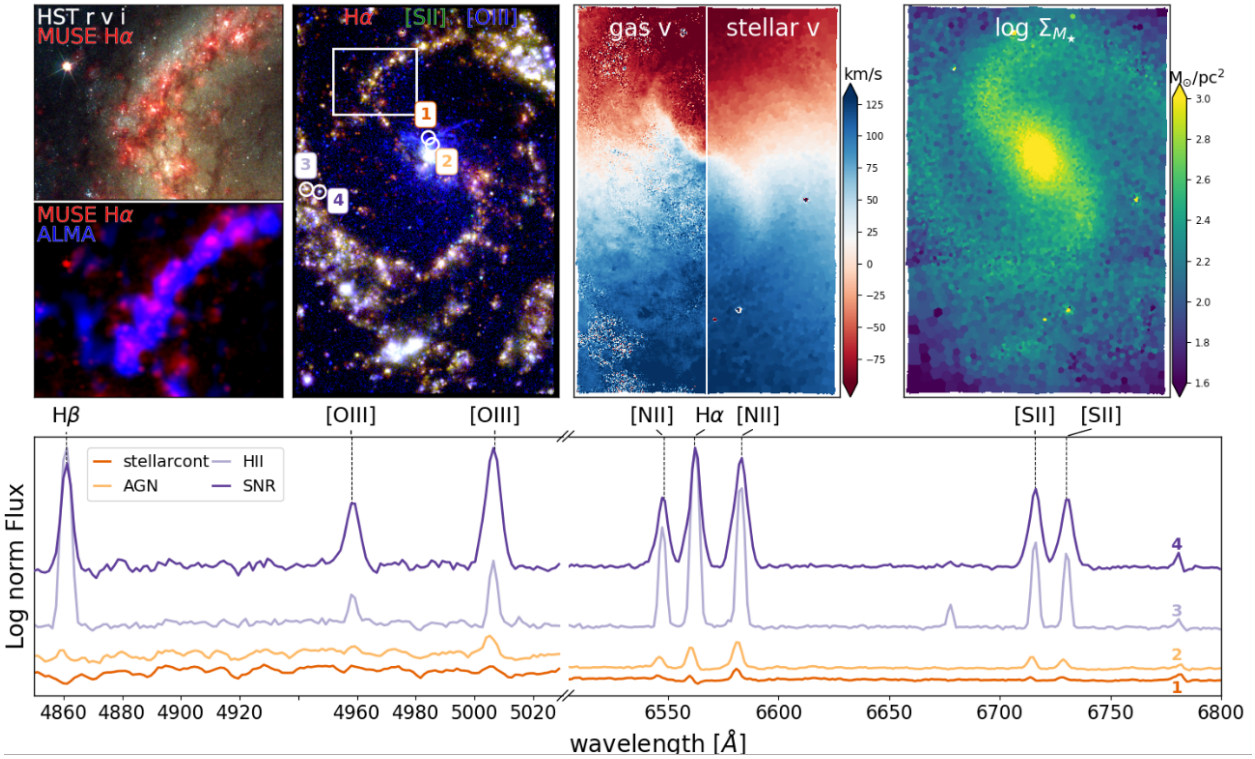

Figure 1.15: Multi-wavelength view of NGC4535. Top, second panel from the left: Emission line maps for Hα in red, [S II] in green, and [O III] in blue. The ionized gas traces star formation occuring preferentially in the spiral arms. Differences in the relative strenght of these emission lines are indicative of variations on the physical conditions of the gas. Top, second panel from right: gas and stellar velocity fields, mapped by MUSE. The maps show clear deviations from regular rotation, indicative of non-circular motion driven by the spiral and bar structures. Top, right panel: The stellar mass surface density map of the galaxy, important to constrain the underlying gravitational potential. Top, left panels: Zooming into one section of the spiral arm (white box in emission line maps), showing the spatial offset between the HST star clusters and ionized gas (upper panel) and between the ionised gas and ALMA molecular gas (lower panel), demonstrating the evolution of the star-forming cycle across the spiral pattern. Bottom panel: spectra extracted from the regions labeled from 1 to 4 in the emission line map, chosen to exemplify the typical characteristics of different regions: 1- dominated by stellar continuum (red); 2- AGN (orange); 3- H II regions (light purple), and 4- supernova remnants (SNR; purple). Credits: Emsellem et al. (2022)

The PHANGS-MUSE survey consists of 168 MUSE pointings and a total of nearly 15×10^6 spectra, at a median physical resolution of 50pc. Each VLT/MUSE pointing consists of a 1' $\times$ 1' field of view sampled at 0.2" per pixel, with a typical spectral resolution of ~ 2.5Å (~ 70 km s^{-1}) covering the wavelength range of $4800 - 9300$Å. Nine out of the 19 galaxies were observed using wide-field adaptive optics (AO). The angular resolution ranges from ~ 0.5" to ~ 1.0" for the targets with and without AO, respectively.

Given that the PHANGS-MUSE effort started at the same time as the PHANGS-ALMA Large Programme, the target selection focused on the 19 galaxies that were already observed as part of the ALMA pilot projects, or had ALMA archival data of similar characteristics.

The sample covers a wide range of stellar masses ($9.4 < \log\log M/M_* < 11.0$), but is biased towards high masses and high SFR values (see Fig. 1.14). The sample does not include any of the Green Valley targets from PHANGS-ALMA survey.

The main scientific goals of the PHANGS-MUSE survey can be summarized as follows:

- Study the interplay between stellar mass, molecular gas mass, and SFR surface densities at small spatial scales (i.e. star-forming scaling relations, see Sec. 1.6) to get insights on the physics that modulate the formation of stars.
- Investigate the impact of stellar feedback across different galactic environments.
- Quantifying the chemical enrichment and mixing of material in galactic disks.
- Study the role of different dynamical regimes (gas flows, compression, or shocks, etc.) on the triggering, boosting or inhibiting of star formation.
- Further emission-line based studies, such as precise distance determination via planetary nebula luminosity functions, or identification of supernova remnants.

Finally, it is informative to compare PHANGS-MUSE with other programmes aiming at obtaining both molecular gas and optical IFU spectroscopy of nearby galaxies. This multi-wavelength combination is extremely valuable to study ISM physical conditions, linking molecular- and ionized-gas properties with galactic potential and structure. The only comparable efforts in this sense are EDGE-CALIFA (Bolatto et al., 2017), consisting of a sample of 126 galaxies, and ALMaQUEST (Lin et al., 2020), with a sample of 46 galaxies. Although the larger samples of these surveys provide a more uniform sampling of the main sequence, and extend to the Green Valley, they both observe galaxies at a resolution of the order of ∼kpc, insufficient to resolve the physics of star formation on the scale of individual clouds, and address the science questions intended by PHANGS-MUSE.

There are other relevant optical IFU surveys that lack, however, of a molecular gas view. SAMI (Croom et al., 2012), reaches spatial resolutions of the order of ∼kpc, and is therefore, also unable to resolve individual star forming regions, although it probes a considerable higher number of galaxies. Other MUSE based surveys that reach physical resoutions similar to PHANGS-MUSE are TIMER (Gadotti et al., 2019), MAD (Erroz-Ferrer et al., 2019), and GASP (Poggianti et al., 2017). TIMER focuses on mapping primarily the inner structure of nearby galaxies, and studying the impact of AGNs on galaxy evolution, and hence, it is not representative of the full galactic disk. GASP studies ongoing and past ram pressure stripping events, thus, their sample is designed to address specific science questions, and does not provide a representative sampling of the SFMS galaxies. Finally, the MAD survey focuses on focuses on SFMS galaxies, but obtained only one central MUSE pointing per object (two-pointings mosaic in a few exceptional cases). This implies that MAD probes only the inner regions of nearby galaxies, and the full galactic disk, but at coarser spatial resolution > 200 pc, for most distant galaxies, starting to blend structures at the spatial scale of GMCs and H II regions.

Figure 1.16 shows PHANGS-MUSE compared to other IFU surveys, in terms of number of galaxies, number of spatial resolution elements, and physical resolution.

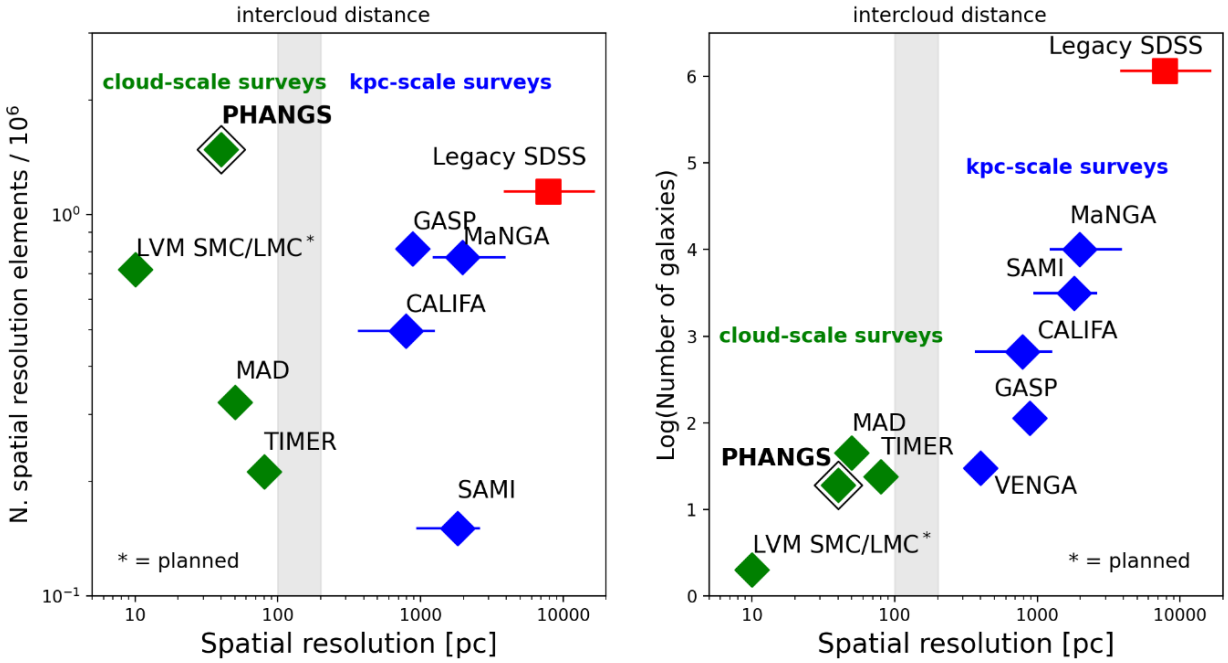

Figure 1.16: Comparison of PHANGS-MUSE with other relevant IFU surveys, in terms of number of galaxies, number of spatial resolution elements, and physical resolution. Surveys that reach the spatial scales of star-forming regions are marked with green diamonds, and surveys that reach ∼kpc scales are marked with blue diamonds. The galaxy-scale SDSS survey (Abazajian et al., 2009) is marked with a red square for reference. PHANGS-MUSE appears ranking high in terms of spatial resolution and number of spatial resolution elements (left). In terms of number of galaxies, PHANGS-MUSE lies on the overall trend line of other IFU surveys. Credits: Emsellem et al. (2022)

PHANGS-MUSE is an incredibly information-rich data set, able to map kinematic and chemical properties of gas and stars at the resolution of star-forming regions. Together with data sets from other PHANGS efforts, they offer a unique multi-wavelength view of the star-forming galaxies in the local Universe, through a balance between representativeness of the sample and spatial resolution. An extensive description of the PHANGS-MUSE survey, and the science-ready data products generated from the MUSE data can be found in Emsellem et al. (2022).

1.9 Outline of this thesis

Studying the mechansims that modulate the evolution of galaxies is important in order to understand how the Universe that we see today formed from its initially homogeneus state. The study of the present-day SFR of galaxies, together with the study of their cosmic star formation history offer a fairly comprehensive view of this evolution. In particular, studying these mechanisms in nearby galaxies offers the additional advantage of a spatially resolved perspective, acknowledging that galaxies are extended objects, in which the physical properties of a given region can drastically differ from the physical properties of a region located somewhere else within the same galaxy.

The overview in galaxy evolution and star formation presented here summarizes a number of recent efforts to understand how nearby galaxies have assembled their stellar mass (and countinue doing so), leading to key findings in the context of galaxy evolution, such as that the SFMS is spatially resolved at sub-galactic spatial scales, implying that the mechanisms that regulate the formation of stars operate at 'local' spatial scales, or that the distribution of stellar populations in late-type galaxies in consistent with an inside-out formation scenario.

However, these efforts have been limited by either a small sample of galaxies, not representative of the local Universe, or by low spatial resolution that does not allow to resolve individual star-forming regions, and therefore, studying the physical conditions of the ISM, and its connection to the local SFR is not straightforward.

In this thesis, I exploit the PHANGS-MUSE and PHANGS-ALMA data sets to study the star-forming scaling relations (Sec. 1.6) and stellar populations (see Sec. 1.7) in nearby galaxies, at spatial scales of the order of $\sim$ 100pc. Specifically, I will address questions such as:

- **What is, or are the main physical mechanisms that set the SFR across galaxies?** In Chapter 2, I will derive the star formation scaling relations at an spatial scale comparable to that of giant molecular clouds, and infer what are the most relevant factors that determine the level of SFR in a given region of the galaxy. I will also explore what are the mechanisms setting the slope of these relations, and how these findings relate to lower-resolution measurements.

- **Can we quantify differences in the physical processes that set the SFR across different galactic environments (e.g., bars and spiral arms)?** In Chapter 3, I will explore the universality of the interplay between local stellar mass, molecular gas mass, and SFR surface densities across different galactic environments (namely spiral arms, bars, centers, rings, and disks). If the relations between these three quantities are the same across different environments, it would imply that stellar mass and molecular gas mass are the only relevant drivers of star formation. Otherwise, it would be an indication that there could be an additional factor(s) playing a role in regulating the formation of stars, that is not captured neither by local stellar mass surface density, nor by local molecular gas surface density.

- **How can we measure gas and stellar population properties from the MUSE mosaic of PHANGS galaxies?** In Chapter 4, I describe the methodology adopted to produce science-ready data products from the MUSE mosaics of galaxies from the PHANGS-MUSE survey. This work is framed in the development of the PHANGS-MUSE data analysis pipeline, of which I am one of the main developers.

- **How are different stellar populations distributed across the disks of main sequence galaxies, and what do these distributions tell us about the assembly history of these galaxies?** In Chapter 5, I will present a detailed study of the stellar populations, deriving spatially resolved SFHs to unveil how galaxies have assembled, and show what we can learn from the spatial distribution of the different stellar populations across galactic disks, at a resolution of $\sim$ 100pc.

Finally, Chapter 6 summarizes the main results of this thesis and provides a brief outlook on possible future avenues.

2 Star formation scaling relations at ∼100 pc from PHANGS: Impact of completeness and spatial scale

The content of this chapter is based in the published article "Star formation scaling relations at ∼100 pc from PHANGS: Impact of completeness and spatial scale", Pessa et al. (2021), of which I am the lead author and has been adapted for this thesis.

The complexity of star formation at the physical scale of molecular clouds is not yet fully understood. We investigate the mechanisms regulating the formation of stars in different environments within nearby star-forming galaxies from the Physics at High Angular resolution in Nearby GalaxieS (PHANGS) sample. Integral field spectroscopic data and radio-interferometric observations of 18 galaxies were combined to explore the existence of the resolved star formation main sequence ($\Sigma_{\rm stellar}$ versus $\Sigma_{\rm SFR}$), resolved Kennicutt–Schmidt relation ($\Sigma_{\rm mol.gas}$ versus $\Sigma_{\rm SFR}$), and resolved molecular gas main sequence ($\Sigma_{\rm stellar}$ versus $\Sigma_{\rm mol.gas}$), and we derived their slope and scatter at spatial resolutions from 100 pc to 1 kpc (under various assumptions). All three relations were recovered at the highest spatial resolution (100 pc). Furthermore, significant variations in these scaling relations were observed across different galactic environments. The exclusion of non-detections has a systematic impact on the inferred slope as a function of the spatial scale. Finally, the scatter of the $\Sigma_{\rm mol.gas+stellar}$ versus $\Sigma_{\rm SFR}$ correlation is smaller than that of the resolved star formation main sequence, but higher than that found for the resolved Kennicutt–Schmidt relation. The resolved molecular gas main sequence has the tightest relation at a spatial scale of 100 pc (scatter of 0.34 dex), followed by the resolved Kennicutt–Schmidt relation (0.41 dex) and then the resolved star formation main sequence (0.51 dex). This is consistent with expectations from the timescales involved in the evolutionary cycle of molecular clouds. Surprisingly, the resolved Kennicutt–Schmidt relation shows the least variation across galaxies and environments, suggesting a tight link between molecular gas and subsequent star formation. The scatter of the three relations decreases at lower spatial resolutions, with the resolved Kennicutt–Schmidt relation being the tightest (0.27 dex) at a spatial scale of 1 kpc. Variation in the slope of the resolved star formation main sequence among galaxies is partially due to different detection fractions of $\Sigma_{\rm SFR}$ with respect to $\Sigma_{\rm stellar}$.

2.1 Introduction

In the current paradigm of evolution of galaxies, star formation occurs inside cold and dense molecular gas clouds. This process is regulated by complex small- and large-scale physics, such as feedback from recently born stars and supernovae resulting from the death of the most massive stars, magnetic fields or hydrostatic pressure exerted by the baryonic mass (Kennicutt & Evans, 2012; Ostriker & Shetty, 2011; Heyer & Dame, 2015; Kruijssen et al., 2019; Krumholz et al., 2019; Chevance et al., 2020b). As a result of the interplay of such regulating mechanisms, different scaling relations at galactic scales arise between the total amount of star formation in a galaxy and the physical quantities that contribute to its regulation.

In this regard, the star formation main sequence (SFMS) is a tight (scatter of ∼0.3 dex) relation between the total star formation rate (SFR) of a galaxy and its total stellar mass. It consists of a power law, with a slope of ∼1, and it has been studied in the local Universe and at a higher redshift (Brinchmann et al., 2004; Daddi et al., 2007; Noeske et al., 2007; Salim et al., 2007; Lin et al., 2012; Whitaker et al., 2012; Speagle et al., 2014; Saintonge et al., 2016; Popesso et al., 2019). Similarly, the Kennicutt–Schmidt relation has been extensively studied as it offers an alternative perspective on what drives the SFR in a galaxy. It correlates the total SFR with the total amount of gas and is consistent with a power law of order unity, even though the methodology does have an impact on the specific quantitative description (Schmidt, 1959; Kennicutt, 1998; Wyder et al., 2009; Genzel et al., 2010; Tacconi et al., 2010; Bigiel et al., 2011; Schruba et al., 2011; Genzel et al., 2012).

Recent studies have demonstrated that these relations hold down to kiloparsec and sub-kiloparsec spatial scales, although their scatter is expected to raise below a critical spatial scale due to statistical undersampling of the star formation process (Schruba et al., 2010; Feldmann et al., 2011; Kruijssen & Longmore, 2014; Kruijssen et al., 2018). The so-called resolved star formation main sequence (rSFMS; Cano-Díaz et al., 2016; Abdurro'uf & Akiyama, 2017; Hsieh et al., 2017; Liu et al., 2018; Medling et al., 2018; Lin et al., 2019; Ellison et al., 2020a; Morselli et al., 2020) and resolved Kennicutt–Schmidt relation (rKS; Bigiel et al., 2008; Leroy et al., 2008; Onodera et al., 2010; Schruba et al., 2011; Ford et al., 2013; Leroy et al., 2013; Kreckel et al., 2018; Williams et al., 2018; Dey et al., 2019) correlate the local star formation rate surface density ($\Sigma_{\rm SFR}$) with the local stellar mass surface density ($\Sigma_{\rm stellar}$) and molecular gas surface density ($\Sigma_{\rm mol.gas}$), respectively. However, there remains debate about the slope of these scaling relations, and it is known that their values depend on the specific approach used for their calculation (e.g., fitting technique; Calzetti et al., 2012; de los Reyes & Kennicutt, 2019). Previous works have uncovered that their slope and scatter may link the physics from global to smaller scales. Moreover, the scatter of the rKS has been interpreted as individual star-forming regions undergoing independent evolutionary life cycles (Schruba et al., 2010; Feldmann et al., 2011), and its dependence on spatial scale provides insight into the timescales of the star formation cycle (Kruijssen & Longmore, 2014; Kruijssen et al., 2018). Additionally, Bacchini et al. (2019a, 2020) found a tight correlation between the gas and the SFR volume densities in nearby disk galaxies, suggesting that the scatter of the rKS could be in part related to projection effects caused by the flaring scale height of gas disks. In addition to the rSFMS and the rKS, recently Lin et al. (2019), Ellison et al. (2020a), and Morselli et al. (2020) reported the existence of a resolved molecular

gas main sequence (rMGMS) as the correlation between the local $\Sigma_{\rm mol.gas}$ and local $\Sigma_{\rm stellar}$, and several other studies have explored different forms of correlations between these locally measured quantities (Matteucci et al., 1989; Shi et al., 2011; Dib et al., 2017; Shi et al., 2018; Dey et al., 2019; Lin et al., 2019; Barrera-Ballesteros et al., 2021a)

The existence of these scaling relations suggests that their global counterparts are an outcome of the local mechanisms that drive star formation, and studying these relations and their respective scatter provides powerful insight into the local physical processes regulating the formation of stars. While the correlation between $\Sigma_{\rm SFR}$ and $\Sigma_{\rm mol.gas}$ is physically more intuitive, since molecular gas is the fuel for new stars, the origin of the relation between $\Sigma_{\rm SFR}$ and $\Sigma_{\rm stellar}$ is more uncertain. It can be understood as the interplay between local hydrostatic pressure of the disk and feedback mechanisms regulating the formation of new stars (Ostriker et al., 2010; Ostriker & Shetty, 2011). On the other hand, using the ALMA-MaNGA QUEnch and STar formation (ALMaQUEST) survey (Lin et al., 2020), Lin et al. (2019) conclude that the rSFMS likely arises due to the combination of the rKS and the rMGMS, while the latter results from stars and gas following the same underlying gravitational potential.

In this chapter we aim to probe these scaling relations to understand the mechanisms that locally regulate star formation, using ∼100 pc spatial resolution data from the PHANGS survey. We measured the slope and scatter of these resolved scaling relations in individual galaxies and in our combined sample. We study the universality of these relations and the processes driving galaxy-to-galaxy variations. Additionally we study how the spatial scale of the data, fitting approach, and systematic assumptions, such as the CO-to-H_2 conversion factor, impact our results.

This chapter is structured as follows: In Sec. 5.2 we present our data set, and in Sec. 3.3 we describe the methods used in our analysis. In Sec. 3.4 we present our main results. In Sec. 2.5 we discuss our findings and their implications. Finally our conclusions are summarized in Sec 3.6.

2.2 Data

We use a sample of 18 star-forming galaxies, all of them are close to the SFMS of galaxies. These galaxies represent a subsample of the Physics at High Angular resolution in Nearby GalaxieS (PHANGS[3]) survey (Leroy et al., 2021a). The galaxies from the PHANGS survey have been selected to have a distance lower than 20 Mpc to resolve the typical scale of star-forming regions (50−100 pc) and to be relatively face on ($i < 60°$) to limit the effect of extinction and make the identification of clouds easier. These galaxies have been chosen to be a representative set of galaxies where most of the star formation is occurring in the local Universe. Our sample is summarized in Table 3.1 where we use the global parameters as reported by Leroy et al. (2021a) based on the distance compilation of Anand et al. (2021) as well as the inclinations determined by Lang et al. (2020).

[3] http://phangs.org/

2.2.1 VLT/MUSE

We make use of the PHANGS-MUSE survey (PI: E. Schinnerer; Emsellem et al., 2022) This survey employs the Multi-Unit Spectroscopic Explorer (MUSE; Bacon et al., 2014) optical integral field unit (IFU) mounted on the VLT UT4 to mosaic the star-forming disk of 19 galaxies from the PHANGS sample. These galaxies correspond to a subset of the 74 galaxies from the PHANGS-ALMA survey (PI: E. Schinnerer; Leroy et al., 2021a). However, we have excluded one galaxy from the PHANGS-MUSE sample (NGC 0628) because its MUSE mosaic was obtained using a different observing strategy, leading to differences in data quality. The target selection for the PHANGS-MUSE sample focused on galaxies from the PHANGS parent sample that had already available ALMA data, as part of the ALMA pilot project, or from the ALMA archival.

The mosaics consist of 3 to 15 individual MUSE pointings. Each pointing provides a $1' \times 1'$ field of view sampled at 0.2 arcsecond per pixel, with a typical spectral resolution of ∼2.5 Å (∼40 km s^{-1}) covering the wavelength range of 4800−9300 Å. The total on-source exposure time per pointing for galaxies in the PHANGS-MUSE Large Program is 43 min. Nine out of the 18 galaxies were observed using wide-field adaptive optics (AO). These galaxies are marked with a black dot in the first column of Table 3.1. The spatial resolution ranges from ∼0.5 to ∼1.0 arcsecond for the targets with and without AO, respectively. Observations were reduced using a pipeline built on `esorex` and developed by the PHANGS team[4] (Emsellem et al., 2022). The total area surveyed by each mosaic ranges from 23 to 692 kpc^2. Once the data have been reduced, we have used the PHANGS data analysis pipeline (DAP, developed by Francesco Belfiore and Ismael Pessa) to derive various physical quantities. The DAP will be described in detail in Emsellem et al. (2022). It consists of a series of modules that perform single stellar population (SSP) fitting and emission line measurements to the full MUSE mosaic. Some of these outputs are described in Secs. 3.2.4 and 3.2.5.

2.2.2 ALMA

The 18 galaxies have CO(2–1) data from the PHANGS-ALMA Large Program (PI: E. Schinnerer; Leroy et al., 2021a). We used the ALMA 12m and 7m arrays combined with the total power antennas to map CO emission at a spatial resolution of 1.0−1.5 arcsecond. The CO data cubes have an rms noise of ∼0.1 K per 2.5 km s^{-1} channel (corresponding to $1\sigma(\Sigma_{\rm mol.gas}) \approx 2$ M$_\odot$ pc^{-2} per 5 km s^{-1} interval). The inclusion of the Atacama Compact Array (ACA) 7m and total power data means that these maps are sensitive to emission at all spatial scales. For our analysis we use the integrated intensity maps from the broad masking scheme, which are optimized for completeness and contains the entirety of the galaxy emission. The strategy for observing, data reduction and product generation are described in Leroy et al. (2021b). As our fiducial $\alpha_{\rm CO}$ conversion factor we adopt the local gas-phase metallicity in solar units ($Z' \equiv Z/Z_\odot$) scaled prescription as described in Accurso et al. (2017) and Sun et al. (2020c), that is $\alpha_{\rm CO} = 4.35 Z'^{-1.6}$ M$_\odot$ pc^{-2} (K km s^{-1})$^{-1}$, adopting a ratio CO(2-1)-to-CO(1-0) = 0.65 (Leroy et al., 2013; den Brok et al., 2021, T. Saito et al. in prep.). The radially-varying metallicity is estimated from the radial profile of gas-phase abundances in H II regions, as explained in Kreckel et al. (2020). Azimuthal variations in the metallicity

[4] https://github.com/emsellem/pymusepipe

Target	RA	DEC	$\log_{10}M_*$	$\log_{10}M_{H_2}$	$\log_{10}SFR$	ΔMS	Distance	Inclination	Mapped area
	(degrees)	(degrees)	($M_\odot$)	($M_\odot$)	($M_\odot\, yr^{-1}$)	(dex)	(Mpc)	(degrees)	(kpc^2)
(1)	(2)	(3)	(4)	(5)	(6)	(7)	(8)	(9)	(10)
NGC 1087	41.6049	−0.49871	9.9	9.2	0.12	0.33	15.85±2.08	42.9	128
NGC 1300•	49.92081	−19.41111	10.6	9.4	0.07	−0.18	18.99±2.67	31.8	366
NGC 1365	53.4015	−36.14040	11.0	10.3	1.23	0.72	19.57±0.77	55.4	421
NGC 1385•	54.36901	−24.50116	10.0	9.2	0.32	0.5	17.22±2.42	44.0	100
NGC 1433•	55.50619	−47.22194	10.9	9.3	0.05	−0.36	18.63±1.76	28.6	441
NGC 1512	60.97557	−43.34872	10.7	9.1	0.11	−0.21	18.83±1.78	42.5	270
NGC 1566•	65.0016	−54.9380	10.8	9.7	0.66	0.29	17.69±1.91	29.5	212
NGC 1672	71.4270	−59.24725	10.7	9.9	0.88	0.56	19.4±2.72	42.6	255
NGC 2835	139.4704	−22.3547	10.0	8.8	0.09	0.26	12.22±0.9	41.3	88
NGC 3351	160.9906	11.7037	10.4	9.1	0.12	0.05	9.96±0.32	45.1	76
NGC 3627	170.0625	12.991	10.8	9.8	0.58	0.19	11.32±0.47	57.3	87
NGC 4254•	184.707	14.41641	10.4	9.9	0.49	0.37	13.1±1.87	34.4	174
NGC 4303•	185.4789	4.47374	10.5	9.9	0.73	0.54	16.99±2.78	23.5	220
NGC 4321•	185.7289	15.82230	10.7	9.9	0.55	0.21	15.21±0.49	38.5	196
NGC 4535•	188.585	8.19797	10.5	9.6	0.33	0.14	15.77±0.36	44.7	126
NGC 5068	199.7281	−21.03874	9.4	8.4	−0.56	0.02	5.2±0.22	35.7	23
NGC 7496•	347.4470	−43.4278	10.0	9.3	0.35	0.53	18.72±2.63	35.9	89
IC5332	353.6145	−36.1011	9.7	–	−0.39	0.01	9.01±0.39	26.9	34

Table 2.1: Summary of the galactic parameters of our sample adopted through this work. •: Galaxies observed with MUSE-AO mode. Values in columns (4), (5) and (6) correspond to those presented in Leroy et al. (2021a). Column (7) shows the vertical offset of the galaxy from the integrated main sequence of galaxies, as defined in Leroy et al. (2019). Distance measurements are presented in Anand et al. (2021) and inclinations in Lang et al. (2020). Uncertainties in columns (4), (5), (6) and (7) are on the order of 0.1 dex. Column (10) shows the area mapped by MUSE.

of the interstellar medium have been previously reported (Ho et al., 2017; Kreckel et al., 2020), however, these variations are small ($0.04-0.05$ dex), implying variations of ~ 0.06 dex in α_{CO}) and therefore do not impact our results. We test the robustness of our results against a constant $\alpha_{CO} = 4.35$ $M_\odot$ pc^{-2} $(K\ km\ s^{-1})^{-1}$, as the canonical value for our Galaxy (Bolatto et al., 2013) in Sec. 2.5.4. IC 5332 has no significant detection of CO(2–1) emission and therefore has been excluded from the rKS and rMGMS analysis.

2.2.3 Environmental masks

We have used the environmental masks described in Querejeta et al. (2021) to morphologically classify the different environments of each galaxy and label them as disk, spiral arms, rings, bars and centers. This classification was done using photometric data mostly from

the Spitzer Survey of Stellar structure in Galaxies (S^{4}G; Sheth et al., 2010). In brief, disks and centers are identified via 2D photometric decompositions of 3.6 μm images (see, e.g., Salo et al., 2015). A central excess of light is labeled as center, independently of its surface brightness profile. The size and orientation of bars and rings are defined visually on the NIR images; for S^{4}G galaxies we follow Herrera-Endoqui et al. (2015). Finally, spiral arms are only defined when they are clearly dominant features across the galaxy disk (excluding flocculent spirals). First, a log-spiral function is fitted to bright regions along arms on the NIR images, and assigned a width determined empirically based on CO emission. For S^{4}G, we rely on the analytic log-spiral segments from Herrera-Endoqui et al. (2015), and performed new fits for the remaining galaxies. These environmental masks allow us to examine the variations of the SFMS, rKS, and rMGMS relations across different galactic environments.

2.2.4 Stellar mass surface density maps

The PHANGS-MUSE DAP (Emsellem et al., 2022) includes a stellar population fitting module, a technique where a linear combination of SSP templates of known ages, metallicities, and mass-to-light ratios is used to reproduce the observed spectrum. This permits us to infer stellar population properties from an integrated spectrum, such as mass- or light-weighted ages, metallicities, and total stellar masses, together with the underlying star formation history (which will be used in Sec. 2.5.4). Before doing the SSP fitting, we correct the full mosaic for Milky Way extinction assuming a Cardelli et al. (1989) extinction law and the $E(B-V)$ values obtained from the NASA/IPAC Infrared Science Archive[5] (Schlafly & Finkbeiner, 2011). In detail, our spectral fitting pipeline performs the following steps: First, we used a Voronoi tessellation (Cappellari & Copin, 2003a) to bin our MUSE data to a minimum signal-to-noise ratio (S/N) of ∼35, computed at the wavelength range of 5300−5500 Å. We chose this value in order to keep the relative uncertainty in our mass measurements below 15%, even for pixels dominated by a younger stellar population. To do this, we tried different S/N levels to bin a fixed region in our sample, and we bootstrapped our data to have an estimate of the uncertainties at each S/N level.

We use then the Penalized Pixel-Fitting (pPXF) code (Cappellari & Emsellem, 2004a; Cappellari, 2017a) to fit the spectrum of each Voronoi bin. To fit our data, we used a grid of templates consisting of 13 ages, ranging from 30 Myr to 13.5 Gyr, logarithmically-spaced, and six metallicity bins $[\mathrm{Z/H}] = [-1.49,\ -0.96,\ -0.35,\ +0.06,\ +0.26,\ +0.4]$. We fit the wavelength range 4850−7000 Å, in order to avoid spectral regions strongly affected by sky residuals. We used templates from the eMILES (Vazdekis et al., 2010, 2012) database, assuming a Chabrier (2003) IMF and BaSTI isochrone (Pietrinferni et al., 2004) with a Galactic abundance pattern.

The SSP fitting was done in two steps. First, we fitted our data assuming a Calzetti et al. (2000) extinction law to correct for internal extinction. We then corrected the observed spectrum using the measured extinction value before fitting it a second time, including a 12 degree multiplicative polynomial in this iteration in the fit. This two-step fitting process accounts for offsets between individual MUSE pointings. The different MUSE pointings are not necessarily observed under identical weather conditions, and therefore, even with careful treatment, we find some systematic differences between the individual MUSE pointings re-

[5] https://irsa.ipac.caltech.edu/applications/DUST/

lated to the different sky continuum levels. We studied regions in our mosaic where different pointings overlap, and found variations on the order of ∼3% (between an identical region in two different pointings). After inducing similar perturbations on a subset of spectra, we found that even these small differences could potentially cause systematic differences in measured stellar-population parameters. Therefore, in the first iteration of the SSP fitting, we measure a reddening value, and in the second iteration, we use a high-degree multiplicative polynomial to correct for those nonphysical features and homogenize the outcome of the different pointings. Additionally, we have identified foreground stars as velocity outliers in the SSP fitting and we have masked those pixels out of the analysis carried out in this chapter.

2.2.5 Star formation rate measurements

As part of the PHANGS-MUSE DAP (Emsellem et al., 2022), we fit Gaussian profiles to a number of emission lines for each pixel of the final combined MUSE mosaic of each galaxy in our sample. By integrating the flux of the fitted profile in each pixel, we were able to construct emission lines flux maps for every galaxy. In order to calculate our final SFR rate measurement we use the Hα, Hβ, S II and O III emission line maps. We de-reddend the Hα fluxes, assuming that $\mathrm{H}\alpha_{\mathrm{corr}}/\mathrm{H}\beta_{\mathrm{corr}} = 2.86$, as appropriate for a case B recombination, temperature $T = 10^4$ K, and density $n_{\mathrm{e}} = 100$ cm^2, following:

$$\mathrm{H}\alpha_{\mathrm{corr}} = \mathrm{H}\alpha_{\mathrm{obs}} \left(\frac{(\mathrm{H}\alpha/\mathrm{H}\beta)_{\mathrm{obs}}}{2.86} \right)^{\frac{k_\alpha}{k_\beta - k_\alpha}} , \tag{2.1}$$

where Hα_{corr} and Hα_{obs} correspond to the extinction-corrected and observed Hα fluxes, respectively, and k_α and k_β are the values of reddening in a given extinction curve at the wavelengths of Hα and Hβ. Opting for an O'Donnell (1994) extinction law, we use $k_\alpha = 2.52$, $k_\beta = 3.66$, and $R_{\mathrm{V}} = 3.1$.

Next, we determine whether the Hα emission comes from gas ionized by recently born stars or by a different source, such as active galactic nuclei (AGN), or low-ionization nuclear emission-line regions (LINER). We performed a cut in the Baldwin-Phillips-Terlevich (BPT; Baldwin et al., 1981) diagram using the [O III]/Hβ and [S II]/Hα line ratios, as described in Kewley et al. (2006), to remove pixels that are dominated by AGN ionization from our sample. In the remaining pixels, we determined the fraction C_{HII} of the Hα emission actually tracing local star formation, and the fraction deemed to correspond to the diffuse ionized gas (DIG), a warm (10^4 K), low density (10^{-1} cm^{-3}) phase of the interstellar medium (Haffner et al., 2009; Belfiore et al., 2015) produced primarily by photoionization of gas across the galactic disk by photons that escaped from H II regions (Flores-Fajardo et al., 2011; Zhang et al., 2017; Belfiore et al., 2022). To this end, we followed the approach described in Blanc et al. (2009) with the modifications introduced in Kaplan et al. (2016). Essentially, we first

use the [S II]/Hα ratio to estimate $C_{\rm HII}$ in each pixel, following:

$$C_{\rm HII} = \frac{\frac{\rm [S\,II]}{\rm H\alpha} - \left(\frac{\rm [S\,II]}{\rm H\alpha}\right)_{\rm DIG}}{\left(\frac{\rm [S\,II]}{\rm H\alpha}\right)_{\rm HII} - \left(\frac{\rm [S\,II]}{\rm H\alpha}\right)_{\rm DIG}} \ , \tag{2.2}$$

where $\left(\frac{\rm [S\,II]}{\rm H\alpha}\right)_{\rm DIG}$ and $\left(\frac{\rm [S\,II]}{\rm H\alpha}\right)_{\rm HII}$ correspond to the typical [S II]/Hα ratio of DIG and H II regions as measured in the faint (10th percentile) and bright (90th percentile) end of the Hα distribution, respectively. Then, we perform a least squares fitting to find the best β and f_0 parameters such that:

$$C_{\rm HII} = 1.0 - \left(\frac{f_0}{\rm H\alpha}\right)^{\beta} \ . \tag{2.3}$$

Equation 2.3 represents the fraction of Hα emission tracing local star formation as a function of the Hα flux in each pixel. For Hα fluxes lower than f_0, the fraction is defined to be zero. This has been done for each galaxy separately. Bright pixels, dominated by star formation ionization have $C_{\rm HII} \sim 1$, while fainter and DIG-contaminated pixels have lower values. We include in the Supporting material 2.7.1 an example of the fitting of the parametrization defined in Eq. 2.3 to our data.

Finally, we compute the Hα emission tracing star formation (H$\alpha_{\rm HII}$) as $C_{\rm HII}\times$ Hα in each pixel, while the fraction $1-C_{\rm HII}$ is deemed to be DIG emission (H$\alpha_{\rm DIG}$). We then calculate the total H$\alpha_{\rm DIG}$ to H$\alpha_{\rm HII}$ ratio ($f_{\rm DIG}$) and rescale the H$\alpha_{\rm HII}$ flux of all pixels by $(1+f_{\rm DIG})$. This correction is performed because photons that ionize the DIG, originally escaped from H II regions. It represents, therefore, a spatial redistribution of the Hα flux. This approach permits us to estimate a star formation rate even in pixels contaminated by non-star-forming emission. A S/N cut of 4 for Hα and 2 for Hβ was then applied before computing the star formation rate surface density map using Eq. 3.2. However, most of the low S/N pixels have $C_{\rm HII} \approx 0$, and therefore, the S/N cut does not largely impact our results. Pixels below this S/N cut, pixels with $C_{\rm HII} \leq 0$ or pixels where $\rm H\alpha_{obs}/H\beta_{obs} < 2.86$, are considered non-detections (see Sec. 3.3.2). In Sec. 3.3.2 we discuss the importance of non-detections (i.e., pixels with non-measured SFR) in our analysis. However, our main findings do not change qualitatively when we set to zero the SFR of these pixels (i.e., pixels that are not dominated by star-forming ionization according to the BPT criterion). Additionally, in Sec. 2.5.4 we discuss the impact of removing all Hα emission not associated with morphologically-defined H II regions.

To calculate the corresponding star formation rate from the Hα flux corrected for internal extinction and DIG contamination, we adopted the prescription described in Calzetti (2013):

$$\frac{\rm SFR}{\rm M_\odot\,yr^{-1}} = 5.5\times10^{-42}\frac{\rm H\alpha_{corr}}{\rm erg\,s^{-1}} \ . \tag{2.4}$$

This equation is scaled to a Kroupa universal IMF (Kroupa, 2001), however, differences

with the Chabrier IMF assumed for the SSP fitting are expected to be small (Kennicutt & Evans, 2012). With these steps we obtain SFR surface density maps for each galaxy in our sample. We acknowledge that Eq. 3.2 assumes a fully-sampled IMF, and that the lowest SFR pixels (especially at high spatial resolution) may not form enough stars to fully sample the IMF. Hence, the measured SFR is more uncertain in this regime . However, due to our methodology to bin the data (see Sec. 3.3.2), the higher uncertainty in the low $\Sigma_{\rm SFR}$ regime has little effect in our analysis.

2.3 Methods

2.3.1 Sampling the data at larger spatial scales

In order to probe the relations under study at different spatial scales, we have resampled our native resolution MUSE and ALMA maps to pixel sizes of 100 pc, 500 pc and 1 kpc. The degrading of the data to larger spatial scales is done by only resampling into larger pixel, rather than performing a convolution before resampling. The 100 pc pixels are generally larger than the native spatial resolution of the maps. The resampling has been done for each one of the three relevant quantities: stellar mass surface density, star formation rate surface density, and molecular gas mass surface density. For stellar mass maps, the resampling was directly performed in the MUSE native resolution stellar mass surface density map, produced by the PHANGS-MUSE DAP. Calculating a resampled star formation rate surface density map required the resampling of each one of the line maps used for the BPT diagnostic and extinction correction. The parameters f_0 and β used for the DIG correction are calculated only at the native MUSE resolution, and do not change with spatial scale. This assumes that the typical DIG flux surface density does not vary with spatial scale, and the measurement at the native resolution is better constrained due to the higher number of pixels. Once the emission line maps were resampled, pixels dominated by AGN ionization were dropped from the analysis. The remaining Hα emission was then corrected by internal extinction and for DIG contamination as explained in Sec. 3.2.5. The DIG contamination correction is done independently at each spatial scale. For the molecular gas mass surface density, we have proceeded similarly to the stellar mass surface density. Additionally we have imposed a S/N cut of 1.5 for the molecular gas mass surface density map after the resampling, dropping the faintest and most uncertain pixels. For each one of the resampled quantities, we have also resampled the corresponding variance map to perform the S/N cut and report the corresponding uncertainty. Finally, we have corrected the maps by inclination, using a multiplicative factor of $\cos(i)$, where i corresponds to the inclination of each galaxy, listed in Table 3.1. The adopted inclinations correspond to those reported in Lang et al. (2020).

Figure 2.1 shows the star formation rate surface density map (top), molecular gas mas surface density map (center), and stellar mass surface density map (bottom) at each of the spatial scales probed in this work (100 pc, 500 pc, and 1 kpc from left to right) for one example galaxy (NGC 1512).

2.3.2 Fitting technique

To fit each scaling relation, we binned the x-axis of our data in steps of 0.15 dex, and calculated the mean within each bin. Fitting bins rather than single data points avoids giving statistically larger weight to the outer part of a galaxy, where more pixels are available. A minimum of 5 data points with nonzero signal per bin was imposed at the 100 pc spatial scale for individual galaxies, in order to avoid sparsely sampled bins in the high or low end of the x-axis. For the full-sample relations, we imposed a minimum of 10 nonzero data points per bin at all spatial scales. We have also tested radial binning in the x-axis (i.e., calculating the means in bins defined as data points located at similar galactocentric radius), but this raised the scatter within each bin so we kept the x-axis binning, namely by stellar (gas) mass surface density.

The error in each bin has been calculated by bootstrapping: For a bin with N data points, we repeatedly chose 100 subsamples (allowing for repetitions), perturbed the data according to their uncertainties, and calculated their mean values. We adopt the standard deviation of the set of 100 mean values as the uncertainty of the mean in that bin. We opted for this approach instead of standard error propagation because the uncertainties of our SFR measurements are too small, and this method offers a more conservative quantification of the scatter within each bin. Similarly, for each binning resultant from the 100 iterations, we fit a power law and calculate a slope. To do this, we use a weighted least square fitting routine (WLS), where each bin is weighted by the inverse of its variance. This is justified since, by construction, the x-axis uncertainty of each bin is negligible, compared to its y-axis uncertainty. The final slope and its error correspond to the mean and standard deviation of the slopes distribution, respectively. This quantification of the error accounts for sample variance and statistical uncertainty of each data point, but it does not reflect the uncertainties induced by systematic effects. Finally, the scatter reported throughout the chapter for the fitted power laws corresponds to the median absolute deviation of each data point, considering detections only, with respect to the best-fitting power law.

However, at physical resolutions of ∼100 pc, we deal with the issue that within each bin, we observe (in the case of the rSFMS) a bimodal distribution of SFR. At a given stellar mass surface density, a fraction of the pixels probed have a nonzero value of SFR that correlates with its corresponding stellar mass surface density value (with a certain level of scatter), while the remaining pixels do not show any SFR within our detection limits. This is either because these pixels are intrinsically non-star-forming, or because their SFRs are lower than our detection threshold. The fraction of these "non-detections" (N/D) is higher in the lower stellar mass surface density regime and close to zero at the high-mass end. This bimodality reflects the fact that star formation is not uniformly distributed across galactic disks – due to temporal stochasticity, or spatial organization of the star formation process due to galactic structure.

Thus, unlike studies done at ∼kpc resolutions, where star-forming regions smaller than the spatial resolution element will be averaged in a larger area, we need to properly account for the N/D fraction when investigating the scaling relations. This requires designing a fitting method such that our measurements at high resolution will be consistent to those obtained at larger spatial scales.

For the analysis presented in this chapter, we are interested in (1) measuring how many stars are being formed per unit time on average at a given stellar mass surface density. This

is different from asking (2) what is the typical SFR surface density at a given stellar mass surface density. The former requires us to include the non-detections as we are interested in averaging the SFR across the entire galactic disk, while the latter only tells us what are the most common SFR values to expect, and will depend on the probed spatial scale.

Measurements at lower spatial resolution are closer to addressing (1), as the physical interpretation of this is that in a given region of constant mass surface density, the mean SFR will be dominated by a few bright star-forming regions rather than by the much more numerous faint star-forming regions. Figures 2.2 and 2.3 exemplify this difference for the rSFMS derived using all the available pixels in our data at a spatial resolution of ∼100 pc. Figure 2.2 shows three different binning schemes for the rSFMS in the bottom panel, and the detection fraction (defined as $1 - f_{\rm N/D}$) of each bin in the top panel, where $f_{\rm N/D}$ quantifies the fraction of N/D in each bin.

When averaging in linear space either including non-detections as zeros (red line) or excluding them from the average calculation (blue line) we address question (1), whereas averaging in log-space (green line) provides information on (2) and hence goes through the bulk of the 2D distribution in the $\log \Sigma_{\rm SFR}$ versus $\log \Sigma_{\rm stellar}$ plane. Figure 2.3 shows the SFR distribution of pixels at an average $\log \Sigma_{\rm stellar}$ $[{\rm M}_{\odot}\,{\rm pc}^{-2}] \approx 8.5$, and the average $\log \Sigma_{\rm SFR}$ for this stellar mass surface density bin computed with each one of the three binning schemes is shown by the vertical lines (using the same color scheme as for Fig. 2.2). Non-detections in this bin are highlighted in brown. Here it becomes clear that while the mean in log-space (green line) matches the peak of the nonzero distribution, the means in linear space including or excluding non-detections (red and blue lines) are shifted toward higher values. Additionally the mean in linear space excluding non-detections (blue line) will always be greater or equal to the mean in linear space when non-detections are accounted for, as zeros in the calculation of the average (red line).

For our analysis we are interested in understanding if and how the star formation scaling relations (i.e., rSFMS, rKS and rMGMS) vary with measurement scale, and therefore we adopt the mean measured in linear space as our fiducial approach (i.e., red line in Fig. 2.2). To probe the effect of excluding non-detections on the slope determination, we use the blue binning scheme (i.e., mean in linear space excluding N/D) in order to perform a fair comparison to the fiducial case. However, our results (in terms of impact of spatial scale in the measured slope) are qualitatively unchanged if we use the mean in log space (i.e., green line) in this case instead.

Finally, we highlight here that for our fiducial approach, we are interested in probing the scaling relations across the entire galactic disk. Hence, we consider all the pixels from a given galaxy in the computation of the scaling relations, including faint and more uncertain SFR measurements, as well as N/D. We note that a pixel is defined as N/D (in a given scaling relation) if it has a nonzero measurement in the quantity shown on the x-axis, and a value below our detection limits in the quantity shown on the y-axis, i.e. a non-detection in molecular gas will lead to the omission of this pixel in the rKS, while it will be treated as an N/D in the rMGMS.

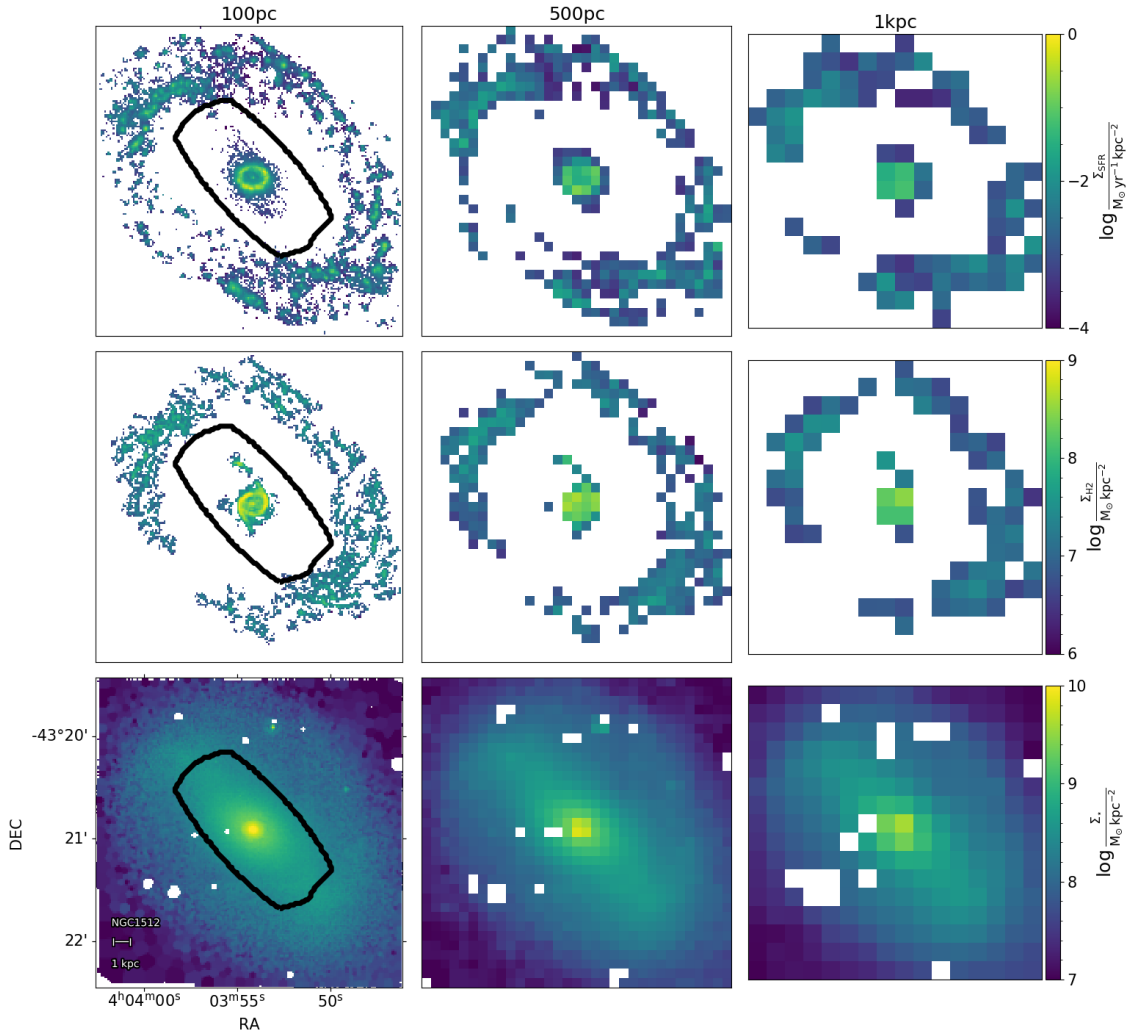

Figure 2.1: Example of SFR, molecular gas, and stellar mass surface density (top, middle, and bottom row) at spatial scales of 100 pc, 500 pc and 1 kpc (left, middle, and right column) for one of the galaxies in our sample (NGC 1512). The black contour in each row encloses the pixels within the bar of the galaxy. Foreground stars have been masked in the stellar mass surface density maps (white pixels in bottom row).

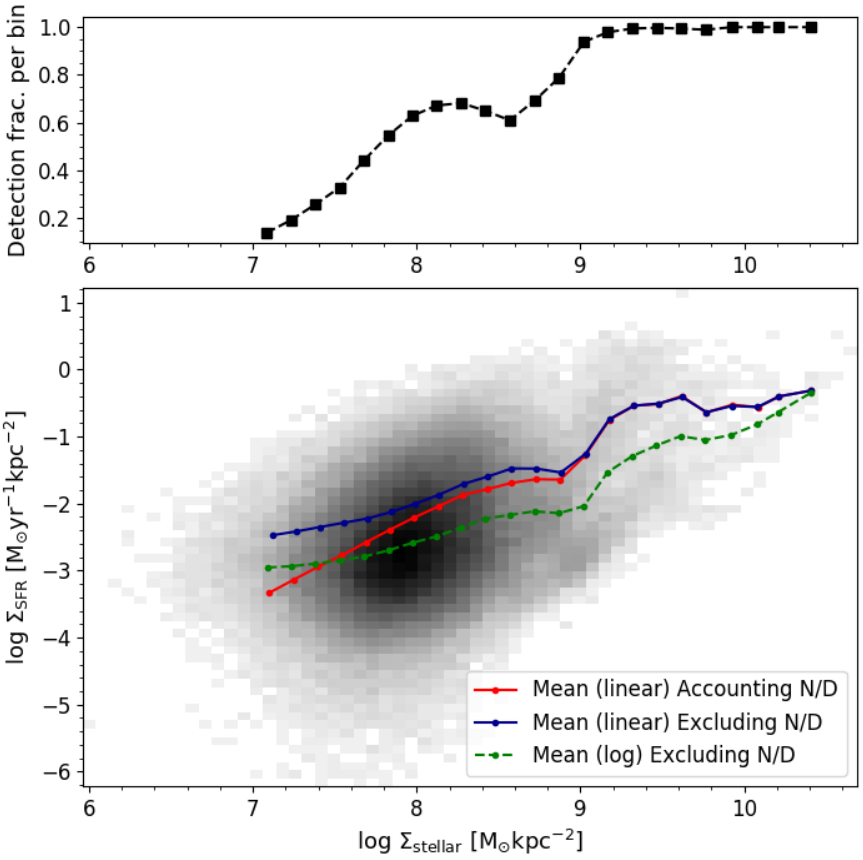

Figure 2.2: Bottom panel: 2D distribution of pixels in the overall rSFMS (i.e. including all pixels in our sample) and the three different binning schemes described in Sec. 3.3.2. As explained in the main text, different binning schemes address different questions. The red line shows the fiducial binning scheme adopted in this paper. Top panel: Detection fraction of our SFR surface density tracer within each stellar mass surface density bin ranging from ∼20% in the low surface density regime to 100% at the high surface density end.

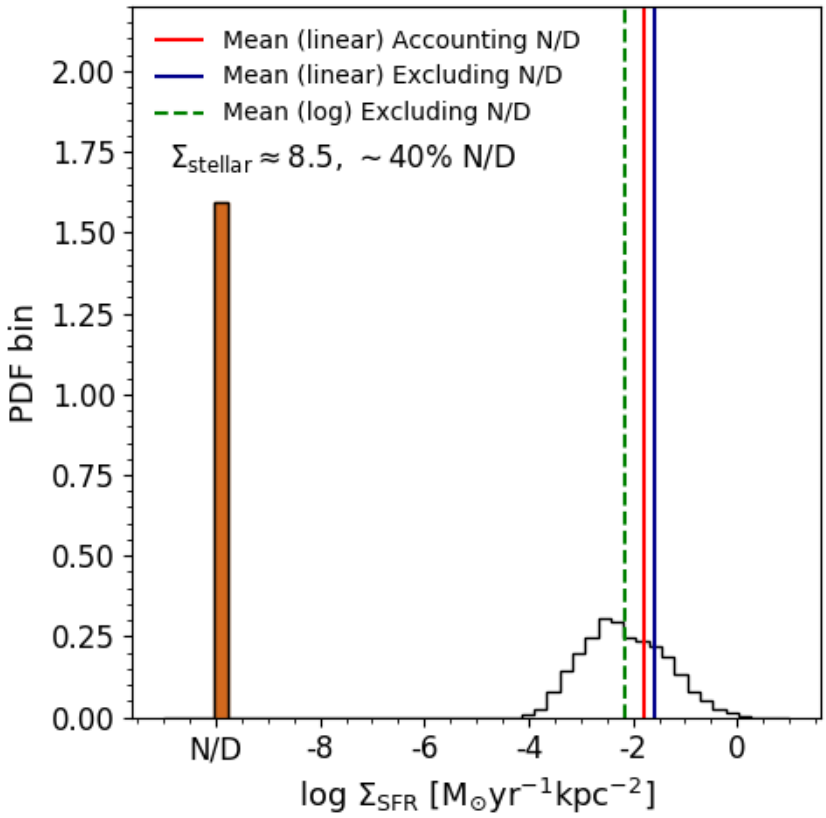

Figure 2.3: Distribution of the SFR surface density values within the mass bin of $\log \Sigma_{\rm stellar}$ [$M_\odot$ pc^{-2}] ≈ 8.5. Around 40% of the pixels are not detected in $\Sigma_{\rm SFR}$ and we observe a bimodality in the distribution. These non-detections have been highlighted in brown and moved to an artificial value (N/D). The vertical lines correspond to the derived average value for the three binning schemes in Fig. 2.2. The mean in log-space (green dashed line) matches the peak of the distribution of detections, while the mean in linear space (red and blue solid lines) correspond to the average SFR at this stellar mass surface density, including and excluding N/D, respectively.

2.4 Results

In this section we present our measurements of the three relations under study. We recover all three scaling relations at a spatial scale of 100 pc and we explore how these relations change when the data are degraded to lower spatial resolutions. We present each relation when considering all available pixels from the full galaxy sample, and derived for each individual galaxy to study galaxy-to-galaxy variations. As mentioned in Section 3.2.2, IC 5332 has not been detected in CO(2–1) emission and therefore, the rKS and rMGMS have been measured for the remaining 17 galaxies only.

2.4.1 Scaling relations using the full sample

Figure 2.4 shows the 2D histograms of the overall rSFMS (left), rKS (center), and rMGMS (right), and their corresponding best-fitting power laws (red dashed line and red dots, respectively) at 100 pc spatial scale.

The number of data points used is 313227, 110084 and 309569 for the rSFMS, rKS, and rMGMS, respectively. This number is smaller for the rMGMS than for the rSFMS as IC 5332 is missing in the former. In the same order, the total detection fraction, defined as the fraction of pixels with a nonzero detection in the y-axis ($1 - f_{\mathrm{N/D}}$), is 0.50, 0.84, and 0.35. This means that about 16−65% of the data points with a valid measurement of the property on the x-axis are not detected in the property on the y-axis. This reflects the high level of stochasticity dominating these relations at 100 pc spatial scale.

Out of these three relations, we find that the rMGMS has the lowest scatter ($\sigma \approx 0.34$ dex), followed by the rKS and the rSFMS with scatter $\sigma \approx 0.41$ dex and $\sigma \approx 0.51$ dex, respectively (see bottom row in Table 2.4). However, one must be careful when interpreting these numbers, since the scatter is computed using the nonzero pixels only. Due to our methodology, we include faint nonzero SFR pixels (see Sec. 3.3.2) that enhance the scatter of the rSFMS and the rKS, especially at high resolution (see Sec. 2.5.1).

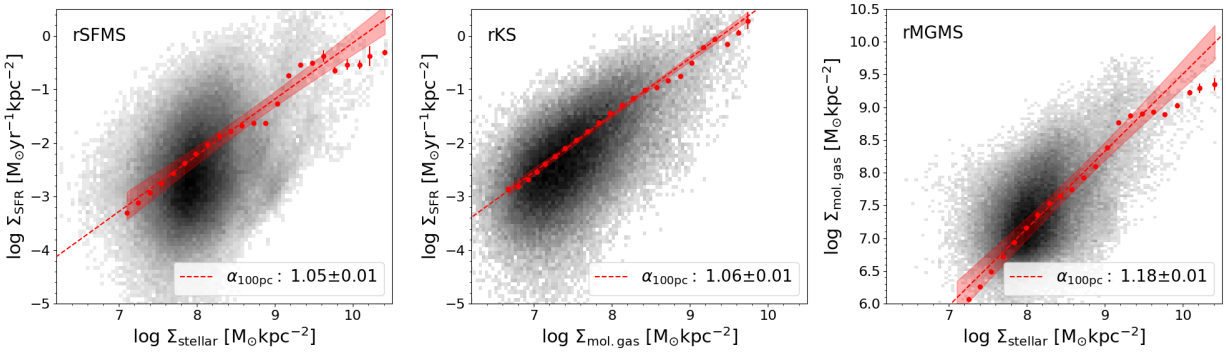

Figure 2.4: 2D distribution of the overall resolved star formation main sequence (left), resolved Kennicutt–Schmidt relation (center), and molecular gas main sequence (right) at 100 pc spatial scale. The red points show the mean binned data and the red dashed line is the best-fitting power law. The colored region shows the 98% confidence interval of the linear fit.

Reference	$\alpha_{\rm rSFMS}$	$\alpha_{\rm rKS}$	$\alpha_{\rm rMGMS}$	spatial scale
Sánchez et al. (2021)	1.01 ± 0.015	0.95 ± 0.21	0.93 ± 0.18	∼kpc
Ellison et al. (2020a)	0.68 ± 0.01	0.86 ± 0.01	0.73 ± 0.01	∼kpc
Barrera-Ballesteros et al. (2021a)	0.92	0.54	-	∼2 kpc
Morselli et al. (2020)	0.74 ± 0.25	0.83 ± 0.12	0.94 ± 0.29	∼500 pc
Lin et al. (2019)	1.19 ± 0.01	1.05 ± 0.01	1.1 ± 0.01	∼kpc
Dey et al. (2019)	–	1.0 ± 0.1	–	∼kpc
Medling et al. (2018)	0.72 ± 0.04	–	–	∼kpc
Abdurro'uf & Akiyama (2017)	0.99	–	–	∼kpc
Hsieh et al. (2017)	0.715 ± 0.001	–	–	∼kpc
Cano-Díaz et al. (2016)	0.72 ± 0.04	–	–	∼kpc
Leroy et al. (2013)	–	1.0 ± 0.15	–	∼kpc
Schruba et al. (2011)	–	0.9 ± 0.4	–	∼0.2−2 kpc
Blanc et al. (2009)	–	0.82 ± 0.05	–	∼750 pc
Bigiel et al. (2008)	–	0.96 ± 0.07	–	∼750 pc

Table 2.2: Summary of some previously reported values for the slopes of the rSFMS, rKS law and rMGMS. The spatial scale at which each study was carried is indicated in the last column.

We have measured a slope of 1.05 ± 0.01 for the rSFMS, 1.06 ± 0.01 for the rKS, and 1.18 ± 0.01 for the rMGMS. In the same order, the intercepts that set the normalization of these relations are -10.63, -9.96, -2.23. These numbers are within the range of previously reported values, using lower resolution data. Differences in the slope possibly arise due to the use of different fitting methods (Hsieh et al., 2017) or differences in the treatment of non-detection (see discussion in Sec. 2.5.2). Similarly, variations in the normalization of these relations are expected due to differences in the assumed CO-to-H_2 conversion factor (see Sec. 2.5.4), as well as in the binning methodology (see Sec. 3.3.2). Figure 2.2 illustrates that the latter can lead to differences of up to ~ 0.5 dex, with respect to the standard approach of average-in-log, depending on the fraction of N/D in a given bin. We summarize values from recent studies in Table 2.2. Some studies reported more than one value, using different fitting methods, often orthogonal distance regression (ODR) and ordinary least squares (OLS). In that case we show here the OLS value, as we obtained similar numbers for both fitting techniques in our data, when non-detections are excluded from the analysis. The best-fitting slopes and scatter for the overall sample are provided in the bottom row of Table 2.4.

2.4.2 Scaling relations in individual galaxies

Here we explore galaxy-to-galaxy variations for the three scaling relations. Figures 2.5, 2.6, and 2.7 show the rSFMS, rKS, and rMGMS, respectively, for each individual galaxy in our sample. Different colors represent different galactic environments, namely disk, spiral arms, bar, rings (inner and outer), and centers (see Sec. 5.2.2). The black dashed lines show the corresponding overall best-fitting power law from Fig. 2.4 as reference and the magenta dashed line show the best-fitting power law for each individual galaxy. In Sec. 2.4.1 we find

that the rMGMS is the relation with the lowest scatter in our overall sample. Figure 2.7 shows that the distribution of data points in this relation is much more compact (on a logarithmic scale) than in the rSFMS or the rKS. As mentioned earlier, this is due to the inclusion of very faint SFR pixels (see Sec. 3.3.2). As explained in Sec. 2.4.1, the rMGMS is the relation that has the lowest total detection fraction in comparison.

On the other hand, prominent differences between galaxies are seen for the rSFMS (Fig. 2.5). For instance, in some galaxies such as NGC 1365 or NGC 1566, their disk and spiral arm pixels agree well with the overall rSFMS, while in others, like NGC 3351 or NGC 4321, disk, spiral arms, and outer ring pixels tend to exhibit a constant SFR surface density independent of their local stellar mass surface density (albeit probing only a limited range here). Figure 2.8 highlights the diversity in the slopes measured for individual galaxies for the three relations probed. The rSFMS relation shows the largest dispersion in slopes among galaxies ($\sigma \approx 0.34$), followed by the rMGMS ($\sigma \approx 0.32$), and finally the rKS ($\sigma \approx 0.17$), where galaxies show slopes generally closer to the overall value (black diamond). The two galaxies with larger uncertainties in the rKS best-fitting power law slopes correspond to NGC 2835 and NGC 5068, two low-mass and low-SFR galaxies. Figure 2.6 shows that these galaxies have only a small number of data points, hence their uncertain measurements.

Finally, we note that the shape of the rKS relation across different galaxies does not seem to change. While it has a larger scatter than the rMGMS at high resolution (0.41 dex versus 0.34 dex, respectively), the relation is indeed more uniform across different environments. On the contrary, certain galactic environments do impact the shape of the rSFMS and the rMGMS. When present, inner structures (bar, inner ring, and center) often "bend" these scaling relations. In the case of the rSFMS, this "bend" might be related to an increase of SFR in an inner ring or a suppression of SFR in the bulge or bar, which is not reflected by a change in the stellar mass surface density but it is reflected in the molecular gas surface density.

Figure 2.9 highlights variations across different morphological environments. The top row shows binned scaling relations for each environment separately, considering all the pixels in our sample, compared to the overall relation we derived for all environments together. We use the offset ($\Delta_{\rm env}$) defined as the vertical offset between the binned scaling relation from each environment and the overall best-fitting power law, and the slope measured for each environment to quantify deviations from the overall relation. It can be seen that the slope and normalization of the rKS are similar across different galactic environments while the variations for the rSFMS and rMGMS relations are substantially larger (up to $\sim$0.4 dex).

The disk environment (being the largest in area) is dominating the overall slope for rSFMS and rMGMS. The spiral arms share a similar slope, but are systematically offset above the overall relations by up to $\sim$0.4 dex. This is consistent with the findings reported in Sun et al. (2020c), where the authors found a systematic increase of $\Sigma_{\rm mol.gas}$ in spiral arms with respect to inter-arm regions analyzing 28 galaxies from the PHANGS-ALMA survey with identified spiral arms. Querejeta et al. (2021) also report higher average $\Sigma_{\rm mol.gas}$ and $\Sigma_{\rm SFR}$ in spiral arms compared to inter-arm regions, using data from the PHANGS-ALMA survey and narrow-band Hα imaging as SFR tracer. Outer rings (with low $\Sigma_{\rm stellar,mol.gas}$) appear in the rSFMS and rMGMS as flatter features laying below the overall relation, while inner rings (with high $\Sigma_{\rm stellar,mol.gas}$) show up above it. Finally, bars lie systematically below the overall relations, especially in the case of the rSFMS (see discussion in Sec. 2.5.1). To our

Relation	α_{100pc}	σ_{100pc}	α_{500pc}	σ_{500pc}	α_{1kpc}	σ_{1kpc}
rSFMS	1.05 ± 0.01	0.51	1.10 ± 0.02	0.49	1.04 ± 0.04	0.44
rKS	1.06 ± 0.01	0.41	1.06 ± 0.02	0.33	1.03 ± 0.02	0.27
rMGMS	1.18 ± 0.01	0.34	1.26 ± 0.02	0.32	1.20 ± 0.04	0.29

Table 2.3: Slope (α) and scatter (σ) using all the available pixels in our sample, for each one of the scaling relations probed, at spatial scales of 100 pc, 500 pc and 1 kpc.

knowledge this is the first time these three scaling relations are probed separately across different morphological environments of galaxies, at a spatial scale comparable to individual star-forming regions.

We investigated if any global galaxy parameter could be related to the diversity in the measured slopes. In particular, we explored any dependence of the slope on total stellar mass ($M_\star$), total SFR, specific SFR ($sSFR = SFR/M_\star$), and vertical offset of the galaxy from the global star formation main sequence of galaxies (ΔMS) as computed in Leroy et al. (2019). Only correlations for ΔMS are shown here, as the other parameters show even weaker or no correlations. Figure 2.10 shows the difference between the slope derived from the full sample and that of each individual galaxy ($\Delta\alpha_{overall}$) as a function of ΔMS of each galaxy. Specifically, if α_{gal} corresponds to the slope measured for one individual galaxy, and $\alpha_{overall}$ is the slope measured for the overall sample (see Table 2.4), we define

$$\Delta\alpha_{overall} = \alpha_{gal} - \alpha_{overall} \ , \tag{2.5}$$

Figure 2.10 shows the slope variations with respect to ΔMS for the rSFMS (An analog figure for the rKS and the rMGMS is included in the Supporting material 2.7.2 for completeness). NGC 2835 and NGC 5068 are marked as gray points. A weak correlation can be identified between the slope difference in the rSFMS and ΔMS (Pearson correlation coefficient (PCC) of ∼0.49). A potential origin of this correlation is discussed in Sec. 2.5.1. No correlation is found for the slope difference in the rKS or rMGMS with any of the tested global parameters. Table 2.4 summarizes the slopes measured for each galaxy and each scaling relation probed.

2.4.3 Variation of slope and scatter as a function of spatial scale

In this section, we explore how varying the spatial scale of the data affects the three relations. We resample our data to spatial scales of 500 pc, and 1 kpc as explained in Sec. 3.2.6. Figure 2.11 shows the three relations probed at spatial scales of 100 pc, 500 pc, and 1 kpc. The measured slopes and scatter are reported in Table 2.3. At all spatial scales, the slopes show no evidence of systematic dependence with spatial resolution. Uncertainties in the slope measurements are larger at 1 kpc due to the smaller number of data points, while the scatter is systematically lower at larger spatial scales, consistent with the findings reported in Bigiel et al. (2008); Schruba et al. (2010); Leroy et al. (2013); Kreckel et al. (2018). This results from averaging small scales variations of regions at different stages of their evolutionary cycle (e.g., Kruijssen & Longmore, 2014). In fact, at 1 kpc resolution the rKS shows the lowest level of scatter.

Finally, the number of pixels used at 1 kpc resolution drops to 2860, 1510, and 2820, and

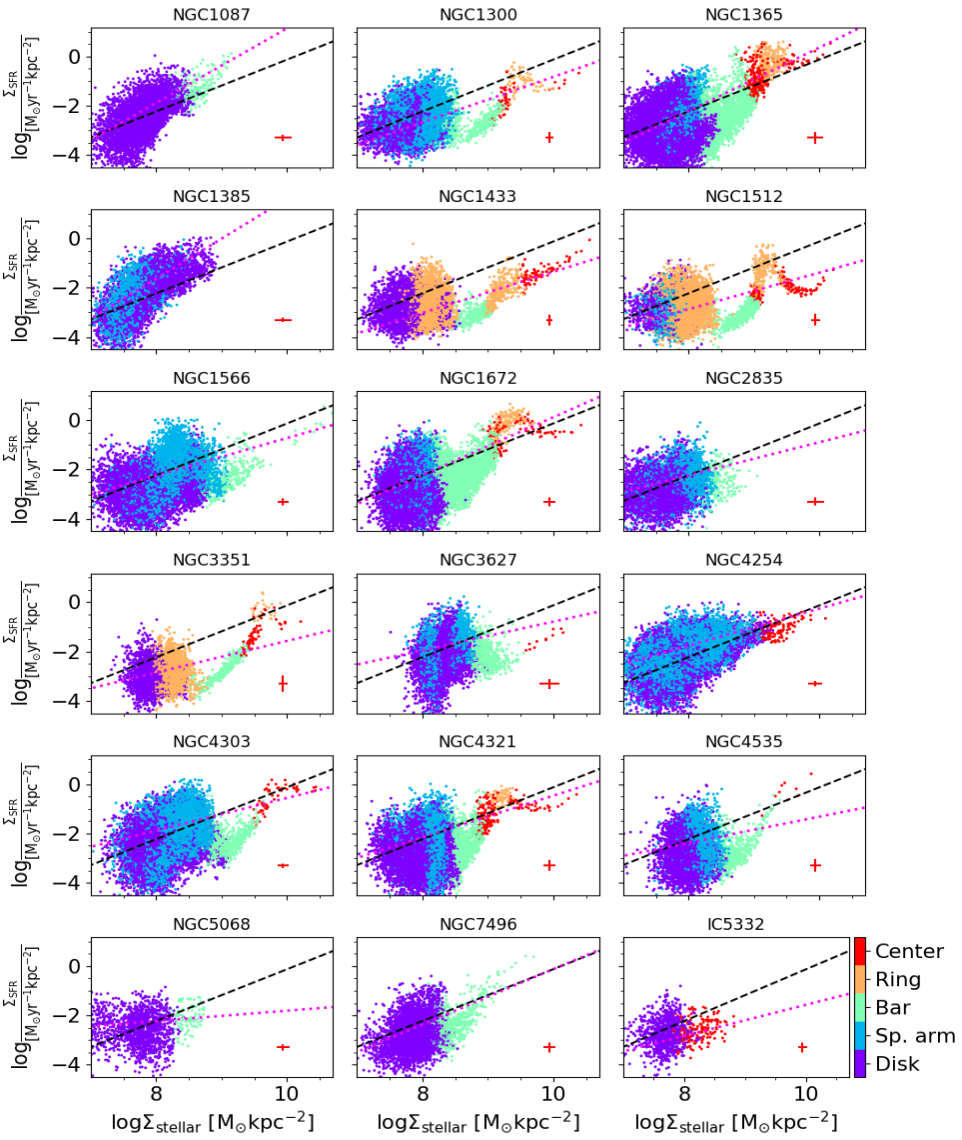

Figure 2.5: rSFMS for each galaxy at 100 pc resolution. Different environment in the galaxies are colored according to the color scale next to the bottom right panel. The dashed black line represents the best-fitting power law to the overall measurement and the magenta line shows the best-fitting power law for each galaxy.

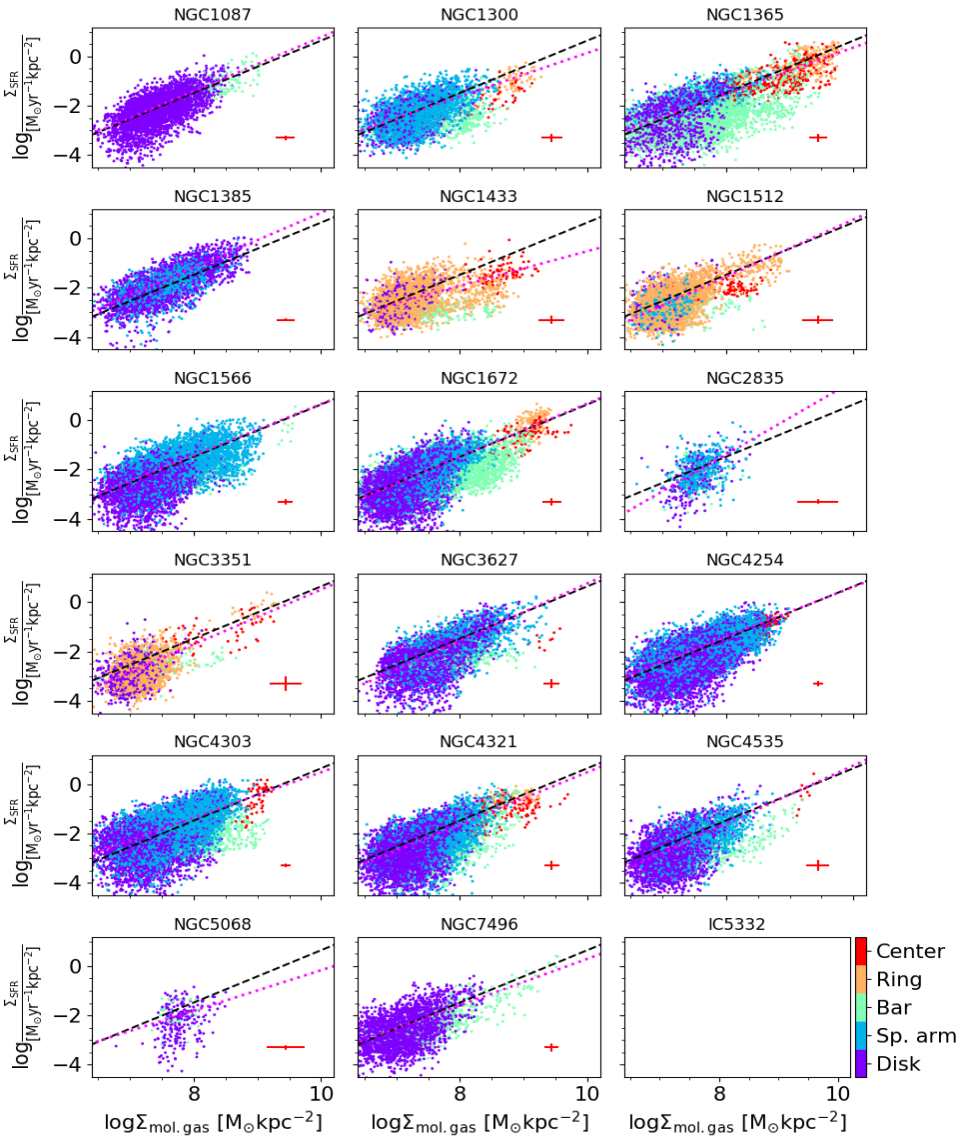

Figure 2.6: rKS for each galaxy at 100 pc resolution. Different environments in the galaxies are colored according to the color scale next to the bottom right panel. The dashed black line represents the best-fitting power law to the overall measurement and the magenta line shows the best-fitting power law for each galaxy.

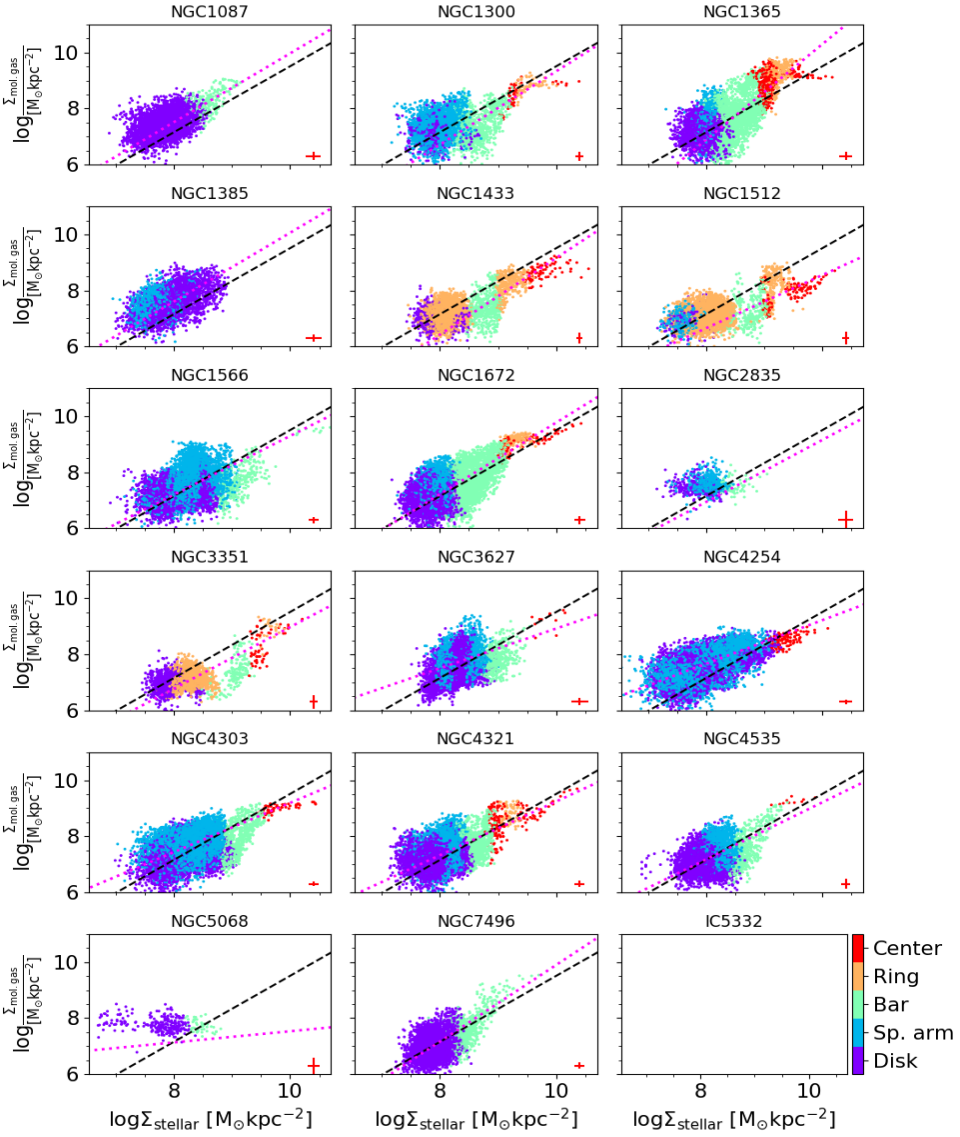

Figure 2.7: rMGMS for each galaxy at 100 pc resolution. Different environments in the galaxies are colored according to the color scale next to the bottom right panel. The dashed black line represents the best-fitting power law to the overall measurement and the magenta line shows the best-fitting power law for each galaxy.

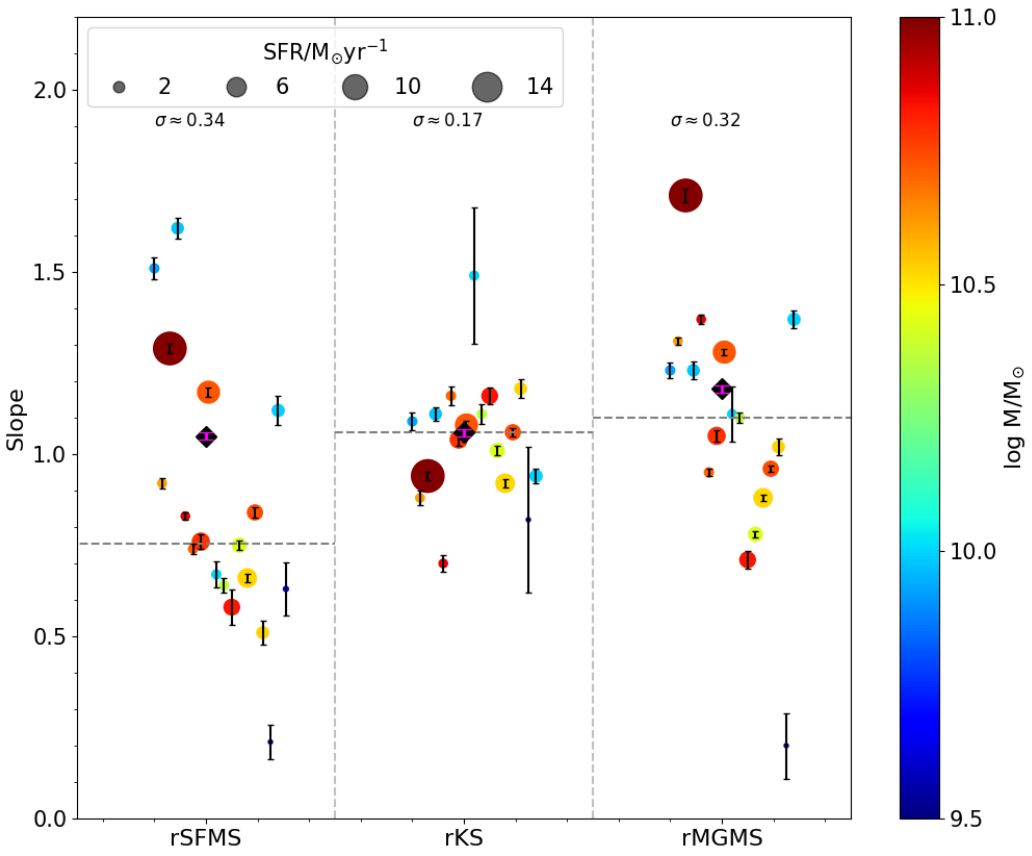

Figure 2.8: Slopes measured for the rSFMS, rKS and rMGMS for the individual galaxies in our sample. Each circle represents a galaxy. The size and color of each point scales with total SFR and stellar mass of the galaxy, respectively. The dispersion of the slope values for each relation is indicated on the top of the panel. The horizontal shift is arbitrary, with galaxies ordered from left to right by NGC number. The two galaxies with larger error bars in the KS law correspond to NGC 2835 and NGC 5068. This is due to the low number of data points available, as can be seen in Fig. 2.6. The black diamond with the magenta error bar indicates the global measurement for each relation. The horizontal gray dashed line show the median slope for each relation, in a galaxy basis.

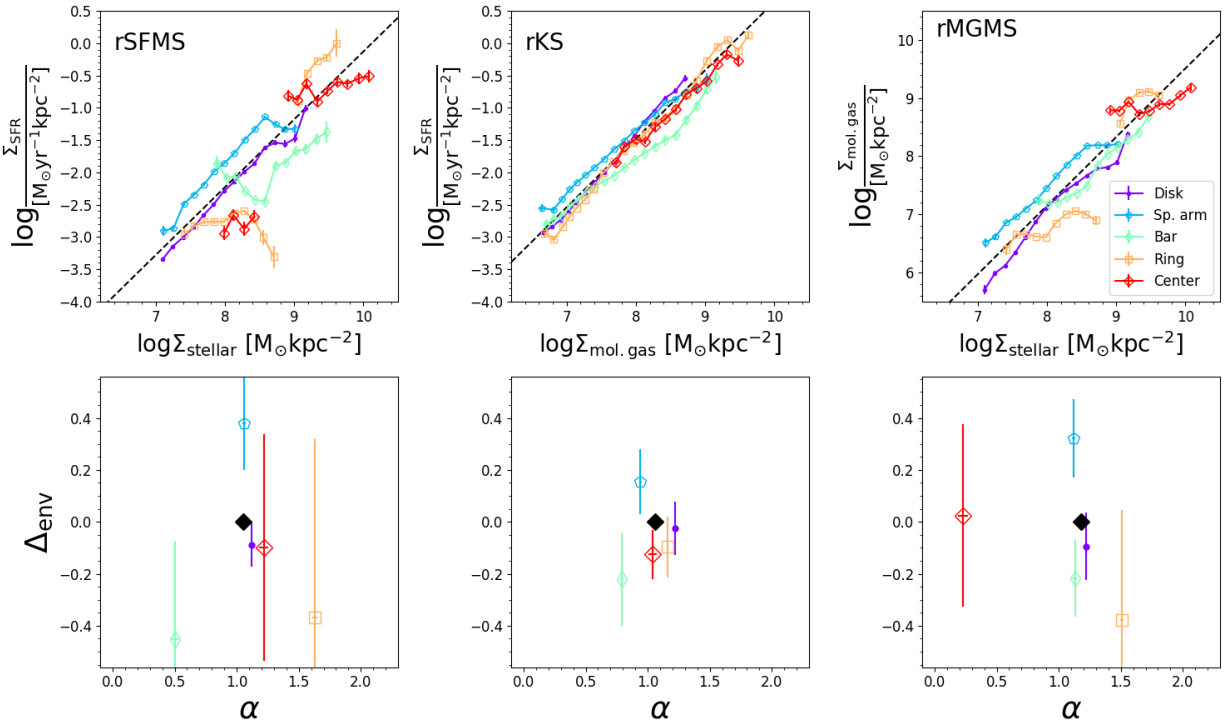

Figure 2.9: Variations across different galactic environments for the rSFMS (left), rKS (center) and rMGMS (right) relations. The top row shows the binned data for each galactic environment separately, following the same color scheme from Fig. 2.7, while the black dashed line shows the overall best-fitting power law to all data points together. The bottom row shows, on the x-axis the slope measured for each individual environment. The vertical offset between each binned environment and the overall best-fitting power law is reported on the y-axis. It has been calculated by fitting a power law with a fixed slope (that of the overall relation) to each binned environment, and computing the intercept difference respect to the overall best fitting power law. Its error-bars represent the standard deviation of the difference between the binned environment and the overall best fit. The black diamond show the slope of the overall best-fitting power law. (See Sec. 2.4.2 for discussion).

Object	$\alpha_{\rm rSFMS}$	$\sigma_{\rm rSFMS}$	$\alpha_{\rm rKS}$	$\sigma_{\rm rKS}$	$\alpha_{\rm rMGMS}$	$\sigma_{\rm rMGMS}$
NGC1087	1.51 ± 0.03	0.40	1.09 ± 0.02	0.32	1.23 ± 0.02	0.28
NGC1300	0.92 ± 0.01	0.40	0.88 ± 0.02	0.38	1.31 ± 0.01	0.33
NGC1365	1.29 ± 0.01	0.52	0.94 ± 0.01	0.47	1.71 ± 0.02	0.43
NGC1385	1.62 ± 0.03	0.44	1.11 ± 0.02	0.32	1.23 ± 0.02	0.30
NGC1433	0.83 ± 0.01	0.38	0.70 ± 0.02	0.38	1.37 ± 0.01	0.28
NGC1512	0.74 ± 0.01	0.42	1.16 ± 0.02	0.37	0.95 ± 0.01	0.25
NGC1566	0.76 ± 0.02	0.48	1.04 ± 0.02	0.40	1.05 ± 0.02	0.33
NGC1672	1.17 ± 0.01	0.49	1.08 ± 0.01	0.42	1.28 ± 0.01	0.32
NGC2835	0.67 ± 0.04	0.42	1.49 ± 0.19	0.39	1.11 ± 0.08	0.25
NGC3351	0.64 ± 0.02	0.38	1.11 ± 0.03	0.36	1.10 ± 0.01	0.22
NGC3627	0.58 ± 0.05	0.50	1.16 ± 0.02	0.42	0.71 ± 0.02	0.31
NGC4254	0.75 ± 0.01	0.47	1.01 ± 0.01	0.37	0.78 ± 0.01	0.29
NGC4303	0.66 ± 0.01	0.51	0.92 ± 0.01	0.44	0.88 ± 0.01	0.31
NGC4321	0.84 ± 0.01	0.50	1.06 ± 0.01	0.40	0.96 ± 0.01	0.28
NGC4535	0.51 ± 0.03	0.49	1.18 ± 0.03	0.43	1.02 ± 0.02	0.28
NGC5068	0.21 ± 0.05	0.45	0.82 ± 0.20	0.47	0.20 ± 0.09	0.19
NGC7496	1.12 ± 0.04	0.48	0.94 ± 0.02	0.40	1.37 ± 0.02	0.29
IC5332	0.63 ± 0.07	0.38	-	-	-	-
Overall	1.05 ± 0.01	0.51	1.06 ± 0.01	0.41	1.18 ± 0.01	0.34

Table 2.4: Slope (α) and scatter (σ) for each galaxy in our sample, for each one of the three relations probed, at 100 pc spatial scale. The overall measurement considering all the valid pixels is included in the last row.

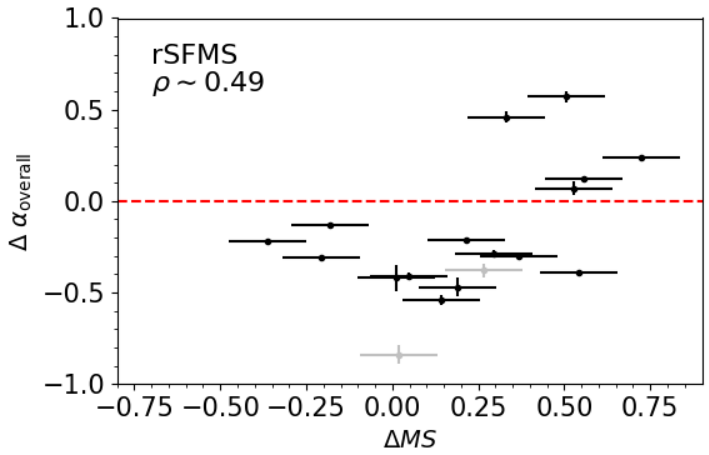

Figure 2.10: Differences in the slope measured for each individual galaxy with respect to the global measurements in Fig. 2.4 for the rSFMS, as a function of their offset from the global SFMS of galaxies. Each dot represent a galaxy in our sample. The gray dots are NGC 2835 and NGC 5068, two low-mass galaxies. The PCC of the correlation is indicated in the top-left corner.

the fraction of pixels with detected signal increases to 0.62, 0.90, and 0.52 for the rSFMS, rKS, and rMGMS, respectively. This represents an increase of 24%, 7%, and 49% with respect to the 100 pc spatial scale.

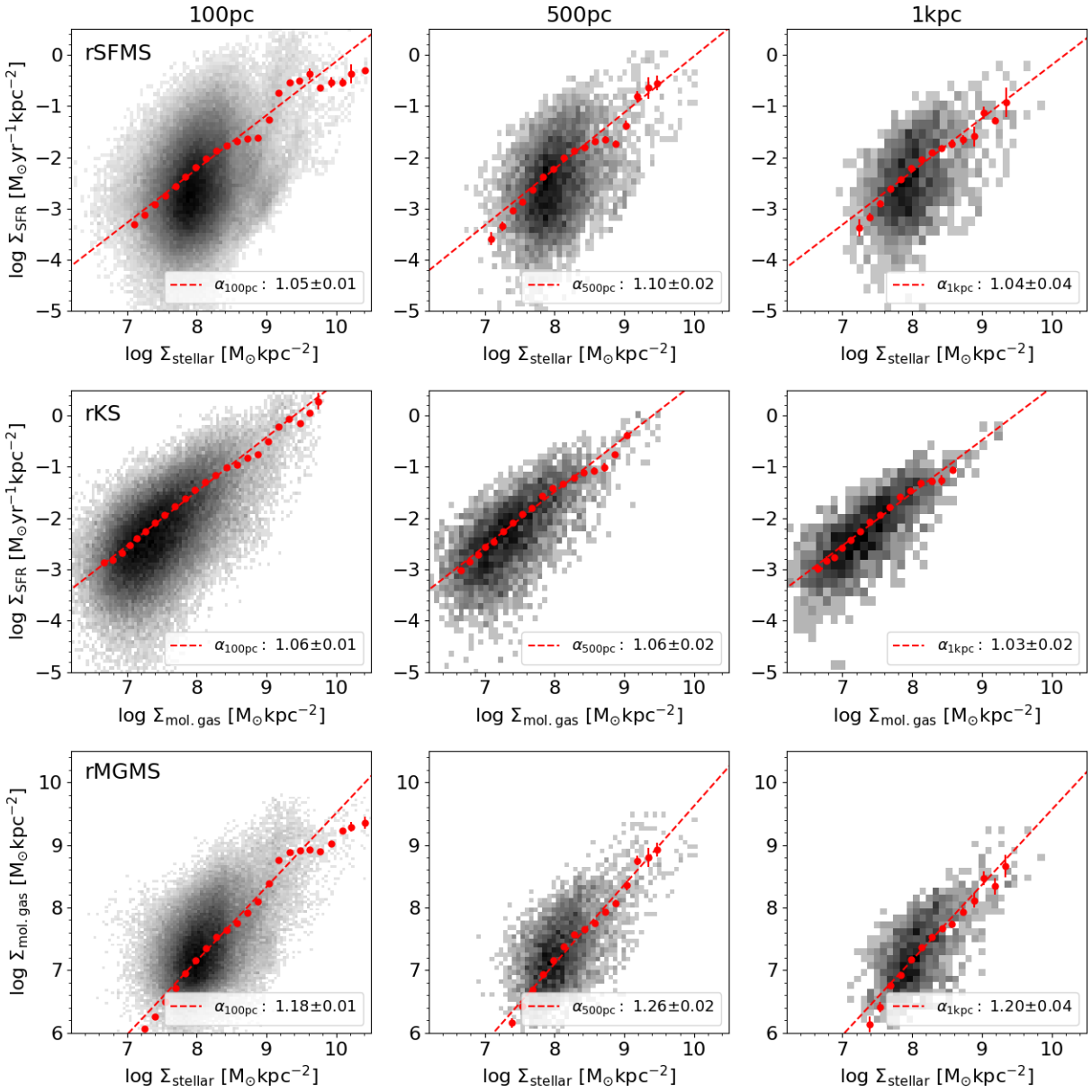

Figure 2.11: 2D histograms of the overall rSFMS (top row), rKS (center row), and rMGMS (bottom row) using all available pixels from our sample and probed at spatial scales of 100 pc (left column), 500 pc (middle column), and 1 kpc (right column). The x-axis binning and the best-fitting power law are indicated with red dots and a red dashed lines, respectively. The measured slope and its error are stated in each panel.

2.5 Discussion

2.5.1 Main findings of our analysis

In the previous section, we presented our results on the scaling relations for both, our overall sample and individual galaxies. Our main findings are summarized in the following.

Variations with spatial scale between and within galaxies

We find in our overall sample that the rMGMS is the relation with the smallest scatter (at a spatial scale of 100 pc), followed by the rKS, and the rSFMS (see Table 2.3). However, the rKS shows the most consistency across different galaxies and environments (i.e., similar values of slope and normalization). Its larger scatter is due to the inclusion of low SFR pixels that deviate more from the overall relation. The consistency of the rKS across different galaxies and environments reflects the direct connection between molecular gas and SFR, since stars form out of molecular gas. Hence, SFR "follows" the molecular gas distribution within short timescales (Hα emission traces star formation in the last $\sim$10 Myr; Calzetti, 2013; Leroy et al., 2012; Catalán-Torrecilla et al., 2015; Haydon et al., 2020) and this produces some correlated features in the shape of the rSFMS and the rMGMS for individual galaxies. NGC 1300, NGC 1512, and NGC 3351 are clear examples of these features. These similar features suggest that differences in the rSFMS across different environments are partially driven by the availability of molecular gas to fuel the formation of stars. However, bars, for example, generally appear below the overall best-fitting power law in the rKS as well, which suggests that variations in star formation efficiency may also play a role in driving the scatter. This consistency (across different galaxies and environments) suggest that physically, it is the more fundamental relation, compared to the rSFMS and the rMGMS, in agreement with what has been found by Lin et al. (2019) and Ellison et al. (2020a).

In contrast, from the perspective of individual galaxies, we see that the galactic environment has a stronger impact on the rSFMS and the rMGMS than on the rKS. In particular, in the rSFMS, bars display a small range of SFR values, all systematically below the overall sequence. This apparent suppression of SFR in bars is consistent with the "star formation desert" (James & Percival, 2018) in barred galaxies. Furthermore, variations in the rSFMS between different galaxies as those presented here have been previously reported (Hall et al., 2018; Liu et al., 2018; Vulcani et al., 2019; Ellison et al., 2020a). Thus, a single power law across the full stellar mass surface density range does not provide a good representation of the $\Sigma_{\rm stellar}$ versus $\Sigma_{\rm SFR}$ plane; instead, different galactic environments may define different relations. However, here we aim at measuring these scaling relations to first order, i.e., a "simple" power law, and finding a more realistic description of the data goes beyond the scope of this chapter.

We also investigated if any global galaxy parameter relates to the galaxy-to-galaxy variations in the slope of the scaling relations studied, and we found a potential correlation between the slope of the rSFMS of a galaxy and its ΔMS parameter. A positive correlation with a globally enhanced SFR could be explained as the increase of SFR happening preferably in the inner and more dense regions of the galaxy. This would lead to a steeper rSFMS in SFR-enhanced galaxies and it is consistent with the findings reported by Ellison et al. (2018), where a global enhancement or suppression of SFR was found to impact the

inner region of a galaxy stronger than its outskirts, studying a sample of galaxies from the MaNGA survey (Bundy et al., 2015). However, we stress here that even though the rSFMS shows hints of a correlation, the scatter and the limited number of data points make it hard to draw a robust conclusion.

Regarding spatial scale, we do not find evidence for a systematic dependence of the slope of these relations on the spatial resolution of the data, and the measurements are consistent within 2σ of their respective uncertainties. On the other hand, the scatter decreases at coarser spatial resolution as small scale variations are averaged out. The rKS is the relation that shows the least scatter at 1 kpc spatial scale.

Origin of observed scatter

Numerous authors have investigated the physical origins of the scatter in these resolved scaling relations and determined how this scatter evolves with spatial scale. According to Schruba et al. (2010) and Kruijssen & Longmore (2014), the scatter in the CO-to-Hα ratio at small spatial scales is dominated by the fact that a given aperture can be either dominated by a peak in the CO emission (i.e. early in the star-forming cycle) or a peak in the Hα emission (i.e. late in the star-forming cycle). At larger spatial scales, these peaks are averaged and this sampling effect diminishes.

Along the same line, Semenov et al. (2017) presented a simple model to conciliate the long molecular gas depletion times measured at galactic scales (∼1−3 Gyr; Kennicutt, 1998; Bigiel et al., 2008; Leroy et al., 2008, 2013) with the apparently shorter depletion times measured on ∼ 100 pc scales (∼40−500 Myr; Evans et al., 2009; Heiderman et al., 2010; Gutermuth et al., 2011; Evans et al., 2014; Schruba et al., 2017). In the proposed scenario, the difference in these time scales originates from the fact that not all the gas is going through the star formation process at the same time. It is suggested that the fraction of molecular gas, that is actively forming stars, is regulated by local (stellar feedback, turbulence, gravitational instabilities) and global (large-scale turbulence, differential rotation) mechanisms that continuously turn on and off the formation of stars. Consequently, several of these star formation cycles must occur in order to process all the molecular gas in a given volume. Thus, at high spatial resolution, a larger scatter in the distribution of depletion times (and thus in the rKS relation) results from the decoupling of the actively star-forming clouds from the quiescent ones.

The local mechanism is discussed more generally in Kruijssen & Longmore (2014) and Kruijssen et al. (2018), where the authors define a critical spatial scale on which the rKS breaks down from its integrated version, due to an incomplete sampling of the star-forming cycle. This spatial scale is defined as a function of the typical separation between independent star-forming regions, and the duration of the shortest phase of the star-forming process. This critical spatial scale equals the smallest region in which the star formation process is statistically well sampled. In this regard, having found the scatters at 100 pc $\sigma_{\mathrm{rSFMS}} > \sigma_{\mathrm{rKS}} > \sigma_{\mathrm{rMGMS}}$ is consistent with the expectation from this evolutionary scenario, provided that $\tau_{\mathrm{H}\alpha} < \tau_{\mathrm{CO}} < \tau_{\mathrm{stars}}$, where τ corresponds to the duration each tracer is visible across the star formation cycle. Due to the fact that the period of time in which young stars ionize their surrounding interstellar medium is shorter than the lifetime of molecular clouds, i.e., $\tau_{\mathrm{H}\alpha} < \tau_{\mathrm{CO}}$ (Kruijssen et al., 2019; Chevance et al., 2020a), the impact of time evolution on the rMGMS will be smaller than on the rSFMS or the rKS. Consequently, the minimum

spatial scale needed to properly sample the rMGMS is smaller than that needed for the rSFMS or the rKS. At spatial scales of $\gtrsim$1 kpc, we are no longer in this "undersampling" regime, and the rKS shows the least scatter.

However, statistically incomplete sampling is not the only source of scatter for these resolved scaling relations. The slope of the rKS is also sensitive to the conditions present in the interstellar medium, such as metallicity and ultraviolet radiation field (Feldmann et al., 2011). Further Leroy et al. (2013) reported that variations in the measured depletion time ($\tau_{\rm dep} = \Sigma_{\rm mol.gas}/\Sigma_{\rm SFR}$) across different environments at $\sim$kpc spatial scales are consistent with variations of the CO-to-H_2 conversion factor. Similarly for the rSFMS, Ellison et al. (2020b) found that at $\sim$kpc spatial scales, the scatter in this relation is likely driven by local variations in star formation efficiency. Here, we find large variations in these resolved scaling relation for different galaxies and galactic environments, in terms of both slope and normalization, which are particularly strong in the case of the rSFMS and rMGMS. These differences are key in setting their scatter, particularly at 1 kpc spatial scale, where we are no longer in a stochastic regime, for the reasons described earlier.

2.5.2 Role of non-detections in our analysis

In this section, we discuss the impact of excluding non-detections from the analysis. At high spatial resolution the non-detection fraction is quite large and their treatment can drastically alter the results.

Insights from simulations

In Calzetti et al. (2012), the authors studied variations in the slope of the observed rKS with different spatial resolution using simulated galaxies. They found that variations with spatial scale depend mainly on the slope of the true underlying rKS. In particular, for a slope of 1, they found a nearly constant slope in the observed relation (variation of $\sim$0.05) from 200 pc to 1 kpc resolution. However, due to the assumed underlying close H_2–SFR relation, both quantities share the same spatial distribution and hence have basically identical detection fractions which is not necessarily the case for our data.

Similarly, in Hani et al. (2020) the authors used a sample of Milky Way-like galaxies from FIRE-2 simulations to study the rSFMS measured at spatial scales of 100 pc, 500 pc, and 1 kpc. They reported a systematic steepening of this relation at larger spatial scales. It is important to note that only pixels with nonzero SFR values were considered in their analysis. They interpreted that this effect was primarily caused by differences in the detection fraction of the SFR across the galactic disk. A lower detection fraction in outer regions, where the stellar mass surface density is lower, would cause a stronger dilution of the SFR in the low stellar mass surface density regime than in the inner and denser regions when spatially averaging the data. As a consequence, the rSFMS has been measured to be flatter at 100 pc and to steepen at larger spatial scales, where the sparser intrinsic SFR distribution in the low mass surface density regime is leading to lower SFR surface density values.

This steepening of the rSFMS is mainly a consequence of the methodology used (i.e., excluding N/D in the fitting process). In the following, we investigate this effect in our data, and measure how much our slope measurements change under this alternative approach.

Relation	$\alpha_{D/O\,100pc}$	$\sigma_{D/O\,100pc}$	$\alpha_{D/O\,500pc}$	$\sigma_{D/O\,500pc}$	$\alpha_{D/O\,1kpc}$	$\sigma_{D/O\,1kpc}$
rSFMS	0.78 ± 0.01	0.49	0.83 ± 0.03	0.47	0.86 ± 0.04	0.44
rKS	0.97 ± 0.01	0.41	1.00 ± 0.02	0.33	0.98 ± 0.03	0.27
rMGMS	0.74 ± 0.01	0.32	0.83 ± 0.02	0.30	0.88 ± 0.03	0.29

Table 2.5: Slope (α) and scatter (σ) using all the available pixels in our sample, for each one of the scaling relations probed, at spatial scales of 100 pc, 500 pc and 1 kpc. Non-detections are excluded when measuring the slope.

Slope changes in our scaling relations

Figures 2.12, 2.25 and 2.26, show the rSFMS, rKS, and rMGMS, respectively, when non-detections are excluded from the fit. We define $\alpha_{D/O}$ and $\sigma_{D/O}$ as the measured slope and scatter considering pixels with nonzero detections only. Each relation studied here is presented at three spatial scales (100 pc, 500 pc, and 1 kpc from left to right). The slopes and scatter measured in the overall sample at each spatial resolution are summarized in Table 2.5, while Tables 2.6, 2.8, and 2.9 list the slopes and scatter measured for the rSFMS, rKS, and rMGMS, respectively, in each galaxy at each spatial scale. When we exclude non-detected pixels from our analysis, we see a systematic steepening of the slope at larger spatial scales in the rSFMS and the rMGMS. The steepening is particularly strong in the rMGMS due to lower (CO) detection fraction in this relation (∼35% at 100 pc). The rKS is less affected as molecular gas and SFR share a more similar spatial distribution (Schinnerer et al., 2019a; Pan et al., 2022) and non-detections in SFR frequently coincide with a non-detection in molecular gas, resulting in a high detection fraction of SFR for a given molecular gas value in the rKS relation (∼84% at 100 pc).

Additionally, we observe a flattening at the low end of the stellar mass surface density ($\log \Sigma_{stellar}$ [$M_\odot$ kpc^{-2}] $\lesssim 7.5$) in the rSFMS and the rMGMS at 100 pc scale. This flattening is qualitatively similar to that reported by Barrera-Ballesteros et al. (2021a) or Cano-Díaz et al. (2019), attributed to Hα pollution from non-SF emission at low SFR values and due to the Hα detection threshold (see also Salim et al., 2007). As we correct for non-star-forming contributions in our Hα derived SFR maps, we interpret this flattening is caused by the larger fraction of non-detections in these low stellar mass surface density bins. Therefore, excluding non-detections leads to an overestimation of the mean measured in these bins, which results in the observed flattening at low stellar mass surface densities.

Even though we see flatter relations at 100 pc than at 1 kpc for the overall sample when non-detections are excluded, the behavior of individual galaxies is more diverse. Differences between the lowest and highest resolution measurements in each galaxy mainly depend on the spatial distributions of stellar mass and ionized gas (in the case of the rSFMS) across the galactic disk within each galaxy. However, for all galaxies the slopes obtained at 100 pc are flatter when non-detections are excluded, compared to when they are included.

Treatment of non-detections and its effect on the slope of the scaling relations

As explained in Sec. 2.5.2, the flattening of the relations toward small spatial scales arises when non-detections are excluded from the analysis. This is because "empty" regions at smaller spatial scales are averaged at larger spatial scales with regions including detections.

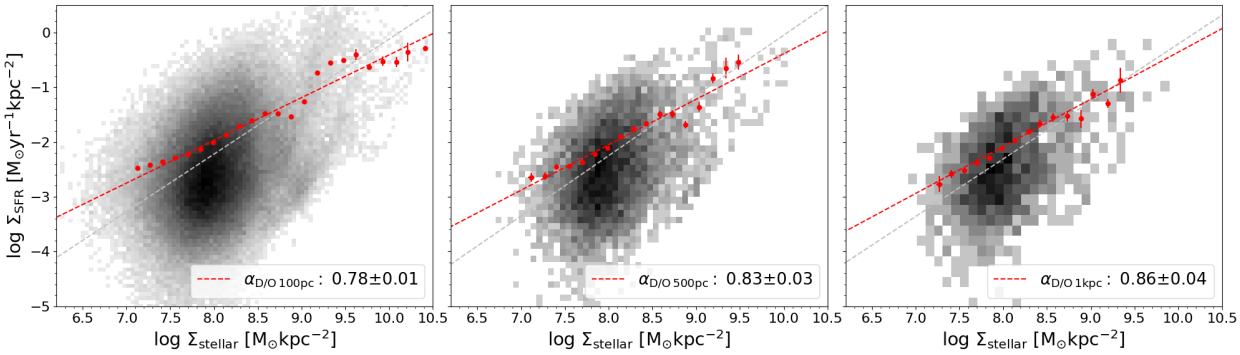

Figure 2.12: 2D distribution of the resolved star formation main sequence considering all galaxies in our sample at three spatial resolutions (100 pc, 500 pc and 1 kpc from left to right). Non-detection pixels have been excluded from the fit. This produces a systematic flattening at higher spatial resolution. The fiducial overall best-fitting power law at each spatial scale is marked with the gray dashed line for reference.

Target	$\alpha_{D/O\,100pc}$	$\sigma_{D/O\,100pc}$	$\alpha_{D/O\,500pc}$	$\sigma_{D/O\,500pc}$	$\alpha_{D/O\,1kpc}$	$\sigma_{D/O\,1kpc}$
NGC1087	1.19 ± 0.03	0.41	1.40 ± 0.03	0.35	1.34 ± 0.03	0.23
NGC1300	0.57 ± 0.01	0.39	0.74 ± 0.01	0.38	0.71 ± 0.01	0.35
NGC1365	1.06 ± 0.01	0.50	1.23 ± 0.01	0.53	1.02 ± 0.01	0.43
NGC1385	1.33 ± 0.03	0.43	1.42 ± 0.03	0.44	1.44 ± 0.03	0.46
NGC1433	0.48 ± 0.01	0.36	0.59 ± 0.01	0.33	0.66 ± 0.01	0.26
NGC1512	0.35 ± 0.01	0.40	0.63 ± 0.01	0.36	0.78 ± 0.01	0.33
NGC1566	0.59 ± 0.02	0.48	0.64 ± 0.02	0.46	0.65 ± 0.02	0.41
NGC1672	1.04 ± 0.01	0.48	1.10 ± 0.01	0.50	1.18 ± 0.01	0.50
NGC2835	0.39 ± 0.03	0.41	0.51 ± 0.03	0.36	0.60 ± 0.03	0.22
NGC3351	0.40 ± 0.02	0.37	1.14 ± 0.02	0.28	1.24 ± 0.02	0.13
NGC3627	0.23 ± 0.03	0.48	0.32 ± 0.03	0.42	0.24 ± 0.03	0.40
NGC4254	0.62 ± 0.01	0.48	0.64 ± 0.01	0.41	0.72 ± 0.01	0.28
NGC4303	0.53 ± 0.01	0.50	0.66 ± 0.01	0.42	0.51 ± 0.01	0.38
NGC4321	0.71 ± 0.01	0.49	0.86 ± 0.01	0.49	0.95 ± 0.01	0.45
NGC4535	0.35 ± 0.03	0.49	0.32 ± 0.03	0.53	0.54 ± 0.03	0.41
NGC5068	0.11 ± 0.04	0.46	0.57 ± 0.04	0.33	-0.48 ± 0.04	0.24
NGC7496	0.77 ± 0.03	0.46	1.25 ± 0.03	0.46	1.19 ± 0.03	0.36
IC5332	0.20 ± 0.05	0.36	0.12 ± 0.05	0.25	-0.09 ± 0.05	0.06

Table 2.6: Slope (α) and scatter (σ) for the rSFMS measured in each galaxy in our sample at spatial scales of 100 pc, 500 pc and 1 kpc. The non-detections have been excluded from the slope measurement.

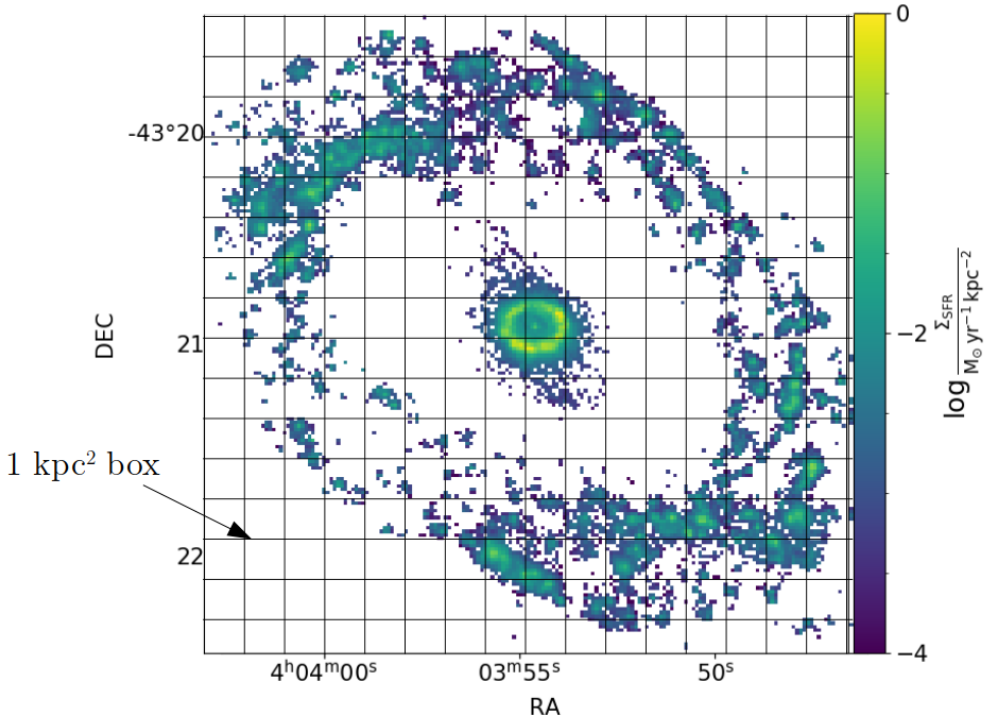

Figure 2.13: Sketch to exemplify the methodology to compute the distribution of the Hα detection fraction. In each 1 kpc^2 box we calculated the filling factor ($\mathrm{DF}_{\mathrm{H}\alpha}$) defined as the fraction of pixels with nonzero SFR.

This effectively dilutes the signal when the data are degraded, and the magnitude of this dilution will depend on the local detection fraction. The spatial distribution of Hα with respect to the stellar mass surface density is complex, and varies not only from galaxy to galaxy, but also between different environments within galaxies. Therefore, the local detection fraction follows an equally complex distribution.

Here we explore if we can recover a relation between the detection fraction and the amount of flattening, despite of the complex distribution of these quantities, using the slope measured at 100 pc spatial scale in a given galaxy, when N/D are excluded from the measurement. We measured the detection fraction of the SFR inside 1 kpc^2 boxes in the 100 pc spatial scale maps. For each box we calculated the corresponding detection fraction ($\mathrm{DF}_{\mathrm{H}\alpha}$), defined as the fraction of pixels with nonzero emission, and we computed the distribution of the $\mathrm{DF}_{\mathrm{H}\alpha}$ within these boxes for each galaxy. Figure 2.13 shows a schematic representation of the approach for one example galaxy.

Figure 2.14 shows the normalized distribution of $\mathrm{DF}_{\mathrm{H}\alpha}$ for each galaxy. The corresponding mean (μ_{DF}) and standard deviation (σ_{DF}) are indicated in each panel. The latter contains information about the spatial configuration of the SFR. A galaxy with a compact (spatially concentrated) configuration will have a rather bimodal distribution of $\mathrm{DF}_{\mathrm{H}\alpha}$ (and consequently higher $\sigma_{\mathrm{DF}_{\mathrm{H}\alpha}}$), where boxes will have mostly ∼0 or ∼1 values, whereas a more clumpy (assembled as individual separated clumps) configuration will lead to a flatter and uniform distribution.

We parametrize the difference in slope when non-detections are excluded from the fit as

compared to the fiducial value as:

$$\Delta\alpha_{\mathrm{D/O}} = \alpha - \alpha_{\mathrm{D/O}} \ , \tag{2.6}$$

where α is the slope measured for a galaxy using the fiducial approach and $\alpha_{\mathrm{D/O}}$ is the slope measured for the same galaxy when non-detections are excluded in the fit.

Figure 2.15 shows the change of slope when non-detections are excluded in the calculation as a function of $\mu_{\mathrm{DF_{H\alpha}}}$ for the galaxies in our sample. The figure shows a negative correlation ($\mathbf{PCC} \approx -0.68$) between $\mu_{\mathrm{DF_{H\alpha}}}$ and the change in the measured slope when non-detections are excluded. This can be interpreted as galaxies with higher average detection fraction are less affected by dilution of their signal, which implies that excluding non-detections has a smaller impact on the measured slope. So, despite of the complexity of the 2D distribution of ionized gas across the galactic disk, we identify a trend between the flattening and the distribution of the detection fraction.

The scatter in the correlation shown in Figure 2.15 is likely because this diagnostic does not include any aspect of the underlying $\Sigma_{\mathrm{stellar}}$ (or $\Sigma_{\mathrm{mol.gas}}$) distribution. Ultimately, the change of the slope will not only depend on the detection fraction in a given region, but also on its underlying $\Sigma_{\mathrm{stellar}}$ (for the rSFMS). Whereas the first is highly driven by local environment (Querejeta et al., 2021, Meidt et al. submitted), the second varies much more smoothly across galactic disks. The detection fraction distribution by its own cannot completely describe the flattening of the slope.

Role of detection fraction in the dispersion of slopes at 100 pc

In this section, we test if the dispersion that we see in the slopes measured for the rSFMS could be linked to differences in the SFR detection fraction distributions. Figure 2.16 shows $\Delta\alpha_{\mathrm{overall}}$ (as defined in Eq. 2.5, the difference in slope of a given galaxy and the full sample) as a function of $\sigma_{\mathrm{DF_{H\alpha}}}$. The figure shows a clear positive correlation ($\mathbf{PCC} \approx 0.72$), meaning that galaxies with larger spread (i.e., larger $\sigma_{\mathrm{DF_{H\alpha}}}$) tend to have a steeper rSFMS (i.e., more positive $\Delta\alpha_{\mathrm{overall}}$) and galaxies with smaller spread tend to have a flatter rSFMS (i.e., more negative $\Delta\alpha_{\mathrm{overall}}$). This can be explained as galaxies with larger $\sigma_{\mathrm{DF_{H\alpha}}}$ (i.e., with a more bimodal distribution of $\mathbf{DF_{H\alpha}}$) are associated with a spatial configuration in which the impact of non-detections is stronger in some regions (usually in the low stellar mass surface density regime) and less significant in others (central regions with higher stellar mass surface densities). This leads to a systematically steeper rSFMS by pulling down the low mass surface density end of the rSFMS, where non-detections dominate, with respect to the high mass surface density end. Galaxies with smaller $\sigma_{\mathrm{DF_{H\alpha}}}$ values show either a flatter $\mathbf{DF_{H\alpha}}$ distribution or a concentration of their values around zero. In these scenarios, non-detections do not contribute to steepen the relation in the same way, since different mass ranges are similarly affected.

We find similar correlations between the detection fraction distributions of the molecular gas tracer and changes in the slope of the rMGMS (see Supporting material 2.7.4). Hence, the detection fraction of Hα (or molecular gas) is a relevant aspect to set the rSFMS (rMGMS) slope when measured at high resolution. This is also consistent with finding a similar dispersion in the slopes of the rSFMS and the rMGMS, and a significantly smaller dispersion in the slopes of the rKS. Due to the more similar spatial distribution between Hα

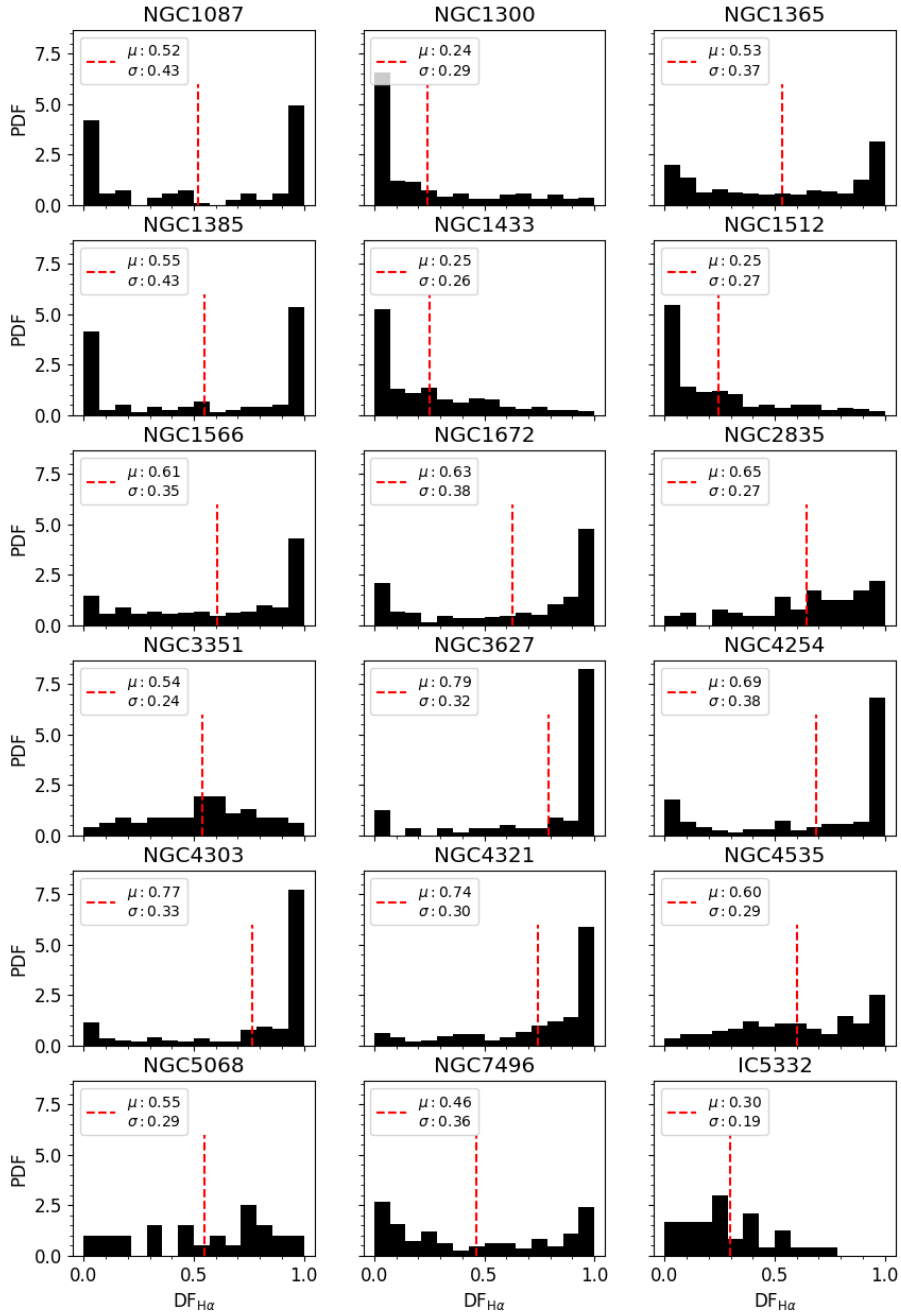

Figure 2.14: Normalized distribution of the H_α detection fraction ($DF_{H\alpha}$) inside 1 kpc^2 size boxes in the galactic disk. Each panel corresponds to a galaxy from our sample. The mean (μ) and standard deviation (σ) are indicated in each panel.

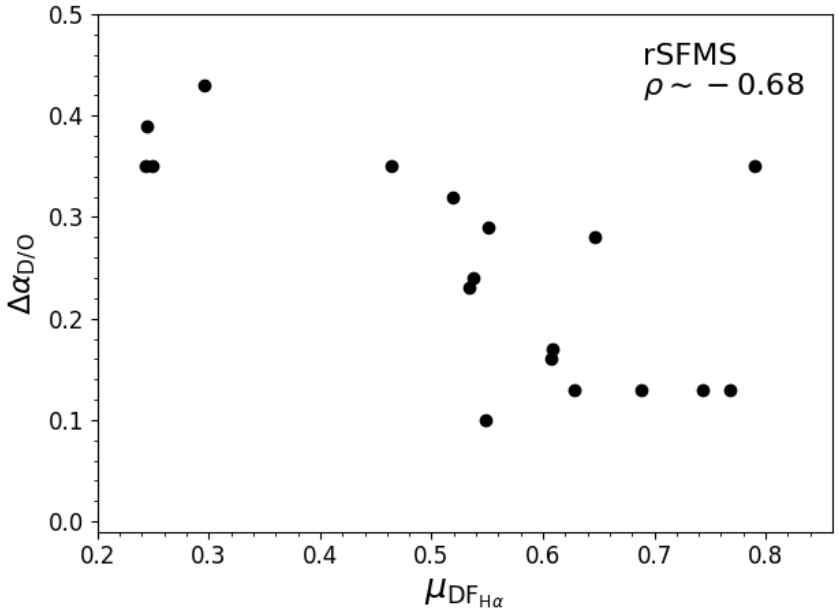

Figure 2.15: Difference between the slope of the rSFMS of each galaxy measured with the fiducial approach and the slope measured when non-detections are excluded, as a function of the mean detection fraction of the SFR tracer in each galaxy ($\mu_{DF_{H\alpha}}$). All values are positive in the y-axis because excluding non-detections always leads to a flatter relation. The PCC of the correlation is indicated in the top-right corner of the panel.

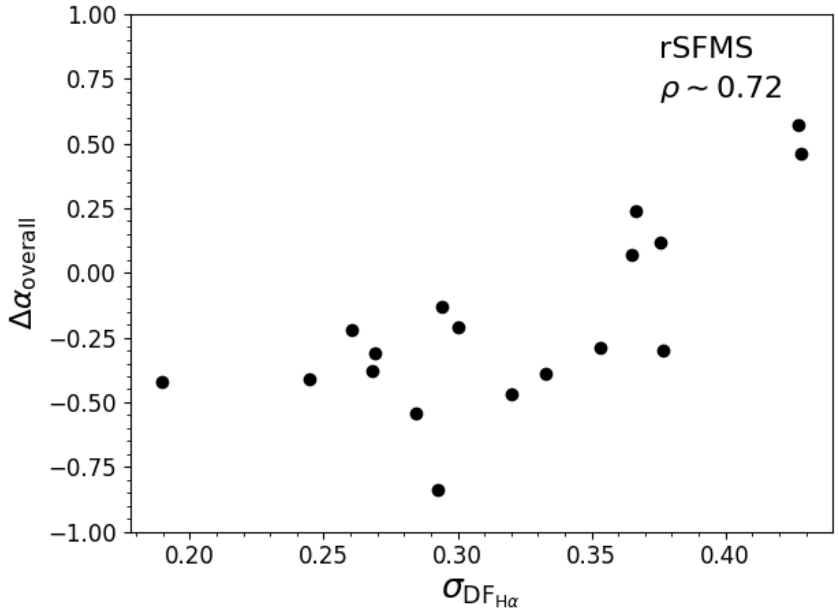

Figure 2.16: Difference between the slope of the rSFMS of each galaxy measured with the fiducial approach and the overall measurement as a function of the standard deviation of the detection fraction distribution of the SFR tracer in each galaxy ($\sigma_{DF_{H\alpha}}$). The PCC of the correlation is indicated in the top-right corner of the panel.

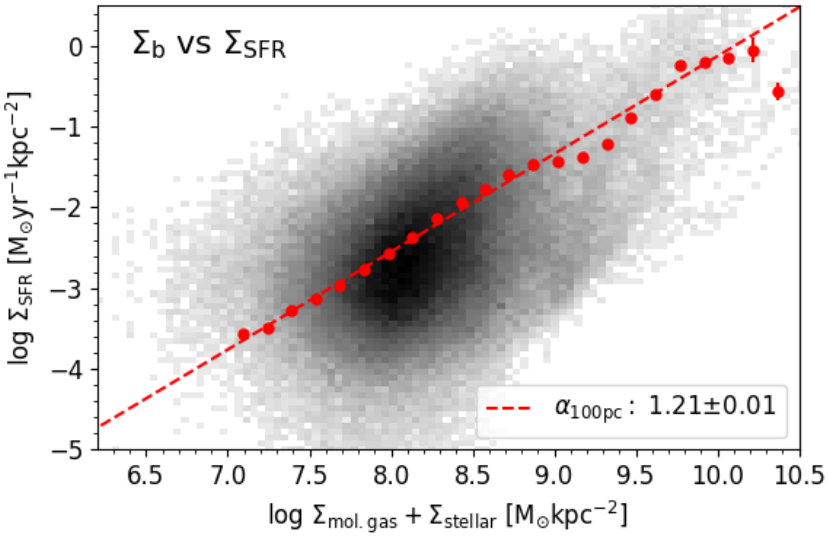

Figure 2.17: Σ_{SFR} as a function of Σ_b, defined as $\Sigma_{mol.gas} + \Sigma_{stellar}$. We explored the existence of a tighter correlation with Σ_b as it is a better tracer for the total hydrostatic pressure exerted by the baryonic mass. We measured a slope of 1.18 ± 0.005 with a scatter, and a scatter lower than the rSFMS and higher than the rKS.

and the molecular gas tracer, differences in the detection fraction are also less extreme.

2.5.3 Role of baryonic mass surface density in regulating SFR

Previous studies have demonstrated that the mid-plane pressure of the interstellar medium impacts its physical properties and consequently the local SFR surface density. Leroy et al. (2008) reported a good correlation between the mid-plane hydrostatic gas pressure and the local SFR surface density and gas depletion time in 23 nearby galaxies in the THINGS (Walter et al., 2008) and HERACLES (Leroy et al., 2009) surveys. Along the same line, Schruba et al. (2019) –studying 8 local galaxies– and Sun et al. (2020a) –studying 28 star-forming galaxies from the PHANGS-ALMA sample– found that the average internal pressure of molecular clouds tends to balance the sum of their own weights and the external interstellar medium pressure. Sun et al. (2020a) also reported a tight relationship between the mid-plane hydrostatic pressure and SFR surface density across their sample. These observations are in line with feedback-driven star formation models (Ostriker et al., 2010; Ostriker & Shetty, 2011), in which the dynamical equilibrium of the interstellar medium in the galaxy gravitational potential regulates the local SFR surface density and vice versa.

Since both stars and molecular gas define the gravitational potential of a galaxy (neglecting the contribution from atomic gas), previous studies have also explored the existence of a relation between Σ_{SFR} and a combination of $\Sigma_{stellar}$ and $\Sigma_{mol.gas}$ (Matteucci et al., 1989; Shi et al., 2011; Dib et al., 2017; Shi et al., 2018; Dey et al., 2019; Lin et al., 2019; Barrera-Ballesteros et al., 2021a; Sánchez et al., 2021).

In Barrera-Ballesteros et al. (2021a), the authors computed the "baryonic" mass surface density as $\Sigma_b = \Sigma_{stellar} + \Sigma_{mol.gas}$ at ∼kpc scales and found that Σ_b tightly correlates with

SFR, with a slope of 0.97 and a residual scatter lower than that measured for the rSFMS or the rKS. We derived the Σ_{b} versus Σ_{SFR} relation at 100 pc spatial scale (see Fig. 2.17) and measured a slope of 1.21 ± 0.01 and a scatter of 0.49 dex. At 500 pc we obtain a slope of 1.22 ± 0.02 and a scatter of 0.46 dex, and at 1 kpc a slope of 1.14 ± 0.03 and a scatter of 0.42 dex. These values of scatter are higher than computed for the rKS and lower than those of the rSFMS at all spatial scales. Thus, we find that $\Sigma_{mol.gas}$ is a better predictor of Σ_{SFR} than Σ_{b}. Differences with Barrera-Ballesteros et al. (2021a) are probably related to the treatment of N/D in the fit (which may directly impact the measured slope, as shown in Sec.2.5.2), and the use of Balmer decrement as molecular gas surface density tracer (which is expected to introduce some level of scatter to the correlation).

However, we stress here that the mid-plane hydrostatic pressure is not necessarily directly proportional to the baryonic mass surface density. Although Σ_{b} is sometimes used as a proxy for the hydrostatic pressure, it does not accurately reflect the gravitational potential felt by the gas disk in galaxies, because the stellar disk and gas disk usually have quite different scale heights (e.g., Ostriker et al., 2010; Bacchini et al., 2019a,b, 2020; Sun et al., 2020c). More careful investigations of the quantitative relation between Σ_{mol}, Σ_{SFR}, and the mid-plane hydrostatic pressure in the future will shed more light on the role of hydrostatic pressure in regulating star formation (e.g., Barrera-Ballesteros et al., 2021a,b).

2.5.4 Systematic effects

In this section, we test how some of our assumptions impact our measurements of the scaling relations probed. In Sec. 2.5.4, we derive the rSFMS and rKS relations after removing diffuse ionized gas (DIG) emission. In Sec. 2.5.4, we use a constant α_{CO} to measure the rKS and the rMGMS. Finally, in Sec. 2.5.4 we show the resultant rSFMS and rKS when a longer timescale SFR tracer is used instead of Hα.

Role of diffuse gas emission

In our fiducial approach, we aim at measuring scaling relations consistently at different spatial scales. Thus, we want to include any detectable SFR emission at high angular resolution (as well as N/D), that would then be averaged in the lower resolution measurement. However, even though we followed the approach described in Sec. 3.2.5 in order to correct the Hα emission by DIG contamination, we could still be left with some amounts of contaminant emission in our analysis. Here, we explore an alternative way to identify the star formation-associated Hα emission at the native MUSE resolution that is suitable to identify individual H II regions. For this, we use the H II region catalog from Santoro et al. (2022). In short, H II regions are identified in the Hα map using HIIphot (Thilker et al., 2000) for resolved sources and DAOStarFinder (Bradley et al., 2020) for point-like sources. A BPT diagnosis using the [O III]/Hβ and [N II]/Hα line ratios of the integrated spectra of each region was then used to select the Hα-emitting regions dominated by star formation, as described in Kewley et al. (2006). Once H II regions have been identified at the native MUSE resolution, we mask all remaining emission before computing our maps at 100 pc, 500 pc, and 1 kpc scales. The fraction of emission removed is on the order of $\sim$30% ($\sim$60% of the pixels with nonzero emission in the fiducial approach are masked), consistent with the diffuse fractions obtained

Relation	α_{100pc}	σ_{100pc}	α_{500pc}	σ_{500pc}	α_{1kpc}	σ_{1kpc}
rSFMS	1.08 ± 0.01	0.58	1.14 ± 0.03	0.63	1.09 ± 0.04	0.61
rKS	1.23 ± 0.01	0.48	1.20 ± 0.02	0.42	1.12 ± 0.03	0.35

Table 2.7: Slope (α) and scatter (σ) using all available pixels in our sample, for the scaling relations probed, at spatial scales of 100 pc, 500 pc and 1 kpc. All the Hα emission not associated with morphologically-defined H II regions has been excluded before re-sampling the maps to the different spatial scales. The methodology used to exclude this emission is described in Sec. 2.5.4

by decomposing the narrowband Hα images of these galaxies into diffuse and compact components in Fourier space (Hygate et al., 2019; Chevance et al., 2020a). This demonstrates that our procedure reliably removes all potentially contaminant emission before resampling the SFR map.

Figure 2.18 shows the resulting SFR map from this different approach at a spatial scale of 100 pc for NGC 1512. Individual H II regions are much more easily distinguished in the resultant map. Quantitatively, this creates large differences, mostly at the edges of H II regions or molecular clouds, where the signal is now averaged with neighboring zero-emission pixels during the resampling and pulled to lower levels of SFR. At the same time, it removes all faint, DIG-contaminated pixels from the relation. Figure 2.19 highlights this effect for the rSFMS of NGC 4254. The top panel shows the rSFMS from the fiducial approach, and the bottom panel shows the same relation using this alternative approach. The color scheme is the same as used in Fig. 2.5, indicating the morphological environment of each pixel. The black dashed line corresponds to the overall fit from the fiducial approach and has been overplotted as reference. Faint DIG-contaminated pixels are removed, which reduces the number of data points in the relation. However, the remaining pixels in the low SFR regime are pulled to even lower values resulting in a qualitatively similar rSFMS.

Figure 2.20 shows the 2D distributions for the rSFMS and the rKS probed at 100 pc, 500 pc, and 1 kpc scale with their corresponding binned trends and best-fitting power laws. The inferred slopes agree relatively well with those obtained using the fiducial method (see Fig. 2.11). Differences are expected since we are now fitting a power law to a subset of pixels (while the rest is classified as N/D). However, the scatter is systematically enhanced in both relations by a factor of $\sim 1.1 - 1.4$, depending on the spatial scale considered. This increase is mainly driven by the effect previously described: the dilution of emission at the edges of H II regions or molecular clouds. Thus, we conclude that we could be underestimating the SF-associated emission by removing too much signal and, thus, introducing additional scatter to the relation. The true scatter of these scaling relations is probably somewhere in between our fiducial approach and applying the strict H II region mask. Hence, in our fiducial approach the scatter of these relations is possibly underestimated due to contaminant Hα emission boosting the SFR of the faintest pixels.

Impact of the chosen CO-to-H_2 conversion factor

As explained in Sec. 3.2.2, our fiducial CO-to-H_2 conversion factor scales with local gas-phase metallicity. In this section, we explore the impact of assuming a constant conversion factor of 4.35 $M_\odot$ pc^{-2} (K km s^{-1})$^{-1}$ (Bolatto et al., 2013) on the measured rKS and rMGMS.

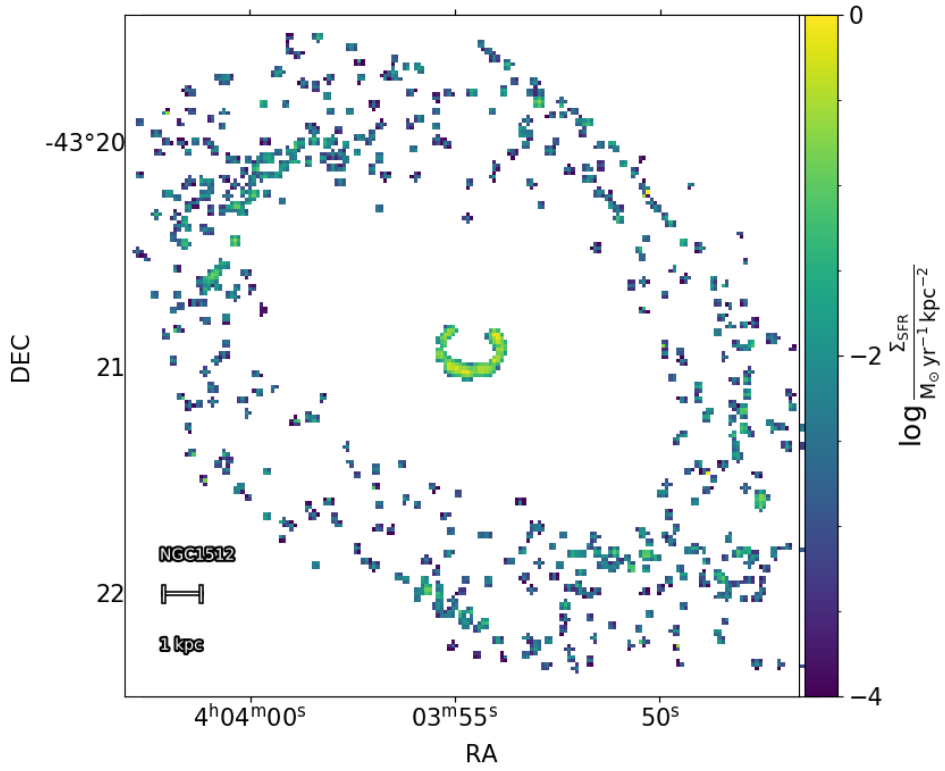

Figure 2.18: Example of SFR surface density at spatial scales of 100 pc, for one of the galaxies in our sample (NGC 1512). All the Hα emission not associated with morphologically-defined H II regions has been excluded before re-sampling the maps. The methodology used to exclude this emission is described on the main text in Sec. 2.5.4.

All of the galaxies in our sample exhibit either a negative or flat metallicity profile (Ho et al., 2015). This leads to a higher CO-to-H_2 conversion factor in the outer part of the galactic disk than in the central part. When the radial gradient is removed, differences between central (usually denser) clouds and outer (usually fainter) clouds are enhanced. This widens the range of molecular gas surface densities probed. Figure 2.21 shows the rKS (top) and rMGMS (bottom) at 100 pc spatial scale using a constant α_{CO}. The best-fitting power law obtained with the fiducial approach is indicated by the gray line. As a consequence of this widened range of molecular gas surface densities from applying a constant CO-to-H_2 conversion factor, the slope of the rKS decreases to 1.01 ± 0.01 and that of the rMGMS increases to 1.28 ± 0.01, representing a change of $\sim$5% and $\sim$8%, respectively, as compared to the fiducial scenario. Finally, the normalization of these relations is also affected by the CO-to-H_2 prescription. Under the assumption of a constant α_{CO}, we find an intercept of -9.29 for the rKS and -3.36 for the rMGMS (for reference, the intercepts computed under our fiducial α_{CO} prescriptions are -9.96 and -2.23, respectively).

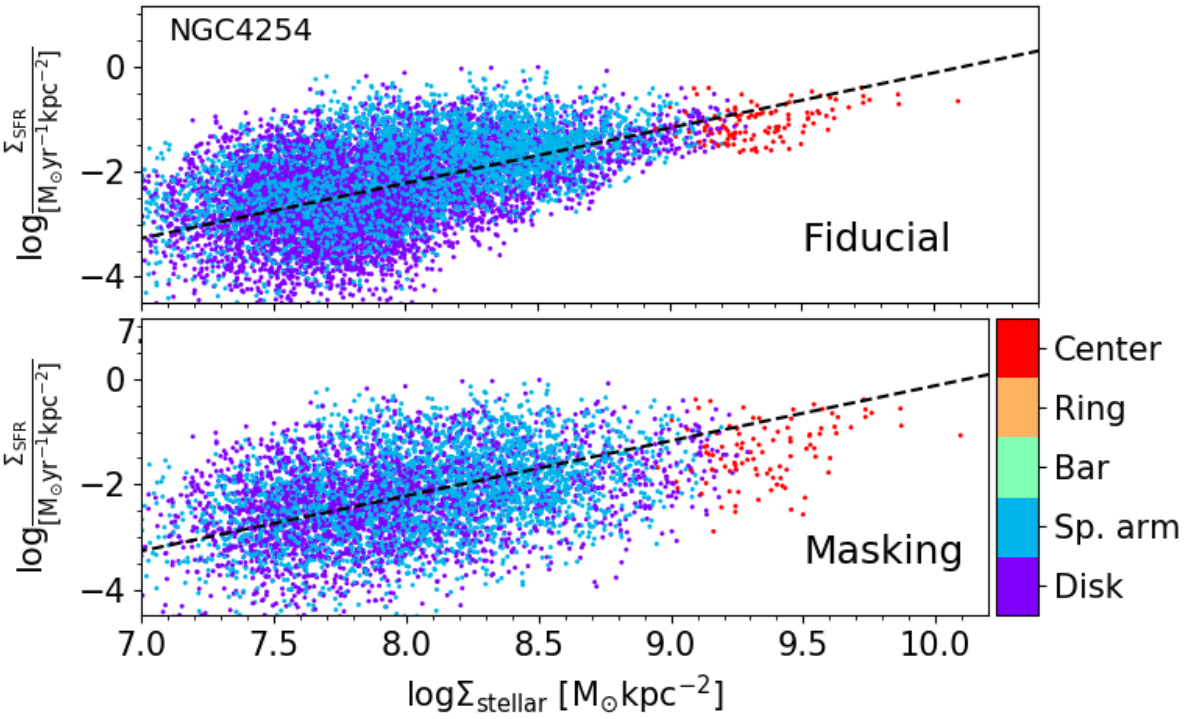

Figure 2.19: rSFMS of one galaxy in our sample (NGC 4254) to illustrate the effect of removing Hα emission not associated with morphologically defined H II regions before resampling the SFR surface density map. Top: fiducial methodology. Bottom: alternative methodology as described in Sec. 2.5.4. The color scheme is the same as in Fig. 2.6. The black line correspond to the global rSFMS measured using all pixels with the fiducial approach (see Fig. 2.4).

Probing SFR on a 150 Myr timescale with spectral fitting

So far, we have used Hα emission as our SFR tracer. Hα is known to trace the formation of stars during the last ∼10 Myr (Calzetti, 2013; Leroy et al., 2012; Catalán-Torrecilla et al., 2015; Haydon et al., 2020). Here we explore how the slope measured for the rSFMS and rKS varies when we use a SFR tracer sensitive to longer star formation timescales. We use the resolved star formation histories (see Sec. 3.2.4) to map the fraction of total stellar mass assembled during the last 150 Myr (i.e., the youngest 4 age bins in our age–metallicity grid). Multiplying this fraction with the stellar mass surface density and dividing it by 1.5×10^7 yr results in a SFR surface density map that probes longer timescales.

A longer timescale SFR tracer smooths the SFR values, i.e., high SFR values from the short timescale are nearly unaffected and low SFR values are pushed to higher values. Figure 2.22 shows how this change impacts the rSFMS (top) and the rKS (bottom). Consequently, both relations are significantly flattened. In particular, the slope of the rSFMS decreases to 0.61 ± 0.01 and the slope of the rKS to 0.60 ± 0.01.

This also drastically reduces the scatter in both relations to 0.27 dex and 0.24 dex, respectively. A decrease in the scatter is consistent with the uncertainty principle reported in Kruijssen & Longmore (2014) and Kruijssen et al. (2018) (also see discussion in Sec. 2.5.1).

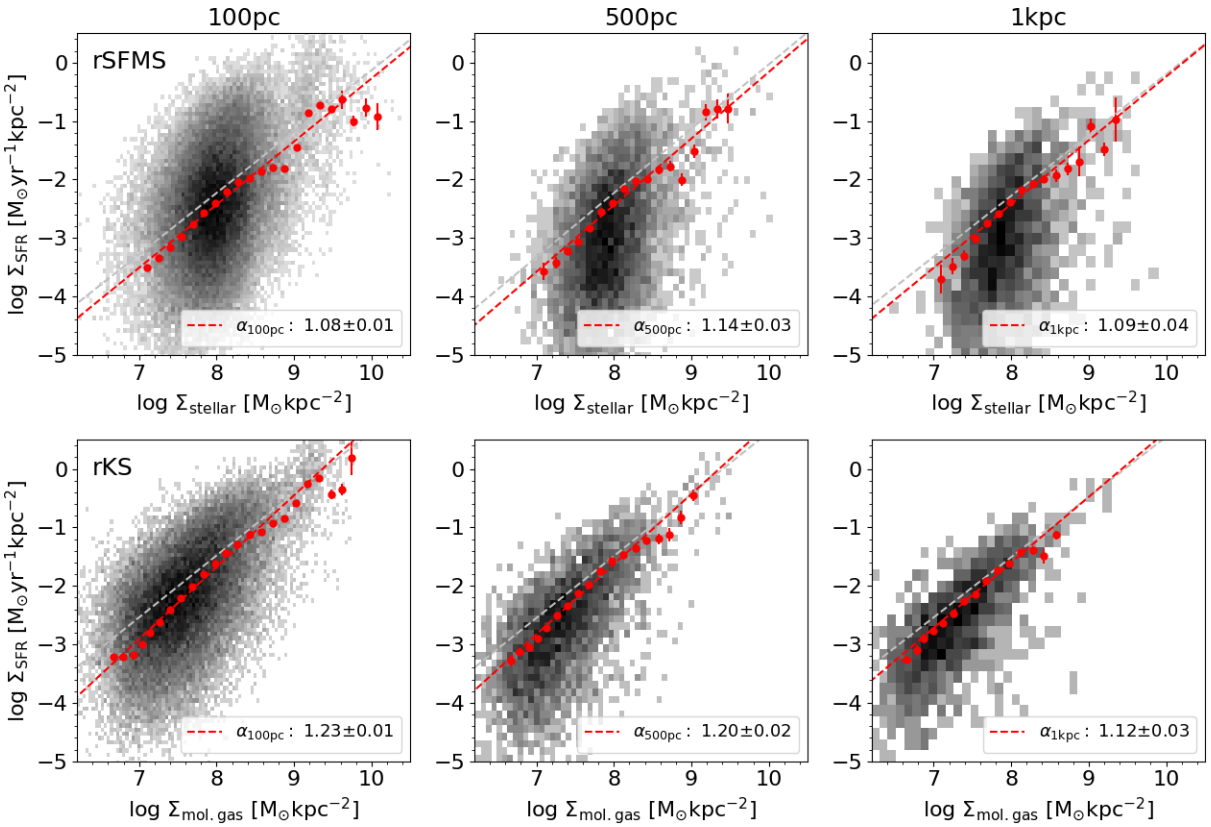

Figure 2.20: Effect of excluding diffuse gas emission before resampling: 2D distributions of the overall rSFMS (top row) and rKS (bottom row) using all the available pixels in our sample, probed at spatial scales of 100 pc (left column), 500 pc (middle column) and 1 kpc (right column). The x-axis binning and the best-fitting power law are indicated with red dots and a red dashed line respectively. The measured slope and its error are indicated in each panel (see Sec. 2.5.4 for details). The fiducial overall best-fitting power law at each spatial scale is marked with the gray dashed line for reference.

Averaging the SFR over a longer time scale increases the period of time in which young stars can be detected (i.e., $\tau_{\rm young-stars} > \tau_{\rm H\alpha}$), and thus reduces the critical spatial scale at which the relation breaks due to statistical undersampling of the star formation process.

We summarize that the timescales involved in the SFR determination strongly influence the resulting slope and scatter of the rSFMS and rKS relations. This agrees with a similar finding presented in Barrera-Ballesteros et al. (2021a).

2.5.5 Implication of our results

While the relation between $\Sigma_{\rm SFR}$ and $\Sigma_{\rm mol.gas}$ is direct, since star formation occurs in molecular clouds, the relation between $\Sigma_{\rm SFR}$ and $\Sigma_{\rm stellar}$ is understood as the interplay between the hydrostatic pressure exerted by the stellar (and cold gas) disk, together with feedback processes (such as stellar winds and supernovae) regulating the star formation. However, given that we found the rKS was tighter than the rSFMS and the $\Sigma_{\rm SFR}$ versus $\Sigma_{\rm b}$ correlation,

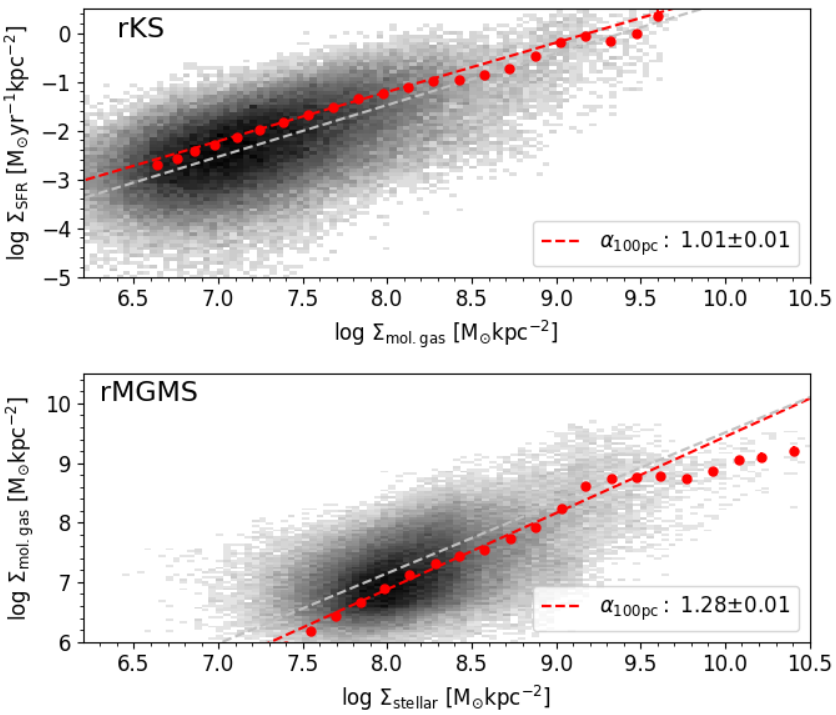

Figure 2.21: rKS (top) and rMGMS (bottom) measured using all pixels from our sample and assuming a constant CO-to-H_2 conversion factor. This conversion factor leads to a flatter rKS and a steeper rMGMS (see Sec. 2.5.4 for a discussion). The best fit power law obtained with the fiducial approach is indicated with the gray line.

we conclude that it is mainly the amount of available molecular gas that regulates the star formation rate rather than the amount of stellar or baryonic mass. This agrees well with what was reported by Lin et al. (2019), where the authors also conclude that the rSFMS could originate from the existence of the rKS and the rMGMS, where the latter can be explained either as the molecular gas following the gravitational potential of the stellar disk or both, stars and gas following the same underlying potential defined by the total mass. The similarities between the rSFMS and the rMGMS in our data across different galactic environments (see Figs. 2.5 and 2.7) and the high scatter of the rSFMS as compared to the other two scaling relations suggest that this might be the case, and that the substantial variations in the rSFMS are driven by a combination of abundance/lack of molecular gas to fuel star formation as well as variations in star formation efficiency.

The rMGMS is the relation with the least scatter among the three relations at a spatial scale of 100 pc, consistent with the expectation from the perpective of the time-scales of the star-forming cycle. The same was recently reported in Ellison et al. (2020a) in an analysis carried out at kpc spatial scales. Interestingly, the rKS exhibits the most homogeneous behavior across different environments and between galaxies when measured at 100 pc scales. Variations in the slope of the rSFMS and the rMGMS across different galaxies seem to be related to differences in the detection fraction of either the SFR tracer or the molecular gas tracer. This effect is less important in the rKS, since molecular and ionized gas share more similar spatial distributions.

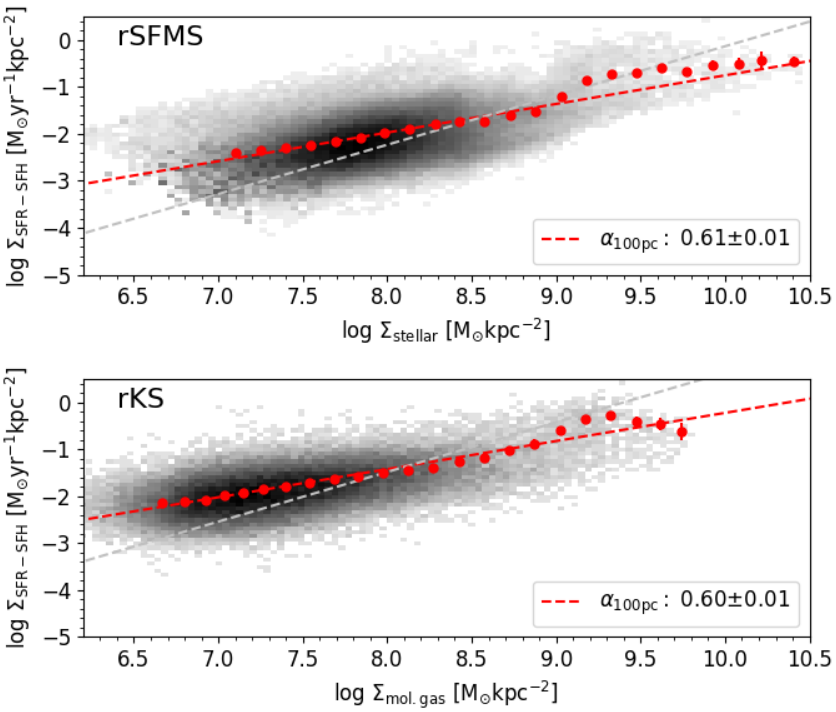

Figure 2.22: rSFMS (top) and rKS (bottom) measured at 100 pc resolution, using all available pixels from our sample and adopting a SFR tracer with a longer timescale. We have used the derived SFH to compute a SFR tracer sensitive to SF episodes in the last 150 Myr. This smooths the SFR measurements, flattens both relations, and reduces their scatter. The red dashed line show best-fitting power law to the binned data (red points). The best fit obtained with the fiducial approach is indicated with the gray line.

2.6 Summary

We have used VLT/MUSE and ALMA data from the PHANGS survey to derive SFR, molecular gas mass, and stellar mass surface densities across the galactic disks and to study the rSFMS (Σ_{SFR} versus $\Sigma_{stellar}$), rKS (Σ_{SFR} versus $\Sigma_{mol.gas}$), and rMGMS ($\Sigma_{mol.gas}$ versus $\Sigma_{stellar}$) relations in a sample of 18 star-forming galaxies at spatial scales of 100 pc, 500 pc, and 1 kpc. We tested for systematic differences induced by spatial scales considered, fitting approaches used, and assumptions made. Additionally, we have explored the $\Sigma_{stellar+mol.gas}-\Sigma_{SFR}$ correlation in our data to probe the effect of the mid-plane hydrostatic pressure of the disk as a regulator of the local SFR surface density. We applied a different approach to remove non-star-forming (diffuse) emission contaminating our SFR tracer before measuring the scaling relations, a different CO-to-H_2 conversion factor prescription, and a SFR tracer probing a longer timescale. Our main findings can be summarized as follows:

1. We have recovered all three scaling relations at a spatial scale of 100 pc. Of the three relations, rMGMS shows the least scatter (0.34 dex) for our global data set, whereas the rKS is the relation that shows the highest level of consistency between different galaxies and across environments. Its higher scatter in the high resolution (100 pc)

measurement is related to the inclusion of very low surface density SFR data points, following our methodology to recover all potential SFR emission. When probed at 1 kpc scales, these data points are averaged over a larger region and the rKS shows the least scatter among the three relations (see Sec. 2.4.1).

2. At 100 pc, we found that the scatter of the scaling relations follows $\sigma_{\rm rSFMS} > \sigma_{\rm rKS} > \sigma_{\rm rMGMS}$. This is consistent with the expectation from the evolutionary scenario perspective, given $\tau_{\rm H\alpha} < \tau_{\rm CO} < \tau_{\rm stars}$, where τ corresponds to the duration each tracer is visible across the star formation cycle (see Secs. 2.4.1 and 2.5.1).

3. We found significant variations in the studied scaling relations across different galactic environments. These variations are particularly strong in the case of the rSFMS and the rMGMS. The disk is the dominant feature in setting the slope, being the largest in area, while spiral arms share a similar slope, but are offset above the overall relations by up to 0.4 dex. Bars lie systematically below the overall relations (see Sec. 2.4.2).

4. We searched for global parameters that could be driving the dispersion in the measured slopes between the galaxies in our sample. We found a correlation with ΔMS, which implies that a global enhancement of SFR could change the slope of the scaling relations measured in a galaxy. However, we found a tighter correlation between the standard deviation of the distribution of the SFR tracer detection fraction with the deviation from the overall rSFMS slope. This can be explained by the fact that in galaxies with a larger spread in the detection fraction distribution, outer regions have typically a lower detection fraction values. Thus, the low stellar mass surface density regime will be more affected by non-detections than the inner region with a higher detection fraction, resulting in a steeper rSFMS (see Secs. 2.4.2 and 2.5.2).

5. As long as non-detections are included in the measurement of the slope, the spatial scale of the data do not greatly or systematically impact the measured slope. The scatter on the other hand decreases at larger spatial scales (see Sec. 2.4.3).

6. Excluding non-detections from the analysis artificially flattens the relation at smaller spatial scales, resulting in a steepening when the analysis is carried out at larger spatial scales. This is because pixels with nonzero signal are averaged with the non-detection pixels at larger spatial scales. Furthermore, this effectively causes an artificial flattening of the rSFMS and the rMGMS at the low mass surface density end in the 100 pc scale measurement (see Sec. 2.5.2).

7. How much the slope of a galaxy is flattened when non-detections are excluded at 100 pc spatial scale depends on the 2D distribution of ionized gas with respect to the stellar mass surface density (in the case of the rSFMS). We computed the distribution of the Hα detection fraction ($\mathbf{DF}_{\rm H\alpha}$) and we found a correlation between the mean of the detection fraction distribution and the change in slope when non-detections are not included as compared to the fiducial approach (see Sec. 2.5.2).

8. At all spatial scales, the scatter in the $\Sigma_{\rm b}$ versus $\Sigma_{\rm SFR}$ relation is higher than that seen for the rKS. We interpret this behavior such that the amount of available gas plays a primary role in locally regulating the SFR (see Sec. 2.5.3).

9. We removed all non-star-forming (diffuse) emission before resampling the SFR surface density maps, in order to reduce the level of contamination in our data. This strongly affects the level of emission at the edges of H II regions and molecular clouds, and increases the scatter of the rSFMS and the rKS. This suggests that with our fiducial approach, we may underestimate the real scatter of these relations due to diffuse non-SF-related flux boosting the emission of the faintest SF pixels (see Sec. 2.5.4).

10. We have recomputed the rKS and the rMGMS under the assumption of a constant CO-to-H_2 conversion factor. Removing the metallicity-dependent radial gradient from the conversion factor leads to a slightly flatter rKS (∼5% flatter) and a slightly steeper rMGMS (∼8% steeper) (see Sec. 2.5.4).

11. We have recomputed the rSFMS and the rKS at 100 pc scale using a longer timescale SFR tracer derived from the MUSE star formation histories. This longer timescale tracer smoothens the SFR values with respect to the shorter timescale tracer. Both relations are significantly flattened and their scatter is drastically reduced (see Sec. 2.5.4).

Studying star formation in nearby galaxies at high physical resolution is a powerful tool to connect extragalactic observations with measurements in our own Galaxy. Assessing star formation scaling relations across different galaxy populations and quantifying systematic variations in different galactic environments will provide valuable insights in how galaxies grow and evolve in the local universe.

2.7 Supporting material

2.7.1 Fitting of the $C_{\rm HII}$ parametrization

Figure 2.23 shows the $C_{\rm HII}$ values (i.e., the fraction of Hα flux tracing star formation as defined in Eq. 2.2) of the pixels in the NGC 1512 map, as a function of their Hα flux surface density. The solid black line shows the paramatrization defined in Eq. 2.3, and the best-fit parameters f_0 and β are listed in the top of the panel.

2.7.2 $\Delta\alpha_{\rm overall}$ as a function of ΔMS for the rKS and the rMGMS

Figure 2.24 shows the dependence of $\Delta\alpha_{\rm overall}$ (as defined in Eq. 2.5) from ΔMS, for the rKS and the rMGMS relations. We do not report any level of correlation between these parameters, and these figures are included here for completeness only.

2.7.3 Measurement of the rKS and rMGMS at different spatial scales excluding non-detections

We include here the figures and tables with the measurement of the rKS and the rMGMS when non-detections are excluded from the analysis. Figures 2.25 and 2.26 show the obtained overall rKS and rMGMS respectively, at spatial scales from 100 pc to 1 kpc. Tables 2.8 and 2.9 show the corresponding slope and scatter obtained for the same relations in each individual galaxy at the different spatial scales.

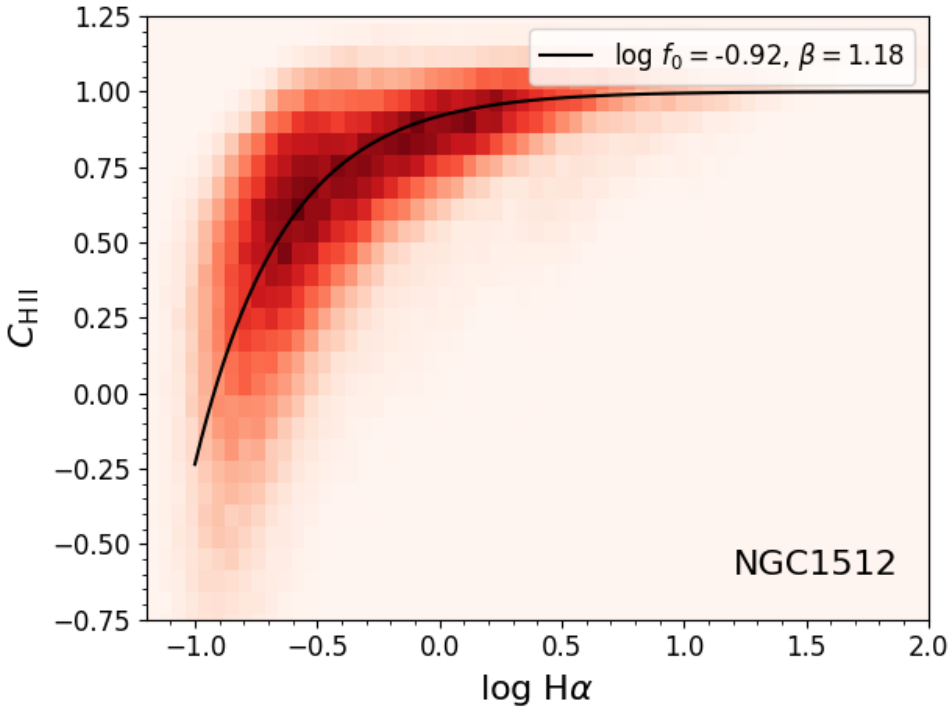

Figure 2.23: 2D distribution of the C_{HII} fraction values of the pixels at the MUSE native resolution in NGC 1512 as defined in Eq. 2.2, as a function of the log Hα flux surface density of each pixel, in units of 10^{-20} erg s^{-1} cm^{-2} pc^2. The black solid line shows the best-fitting parametrization, as described in Eq. 2.3. The obtained f_0 and β parameters are shown in the top of the panel.

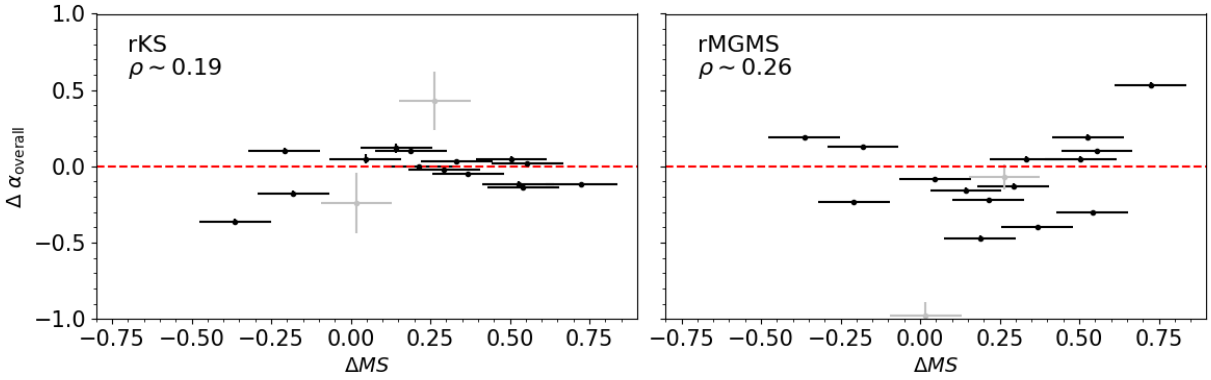

Figure 2.24: Differences in the slope measured for each individual galaxy with respect to the global measurements in Fig. 2.4 for the rKS (left) and the rMGMS (right), as a function of their offset from the global SFMS of galaxies. Each dot represent a galaxy in our sample. The gray dots are NGC 2835 and NGC 5068, two low-mass galaxies. The PCC of the correlation is indicated in the top-left corner of each panel.

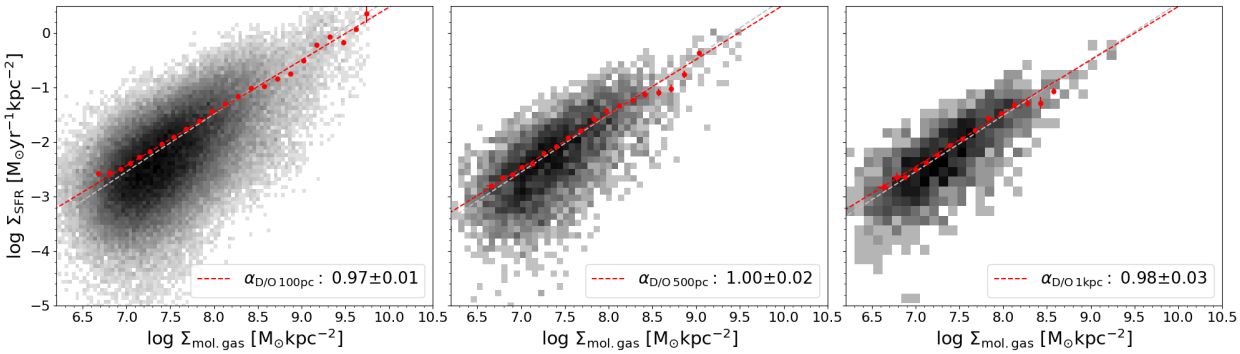

Figure 2.25: 2D distribution of the resolved Kennicutt–Schmidt relation considering all galaxies in our sample at three spatial resolutions (100 pc, 500 pc and 1 kpc from left to right). Non-detection pixels have been excluded from the fit. The fiducial overall best-fitting power law at each spatial scale is marked with the gray dashed line for reference.

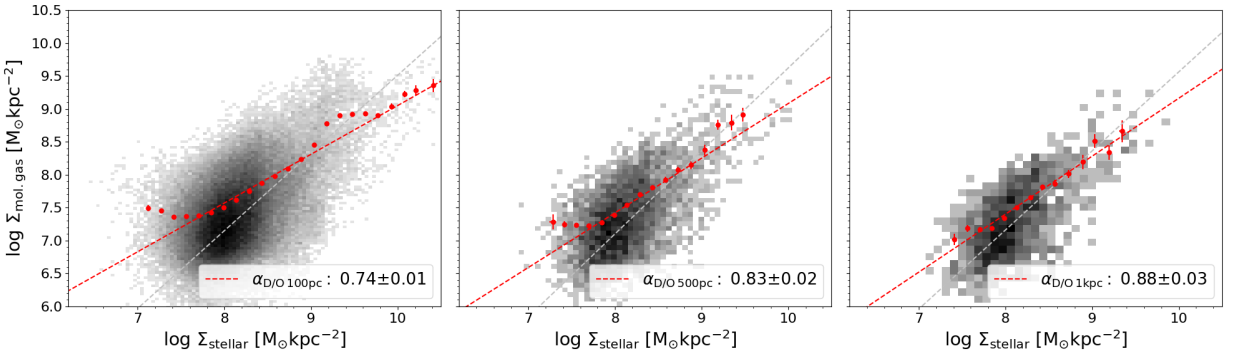

Figure 2.26: 2D distribution of the molecular gas main sequence considering all galaxies in our sample at three spatial resolutions (100 pc, 500 pc and 1 kpc from left to right). Non-detection pixels have been excluded from the fit. This produces a systematic flattening at higher spatial resolution. The fiducial overall best-fitting power law at each spatial scale is marked with the gray dashed line for reference.

2.7.4 Role of the detection fraction of the molecular gas tracer in the slope of the rMGMS

Figure 2.27 shows how much the slope of the rMGMS in each galaxy varies when non-detections are excluded from its calculation, as a function of the mean in the distribution of the molecular gas tracer ($\mu_{\mathrm{DF_{CO}}}$). We find a negative correlation (PCC ≈ -0.77), similar to that of the rSFMS. The outlier is the galaxy NGC 2835, which has a large uncertainty on its measured slope. Figure 2.28 shows the difference between the slope of the rMGMS for each galaxy and the global measurement as a function of the standard deviation of the distribution of the molecular gas tracer ($\sigma_{\mathrm{DF_{CO}}}$). The level of correlation we find here is modest (PCC ≈ 0.50), in contrast to that of the rSFMS slope differences and the SFR tracer distribution. This could be due to the completeness limit of our molecular gas tracer. As stated in Section 2.4.1, the rMGMS is the relation with the lowest total detection fraction ($\sim$35%). The detection insensitivity to a fainter component should not impact our slope

Target	$\alpha_{\mathrm{D/O\,100pc}}$	$\sigma_{\mathrm{D/O\,100pc}}$	$\alpha_{\mathrm{D/O\,500pc}}$	$\sigma_{\mathrm{D/O\,500pc}}$	$\alpha_{\mathrm{D/O\,1kpc}}$	$\sigma_{\mathrm{D/O\,1kpc}}$
NGC1087	1.06 ± 0.02	0.32	1.04 ± 0.02	0.24	1.00 ± 0.02	0.20
NGC1300	0.76 ± 0.02	0.39	0.80 ± 0.02	0.28	0.70 ± 0.02	0.24
NGC1365	0.92 ± 0.01	0.46	0.87 ± 0.01	0.45	0.89 ± 0.01	0.41
NGC1385	1.08 ± 0.02	0.32	1.15 ± 0.02	0.26	1.19 ± 0.02	0.20
NGC1433	0.54 ± 0.02	0.38	0.76 ± 0.02	0.31	0.70 ± 0.02	0.25
NGC1512	0.95 ± 0.03	0.37	1.10 ± 0.03	0.28	0.88 ± 0.03	0.24
NGC1566	0.93 ± 0.02	0.40	0.96 ± 0.02	0.29	0.86 ± 0.02	0.26
NGC1672	1.03 ± 0.01	0.42	0.96 ± 0.01	0.37	1.06 ± 0.01	0.33
NGC2835	1.45 ± 0.20	0.39	-	-	-	-
NGC3351	1.02 ± 0.02	0.36	1.21 ± 0.02	0.26	1.22 ± 0.02	0.09
NGC3627	1.06 ± 0.02	0.42	1.05 ± 0.02	0.31	1.15 ± 0.02	0.23
NGC4254	0.95 ± 0.01	0.37	0.96 ± 0.01	0.28	1.01 ± 0.01	0.23
NGC4303	0.86 ± 0.01	0.43	0.81 ± 0.01	0.36	0.79 ± 0.01	0.25
NGC4321	0.98 ± 0.01	0.40	0.92 ± 0.01	0.33	1.00 ± 0.01	0.26
NGC4535	0.98 ± 0.03	0.43	1.01 ± 0.03	0.35	0.92 ± 0.03	0.28
NGC5068	0.55 ± 0.20	0.48	-	-	-	-
NGC7496	0.82 ± 0.02	0.40	1.10 ± 0.02	0.35	1.00 ± 0.02	0.32
IC5332	-	-	-	-	-	-

Table 2.8: Slope (α) and scatter (σ) for the rKS measured in each galaxy in our sample at spatial scales of 100 pc, 500 pc and 1 kpc. The non-detections have been excluded from the slope measurement.

measurements, as our methodology is robust against the detection threshold. However, the detection fraction distribution will be affected. This leads to systematically lower values of $\mu_{\mathrm{DF_{CO}}}$ for all galaxies. On the other hand, the impact in $\sigma_{\mathrm{DF_{CO}}}$ is less systematic, and will depend on the mean of the distribution in each galaxy. We found a better correlation (PCC ≈ -0.70) of $\Delta\alpha_{\mathrm{overall}}$ with $\mu_{\mathrm{DF_{CO}}}$ instead. Figure 2.29 shows the difference in the rMGMS slope with the overall slope as a function of $\mu_{\mathrm{DF_{CO}}}$, excluding the two galaxies with the more uncertain measurements (NGC 2835 and NGC 5068). The negative correlation implies that galaxies with a lower mean detection fraction of the molecular gas tracer have a steeper rMGMS.

Target	$\alpha_{\mathrm{D/O\,100pc}}$	$\sigma_{\mathrm{D/O\,100pc}}$	$\alpha_{\mathrm{D/O\,500pc}}$	$\sigma_{\mathrm{D/O\,500pc}}$	$\alpha_{\mathrm{D/O\,1kpc}}$	$\sigma_{\mathrm{D/O\,1kpc}}$
NGC1087	0.75 ± 0.02	0.27	0.94 ± 0.02	0.20	0.98 ± 0.02	0.18
NGC1300	0.73 ± 0.01	0.28	0.87 ± 0.01	0.26	0.89 ± 0.01	0.28
NGC1365	1.17 ± 0.01	0.38	1.38 ± 0.01	0.37	1.50 ± 0.01	0.29
NGC1385	0.68 ± 0.02	0.30	0.87 ± 0.02	0.29	0.91 ± 0.02	0.23
NGC1433	0.83 ± 0.01	0.23	0.93 ± 0.01	0.20	1.01 ± 0.01	0.20
NGC1512	0.55 ± 0.01	0.22	0.75 ± 0.01	0.18	0.87 ± 0.01	0.17
NGC1566	0.66 ± 0.01	0.30	0.77 ± 0.01	0.27	0.81 ± 0.01	0.23
NGC1672	1.04 ± 0.01	0.30	1.09 ± 0.01	0.30	1.19 ± 0.01	0.26
NGC2835	-0.02 ± 0.06	0.15	-	-	-	-
NGC3351	0.80 ± 0.01	0.20	1.02 ± 0.01	0.15	0.94 ± 0.01	0.11
NGC3627	0.52 ± 0.02	0.32	0.56 ± 0.02	0.26	0.58 ± 0.02	0.24
NGC4254	0.64 ± 0.01	0.29	0.70 ± 0.01	0.23	0.77 ± 0.01	0.16
NGC4303	0.69 ± 0.01	0.31	0.75 ± 0.01	0.28	0.77 ± 0.01	0.21
NGC4321	0.76 ± 0.01	0.28	0.94 ± 0.01	0.24	1.02 ± 0.01	0.21
NGC4535	0.85 ± 0.02	0.27	0.96 ± 0.02	0.25	1.04 ± 0.02	0.23
NGC5068	-0.20 ± 0.05	0.13	-	-	-	-
NGC7496	0.97 ± 0.03	0.28	1.32 ± 0.03	0.23	1.34 ± 0.03	0.16
IC5332	-	-	-	-	-	-

Table 2.9: Slope (α) and scatter (σ) for the rMGMS measured in each galaxy in our sample at spatial scales of 100 pc, 500 pc and 1 kpc. The non-detections have been excluded from the slope measurement.

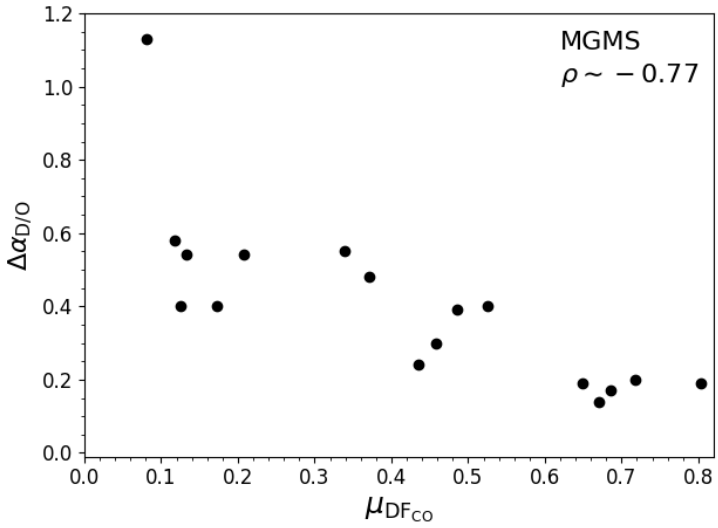

Figure 2.27: Difference between the slope of the rMGMS of each galaxy measured with the fiducial approach and the slope measured when non-detections are excluded, as a function of the mean detection fraction of the molecular gas tracer in each galaxy ($\mu_{\mathrm{DF_{CO}}}$). All values are positive in the y-axis because excluding non-detections always leads to a flatter relation. The PCC of the correlation is indicated in the top-right corner of the panel.

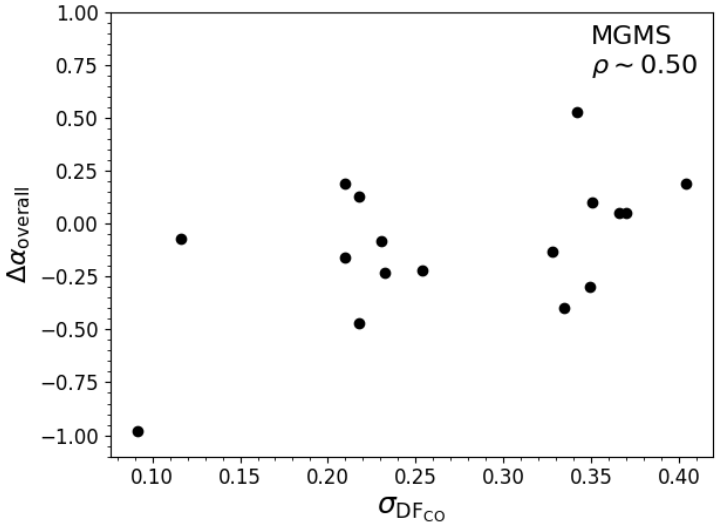

Figure 2.28: Difference between the slope of the rMGMS of each galaxy measured with the fiducial approach and the global measurement as a function of the standard deviation of the detection fraction distribution of the molecular gas tracer in each galaxy ($\sigma_{\mathrm{DF_{CO}}}$). The PCC of the correlation is indicated in the top-right corner of the panel.

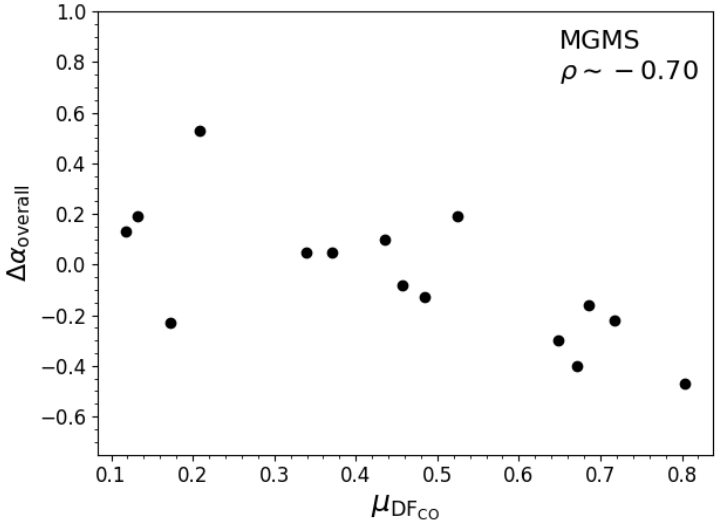

Figure 2.29: Difference between the slope of the rMGMS of each galaxy measured with the fiducial approach and the global measurement as a function of the mean of the detection fraction distribution of the molecular gas tracer in each galaxy ($\mu_{\mathrm{DF_{CO}}}$). The PCC of the correlation is indicated in the top-right corner of the panel.

3 Variations in the $\Sigma_{\rm SFR}-\Sigma_{\rm mol}-\Sigma_{\star}$ plane across galactic environments in PHANGS galaxies

The content of this chapter is based in the accepted for publication article "Variations in the $\Sigma_{\rm SFR}-\Sigma_{\rm mol}-\Sigma_{\star}$ plane across galactic environments in PHANGS galaxies", Pessa et al. (2022), of which I am the lead author and has been adapted for this thesis.

There exists some consensus that the stellar mass surface density ($\Sigma_{\star}$) and molecular gas mass surface density ($\Sigma_{\rm mol}$) are the main quantities responsible for locally setting the star formation rate. This regulation is inferred from locally resolved scaling relations between these two quantities and the star formation rate surface density ($\Sigma_{\rm SFR}$), which have been extensively studied in a wide variety of works. However, the universality of these relations is debated. Here, we probe the interplay between these three quantities across different galactic environments at a spatial resolution of 150 pc. We performed a hierarchical Bayesian linear regression to find the best set of parameters $C_{\star}$, $C_{\rm mol}$, and $C_{\rm norm}$ that describe the star-forming plane conformed by $\Sigma_{\star}$, $\Sigma_{\rm mol}$, and $\Sigma_{\rm SFR}$, such that $\log\Sigma_{\rm SFR} = C_{\star}\log\Sigma_{\star} + C_{\rm mol}\log\Sigma_{\rm mol} + C_{\rm norm}$. We also explored variations in the determined parameters across galactic environments, focusing our analysis on the $C_{\star}$ and $C_{\rm mol}$ slopes. We find signs of variations in the posterior distributions of $C_{\star}$ and $C_{\rm mol}$ across different galactic environments. The dependence of $\Sigma_{\rm SFR}$ on $\Sigma_{\star}$ spans a wide range of slopes, with negative and positive values, while the dependence of $\Sigma_{\rm SFR}$ on $\Sigma_{\rm mol}$ is always positive. Bars show the most negative value of $C_{\star}$ (-0.41), which is a sign of longer depletion times, while spiral arms show the highest $C_{\star}$ among all environments (0.45). Variations in $C_{\rm mol}$ also exist, although they are more subtle than those found for $C_{\star}$. We conclude that systematic variations in the interplay of $\Sigma_{\star}$, $\Sigma_{\rm mol}$, and $\Sigma_{\rm SFR}$ across different galactic environments exist at a spatial resolution of 150 pc, and we interpret these variations to be produced by an additional mechanism regulating the formation of stars that is not captured by either $\Sigma_{\star}$ or $\Sigma_{\rm mol}$. Studying environmental variations in single galaxies, we find that these variations correlate with changes in the star formation efficiency across environments, which could be linked to the dynamical state of the gas that prevents it from collapsing and forming stars, or to changes in the molecular gas fraction.

3.1 Introduction

The conversion of cold dense molecular clouds into stars ultimately occurs when the supporting pressures are insufficient to prevent gravitational collapse. While simple calculations only include gas pressure, both magnetic fields (e.g., Shu et al., 1987) and turbulence (Mac Low & Klessen, 2004) have been proposed as mechanisms able to prevent gravitational collapse. In the case of magnetic fields, the collapse is prevented because the neutral hydrogen is coupled with ionized hydrogen, which is tied to the interstellar magnetic field and therefore resists collapse. For the latter proposed mechanism, supersonic turbulent motions act as an additional source of pressure. Once this pressure is no longer sufficient to support the self-gravity of the cloud, it collapses. The collapse of the molecular cloud, which might be triggered by an external source of pressure, leads to its fragmentation (Hoyle, 1953), where individual fragments will form stars.

Despite the complexity of this process, several studies have reported correlations between the locally (approximately kpc and sub-kpc scales) measured star formation rate surface density (Σ_{SFR}), and spatially resolved quantities, such as the local stellar mass surface density ($\Sigma_{\star}$), also known as the "resolved" star formation main sequence (rSFMS; Cano-Díaz et al., 2016; Abdurro'uf & Akiyama, 2017; Hsieh et al., 2017; Lin et al., 2019; Morselli et al., 2020; Ellison et al., 2021), or the local molecular gas surface density (Σ_{mol}), also known as the resolved Kennicutt–Schmidt relation (rKS; Bigiel et al., 2008; Leroy et al., 2008; Blanc et al., 2009; Onodera et al., 2010; Bigiel et al., 2011; Schruba et al., 2011; Ford et al., 2013; Leroy et al., 2013; Kreckel et al., 2018; Williams et al., 2018; Dey et al., 2019). The scatter of these correlations is expected to dramatically increase below a critical spatial scale due to statistical undersampling of the time evolution of the star formation process (Schruba et al., 2010; Feldmann et al., 2011; Kruijssen & Longmore, 2014; Kruijssen et al., 2018). Pessa et al. (2021) recently confirmed such an increase in scatter with decreasing physical resolution down to ∼100 pc in a sample of 18 nearby galaxies. These local relationships also have well-studied global manifestations, the star-forming main sequence of galaxies (SFMS; Brinchmann et al., 2004; Daddi et al., 2007; Noeske et al., 2007; Salim et al., 2007; Lin et al., 2012; Whitaker et al., 2012; Speagle et al., 2014; Saintonge et al., 2016; Popesso et al., 2019), and the galaxy-integrated Kennicutt–Schmidt relation (Schmidt, 1959; Kennicutt, 1998; Wyder et al., 2009; Genzel et al., 2010; Tacconi et al., 2010) express relationships among the same quantities for entire galaxies. These galactic-scale relations are key to our current understanding of galaxy evolution and star formation across cosmic time. Studying their spatially resolved versions provides critical insights into their physical origin.

These resolved correlations arise as a result of some mechanism controlling the formation of stars. Many studies have investigated the dependence on $\Sigma_{\star}$ (through the hydrostatic pressure exerted by the galactic potential) and by Σ_{mol} (being the fuel to form stars), as well as a combination of these parameters (e.g., Matteucci et al., 1989; Shi et al., 2011, 2018; Dey et al., 2019; Barrera-Ballesteros et al., 2021a). When approaching this topic empirically, some authors have studied a 2D plane in the 3D space spanned by Σ_{SFR}, $\Sigma_{\star}$ and Σ_{mol} (Dib et al., 2017; Lin et al., 2019; Sánchez et al., 2021), which would imply a scenario where both $\Sigma_{\star}$ and Σ_{mol} are responsible for modulating the formation of stars. While there is consensus that these are the main quantities that correlate with SFR to first order, there is debate about the universality of these correlations. Whereas Sánchez et al. (2021), using data from

the CALIFA survey (Sánchez et al., 2012), concluded that the scatter in these relations is fully dominated by individual errors, Ellison et al. (2021) used data from ALMaQUEST (Lin et al., 2020) and found that the scatter in these correlations is dominated by galaxy-to-galaxy variations. Similarly, in Pessa et al. (2021), using high physical resolution data provided by MUSE, the authors found not only galaxy-to-galaxy variations, but also significant variations in these scaling relations across galactic environments. That is, they found different relations for spiral arms, disk, bars, centers and rings.

In this chapter, we aim to test the universality of a two-dimensional (2D) planar star formation relation, defined as $\Sigma_{\rm SFR} \propto \Sigma_{\star}^{a}\Sigma_{\rm mol}^{b}$. If the SFR in a given region is primarily driven by these two quantities, then, this 'star-forming plane' should not change significantly between individual galaxies or among different galactic environments. On the other hand, significant variations in the best-fit star-forming plane among different locations would indicate that such a relationship offers an incomplete description of the data and hint at additional quantities or functional forms that are key to regulating star formation in galaxies.

The Physics at High Angular resolution in Nearby GalaxieS (PHANGS[6]) surveys (Leroy et al., 2021a; Emsellem et al., 2022; Lee et al., 2022) provide the opportunity to explore the relation between these three quantities at a high physical resolution (∼150 pc), making it possible to isolate galactic environments and study them separately. PHANGS targets probe a diversity of environments (centers and bulges, disks, bars, spiral arms) spanning a range of physical conditions (gas surface density, stellar surface density, dynamical pressure, orbital period, shear rate, streaming motions, gas phase metallicity; Meidt et al., 2018, 2020; Jeffreson et al., 2020; Kreckel et al., 2020; Emsellem et al., 2022; Querejeta et al., 2021). Recent works have shown that ∼100−150 pc scale surface density, velocity dispersion, and dynamical state of the molecular gas in these environments are sensitive to the local conditions (Colombo et al., 2014; Sun et al., 2020a; Rosolowsky et al., 2021) in a manner that appears to influence how molecular clouds form stars (Meidt, 2016; Querejeta et al., 2021). Thus, investigating differences in the interplay of $\Sigma_{\rm SFR}$, $\Sigma_{\star}$ and $\Sigma_{\rm mol}$ across these galactic environments could be key to understand the galaxy-to-galaxy variations reported by Ellison et al. (2021) and Pessa et al. (2021), as relative contributions from different environments will vary from one galaxy to another.

The chapter is structured as follows: in Sec. 5.2 we describe the data and data products used in this work. In Sec. 3.3 we describe in detail the methodology adopted to perform our analyses. In Sec. 3.4 and 3.5 we present our findings and discussions. Finally, our main conclusions are presented in Sec. 3.6.

3.2 Data

In this section, we cover only the main aspects of our data set. We refer the reader to Leroy et al. (2021b), Emsellem et al. (2022) and Pessa et al. (2021) for a more detailed description of our data. We use a sample of 18 star-forming galaxies from the overlap of the PHANGS–ALMA and PHANGS–MUSE samples. In order to resolve the typical separation between star-forming regions (∼100 pc), and limit the effect of extinction, the galaxies studied in this chapter have been selected to have distances less than 20 Mpc and low inclinations ($i < 60°$).

[6] http://phangs.org/

Our sample is summarized in Table 3.1 where we use the global parameters from Leroy et al. (2021a), which leveraged the distance compilation of Anand et al. (2021) and the galaxy orientations determined by Lang et al. (2020).

3.2.1 VLT MUSE

We make use of the PHANGS–MUSE survey (PI: E. Schinnerer; Emsellem et al., 2022). This survey employs the Multi-Unit Spectroscopic Explorer (MUSE; Bacon et al., 2014) optical integral field unit (IFU) mounted on the Very Large Telescope (VLT) Unit Telescope 4 to mosaic the star-forming disk of 19 galaxies from the PHANGS sample. This sample corresponds to a subset of the 90 galaxies from the PHANGS–ALMA survey (PI: E. Schinnerer; Leroy et al., 2021a). For the sake of homogeneity of the data set, one galaxy from the PHANGS–MUSE sample (NGC 0628) has been excluded because its MUSE mosaic was obtained using a different observing strategy.

The mosaics consist of 3 to 15 individual MUSE pointings, each with a total on-source exposure time of 43 min. Nine out of the 18 galaxies were observed with adaptive optics (AO) assistance. These galaxies are marked with a black dot in the first column of Table 3.1. Each pointing provides a $1' \times 1'$ field of view sampled at 0.2" per pixel, with a typical spectral resolution of $\sim$2.5 Å ($\sim$70 km s^{-1}) covering the wavelength range of 4800$-$9300 Å. Observations were reduced using recipes from the MUSE data reduction pipeline provided by the MUSE consortium (Weilbacher et al., 2020), executed with ESOREX using the python wrapper developed by the PHANGS team[7] (Emsellem et al., 2022). Once the data have been reduced, we have used the PHANGS data analysis pipeline (DAP) to derive various physical quantities, as described in detail in Emsellem et al. (2022). DAP is based on the GIST pipeline (Bittner et al., 2019), and consists of a series of modules that perform single stellar population (SSP) fitting and emission line measurements to the full MUSE mosaic. Some outputs from the pipeline relevant for this study are described in Secs. 3.2.4 and 3.2.5.

3.2.2 ALMA CO mapping

Our sample of 18 galaxies have CO(J=2–1) [hereafter CO(2–1)] data from the PHANGS–ALMA survey (PI: E. Schinnerer; Leroy et al., 2021a). We used the ALMA 12m and 7m arrays combined with the total power antennas to map CO(2–1) emission at a spatial resolution of 1.0" $-$1.5" (version 4.0 of internal distribution, which is the first public data release). The molecular gas surface density maps have a typical uncertainty of $\sim$1.2 $M_{\odot}$ pc^{-2} at a spatial resolution of 150 pc. We use integrated intensity maps and associated statistical uncertainty maps constructed using the PHANGS–ALMA "broad masking" scheme. These broad masks are designed to incorporate all emission detected at any scale in the PHANGS–ALMA data. As a result they have high completeness, that is to say, they include most of the flux in the galaxy, at the expense of also having more low-confidence pixels than a more stringent masking technique (see Leroy et al., 2021a,b, for details and completeness estimates at 150 pc). A signal-to-noise (S/N) cut of 1 is then applied to drop the most uncertain emission. The strategy for observation, data reduction and product generation are described in Leroy et al. (2021a,b).

[7] https://github.com/emsellem/pymusepipe

Target	RA	DEC	$\log_{10}M_*$	$\log_{10}M_{H_2}$	$\log_{10}$SFR	ΔMS	Distance	Inclination	Mapped area
	(degrees)	(degrees)	($M_\odot$)	($M_\odot$)	($M_\odot\, yr^{-1}$)	(dex)	(Mpc)	(degrees)	(kpc^2)
(1)	(2)	(3)	(4)	(5)	(6)	(7)	(8)	(9)	(10)
NGC 1087	41.6049	−0.49871	9.9	9.2	0.12	0.33	15.85±2.08	42.9	128
NGC 1300•	49.92081	−19.41111	10.6	9.4	0.07	−0.18	18.99±2.67	31.8	366
NGC 1365	53.4015	−36.14040	11.0	10.3	1.23	0.72	19.57±0.77	55.4	421
NGC 1385•	54.36901	−24.50116	10.0	9.2	0.32	0.5	17.22±2.42	44.0	100
NGC 1433•	55.50619	−47.22194	10.9	9.3	0.05	−0.36	18.63±1.76	28.6	441
NGC 1512	60.97557	−43.34872	10.7	9.1	0.11	−0.21	18.83±1.78	42.5	270
NGC 1566•	65.0016	−54.9380	10.8	9.7	0.66	0.29	17.69±1.91	29.5	212
NGC 1672	71.4270	−59.24725	10.7	9.9	0.88	0.56	19.4±2.72	42.6	255
NGC 2835	139.4704	−22.3547	10.0	8.8	0.09	0.26	12.22±0.9	41.3	88
NGC 3351	160.9906	11.7037	10.4	9.1	0.12	0.05	9.96±0.32	45.1	76
NGC 3627	170.0625	12.991	10.8	9.8	0.58	0.19	11.32±0.47	57.3	87
NGC 4254•	184.707	14.41641	10.4	9.9	0.49	0.37	13.1±1.87	34.4	174
NGC 4303•	185.4789	4.47374	10.5	9.9	0.73	0.54	16.99±2.78	23.5	220
NGC 4321•	185.7289	15.82230	10.7	9.9	0.55	0.21	15.21±0.49	38.5	196
NGC 4535•	188.585	8.19797	10.5	9.6	0.33	0.14	15.77±0.36	44.7	126
NGC 5068	199.7281	−21.03874	9.4	8.4	−0.56	0.02	5.2±0.22	35.7	23
NGC 7496•	347.4470	−43.4278	10.0	9.3	0.35	0.53	18.72±2.63	35.9	89
IC5332	353.6145	−36.1011	9.7	–	−0.39	0.01	9.01±0.39	26.9	34

Table 3.1: Summary of the galactic parameters of our sample adopted through this work. •: Galaxies observed with MUSE-AO mode. Values in columns (4), (5) and (6) correspond to those presented in Leroy et al. (2021a). Column (7) shows the vertical offset of the galaxy from the integrated main sequence of galaxies, as defined in Leroy et al. (2019). Distance measurements are presented in Anand et al. (2021) and inclinations in Lang et al. (2020). Uncertainties in columns (4), (5), (6) and (7) are on the order of 0.1 dex. Column (10) shows the area mapped by MUSE.

We adopt the local gas-phase metallicity (in solar units) prescription for our fiducial α_{CO} conversion factor following Sun et al. (2020c) and partially based on Accurso et al. (2017), following $\alpha_{CO} = 4.35(Z/Z_\odot)^{-1.6}\ M_\odot\ \mathrm{pc}^{-2}\ (\mathrm{K\ km\ s}^{-1})^{-1}$, adopting a ratio CO(2–1)-to-CO(1–0) = 0.65 (Leroy et al., 2013; den Brok et al., 2021; Leroy et al., 2021b, T. Saito et al. in prep.). Metallicity gradients are measured from the gas-phase abundances in H II regions, as explained in Kreckel et al. (2020) and Santoro et al. (2022). Azimuthal variations in the gas-phase metallicity have been previously reported (Ho et al., 2017; Kreckel et al., 2020; Williams et al., 2022a), however, these variations are small (0.04−0.05 dex), implying variations of ∼0.06 dex in α_{CO} and therefore do not impact our results. We test the robustness of our results against a constant $\alpha_{CO(1-0)} = 4.35\ M_\odot\ \mathrm{pc}^{-2}\ (\mathrm{K\ km\ s}^{-1})^{-1}$, as the canonical value for our Galaxy (Bolatto et al., 2013) in Sec. 3.5.3.

3.2.3 Environmental masks

We used the environmental masks described in Querejeta et al. (2021) to morphologically classify the different environments of each galaxy and label them as disks, spiral arms, rings, bars and centers. This classification was done using photometric data mostly from the Spitzer Survey of Stellar Structure in Galaxies (S^{4}G; Sheth et al., 2010). In brief, disks and centers are identified via 2D photometric decompositions of 3.6 μm images (see, e.g., Salo et al., 2015). A central excess of light is labeled as center, independently of its surface brightness profile. The size and orientation of bars and rings are defined visually on the NIR images; for S^{4}G galaxies, the classification follows Herrera-Endoqui et al. (2015). Finally, spiral arms are only defined when they are clearly dominant features across the galaxy disk (excluding flocculent spirals). A log-spiral function is fitted to bright regions along arms on the NIR images, and assigned a width determined empirically based on CO emission.

3.2.4 Stellar mass surface density maps

The PHANGS–MUSE DAP (Emsellem et al., 2022) includes a stellar population fitting module, where a linear combination of single stellar population templates of specific ages and metallicities are used to reproduce the observed spectrum. We assume a Calzetti et al. (2000) extinction law to account for extragalactic attenuation in the fitting. This permits us to infer stellar population properties from an integrated spectrum, such as mass- or light-weighted ages, metallicities and total stellar masses, together with the underlying star formation history. Before doing the SSP fitting, we correct the full mosaic for Milky Way extinction assuming a Cardelli et al. (1989) extinction law and the $E(B-V)$ values obtained from the NASA/IPAC Infrared Science Archive[8] (Schlafly & Finkbeiner, 2011).

In detail, our spectral fitting pipeline performs the following steps: First, we use a Voronoi tessellation (Cappellari & Copin, 2003a) to bin our MUSE data to a minimum S/N of ∼35, computed at the wavelength range of 5300−5500 Å. We use then the Penalized Pixel-Fitting (pPXF) code (Cappellari & Emsellem, 2004a; Cappellari, 2017a) to fit the spectrum of each Voronoi bin. To fit our data, we used a grid of templates consisting of 13 ages, logarithmically spaced and six metallicity bins. We fit the wavelength range 4850−7000 Å, in order to avoid spectral regions strongly affected by sky residuals. We used templates from the eMILES (Vazdekis et al., 2010, 2012) database, assuming a Chabrier (2003) IMF and BaSTI isochrone (Pietrinferni et al., 2004) with a Galactic abundance pattern.

The stellar mass map is then reconstructed using the weights assigned by pPXF to each SSP spectrum, given that the current stellar mass of each template is known. Finally, we have identified foreground stars as velocity outliers in the SSP fitting and we have masked those pixels for the analysis carried out in this chapter.

3.2.5 Star formation rate measurements

As part of the PHANGS–MUSE DAP (Emsellem et al., 2022), we fit single Gaussian profiles to a number of emission lines for each pixel of the final combined MUSE mosaic of each galaxy in our sample. By integrating the flux of the fitted profile in each pixel, we construct

[8] https://irsa.ipac.caltech.edu/applications/DUST/

emission line flux maps for every galaxy. We calculate SFR from extinction-corrected Hα. In detail, we dereddened the Hα fluxes, assuming that $\mathrm{H}\alpha_{\mathrm{corr}}/\mathrm{H}\beta_{\mathrm{corr}} = 2.86$, as appropriate for a case B recombination (Osterbrock, 1989), temperature $T = 10^4$ K and density $n_{\mathrm{e}} = 100$ cm^{-3}, following:

$$\mathrm{H}\alpha_{\mathrm{corr}} = \mathrm{H}\alpha_{\mathrm{obs}} \left(\frac{(\mathrm{H}\alpha/\mathrm{H}\beta)_{\mathrm{obs}}}{2.86} \right)^{\frac{k_\alpha}{k_\beta - k_\alpha}} , \tag{3.1}$$

where Hα_{corr} and Hα_{obs} correspond to the extinction-corrected and observed Hα fluxes, respectively, and k_α and k_β are the values of a given extinction curve at the wavelengths of Hα and Hβ. Opting for an O'Donnell (1994) extinction law, we use $k_\alpha = 2.52$, $k_\beta = 3.66$ and $R_V = 3.1$.

Next, we remove pixels that are dominated by active galactic nuclei (AGN) or low-ionization nuclear emission-line regions (LINER) ionization from our sample, performing a cut in the Baldwin–Phillips–Terlevich (BPT; Baldwin et al., 1981) diagram using the [O III]/Hβ and [S II]/Hα line ratios, as described in Kewley et al. (2006).

For the remaining pixels, we determined the fraction of the Hα emission tracing local star formation (C_{HII}) and the fraction deemed to correspond to the diffuse ionized gas (DIG). DIG is a warm (10^4 K), low density (10^{-1} cm^{-3}) phase of the interstellar medium (Haffner et al., 2009; Belfiore et al., 2015) produced primarily by photoionization of gas across the galactic disk by photons that escaped from H II regions (Flores-Fajardo et al., 2011; Zhang et al., 2017; Belfiore et al., 2022).

To this end, we use the [S II]/Hα ratio to estimate C_{HII} in each pixel, following Blanc et al. (2009) and Kaplan et al. (2016). After performing this correction and removing the DIG contribution of the Hα flux, we rescale the DIG-corrected Hα map by 1 plus the fraction of flux removed, to keep the total Hα flux constant. We perform this rescaling because photons that ionize the DIG are believe to originally have leaked out from H II regions[9]. This correction represents then a spatial redistribution of the Hα flux. We refer the reader to Pessa et al. (2021) for a detailed description of this procedure. This approach permits us to estimate a star formation rate in pixels contaminated by non-star-forming emission. A S/N cut of 3 for Hα and 1 for Hβ was then applied before computing the star formation rate surface density map using Eq. (3.2), effectively removing ∼13% of pixels in our sample. While 13% is not insignificant, we note that the majority have $C_{\mathrm{HII}} \approx 0$, and therefore our S/N cut does not largely impact our results. Pixels below this S/N cut, pixels with $C_{\mathrm{HII}} \leq 0$ or pixels where $\mathrm{H}\alpha_{\mathrm{obs}}/\mathrm{H}\beta_{\mathrm{obs}} < 2.86$, are considered nondetections (see Sec. 3.3.2). To calculate the corresponding star formation rate from the Hα flux, after correcting it for internal extinction and DIG contamination, we adopted the prescription of Calzetti (2013):

$$\frac{\mathrm{SFR}}{M_\odot\ \mathrm{yr}^{-1}} = 5.5 \times 10^{-42} \frac{\mathrm{H}\alpha_{\mathrm{corr}}}{\mathrm{erg\ s}^{-1}} . \tag{3.2}$$

This equation is scaled to a Kroupa universal IMF (Kroupa, 2001). Differences with the Chabrier IMF assumed for the SSP fitting are expected to be small (∼1.05; Kennicutt &

[9]While other sources of DIG ionzing photons exist (e.g., evolved post-AGB stars), and can be relatively important in more passive systems, all galaxies in PHANGS–MUSE sample are actively star froming galaxies, which justifes the assumption that DIG ionization is dominated by UV leakage from H II, regions.

Evans, 2012). With these steps we obtain SFR surface density maps for each galaxy in our sample. We acknowledge that Eq. (3.2) assumes a fully sampled IMF, and that the lowest SFR pixels (especially at the ∼150 pc resolution of our data) may not form enough stars to fully sample the IMF. Hence, the measured SFR is more uncertain in this regime. We decided to exclude from our analysis the regions with low coverage of SFR or molecular gas surface density (see Sec. 3.3.2), hence minimizing the impact of the low SFR regime on our results.

3.2.6 Probing larger spatial scales

In Sec. 3.4.2, we investigate the effect of spatial resolution on our measurements. To do this, we first convolve our MUSE maps to a common fixed reolution of 150 pc, and then we rebin our 150 pc resolution MUSE and ALMA maps to have pixel sizes of 150 pc, 200 pc, 300 pc, 500 pc and 1 kpc. Then we replicate our measurements using these rebinned maps. We conduct an identical rebinning process for all three relevant quantities: stellar mass surface density, star formation rate surface density and molecular gas mass surface density (see Pessa et al., 2021, for a detailed description). After beginning with matched resolution 150 pc MUSE and ALMA data, we favor this rebinning approach rather than, for example, convolution to a coarser Gaussian beam, because it minimized pixel-to-pixel covariance and yields approximately statistically independent measurements. Our core results use the 150 pc pixels, which are larger than the native spatial resolution of the maps for all galaxies, except for NGC 1672, which has an ALMA native resolution of ∼180 pc.

The rebinning step is followed by an inclination correction, simply using a $\cos(i)$ multiplicative term, where i is the inclination of each galaxy as listed in Table 3.1 (adopted from Lang et al., 2020). All following results and conclusions in the next Sections pertain to a fixed spatial resolution of 150 pc, unless specifically stated (see Sec. 3.4.2).

3.3 Methods

In this section, we present our methodology to fit a 2D plane (i.e. power law) predicting $\log_{10}\Sigma_{SFR}$ as function of $\log_{10}\Sigma_{\star}$ and $\log_{10}\Sigma_{mol}$. We fit planes separately to the data for each distinct galactic environment, as well as to the full sample. Because the fitting can be potentially biased by the influence of nondetections in either Σ_{SFR} or Σ_{mol}, we explain our approach to nondetections first and then describe the full fitting method.

3.3.1 Nondetections in our data

In Pessa et al. (2021), we found that the adopted treatment of nondetections can have a considerable impact on the derived slope of fitted scaling relations. Here, nondetections (N/Ds) are pixels with a value of Σ_{SFR} or Σ_{mol} lower than our defined detection threshold. As stellar mass is detected essentially everywhere in our maps at high significance, nondetections in $\Sigma_{\star}$ are essentially a nonissue.

This impact of N/Ds becomes particularly strong when performing measurements at high spatial resolution, where a larger fraction of pixels are deemed to be N/Ds. For more

discussion of how such sparse maps emerge from timescale effects or other stochasticity, see Pessa et al. (2021) and references therein.

In Pessa et al. (2021), we overcame this issue by binning the data before fitting a power law. Here we are trying to fit a 2D plane, and discretizing the data in higher dimensions becomes problematic, so we do not proceed in the same way. Instead, we opt here to focus our analysis only on those $\Sigma_\star$ ranges that have high detection fractions in both $\Sigma_{\rm SFR}$ and $\Sigma_{\rm mol}$. Here the detection fraction is defined as the fraction of pixels with a measurement of $\Sigma_{\rm SFR}$ (or $\Sigma_{\rm mol}$) above our detection threshold in a given $\Sigma_\star$ bin. As a reminder, we required $S/N > 1$ for the ALMA CO intensity, $S/N > 3$ for the Hα and $S/N > 1$ for the Hβ at the native resolution, and N/Ds are a nonissue for stellar mass.

The top panels of Fig 3.1 show the detection fraction of $\Sigma_{\rm SFR}$ and $\Sigma_{\rm mol}$ in each bin of $\Sigma_\star$, and the bottom panels show rSFMS and rMGMS binned for each individual environment (colors) and for the full sample (black). Two types of lines are shown, solid lines represent the binned trend accounting for N/Ds, and dashed lines represent the binned trend neglecting N/Ds. It is easy to see in the bottom panels that for all environments the two lines deviate, that is, neglecting N/Ds from the analysis systematically leads to flatter slopes. This bias in the slope is due to varying fractions of N/Ds across the $\Sigma_\star$ range, usually being higher at the low $\Sigma_\star$ end. To minimize the impact of N/Ds on our measurements, we confine our analysis only to those $\Sigma_\star$ ranges, where the detection fraction (of both $\Sigma_{\rm SFR}$ and $\Sigma_{\rm mol}$) is higher than 60%. In Supporting material 3.7.2, we discuss how using a different detection fraction threshold impacts our results, and we show that a threshold of 60% provides a good compromise between minimizing the impact of N/Ds in our analysis, while maintaining the statistical significance of our data.

We impose the detection fraction threshold independently for each environment, that is, the range of $\Sigma_\star$ values used for 'spiral arms' is different to that used for 'disks'. This approach allows us to maximize the number of data points used in the analysis.

We do caution that our approach to the different galactic environments might impose some bias on the results. The spiral arms defined by Querejeta et al. (2021) tend to have more gas and more star formation at fixed $\Sigma_\star$. Because they were identified partially based on multiwavelength data that trace gas and SFR, this is somewhat by construction. It is not *a priori* certain that spiral arms must behave distinctly from other environments in the $\Sigma_\star - \Sigma_{\rm SFR} - \Sigma_{\rm mol}$ space, but some bias might be expected from how we set up the analysis. This also manifests in the detection threshold cuts: because spiral arms have higher $\Sigma_{\rm mol}$ and $\Sigma_{\rm SFR}$ at fixed $\Sigma_\star$, detections extend to lower $\Sigma_\star$ for these environments and we might also expect a different best-fitting plane. This is already somewhat evident in Fig. 3.1, where the "Sp. arm" environment shows higher detection fractions at fixed $\Sigma_\star$ than other cases.

It is worth noting that we are not dropping a large fraction of our data by imposing these thresholds. Indeed, only ∼20% of our 150 pc pixels are removed from the entire sample across all environments. Given that different galactic environments sample different parts of the galactic disk and therefore different (typical) surface densities, the adopted N/D thresholds are most relevant for the disk environment, which extends to the largest galactic radii and therefore (also) samples low surface densities. As a result, ∼38% of its original pixels do not satisfy the threshold. For all other environments, the fraction of pixels dropped is only <5%. After performing this cut, the disk still remains the galactic environment with the largest number of pixels. Thus, we are only mildly increasing the statistical uncertainty of

our results with this approach, and it permits us to reduce any bias in the reported quantities by considering only those $\Sigma_\star$ regimes not dominated by nondetections.

3.3.2 Fitting technique

In this work, we aim at finding the best set of parameters $C_\star$, $C_{\rm mol}$ and $C_{\rm norm}$ that describe the star-forming plane conformed by the quantities $\log\Sigma_{\rm SFR}$, $\log\Sigma_\star$ and $\log\Sigma_{\rm mol}$, such that:

$$\log\Sigma_{{\rm SFR},i} = C_{\star,i}\log\Sigma_\star + C_{{\rm mol},i}\log\Sigma_{\rm mol} + C_{{\rm norm},i}\ , \tag{3.3}$$

where the subindex i stands for each galactic environment. If $\Sigma_\star$ and $\Sigma_{\rm mol}$ are the only quantities that determine $\Sigma_{\rm SFR}$ in a given region of a galaxy, then this plane should not change between different galactic environments. However, given that galactic environments represent a diversity of other physical conditions including gas phase metallicity, stellar age, stellar geometry (flattened vs. triaxial), shear rate, radial flows and the gas structure and organization, then we might expect there to be additional factors that influence gas stability and star formation at fixed $\Sigma_{\rm mol}$ and $\Sigma_\star$ (i.e., Hunter et al., 1998; Martig et al., 2009; Krumholz et al., 2018; Meidt et al., 2018, 2020; Gensior et al., 2020; Gensior & Kruijssen, 2021). Thus, the question we aim to address in this chapter is whether there is a single relationship between $\Sigma_{\rm SFR}$, $\Sigma_\star$ and $\Sigma_{\rm mol}$ which is valid in all environments, or if this relation differs between (some) environments. In the latter case, can we also aim at identifying the parameter(s) setting the level of $\Sigma_{\rm SFR}$, besides $\Sigma_\star$ and $\Sigma_{\rm mol}$.

To minimize the covariance between model parameters, we normalize the distributions of the three involved variables, $\log\Sigma_{\rm SFR}$, $\log\Sigma_\star$ and $\log\Sigma_{\rm mol}$, by their (full sample) mean before fitting the data (i.e. centering). After the data are normalized, we find the best set of parameters $C_\star$, $C_{\rm mol}$ and $C_{\rm norm}$ such that:

$$\begin{aligned}\log\Sigma_{\rm SFR} - \langle\log\Sigma_{\rm SFR}\rangle = C_\star(\log\Sigma_\star - \langle\log\Sigma_\star\rangle) \\ + C_{\rm mol}(\log\Sigma_{\rm mol} - \langle\log\Sigma_{\rm mol}\rangle) + C_{\rm norm}\ ,\end{aligned} \tag{3.4}$$

where the quantities inside the '$\langle\,\rangle$' brackets represent the mean of each distribution, across the full sample. Collecting these terms, we can define a new recentered normalization $\hat{C}_{\rm norm}$ so that:

$$\hat{C}_{\rm norm} = C_{\rm norm} + \langle\log\Sigma_{\rm SFR}\rangle - C_\star\langle\log\Sigma_\star\rangle - C_{\rm mol}\langle\log\Sigma_{\rm mol}\rangle\ . \tag{3.5}$$

For consistency we apply a fixed normalization to the data ($\langle\log\Sigma_\star\rangle = 8.11$, $\langle\log\Sigma_{\rm mol}\rangle = 7.25$ and $\langle\log\Sigma_{\rm SFR}\rangle = -2.48$) throughout this work, that is, we use the same average values at different spatial resolutions (Sec. 3.4.2), and when exploring environments in individual galaxies (Sec. 3.5.2).

We choose to fit a single $C_{\rm norm}$ value for all different galactic environments to avoid degeneracies between the normalization ($C_{\rm norm}$) and the slopes of the planes ($C_\star$ and $C_{\rm mol}$). This choice focuses our analysis specifically on variations of the dependency on $\Sigma_\star$ and $\Sigma_{\rm mol}$. However, we stress that the main conclusions of this chapter are not affected by this approach.

We designed our methodology (i.e. unique normalization and detection threshold) to test for environment-driven differences in the plane relating $\log \Sigma_{\star}$, $\log \Sigma_{\rm SFR}$, and $\log \Sigma_{\rm mol}$. The existence of such differences is of considerable interest, because it can reveal the degree to which physics covariant with the environment definitions impact the star formation process. However, we caution that our methodology is not necessarily the optimal approach to determine the 'real' slopes of the star-forming plane. Environment may also affect the normalization ($C_{\rm norm}$). Because we keep $C_{\rm norm}$ fixed, our fitting method may allow some of the signal associated with normalization variation to the derived slopes ($C_{\star}$ and/or $C_{\rm mol}$).

In order to find the best-fitting parameters that describe the star-forming plane in each environment, as defined in Eq. (3.3), we perform a Bayesian hierarchical linear regression, based on routines from the `PyMC3` python package (Salvatier et al., 2016). The hierarchical linear regression represents the middle ground between assuming that different environments are completely independent populations, and assuming that they all are identical and described by the same model. Instead, it assumes that the parameters of the models that describe the data sets of different galactic environments have some underlying similarity. That is, the coefficients that describe the star-forming plane in different galactic environments are assumed to follow the same underlying 'hyperprior' distribution, defined by a common set of 'hyperparameters'. We choose weakly informative hyperpriors in order to ensure that our results are not dominated by the priors. The hyperprior distributions considered are the following:

$$C_{\star,\mu} \sim \mathcal{N}(1, 10^2) \ , \tag{3.6}$$
$$C_{\star,\sigma} \sim \mathcal{H}(5^2) \ , \tag{3.7}$$
$$C_{\rm mol,\mu} \sim \mathcal{N}(1, 10^2) \ , \tag{3.8}$$
$$C_{\rm mol,\sigma} \sim \mathcal{H}(5^2) \ , \tag{3.9}$$

where $\mathcal{N}(\mu, \sigma^2)$ and $\mathcal{H}(\sigma^2)$ stand for Normal and Half-Normal distributions, respectively, with mean μ and variance σ^2. The prior distribution of each coefficient is then defined as

$$C_j \sim \mathcal{N}(C_{j,\mu}, C_{j,\sigma}) \ , \tag{3.10}$$

for j in $\{\star, \rm mol\}$. In addition to these hyperpriors, we adopt the following priors for the normalization coefficient.

$$C_{\rm norm,\mu} \sim \mathcal{N}(0, 10^2) \ , \tag{3.11}$$
$$C_{\rm norm,\sigma} \sim \mathcal{H}(5^2) \ . \tag{3.12}$$

Finally, we include an additional term to account for intrinsic dispersion, which is common for all environments, and its prior is defined as

$$\epsilon \sim \mathcal{N}(0, \sigma_{\rm intr}) \ , \tag{3.13}$$

where $\sigma_{\rm intr}$ corresponds to the intrinsic dispersion of the data with respect to the model, and for its prior distribution we use:

$$\sigma_{\rm intr} \sim \mathcal{HC}(5^2) \ , \tag{3.14}$$

	$C_{\star}$	C_{mol}	N_{pix}
Disk	0.17 ± 0.02	0.87 ± 0.01	18977
Sp. arm	0.45 ± 0.02	0.89 ± 0.01	15743
Bar	-0.41 ± 0.01	0.83 ± 0.01	7286
Ring	-0.08 ± 0.02	1.01 ± 0.01	7399
Center	0.20 ± 0.05	0.88 ± 0.04	587
All	-0.04 ± 0.01	0.92 ± 0.01	49992

Table 3.2: Mean and standard deviation of the posteriors distributions in Fig. 3.2, for each parameter and each galactic environment. Additionally to the above parameters, we obtain $C_{norm} = -0.01$ and an overall intrinsic dispersion $\sigma_{intr} \approx 0.63$ dex. The number of pixels included in each environment is indicated in the last column.

where $\mathcal{HC}(\sigma^2)$ stands for Half-Cauchy distribution, a common choice for a prior distribution of a scaling parameter like the intrinsic scatter. We find that σ_{intr} describes well the standard deviation in the fit residuals of our data.

We use four Markov chain Monte Carlo (MCMC) chains to sample the posterior distributions, each one of them having 2000 iterations plus 2000 additional burn-in iterations. The posterior is sampled using the `NUTS` algorithm (Homan & Gelman, 2014). The convergence of the MCMC chains is ensured by using the $\hat{R} \approx 1$ criterion (Gelman & Rubin, 1992). Essentially, $\hat{R}$ corresponds to the ratio of the between-chain variance and the within-chain variance. In Supporting material 3.7.1, we use a toy model to test the accuracy of the hierarchical modeling, and find that this approach correctly recovers the test values in mock data sets.

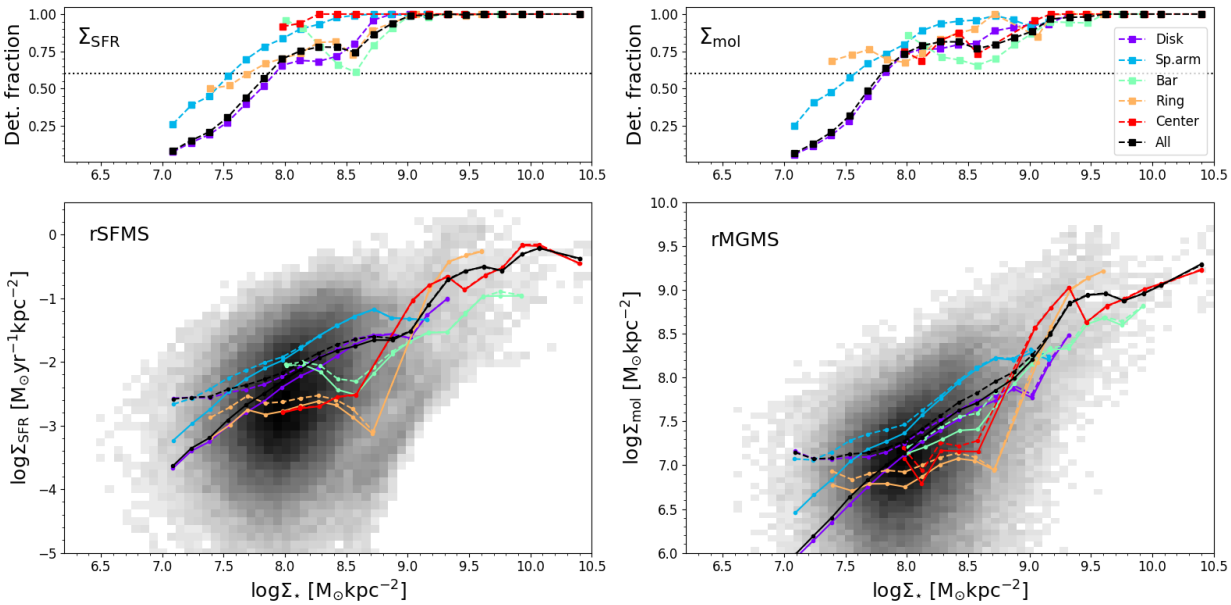

Figure 3.1: rSFMS (bottom left) and rMGMS (bottom right) measured at 150 pc resolution for all galaxies in our sample. For reference and to guide the eye, the various solid colored lines represent the binned trends (bins of 0.15 dex) obtained for each environment, accounting for nondetections as detailed in Pessa et al. (2021). The black solid line shows the same measurement for all environments simultaneously. The dashed lines show the binned trends obtained when nondetections are neglected from the analysis. The panels on the top row show the detection fraction of Σ_{SFR} (left) and Σ_{mol} (right), defined as the fraction of pixels with a measurement above our detection threshold in each bin of $\Sigma_\star$. The horizontal dotted line marks the detection fraction level of 60%.

3.4 Results

3.4.1 Star-forming plane across galactic environments at 150 pc resolution

Figure 3.2 shows the posterior distributions of each one of the parameters that define the star-forming plane in each galactic environment, following the same color code as in Fig. 3.1. The mean and standard deviation of each one of these distributions are reported in Table 3.2, as well as the number of pixels used in the fit for each environment. We firstly note that the marginalized posteriors of $C_\star$ and C_{mol} of different environments are significantly different ($>1\sigma$ in most of cases). The posterior distributions of $C_\star$ and C_{mol} are significantly broader for galaxy centers than for the rest of environments. This could either be statistical (i.e., due to the smaller number of pixels probing this environments) or intrinsic (i.e. different galaxy centers have different scaling relations). The posterior of C_{norm} is only shown for the full sample, since we model a single normalization for all environments as explained in Sec. 3.3.2. As a single value of C_{norm} is fitted for the full sample, the posterior distribution of C_{norm} is considerably narrower than that of $C_\star$ and C_{mol}. Thus, the x-axis in the right-most panel has smaller bins, and the distribution of C_{norm} has been renormalized for an easier

visualization. After correcting for the centering of the data (Eq. 3.5), this value of C_{norm} implies an absolute normalization $\hat{C}_{norm}$ of -8.83. This value represents a characteristic depletion time of $\sim$1.5 Gyr, well within the range of values reported in Querejeta et al. (2021).

We note that $C_{\star}$ parametrizes the rate of change of the rKS normalization, associated with $\Sigma_{\star}$, and the index of the power law spans a wide range of values, changing sign significantly across the sample, from about -0.41 to 0.45. Interestingly, bars have a very negative value of $C_{\star}$ (~ -0.4), meaning that they show longer depletion times at higher $\Sigma_{\star}$ values. While this low value of $C_{\star}$ is certainly an indication of lower star formation efficiencies, compared to other environments, we remind the reader that due to our adopted approach of using a single normalization across different galactic environments, a negative $C_{\star}$ could be interpreted also as the slope trying to capture a vertical offset between environments.

In Sec. 3.5.2, we discuss the possibility of this low value of $C_{\star}$ being linked to lower star formation efficiencies (SFE) driven by radial and/or turbulent motion of gas in bars. In contrast, spiral arms show the highest values of $C_{\star}$ ($\sim$0.45), leading to shorter depletion times at higher $\Sigma_{\star}$ values. As $\Sigma_{\star}$ varies strongly as a function of radius, $C_{\star}$ expresses a radial trend in the normalization of the molecular gas scaling relation. Analogous variations were reported in Muraoka et al. (2019), where the authors report radial variations of a factor 2$-$3 in the SFE of individual nearby galaxies from the CO Multi-line Imaging of Nearby Galaxies (COMING) project (Sorai et al., 2019).

On the other hand, C_{mol} shows a more homogeneous behavior with values in the range of 0.83 to 1.01, which implies that higher Σ_{mol} leads to higher Σ_{SFR} everywhere in the galaxy. Subtle variations are found for bars having the lowest values ($C_{mol} \sim 0.83$) or rings having the largest value ($C_{mol} \sim 1.01$). It is interesting to note that while rings show nearly a linear slope in molecular gas, other galactic environments exhibit a sublinear behavior. While a linear relation implies a constant depletion time (defined as $\tau = \Sigma_{mol}/\Sigma_{SFR}$), a sublinear slope leads to a depletion time that increases with gas surface density (neglecting changes in $C_{\star}$). Shetty et al. (2014) examined different possibilities to physically interpret this sublinearity. On one hand, differences in the molecular gas properties such as star formation efficiency or volume density (see Bacchini et al., 2019a, 2020) could lead to variations of the depletion time. Alternatively, variations in the depletion time could be produced by a diffuse component of the molecular gas (i.e., molecular gas not actively forming stars). Schinnerer et al. (2019a) and Pan et al. (2022) found that a significant fraction of molecular gas is indeed decoupled from the Hα emission in PHANGS galaxies. Although for this analysis, we choose only pixels that show both molecular and ionized gas emission, quiescent gas could still be present in our data due to projection effects. In this scenario, the sublinearity is an indication that the fraction of diffuse molecular gas grows with Σ_{mol}. We highlight that this sublinearity persists for bars, disks and spiral arms, when we let C_{norm} free for each individual environment.

A third possibility is that variations in the depletion times are driven by variations in the real underlying α_{CO} conversion factor or CO(2–1)-to-CO(1–0) line ratios. Leroy et al. (2022) studied variations in the $R_{21} \equiv$ CO(2–1)-to-CO(1–0) line ratio within PHANGS galaxies, and reported a central enhancement of R_{21} of a factor of $\sim$0.18 dex. Such anticorrelation of R_{21} with galactocentric radius (and thus, correlation with Σ_{SFR}) implies our fiducial choice of $R_{21} = 0.65$ could potentially lead to an overestimation of the total molecular gas content in the inner and denser regions of the galaxy, and to an underestimation of the gas

content in the outer regions. This can effectively depress the measured $C_{\rm mol}$ slope by up to $\sim$0.15. This effect likely plays a more relevant role in the global measurement, considering all environments, due to the larger dynamic range of $\Sigma_\star$. However, it can not be ruled out that it is also, partially, driving the sublinearity found in the single-environment measurements.

Figure 3.3 shows the covariance between the posterior distributions of the parameters $C_\star$ and $C_{\rm mol}$ measured for each galactic environment. As $C_\star$ and $C_{\rm mol}$ are the coefficients of the linear combination to predict $\log\Sigma_{\rm SFR}$ of a given pixel from its $\log\Sigma_\star$ and $\log\Sigma_{\rm mol}$ measurements, they show a negative covariance, that is, a higher $C_\star$ implies a lower value of $C_{\rm mol}$. The covariance is much larger for centers likely due to the lower number of pixels in these environments (see Table 3.2), but could also be connected to a physically more heterogeneous behavior of centers. On the other hand, the covariance in disks is significantly smaller. In Supporting material 3.7.1, we show that this covariance arises, in part, as an artifact of the fitting procedure. However, the covariance could be also partially due to the fact that $\Sigma_\star$ and $\Sigma_{\rm mol}$ are physically highly correlated quantities, through the rMGMS, thus the covariance reflects the slope between them.

Figure 3.4 provides an alternative visualization of the 2D planes obtained with the fitting procedure. It shows the partial residual for each independent variable after removing the dependency on the second independent variable. Specifically, we define $\delta_\star$ and $\delta_{\rm mol}$ as

$$\delta_\star = \log\Sigma_{\rm SFR} - C_{\rm norm} + C_{\rm mol}\log\Sigma_{\rm mol}\ , \tag{3.15}$$

$$\delta_{\rm mol} = \log\Sigma_{\rm SFR} - C_{\rm norm} + C_\star\log\Sigma_\star\ , \tag{3.16}$$

to visualize the partial residuals as a function of $\Sigma_\star$ and $\Sigma_{\rm mol}$, respectively. The figure shows in each row the residuals for a given environment as a 2D histogram. The bottom row shows the residuals for the full sample. The slope in each panel corresponds to the best-fitting value of $C_\star$ (left column) and $C_{\rm mol}$ (right column) for each environment.

The sharp cut at low $\Sigma_\star$ in the x-axis of the left panels is a consequence of the adopted detection threshold for each galactic environment as described in Sec. 3.3.2. The figure shows the range of slopes derived for the different environments probed. Spiral arms are the environment that show the most positive trend for $\Sigma_\star$, while centers and disks show more subtle positive trends. In contrast, bars show the most negative $C_\star$ values of all environments. Similarly, bars also exhibit the lowest values of $C_{\rm mol}$, which can be understood as a lower efficiency at converting molecular gas into stars toward higher values of $\Sigma_{\rm mol}$. On the other hand, star-forming rings show the largest $C_{\rm mol}$ value (≈ 1.01), which indicates a nearly constant depletion time across the $\Sigma_{\rm mol}$ range. We inspect these trends per environment and find that they are not driven by individual galaxies and that, indeed, the trends of the multiple galaxies are consistent with each other. These trends reveal that the galaxy-to-galaxy variations in the scaling relations reported in Ellison et al. (2021) and Pessa et al. (2021) could plausibly be explained by a different relative contribution of the different galactic environments across the sample galaxies.

3.4.2 Effect of spatial resolution

In this section, we explore how the spatial scale of the data impacts our measurements. We degraded our data, as explained in Sec. 3.2.6, and repeated the measurement of $C_\star$, $C_{\rm mol}$ and

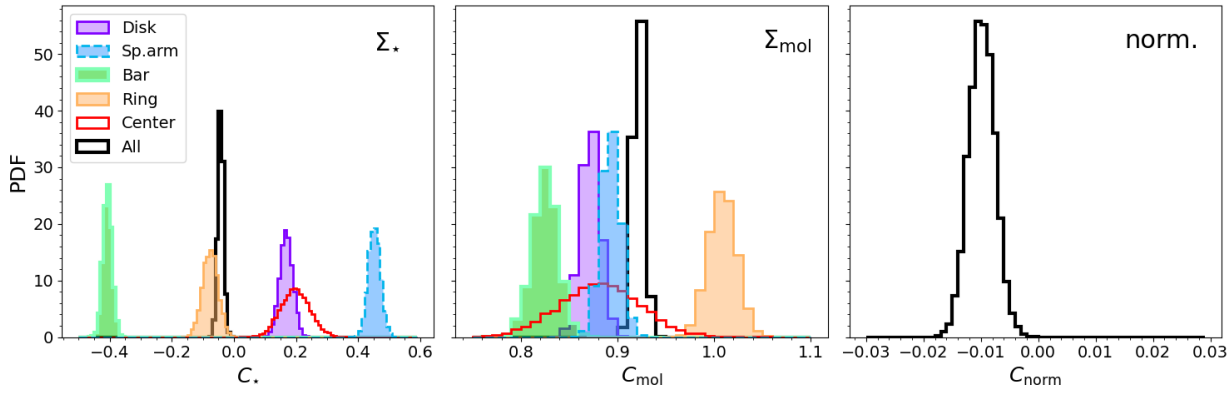

Figure 3.2: Posterior distributions for the coefficients $C_{\star}$, $C_{\rm mol}$ and $C_{\rm norm}$ that define the star-forming plane in each galactic environment, measured at a spatial resolution of 150 pc. As the posterior distribution of $C_{\rm norm}$ is considerably narrower than that of $C_{\star}$ and $C_{\rm mol}$, the x-axis has been binned in smaller bins and the distribution renormalized for an easier visualization.

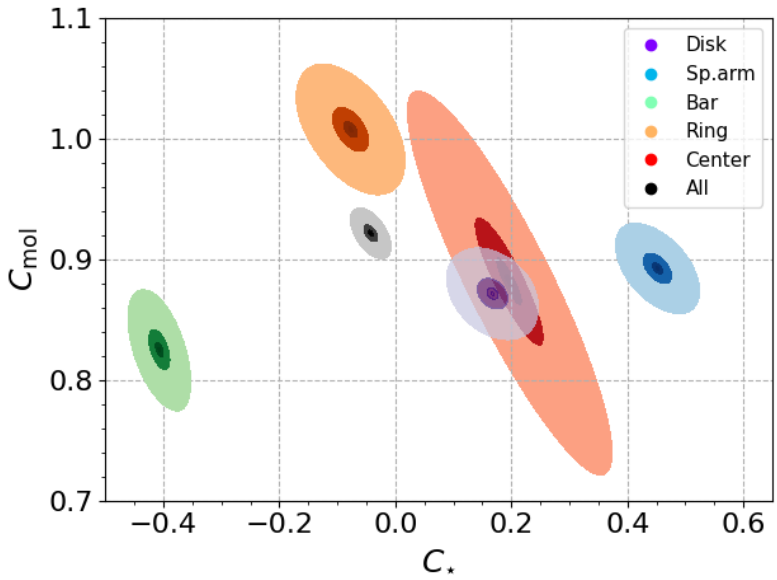

Figure 3.3: Posteriors distributions of the coefficients $C_{\star}$ and $C_{\rm mol}$ for each separate environment, measured at an spatial resolution of 150 pc, to show the covariance between them. The posteriors have been smoothed using a Gaussian kernel. The color scale for each environment indicates the 1-, 2- and 3-sigma confidence intervals.

$C_{\rm norm}$, following the same procedure as detailed in Sec. 3.3.2. Figure 3.5 displays the mean of the distribution of each parameter, for each galactic environment, as a function of the spatial scale of the data. The error-bars show the standard deviation of the corresponding posterior distribution. The bottom panel shows the 'real' normalization value $\hat{C}_{\rm norm}$, as defined in Eq. (3.5). It is clear that different environments have different coefficients in their scaling relations at ∼150 pc resolution, but the differences are reduced when looking at larger spatial scales. This is likely due to a combination of two effects: (i) At larger spatial scales, the

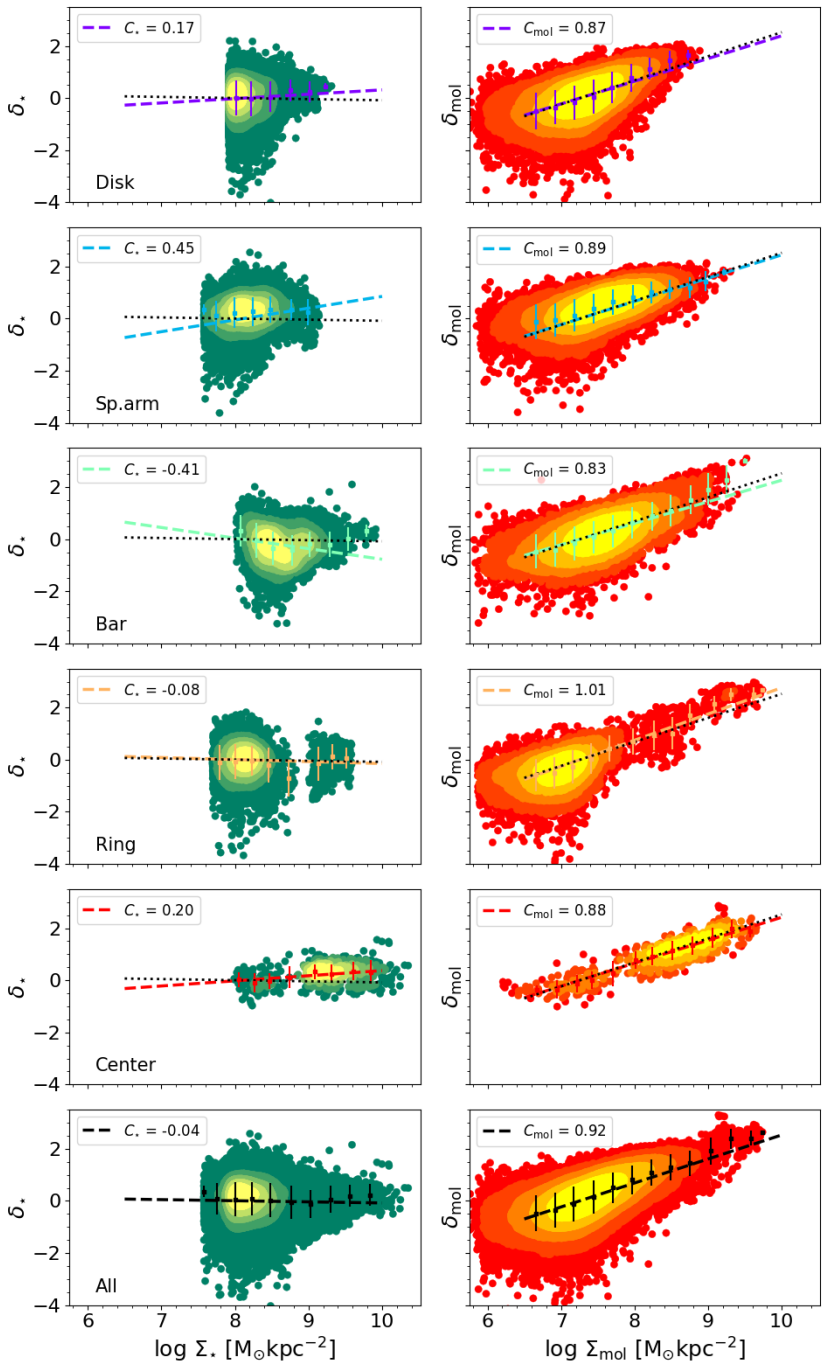

Figure 3.4: Partial residual for each independent variable, dropping the dependency from the second independent variable, found for each individual environment and for all environments together as a function of $\Sigma_\star$ (left) and $\Sigma_{\rm mol}$ (right), measured at an spatial resolution of 150 pc. The binned data are shown for each corresponding environment. The trend for the full sample is overplotted as a black dotted line.

light from different environments is blended, and (ii) the number of available pixels decreases drastically at larger spatial scales, from a total sample size of ∼50,000 to ∼1200 making the

measurement statistically less certain. Whereas (ii) would have an effect across the whole range of spatial scales probed, (i) will be relevant only at spatial scales larger than that of the typical structural size of each environment.

Figure 3.6 explicitly shows the posterior distributions of $C_{\star}$ and C_{mol}, for each environment and spatial scale probed. It shows that at spatial scales larger than 300 pc, the differences between the posteriors of different environments become smaller than 1σ (with respect to the full-sample measurement), especially for C_{mol}. This spatial scale roughly matches the width of the spiral arms in our Galaxy (Reid et al., 2014). In our sample, rings, spiral arms and centers are found to have sizes on the order of a few hundreds parsecs (Querejeta et al., 2021), and therefore, their emission is expected to blend at spatial scales larger than this. On the other hand, bars have larger typical sizes, on the order of several kpc, which is consistent with finding that differences in the posterior distributions of their scaling relation parameters persist up to scales of $\sim$500 pc in both, $C_{\star}$ and C_{mol}. This homogeneization toward lower spatial resolutions agrees well with the absence of systematic galaxy-to-galaxy variations reported in Sánchez et al. (2021), using data from the CALIFA (Sánchez et al., 2012) and EDGE (Bolatto et al., 2017) surveys.

It is also worth noting the general trends of $C_{\star}$ and C_{mol} toward larger spatial scales. While the posteriors of $C_{\star}$ are shifted toward more negative values, the posteriors of C_{mol} move toward steeper slopes. These changes are likely a combination of the effect of N/Ds in our data (even though we remove the $\Sigma_{\star}$ ranges more critically affected by N/Ds to minimize their impact), and the $C_{\star}-C_{mol}$ covariance. The former could induce a steepening in these slopes, while the latter would drive their (a)symmetry.

Finally, we find that galactic environments are not only different in terms of the coefficients describing their star-forming plane, but also in terms of the scatter around it. The top panel of Fig. 3.7 shows the scatter (defined as the standard deviation of the residuals) of each environment with respect to its modeled star-forming plane, at the different spatial scales probed (solid lines).

The first noticeable feature is how the scatter decreases toward larger spatial scales. The same trend is reported in Pessa et al. (2021) for the 1D scaling relations. This effect has been associated with the decoupling of different stages of the star-forming cycle at high spatial resolution, in other words, a given aperture can be either dominated by a peak in the CO emission (i.e. early in the star-forming cycle) or a peak in the Hα emission (i.e. late in the star-forming cycle) (e.g., Schruba et al., 2010; Feldmann et al., 2011; Leroy et al., 2013; Chevance et al., 2020a,b). At larger spatial scales, these peaks are averaged, which diminishes the sampling effect. (Schruba et al., 2010; Kruijssen & Longmore, 2014; Semenov et al., 2017; Kruijssen et al., 2018). The fraction of pixels containing only molecular gas or only ionized gas has been empirically characterized in Schinnerer et al. (2019a) and Pan et al. (2022). Both works found that $\sim$500 pc is a critical spatial scale, below which distinguishing particular stages of the star formation process is possible, in nearby star-forming galaxies. In this line, Kruijssen et al. (2019) and Chevance et al. (2020a) found that the typical distance between independent star-forming regions is 100$-$300 pc. J. Kim et al. (in prep.) and Machado et al. (in prep.) report an average distance of $250-300$ pc in the full PHANGS sample.

The figure also shows that at $\sim$150 pc, the scatter in certain environments is significantly lower than in others. Centers and spiral arms show a particularly low scatter, whereas disk is

the only environment that shows a scatter larger than the full sample. It is also worth noticing that the rate at which the scatter decreases with increasing spatial scale also varies across environments, with bars showing the flattest trend between 150 and 300 pc, while rings and centers showing the steepest trend. Together with the scatter, this indicates variations in the properties of the molecular clouds, such as differences in their lifetimes, or a different typical separation between clouds (as suggested by Chevance et al., 2020a). In this line, Henshaw et al. (2020) found evidence that fragmentation indeed occurs on smaller size scales in centers and potentially also (but to a lesser extent) in spiral arms. This idea would be consistent with the higher scatter, and its flatter decrease toward larger spatial scale that we see in bars and disks, resulting from a lower spatial density of star-forming regions, as compared to rings, spiral arms or centers. Additional variations in the intrinsic properties of molecular clouds have been reported in previous works (Sun et al., 2018, 2020c,a; Rosolowsky et al., 2021). Sun et al. (2020c), using data from PHANGS–ALMA, found that cloud-scale molecular gas surface density, velocity dispersion and turbulent pressure of molecular clouds depend on local environmental conditions. Similarly, Colombo et al. (2014) used data from the PdBI Arcsecond Whirlpool Survey (PAWS; Schinnerer et al., 2013) to characterize variations of molecular gas properties across galactic environments, and concluded that this environmental variations are a consequence of the combined action of large-scale dynamical processes and feedback from high-mass star formation. A similar conclusion was obtained by Renaud et al. (2015), where the authors used hydrodynamical simulations to study the regulation of the star formation in bars.

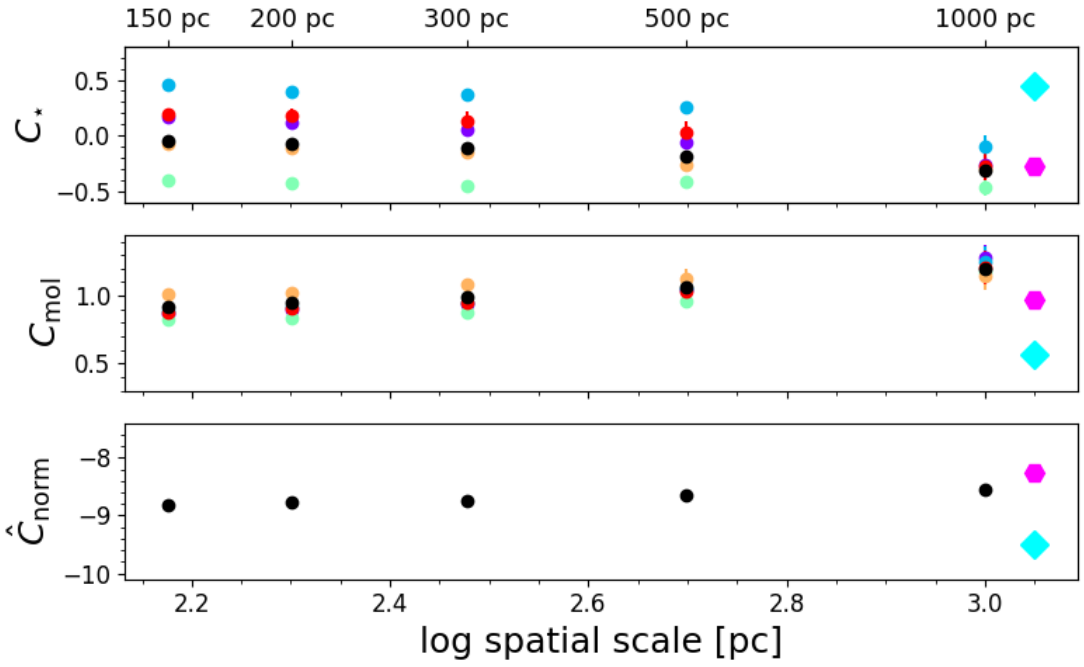

Figure 3.5: Change of the coefficients that define the star-forming planes in each galactic environment with spatial scale. The color code for each environment is the same as used in Fig. 3.1. The cyan diamond and a magenta hexagon indicate the results reported by Sánchez et al. (2021) (EDGE–CALIFA sample) and Lin et al. (2019), respectively.

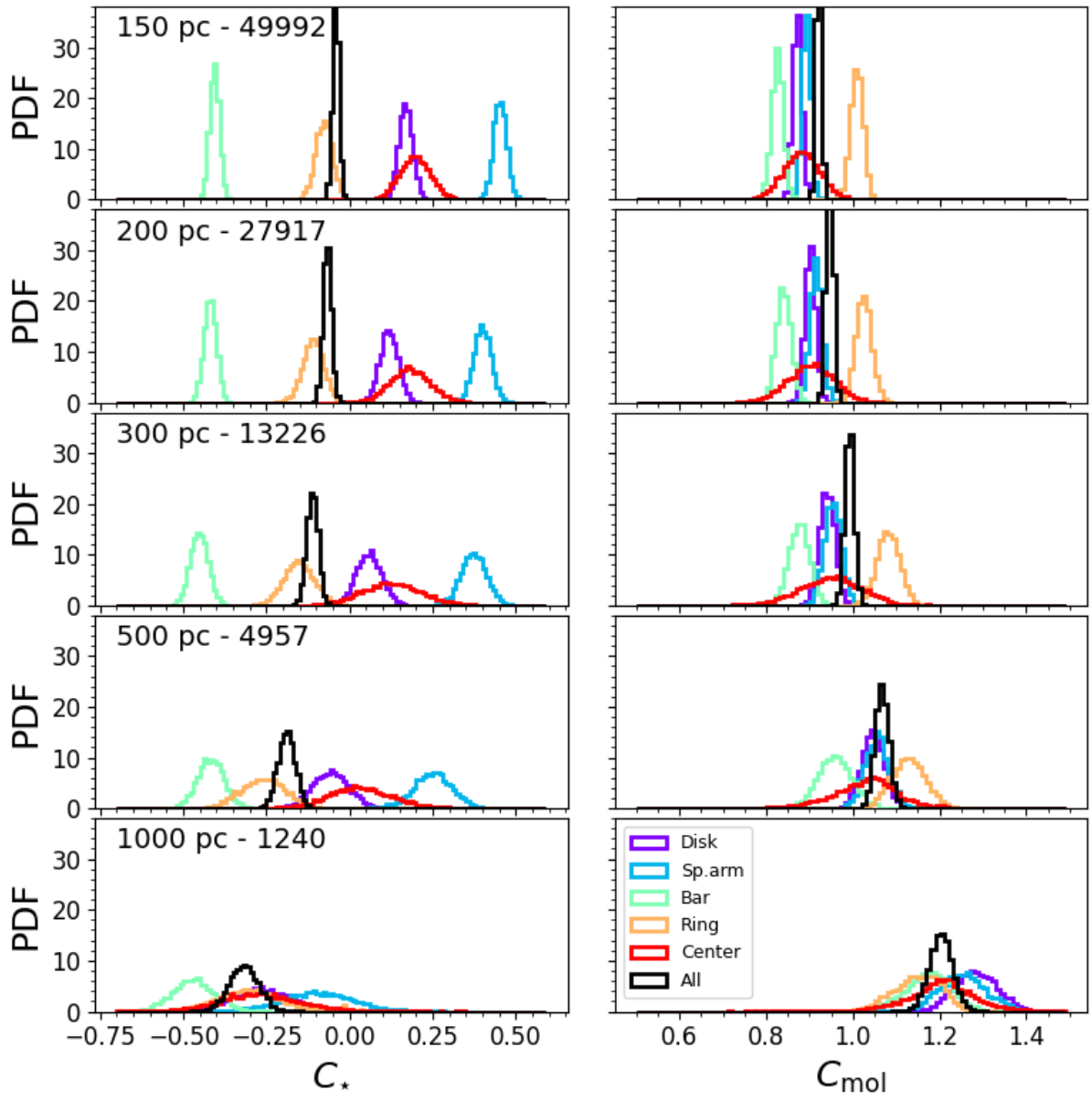

Figure 3.6: Posterior distribution of the coefficients that define the star-forming planes in each galactic environment, at each one of the spatial scales probed, from 150 pc to 1 kpc. The spatial scale and the number of pixels used for each measurement are indicated in the top left corner for each row.

3.4.3 Plane versus single power law

Here we explore whether a 2D plane offers a more accurate prediction of Σ_{SFR} than the rKS. For this comparison, we find the best-fitting power law in each environment following the same prescription described in Sec. 3.3.2 (i.e., centering the data and using a single C_{norm} value), dropping the dependency on $\Sigma_{\star}$ (i.e., removing $C_{\star}$ from the model). The top panel of Fig. 3.7 shows as dashed lines the scatter with respect to the rKS measured for each

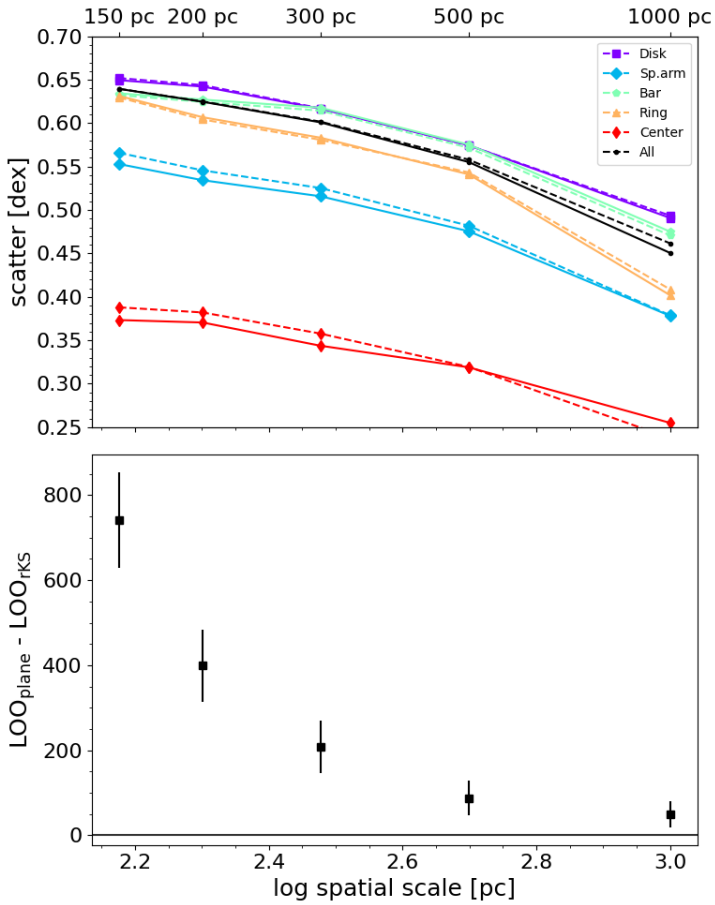

Figure 3.7: Comparison between plane and single power law models. *Top*: Scatter with respect to the star-forming 2D plane (solid) and rKS (dashed) determined for each galactic environment, at the different spatial scales probed. *Bottom*: Difference of the LOO score measured for the plane and the rKS models, where a > 0 indicates a preference for the plane model. The error bars are the 3σ standard errors. The black horizontal line at 0 marks where there would be no preference between the models. The plane model is preferred over the rKS at all spatial scales, increasingly so at finer spatial scales.

galactic environment, at each one of the spatial scales probed. The figure shows that when we separate the data by environment, the additional dependency of $\Sigma_\star$ does not reduce the scatter significantly. Moreover, rKS shows a slightly smaller scatter than the 2D plane in some environments. This is a consequence of the low predictive power found for $\Sigma_\star$, with respect to $\Sigma_{\rm mol}$ (i.e. $C_{\rm mol} > C_\star$), to predict $\Sigma_{\rm SFR}$. However, it should be kept in mind that the lower predictive power found for $\Sigma_\star$ could be, at least partially, related to its limited dynamic range, as shown by Fig. 3.4. Nevertheless, this finding is consistent with Lin et al. (2019), where the authors find that the 'extended' version of the rKS (i.e. with an additional dependency of $\Sigma_\star$) has its scatter only slightly reduced with respect to the conventional rKS.

Despite offering only a modest improvement in the scatter, we find that the plane model is formally favored over the rKS at all spatial scales. We compare the models using leave-one-out (LOO; Sammut & Webb, 2010) cross-validation, a standard model comparison method

(Vehtari et al., 2017). The LOO cross validation is computationally more expensive than other forms of cross validations (e.g., K-fold, random subsampling), but it offers a more robust estimate of the predictive accuracy of a model, and it is suitable for relatively small datasets.

The bottom panel of Fig. 3.7 shows the difference of the LOO statistics for both models (the environmental separation is included in each model), where a higher LOO statistic indicates the preferred model. The figure shows that the LOO statistic for the plane model is higher than for the rKS model at all spatial scales at the $>3\sigma$ level, and that the preference for the plane model becomes stronger at high spatial resolution. For this comparison, we checked that the measured σ_{intr} at each spatial scales captures the different levels of scatter of the data across the range of spatial scales probed, making the decrease in the LOO statistic not primarily driven by the intrinsic scatter.

This result is consistent with Fig. 3.6, which shows that the width of the posterior distributions of $C_{\star}$ increases toward larger spatial scales in all environments, and thus nonzero $C_{\star}$ are more constrained on finer spatial scales. This means that including the $C_{\star}$ in the model is more important at smaller scales, but less critical at larger spatial scales. An explanation for this is that in the high spatial resolution measurements, the high Σ_{SFR} (and Σ_{mol}) regions are often located in the inner regions of the galaxy (and vice-versa). However, at lower spatial resolutions, Σ_{SFR} (and Σ_{mol}) is diluted in a larger regions, due to its intrinsic patchy configuration. As this does not occur with $\Sigma_{\star}$, this results in $\Sigma_{\star}$ providing less information to predict Σ_{SFR}, compared to Σ_{mol}, toward lower resolutions.

3.5 Discussion

3.5.1 Comparison to previous findings

Here we compare our results with those in the literature. Our results agree relatively well with those reported in Lin et al. (2019), where the authors used ALMaQUEST (Lin et al., 2020) data to explore the extended version of the rKS relation (Shi et al., 2011, 2018). In terms of the coefficients we use in this chapter, they found $C_{\star} = -0.29$, $C_{mol} = 0.97$ and $C_{norm} = -8.27$. These numbers agree with those we report here (see Table 3.2), not only in their absolute values but also in terms of the relative predicting power of $\log\Sigma_{\star}$ and $\log\Sigma_{mol}$ to predict $\log\Sigma_{SFR}$. Shi et al. (2018) performed similar measurements using data from The H I Nearby Galaxy Sample (THINGS; Walter et al., 2008) and from the *GALEX* data archive (using total gas surface density rather than molecular gas). Interestingly, in terms of the same coefficients, they found $C_{\star} = 0.55$, $C_{mol} = 1.09$ and $C_{norm} = -10.47$. This is roughly consistent with the idea that mid-plane pressure helps to regulate current star-formation, as pressure scales as $\Sigma_{\star}^{0.5}\Sigma_{gas}$ (Shi et al., 2018). Furthermore, they found that outer disks of dwarfs galaxies and local luminous infrared galaxies show the largest offset in this relation, whereas local spirals show almost no offset. This is an intriguing result, as we also find a relatively similar behavior for spiral arms. However, we stress that this comparison has the caveats of (i) local spiral galaxies host different environments (not only spiral arms) and (ii) the study carried out in Shi et al. (2018) uses data with different spatial resolutions. Nevertheless, this is an interesting comparison that could indicate that mid-plane hydrostatic pressure plays a more relevant role in spiral arms than in other environments.

On the other hand, in Sánchez et al. (2021), the authors performed a similar measurement using data from the CALIFA and EDGE surveys. For the EDGE–CALIFA sample, which represents a better reference for comparison in terms of molecular gas tracer and spatial scale, they found $C_\star = 0.44 \pm 0.01$, $C_{\rm mol} = 0.57 \pm 0.01$ and $C_{\rm norm} = -9.5 \pm 0.01$. These coefficients partially agree with our results, in terms of the lower relative importance of $\log \Sigma_\star$ to predict the $\log \Sigma_{\rm SFR}$ value with respect to $\log \Sigma_{\rm mol}$. However, significant quantitative differences between the measured coefficient exist. The differences persist even if we exclude the detection-fraction-threshold step from the fitting (this does not change our results significantly at a spatial resolution of $\sim$1 kpc).

Part of the differences we see here are in the statistical questions we are exploring with respect to the variation of these scaling relationships with environment. Sánchez et al. (2021) demonstrate the importance of the statistical framework for interpreting the results of these regressions. Our hierarchical Bayesian approach for this analysis provides a framework for analyzing the data within well-resolved environments that could not be addressed at coarser resolution by the complementary EDGE–CALIFA sample, despite its much larger size, compared to our PHANGS–MUSE sample. A direct comparison is not possible since PHANGS–MUSE galaxies all have distances lower than 20 Mpc, and an overlap between both samples does not exist. Nevertheless, it is worth mentioning that Sánchez et al. (2021) also report measurements using their CALIFA–only sample, where the molecular gas estimates are based on the ISM dust attenuation prescription reported in Barrera-Ballesteros et al. (2021a). For this sample, they obtained $C_\star = 0.66 \pm 0.02$, $C_{\rm mol} = 0.38 \pm 0.01$ and $C_{\rm norm} = -9.9 \pm 0.05$. These numbers are in stronger disagreement with our results, not only due to the differences in the values of the measured slopes, but also in the relative importance of $\log \Sigma_\star$ and $\log \Sigma_{\rm mol}$ to predict the $\log \Sigma_{\rm SFR}$ Hence, any comparison of results should be made carefully, as differences in the sample, such as the molecular gas tracer, could lead to different conclusions. The results reported in Sánchez et al. (2021) (EDGE–CALIFA sample) and in Lin et al. (2019) are indicated in Fig. 3.5 as a cyan diamond and a magenta hexagon, respectively.

Other studies have also explored systematic difference across galactic environments. In Querejeta et al. (2021), the authors used 74 galaxies of the PHANGS sample to measure the distributions of $\Sigma_{\rm mol}$, $\Sigma_{\rm SFR}$ and depletion times across galactic environments at a fixed spatial scale of $\sim$1.5 kpc. They found a strong correlation between molecular gas and SFR surface densities, with a global slope of $N = 0.97$, but little variation across galactic environments. However, they reported a slight offset toward shorter depletion times for centers ($\tau_{\rm dep} = 1.2$ Gyr), and longer depletion times for bars ($\tau_{\rm dep} = 2.1$ Gyr). This result is consistent with our measurement of the lowest $C_\star$ in this environment at a spatial resolution of $\sim$1 kpc. On the other hand, we do not find that $C_\star$ in centers is higher than in the other environments. However, this specific measurement is highly uncertain (due to the low number of 'center' pixels at this resolution in our study) and thus, a proper comparison is not possible. Overall, they did not find evidence of strong variations in how efficiently different environment form stars. Not finding strong differences across environments is also consistent with the homogenization of galactic structure at large spatial scales which we report in this work (see Sec. 3.4.2).

3.5.2 What drives the environmental variations we see?

In previous sections, we reported the coefficients that describe the star-forming plane for each individual galactic environment. Furthermore, we find significant differences in the star-forming planes associated with these different environments, particularly for bars, spiral arms and rings. In this section, we explore which parameter(s) could be driving the differences we report in Sec. 3.4.

To perform this exploration, we measure $C_{\star}$, C_{mol} and C_{norm} in each environment of each individual galaxy in our sample (following the same procedure detailed in Sec. 3.3.2), and search for correlations between the coefficients obtained in each environment, and a set of additional parameters:

- Molecular gas fraction; $\log f_{mol}$, calculated as $\log(\Sigma_{mol}/\Sigma_{\star})$
- Star formation efficiency; $\log \mathrm{SFE}$, calculated as $\log(\Sigma_{SFR}/\Sigma_{mol})$
- Free fall time (t_{ff}), calculated following Utomo et al. (2018), i.e. $t_{ff} = \sqrt{\frac{3\pi}{32G}\left(\frac{H}{\Sigma_{mol}}\right)}$, where G is the gravitational constant and H is the vertical scale height of the molecular gas layer which can be estimated as $H = \sqrt{\frac{\sigma_{mol}^2 h_{\star}}{G\Sigma_{\star}}}$, with σ_{mol} corresponding to the velocity dispersion of the molecular gas component, and $h_{\star}$ is the typical stellar scale height, for which we adopt a value of 300 pc (Utomo et al., 2018).
- Depletion time in units of free fall time; τ/t_{ff}, where $\tau = \Sigma_{mol}/\Sigma_{SFR}$ and t_{ff} is calculated as described above.
- Mid-plane hydrostatic pressure; $\log P_h$, calculated following Elmegreen (1989) as $P_h = \frac{\pi}{2} G\Sigma_{mol}\left(\Sigma_{mol} + \frac{\sigma_{mol}}{\sigma_{\star}}\Sigma_{\star}\right)$. This approach neglects the contribution from atomic gas, however, the relative contribution of atomic gas with respect to molecular gas in these galaxies and this regime of Σ_{mol} values is expected to be subdominant (Bigiel et al., 2008; Schruba et al., 2019, Leroy et al (in prep.)). Barrera-Ballesteros et al. (2021b) explore the role of P_h in regulating Σ_{SFR}, and they found a tight (scatter ~ 0.2 dex) correlation between these two quantities. Sun et al. (2020a) also found that Σ_{SFR} correlates with the dynamical equilibrium pressure of the ISM. This is encouraging to explore if differences between environments could be driven by differences in the mid-plane hydrostatic pressure, which has the additional dependencies on σ_{mol} and $\sigma_{\star}$.
- Gas-phase metallicity; $[Z/H]_{gas}$, modeled from emission-line measurements in the MUSE data, allowing for azimuthal variations, as detailed in Williams et al. (2022b).
- Stellar velocity dispersion; $\sigma_{\star}$, resulting of SSP fitting of the MUSE data (see Sec. 3.2.4).
- Hα velocity dispersion; $\sigma_{H\alpha}$, measured from the MUSE data (see Sec. 3.2.5).
- Molecular gas velocity dispersion; σ_{mol}, measured from the ALMA data (Leroy et al., 2021b).

We have additionally considered stellar population parameters measured by SSP fitting of the MUSE data (Emsellem et al., 2022, I. Pessa et al. in prep.)

- light-weighted stellar age; $\log \mathbf{AGE_{LW}}$
- mass-weighted stellar age; $\log \mathbf{AGE_{MW}}$
- light-weighted stellar metallicity; $[Z/H]_{\mathrm{LW}}$
- mass-weighted stellar metallicity; $[Z/H]_{\mathrm{MW}}$

A similar exploration of parameters was carried out by Dey et al. (2019), using data from the EDGE–CALIFA sample, performing a data-driven approach to investigate what shapes the SFR, finding that Σ_{SFR} scales primarily with $\Sigma_{\star}$ and Σ_{mol}. Conversely, we perform this exploration in order to understand what is driving the environmental differences we see in the plane spanned by these three quantities.

We compute the mean of the distribution of these quantities in each environment (considering only those pixels that were used for the fitting of the plane), and measure the weighted Pearson's correlation coefficient (ρ) between these environmental-averaged quantities and the corresponding coefficients. For this latter step, we consider only the subset of galaxies that satisfy the following criteria:

1. Probe at least three different environments.
2. Host galaxy has a bar and spiral arms.
3. Fraction of pixels removed due to the imposed detection threshold is $< 50\%$.

These selection criteria ensure that we select galaxies in which we can simultaneously probe several environments, including bars and spiral arms, which are the environments that exhibit the largest differences, especially in terms of $C_{\star}$ (see Fig. 3.2), and that most of the pixels of these galaxies are actually used in the fitting. Out of our sample, 8 galaxies satisfy the listed conditions (NGC 1300, NGC 1365, NGC 1512, NGC 1566, NGC 1672, NGC 3627, NGC 4303, NGC 4321). As a result of these conditions, we drop from our sample galaxies with total stellar mass of $\log M_{\star}[M_{\odot}] < 10.6$. We perform this exploration on an individual-galaxy basis because we acknowledge that, while different environments usually exhibit different properties in a given galaxy, the same environments are not necessarily identical across different galaxies.

For this subset of galaxies, we quantify the level of correlation between each of the parameters listed, and the coefficients $C_{\star}$ and C_{mol} obtained for each environment, using the 'overall' Pearson's correlation coefficient, defined as:

$$\langle \rho \rangle = \frac{|\sum_{i=1}^{\mathbf{n_{gal}}} \rho_i|}{\mathbf{n_{gal}}} \ , \tag{3.17}$$

which corresponds to the average ρ across the subset of galaxies. For each galaxy, the uncertainty in its correlation coefficient ρ_i (i.e., between the plane coefficients and each one of the parameters listed) is estimated by performing 50 Monte-Carlo simulations, perturbing

the measured $C_\star$ and $C_{\rm mol}$ for each environment in each iteration. The uncertainty in $\langle\rho\rangle$ is then calculated using standard error propagation.

Figure 3.8 shows the overall Pearson's correlation coefficient, that quantifies the average level of correlation between the median of each one of the quantities listed on the x-axis for a given environment and its corresponding $C_\star$ (blue) and $C_{\rm mol}$ (orange) value. It is clear that some parameters show a high level of correlation with $C_{\rm mol}$, the highest being the stellar mass-weighted age of the underlying stellar populations. However, we acknowledge that a possible correlation with the average age of the underlying stellar population would likely be a consequence of differences in the star-forming process, rather than driving it. For this reason, we focus on the following high-ρ parameter, $\langle\tau/t_{\rm ff}\rangle$ ($\langle\rho\rangle\sim0.77$).

As $\langle\tau/t_{\rm ff}\rangle$ corresponds to the depletion time normalized by the free fall time, that is, the characteristic time that it would take a gas cloud to collapse under its own gravitational attraction, it is a metric that describes how efficiently the gas is collapsing and forming stars. A high value can be interpreted as a relative excess of molecular gas with respect to SFR, in other words, a larger fraction of the gas is not forming stars (quiescent), compared to an environment with a shorter average depletion time. Figure 3.9 shows explicitly the correlation between $\langle\tau/t_{\rm ff}\rangle$ measured in each environment, and the corresponding $C_{\rm mol}$ coefficient for each individual galaxy in our subset. For most of the subset of galaxies, we see a negative trend (except for NGC 1365). Bars tend to have longer depletion times and lower values of $C_{\rm mol}$, as opposed to spiral arms, that show shorter depletion times and higher values of $C_{\rm mol}$. However, this correlation is not surprising, as $C_{\rm mol}$ quantifies how efficiently molecular gas forms stars, and $\langle\tau\rangle$ corresponds to the inverse of $\langle\log\mathbf{SFE}\rangle$ in a given environment. Thus, environments with on average longer depletion times (or lower SFE) will be naturally described by a lower $C_{\rm mol}$. Nevertheless, this correlation shows that quantifiable differences in depletion time across environments exists, and that these differences lead to variations in the star-forming plane.

Therefore, it is interesting that other parameters that show a high level of correlation with $C_{\rm mol}$ are $\sigma_\star$ and $\sigma_{\rm H\alpha}$. Velocity dispersion encodes information about noncircular motion of gas and stars in the galaxy, such as radial motions along the bar, or turbulence induced by star formation feedback or by AGN activity, for galaxies hosting an AGN (NGC 1365, NGC 1566, NGC 1672, NGC 3627, NGC 7496). Thus, the correlations between $C_{\rm mol}$ and $\sigma_{\star,{\rm H\alpha}}$ could be an imprint of how the noncircular motion of the gas prevents collapse and efficient star formation (leading to longer depletion times). The correlation with $\sigma_{\rm H\alpha}$ is presented in Supporting material 3.7.4 for completeness.

Of the remaining parameters, only two show a potential correlation with $C_{\rm mol}$, $\langle\log\mathbf{SFE}\rangle$ and $\langle f_{\rm mol}\rangle$. The first one is not surprising, as it corresponds to the inverse of $\langle\tau\rangle$. For $\langle f_{\rm mol}\rangle$, we find hints of a positive correlation, that is, a higher gas fraction leads to a higher $C_{\rm mol}$. This implies that stars are formed more efficiently in galactic environments which are more gas-rich.

For $t_{\rm ff}$, $\log P_{\rm h}$, $[Z/H]_{\rm gas}$, $\sigma_{\rm mol}$, $\log[Z/H]_{\rm LW}$ and $\log[Z/H]_{\rm MW}$, we do not find a correlation with $C_{\rm mol}$.

On the other hand, $C_\star$ shows in general lower levels of correlation for most of the parameters probed. This is not unexpected, due to the lower predictive power of $\Sigma_\star$ to predict $\Sigma_{\rm SFR}$ as compared to $\Sigma_{\rm mol}$. Nevertheless, we still see a correlation of $C_\star$ with $\log\mathbf{SFE}$ ($\langle\rho\rangle\sim0.68$). Figure 3.10 shows how environments with higher average star formation efficiency exhibit

higher measured $C_\star$ values. A similar correlation is found for $\langle f_{\rm mol} \rangle$, which is shown in Supporting material 3.7.4 for completeness.

$\langle \tau / t_{\rm ff} \rangle$ and $\log \mathbf{AGE_{LW}}$ show hints of a mild correlation with $C_\star$ ($\langle \rho \rangle \sim 0.5$), but as discussed earlier, the first is expected as depletion time correspond to the inverse of SFE, and the second, if exists, is likely a consequence (rather than a cause) of differences in the star-forming process. None of the remaining parameters show hints of correlation with $C_\star$.

The poor level of correlation of $C_\star$ and $C_{\rm mol}$ with $\langle \log P_{\rm h} \rangle$ can be explained by the fact that $P_{\rm h}$ scales primarily with $\Sigma_{\rm mol}$ and $\Sigma_\star$. These dependencies are already captured by $C_\star$ and $C_{\rm mol}$, thus, $P_{\rm h}$ contributes little additional information.

Finding these correlations with physical conditions in a given galactic environment suggests that an additional parameter is indeed causing the variations we measure across galactic environments (and also can explain galaxy-to-galaxy variations), and thus, playing a relevant role in regulating the SFR. However, determining what is (or are) the key parameter(s) is beyond the scope of this chapter, as we would need a larger sample of galaxies that show a variety of galactic environments, and have, at the same time, high coverage of Hα and CO emission.

Finally, we stress here that due to the relatively low number of galaxies where we can reliably probe several galactic environments (8), and since each one of the correlations has only as many points as different environments the galaxy has, we can only speculate about the influence of an additional parameter in the coefficients of the star-forming plane, rather than robustly establishing a causal relation. Thus, we present this as a possible line of exploration, with intriguing dependencies that need confirmation with larger samples.

3.5.3 Choice of $\alpha_{\rm CO}$ conversion factor

We have tested our main conclusions against a constant $\alpha_{\rm CO}$ conversion factor of 4.35 $M_\odot$ pc^{-2} (K km s^{-1})$^{-1}$ (Bolatto et al., 2013), instead of the metallicity-dependent prescription (described in Sec. 5.2). We found that qualitatively, none of our conclusions are affected by our choice of $\alpha_{\rm CO}$. Figure 3.11 shows the posterior distributions of the coefficients determined at a spatial scale of 150 pc, under the assumption of a constant $\alpha_{\rm CO}$ conversion factor. It is easy to see that even though some specific coefficients may change, the relative difference between environments, and the relative predictive power of $C_\star$ and $C_{\rm mol}$ remains qualitatively the same.

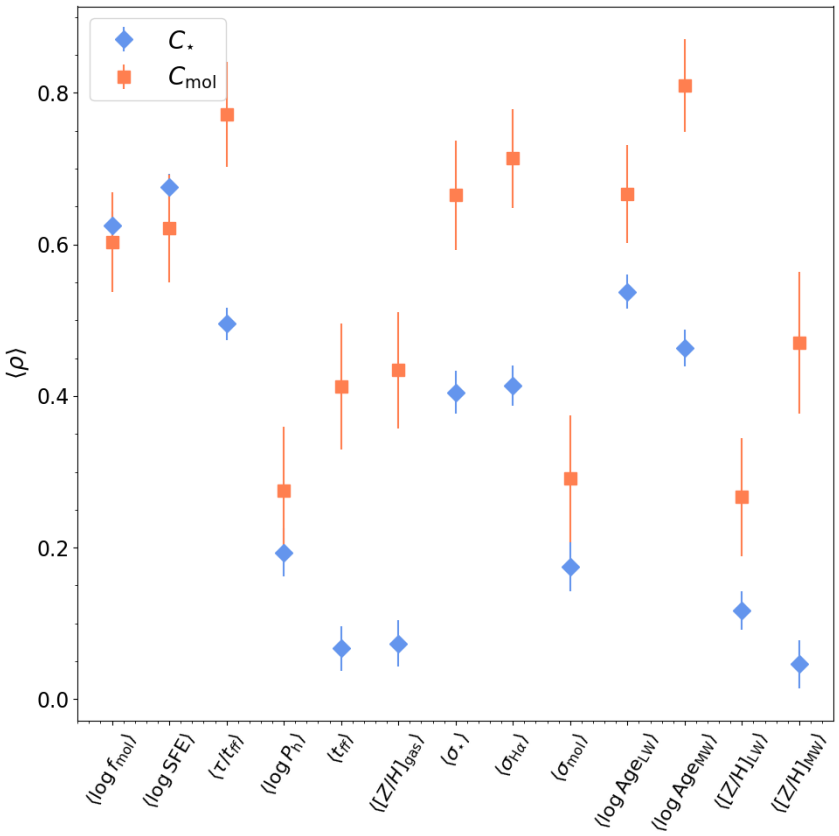

Figure 3.8: Overall Pearson coefficient to quantify the level of correlation between the $C_\star$ and C_{mol} parameters that define the star-forming plane in each environment, and the set of different parameters explored.

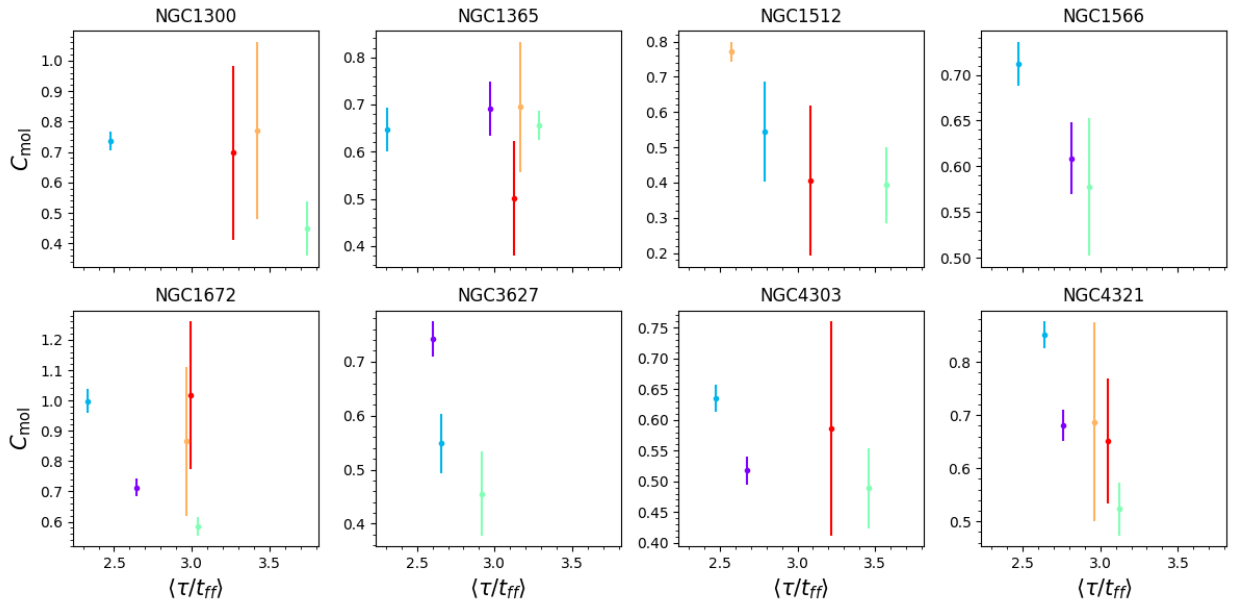

Figure 3.9: $C_{\rm mol}-\langle\tau/t_{\rm ff}\rangle$ correlation across different galactic environments, for the galaxies that satisfy our single-galaxy selection criteria. The color code for each environment is the same as used in Fig. 3.1.

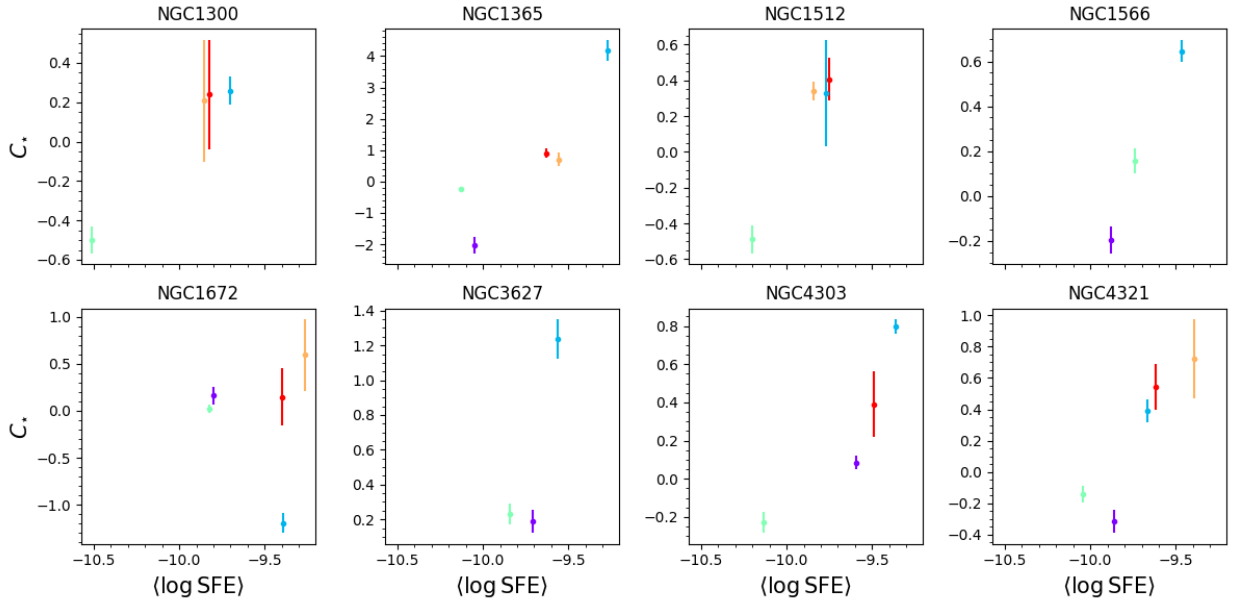

Figure 3.10: $C_\star-\langle\log\,{\rm SFE}\rangle$ correlation across different galactic environments, for the galaxies that satisfy our single-galaxy selection criteria. The color code for each environment is the same as used in Fig. 3.1.

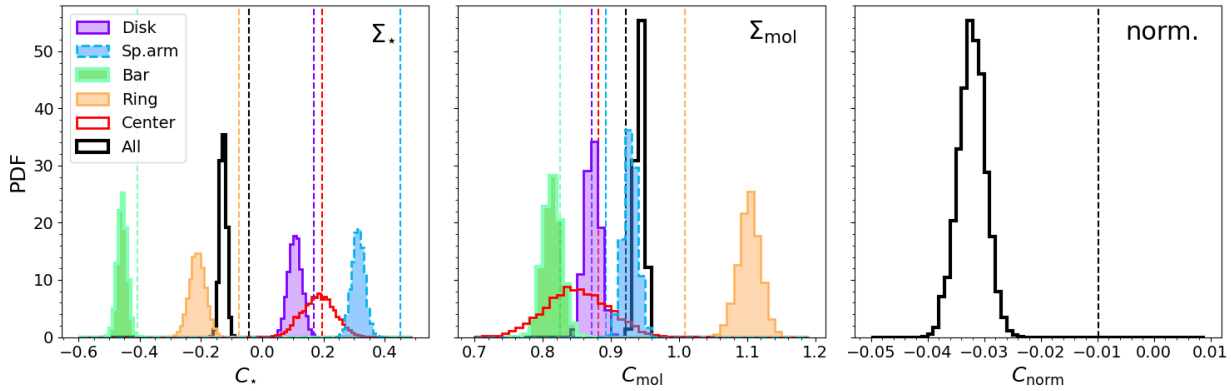

Figure 3.11: Posterior distributions for the coefficients $C_{\star}$, C_{mol} and C_{norm} that define the star-forming plane in each separate environment, using a constant α_{CO}. The vertical dashed lines show the centers of the posteriors distribution obtained under our fiducial choice of α_{CO}. As the posterior distribution of C_{norm} is considerably narrower than that of $C_{\star}$ and C_{mol}, the x-axis has been binned in smaller bins and renormalized for an easier visualization.

3.6 Summary

We have investigated the star-forming plane, conformed by $\Sigma_{\rm SFR}$, $\Sigma_\star$, and $\Sigma_{\rm mol}$ in 18 galaxies from the PHANGS sample at a physical resolution of 150 pc, and explored potential variations driven by galactic environment. Our main conclusions are as follows:

1. We found significant differences ($>1\sigma$) in the coefficients that describe the star-forming plane across galactic environments. These differences are particularly significant for bars, spiral arms and rings. We interpret these variations as evidence for an additional regulator mechanism that is not captured by neither $\Sigma_\star$ nor $\Sigma_{\rm mol}$.

2. These variations between environments homogenize toward lower spatial resolutions. Differences are no longer significant at spatial scales larger than $\sim$500 pc. This is because the combined effect of blending of environments at lower spatial resolutions, and the lower number of pixels per environment at large spatial scales.

3. We find a good agreement with similar measurements done using data from the ALMaQUEST survey. On the other hand, we find a moderate agreement with measurements reported using data from the EDGE–CALIFA sample. Differences with coarser resolution studies are not surprising, as our statistical framework is specifically designed to quantify differences that would be measurable at high spatial resolution only.

4. We used a subset of galaxies from our sample, where we can probe ($\geq$3) several galactic environments, and search for correlations between variations in the coefficients that define the star-forming plane in each environment, and the median of the distribution of a number of variables measured in those environments. We find a strong correlation of $C_{\rm mol}$ with depletion time and Hα velocity dispersion ($\langle\rho\rangle \sim 0.77$ and 0.72, respectively), which could be an imprint of longer depletion times driven by increased turbulent or radial motion in some galactic environments, leading to the environmental differences we observe for the star-forming plane.

Our results are consistent with the existence of additional physics being at play in the regulation of the star formation. However, a larger sample of galaxies where we can simulataneously probe different galactic environments is required to confirm the correlations explored in this work and, thus, to provide a definitive answer as to what is (or are) the additonal parameter(s) modulating the formation of stars.

3.7 Supporting material

3.7.1 Toy model to test the hierarchical fitting

In this section, we use a toy model to test the performance of the hierarchical fitting algorithm and also to explore the origin of the covariance between the parameters $C_\star$ and $C_{\rm mol}$. To this end, we define 20 data subsets, each one having 3000 randomly selected data points from our full data set ($\Sigma_\star$ and $\Sigma_{\rm mol}$). For each subset, a pair of $C_\star$ and $C_{\rm mol}$ is randomly generated from normal distributions centered at 0.5 and 1, respectively, with standard deviation of 1.

C_{norm} is fixed to the value measured in our data at 150 pc for all subsets, to replicate the procedure we used for our data. The three coefficients are then used to generate simulated Σ_{SFR} values for each subset separately. A scatter of $\sim$0.6 dex (comparable to that found in our data) is added to the simulated Σ_{SFR} values.

Once the data subsets are created, we use the hierarchical fitting routine to find the best set of $C_{\star}$ and C_{mol} to describe each subset, whereas C_{norm} is fitted for all subsets simultaneously. In this test, the hyperprior distributions used are $C_{\star,\mu} \sim \mathcal{N}(0.5, 1^2)$, $C_{\star,\sigma} \sim \mathcal{H}(1^2)$, $C_{mol,\mu} \sim \mathcal{N}(1, 1^2)$, $C_{mol,\sigma} \sim \mathcal{H}(1^2)$, $C_{norm,\mu} \sim \mathcal{N}(0, 2^2)$ and $C_{norm,\sigma} \sim \mathcal{H}(2^2)$.

Figure 3.12 shows the plane conformed by the posterior distributions obtained for $C_{\star}$ and C_{mol} for each data subset. The color code represents the posterior of C_{norm}. The black diamond marks the median of the posterior, whereas the blue square shows the real pair of $C_{\star}-C_{mol}$ used to generate each simulated data set. This test primarily demonstrates the accuracy of the hierarchical fitting, as in all cases the real values of the coefficients fall somewhere within the posterior distribution, typically within 1σ of the recovered one. Secondly, this test shows that the covariance between $C_{\star}$ and C_{mol} discussed in Sec. 3.4 is partially an artifact resulting from the fitting, as we recover it even though the real coefficients were chosen independently. However, we can not rule out that the covariance arises as a result of an intrinsic correlation between $\Sigma_{\star}$ and Σ_{mol}.

Nevertheless, this brings up the question of how many data points are required to break this covariance? And thus, how many galaxies would we require to break (or at least reduce) the covariance in the probed galactic environments?

Figure 3.3 provides some clues to these questions. It shows a larger covariance in the environments with fewer data points (centers) than in those environments probed with more pixels (disks and spiral arms), while the lowest covariance is seen in the full sample. Then, if we would aim to reduce the covariance of the measurement in rings or centers ($\sim$500 pixels) to the levels of spiral arms ($\sim$15,000 pixels), we would need a sample on the order of 30 times larger. However, if we restrict the observations exclusively to galaxies that show all different environments (such as NGC 1672 or NGC 4321), the number of additional galaxies would need to be about $\sim$12 times larger. However, this is only an estimation based on the area identified as ring or center in these two galaxies. The exact number will depend on the area occupied by these features in each galaxy.

3.7.2 Choice of detection fraction threshold

Through this chapter we adopt a detection fraction threshold of 60% to our data, which means that we confine our analysis to those $\Sigma_{\star}$ ranges in which we have a detection fraction of Σ_{SFR} and Σ_{mol} higher than this threshold (see Sec. 3.3.1 for a detailed description). Here we show how our results are influenced by the choice of detection fraction threshold.

Figure 3.13 shows the posterior distributions obtained for the coefficients $C_{\star}$ and C_{mol} under different assumptions of detection fraction threshold. The top panel shows the distributions obtained without applying any detection fraction threshold (i.e., using the full sample). The bottom panels show our fiducial adopted value (60%), 50%, and 70%.

Firstly, we note that the posteriors of nondisk environments only change slightly from using the full sample to applying a threshold of 60% in the detection fraction (first three rows). This is because at the 60% level, the fraction of pixels dropped from these environments is

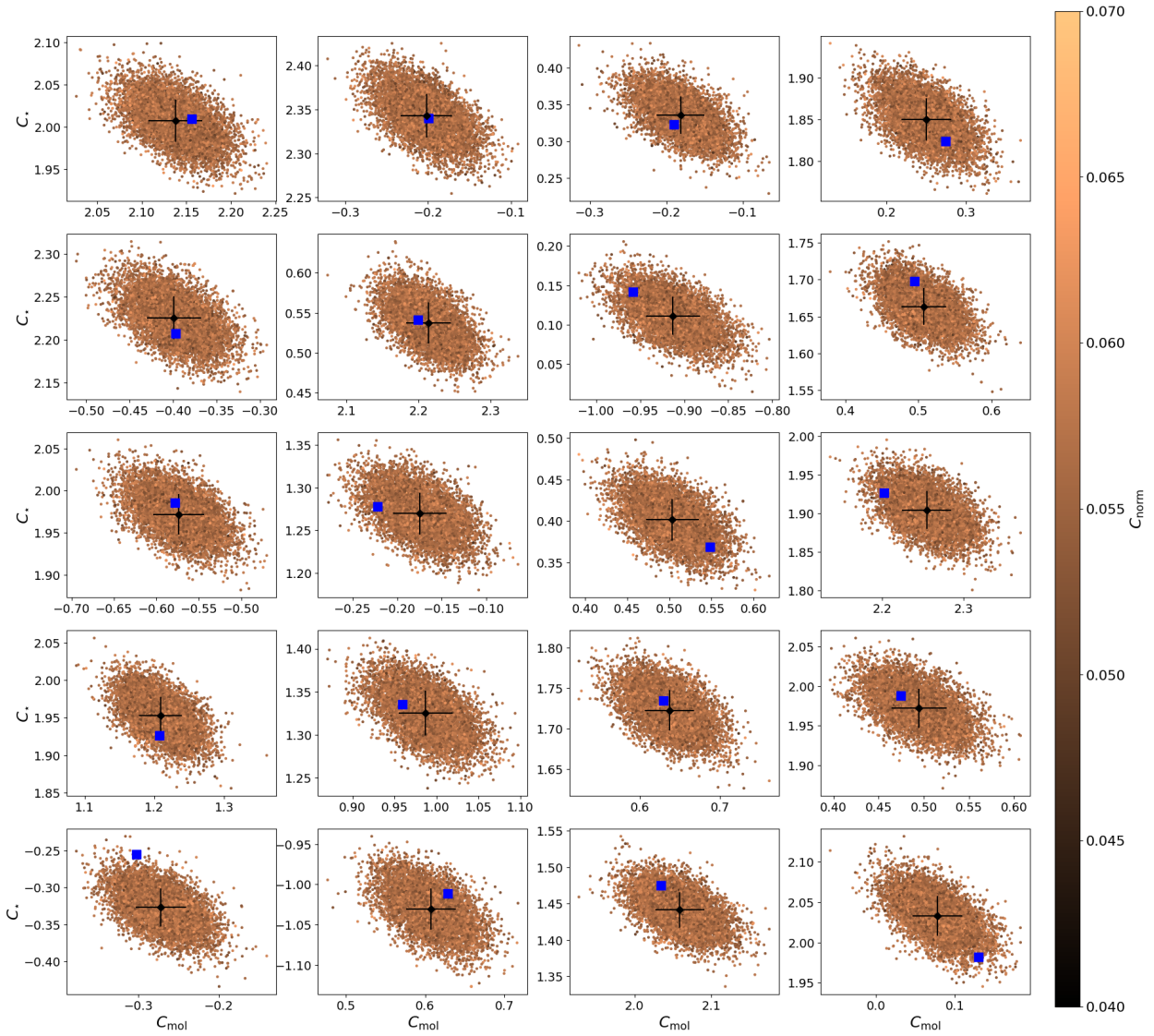

Figure 3.12: Results of the toy model fitting to test accuracy of the hierarchical fitting as well as origin of the $C_\star - C_{\rm mol}$ covariance. Each panel shows the posterior distribution obtained for a simulated data set. The black diamond and its error bar marks the median and 1-sigma of the posterior distribution. The blue square marks the real pair of $C_\star - C_{\rm mol}$ used to generate each simulated data set. The color code scales with the posterior value of $C_{\rm norm}$.

very small (<5%), as explained in Sec. 3.3.1. On the other hand, disks show a clear steepening of the $C_{\rm mol}$ slope in the same range of detection fraction. This behavior is consistent with the expected role of N/Ds in the measurement on the slope (Fig. 3.1).

We also note that only 5000 data points are lost when going from 50% to 60%, while going from 60% to 70% leads to drop ∼22,000 additional data points. Furthermore, at the 70% threshold level, the fraction of data points removed from spiral arms and rings rises to ∼11% and ∼35%, respectively. As a result of this higher number of dropped data points, and the significant truncation of the $\Sigma_\star$ range in which these environments are probed, their

posteriors change drastically at this detection fraction level, becoming unstable with respect to less strict threshold levels. Thus, we conclude here that a 60% threshold (fiducial value) provides a good balance between minimizing the impact of N/Ds on our analysis, and keeping the integrity of our data.

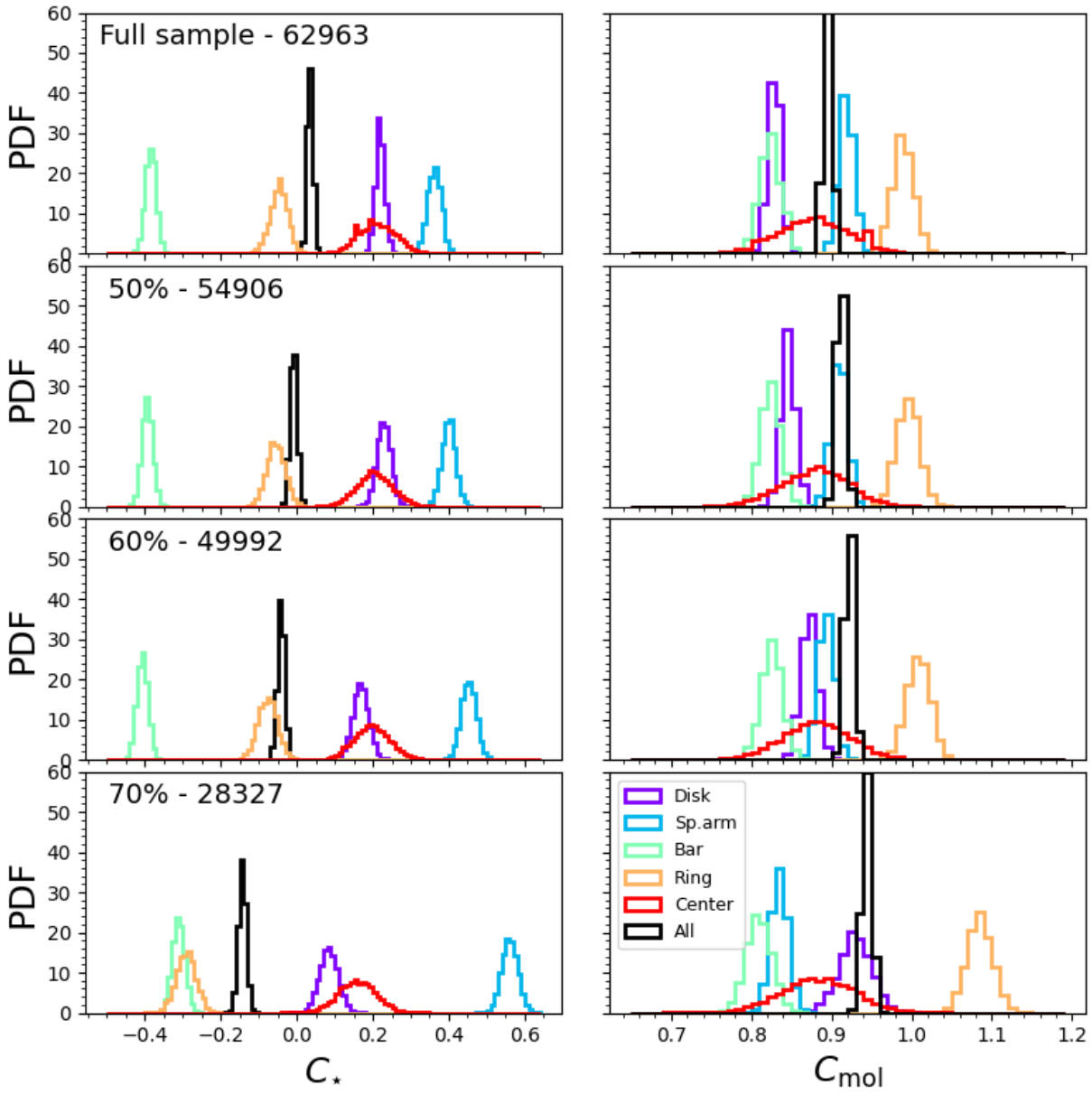

Figure 3.13: Posterior distributions obtained for the coefficients $C_{\star}$ and C_{mol}, following the same methodology described in Sec. 3.3.1, but applying different levels of detection fraction threshold. The top two panels show the base case scenario, using the full sample without applying any detection fraction threshold. The following panels show our fiducial adopted value (60%) and thresholds at 50% and 70%. The threshold level and the number of pixels used for each measurement are indicated in the top left corner for each row.

3.7.3 Global versus per-environment detection fraction threshold

In Sec. 3.3.1 we present our methodology to minimize the impact of N/Ds in the slope measurement, by restricting our analysis to the $\Sigma_\star$ in which each environment has a detection fraction higher than 60%. Here, we present our results under a slightly different approach. Instead of defining the used $\Sigma_\star$ range for each environment separately, we use the same $\Sigma_\star$ range for all environments, defined on the detection fraction of the full sample (black line in Fig. 3.1.)

As our full sample is statistically dominated by the disk environment, this implies that the $\Sigma_\star$ range at which the rest of the environments are probed is truncated to roughly match the $\Sigma_\star$ range in which disks satisfy the detection fraction threshold. In practice, this has an impact mainly in the sampling of spiral arms and rings, which due to their inherently higher detection fractions (Fig. 3.1), can be probed in a larger range of $\Sigma_\star$ values following our fiducial approach.

Figure 3.14 shows the obtained posterior distributions of the $C_\star$ and $C_{\rm mol}$ coefficients in each environment, for four different levels of detection fraction threshold (similar to Fig. 3.13). Due to the truncation of the $\Sigma_\star$ range, the posterior of the spiral arms becomes unstable, and highly dependant on the threshold level applied, reaching almost a value of $C_{\rm mol} \approx 1$ for a detection fraction threshold of 70%. Thus, we opt for a "dynamic" $\Sigma_\star$ range, chosen for each environment separately, as our fiducial approach.

We note that the total number of data points in the sample at this threshold is drastically increased with respect to the fiducial scenario. This is because additional data points from the disk environment are included in the sample (as the detection fraction of the full sample is slightly higher than that for the disk only), at the cost of excluding data points from other environments.

Nevertheless, we find that environmental differences, in terms of $C_\star$ and $C_{\rm mol}$, persist under this different methodology, and thus, qualitatively our conclusions are robust against this different treatment of our data.

3.7.4 Correlation of $\langle \sigma_{\rm H\alpha} \rangle$ and $\langle f_{\rm mol} \rangle$ with coefficients calculated in individual environments of single galaxies

Here we show the correlation between the $C_\star$ and $C_{\rm mol}$ coefficients derived for individual environments in single galaxies (see Sec. 3.5.2) and the second-highest Pearson coefficient parameters in Fig. 3.8. Figure 3.15 shows the $C_{\rm mol}$ calculated for each environment, as a function of the average $\sigma_{\rm H\alpha}$ within that environment, for each galaxy in the subsample defined in Sec. 3.5.2. This correlation could be an imprint of how the dynamical state of the gas might play role in regulating the level of local SFR.

For comparison, Fig. 3.16 shows the correlation between $C_\star$ and $\langle f_{\rm mol} \rangle$ for each environment, for the same galaxies. A positive correlation implies that environments with higher gas fractions also show typically lower depletion times.

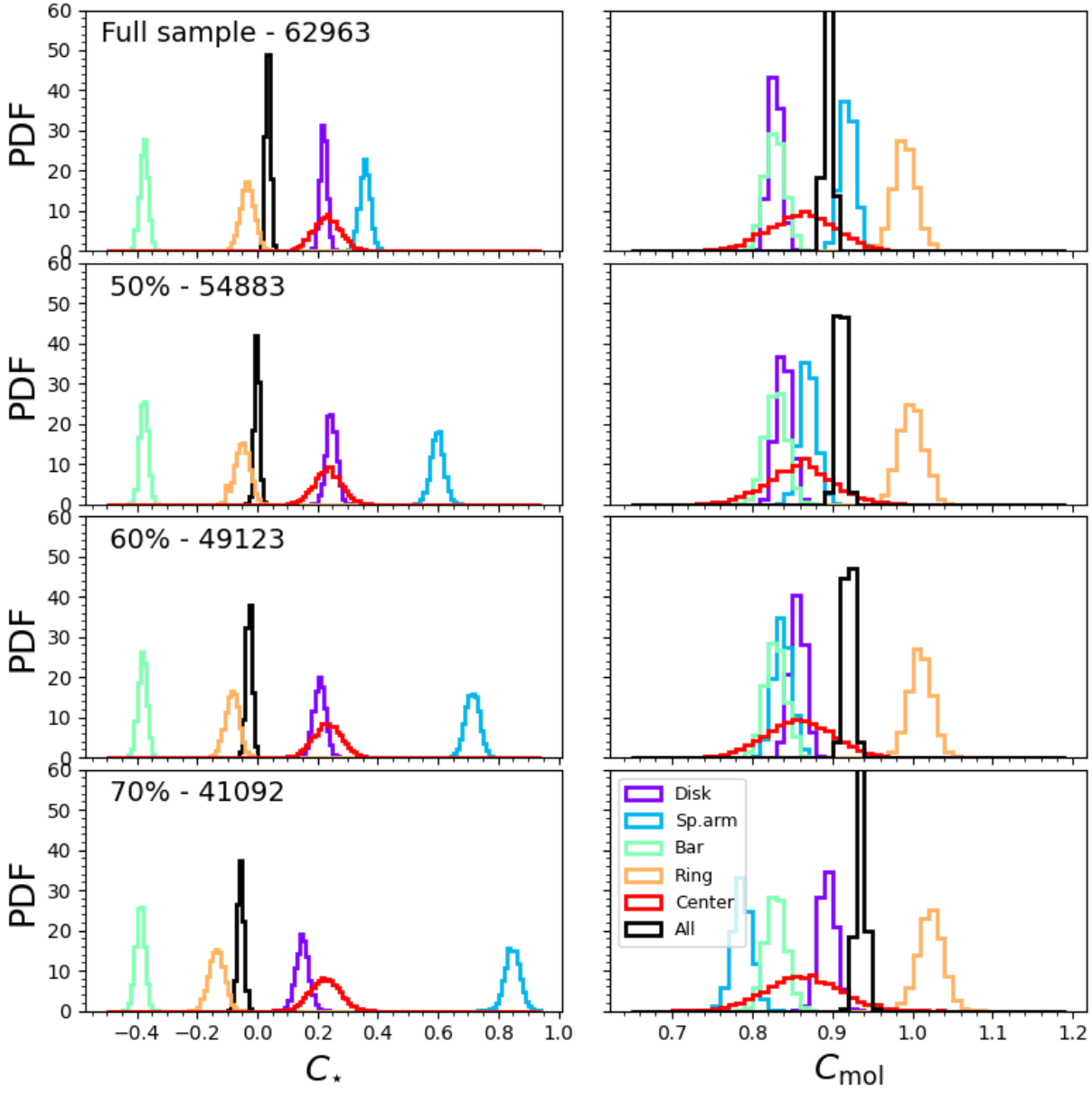

Figure 3.14: Posterior distributions obtained for the coefficients $C_{\star}$ and C_{mol}, restricting the $\Sigma_{\star}$ range of different galactic environments according to the detection fraction of the full sample, for different levels of detection fraction threshold. The top two panels shows the base case scenario, using the full sample without applying any detection fraction threshold. The following panels show our fiducial adopted value (60%) and thresholds at 50% and 70%. The threshold level and the number of pixels used for each measurement are indicated in the top left corner for each row.

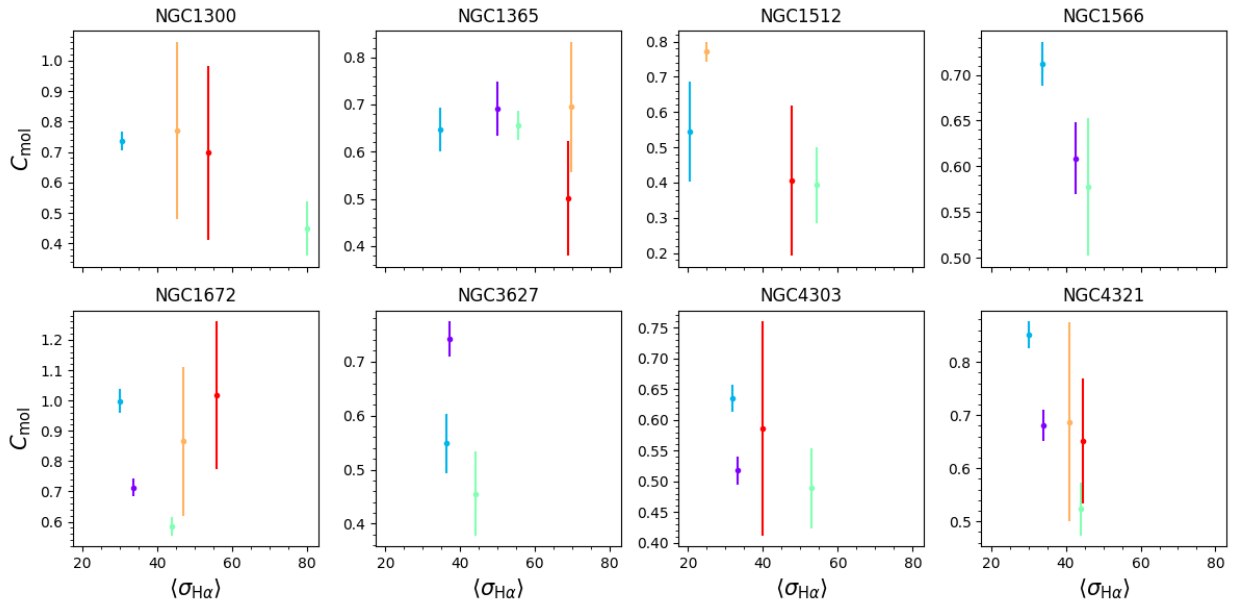

Figure 3.15: $C_{\rm mol}-\langle\sigma_{\rm H\alpha}\rangle$ correlation across different galactic environments, for the galaxies that satisfy our single-galaxy selection criteria. The color code for each environment is the same as used in Fig. 3.1.

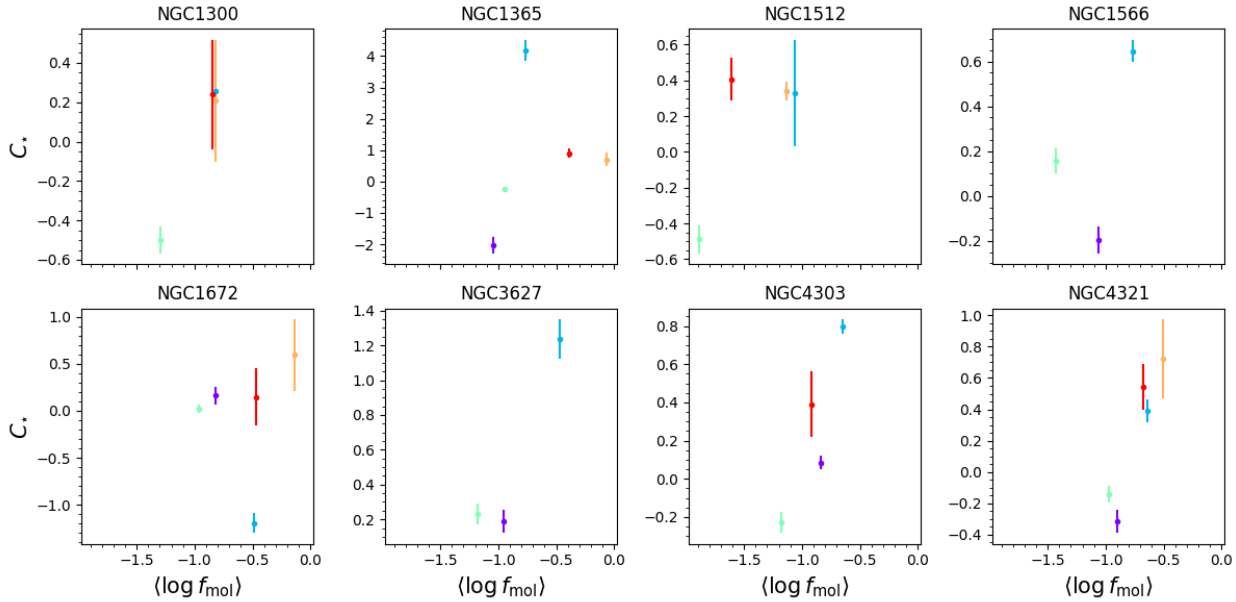

Figure 3.16: $C_\star-\langle f_{\rm mol}\rangle$ correlation across different galactic environments, for the galaxies that satisfy our single-galaxy selection criteria. The color code for each environment is the same as used in Fig. 3.1.

4 Single stellar population fitting

This chapter uses parts of the published article Emsellem et al. (2022) "The PHANGS-MUSE survey. Probing the chemo-dynamical evolution of disc galaxies", of which I am coauthor. Parts of this chapter will be published in a future refereed article (Pessa 2022, in prep.), which is still in progress.

4.1 Introduction

Galaxies are complex entities whose different components, such as stars, different phases of the interstellar gas, or active galactic nuclei (AGN), emit electromagnetic radiation across the full wavelength range, from X-rays to radio. A prime tracer of the physical processes acting in galaxies is the integrated spectral energy distribution (or SED), directly revealing their imprints via radiation (Walcher et al., 2011).

In the wavelength range where stellar light dominates (ultraviolet (UV) to infrared (IR)), the observed spectra of galaxies can be represented as a linear combination of the spectra of single stellar populations (SSPs) attenuated by the presence of dust (plus the emission of the ionized gas), where a single stellar population is a group of stars that were born from the same molecular cloud, hence, sharing the same age and chemical properties (Tinsley, 1980). Thus, the combination of SSPs that is able to reproduce the observed SED of a galaxy is essentially reflecting the star formation history (SFH) that the galaxy has undergone through its life. The study of the SFHs of galaxies through the determination of the properties of their stellar populations is also known as full spectrum fitting or fossil record method (Tinsley, 1968).

Many codes have been developed to address this problem, such as MOPED (Heavens et al., 2000), STARLIGHT (Cid Fernandes et al., 2005), pPXF (Cappellari & Emsellem, 2004a), STECKMAP (Ocvirk et al., 2006), VESPA (Tojeiro et al., 2007), and ULySS (Koleva et al., 2009). Overall, the fossil record method can be essentially implemented in two different ways; parametric, in which one adopts a specific functional form for the SFH, and that offers the advantage of producing an easily interpretable output, and non-parametric, in which the SFH is defined as a a number of bursts of star-formation, where each burst is represented by a SSP model with known properties (i.e., age, metallicity). This latter approach has the flexibility to reproduce with more detail spectral features, but its output is harder to interpret than in the parametric approach (Sánchez, 2020).

A drawback of the full spectrum fitting technique that it relies heavily on the ingredients assumed to synthesize the single stellar populations models, this is, stellar libraries, stellar evolution models (a.k.a. isochrones), and the assumed initial mass function (IMF) (Walcher et al., 2011; Martins, 2021). Furthermore, different codes used to fit the observed spectrum might also lead to systematic differences in the results (e.g., Magris C. et al., 2015; San Roman et al., 2019), while providing equally good fits. These differences arise partly due to the degeneracies existing between the involved parameters (i.e., age, metallicity, dust content; see, e.g., de Meulenaer et al., 2013). Systematic differences are stronger when fitting the spectra of blue late-type galaxies (LTGs) than for quiescent early-type galaxies (ETGs) (Magris C. et al., 2015), since LTGs have more complicated SFHs, exhibiting young stellar populations that outshine older stars. Moreover, not only the fitting of whole LTGs presents difficulties. The fitting of young regions at smaller-scales has also proven to be a challenge (e.g., Carrillo et al., 2020; Bittner et al., 2020). This is likely due to a combination of factors such as template mismatch, existing degeneracies, nebular line and continuum emission contribution, and the fact that recently formed stars are likely under different physical conditions (e.g., higher extinction values, see, e.g., Messa et al., 2021).

Despite its limitations, this method has proven to be an extremely powerful tool to interpret the integrated SED of galaxies, where we can not resolve individual stars, and ultimately unveil the assembly history of galaxies (e.g., Wilkinson et al., 2015; López Fernández et al., 2018; Zhuang et al., 2019; Neumann et al., 2020). For this reason, we have implemented a full spectrum fitting module to compute the SFHs of galaxies from the PHANGS-MUSE survey (Emsellem et al., 2022), as part of the PHANGS-MUSE data analysis pipeline (DAP; Emsellem et al., 2022). This module has been developed with the goal to address targets observed with MUSE at a spatial resolution on the order of ~ 100 pc, sufficient to resolve galactic morphological features, such as rings or spiral arms, with typical widths of a few hundred parsecs (Querejeta et al., 2021). In this chapter, we describe in detail the implementation of the DAP, with special emphasis on the full spectral fitting approach adopted to compute reliable SFHs, and the quality assessment of the data products yielded by our approach.

This chapter is structured as follows: In Sec. 4.2 we describe the requirements and the steps of the DAP. In Sec. 4.3 we present a quality assessment of the data products yielded by the full spectral fitting. In Sec. 4.4, we describe our approach to further improve the fitting of regions dominated by young stellar populations. Finally, we present the summary and conclusions of this work in Sec. 4.5.

4.2 PHANGS-MUSE Data Analysis Pipeline

The aim of the data analysis pipeline for PHANGS-MUSE is to generate high-level data products (i.e., fluxes, kinematics etc) for both, the stellar continuum and the ionized gas emission lines. Several software tools have been developed to this aim in recent years, especially to process the data associated with large IFU surveys: CALIFA, MaNGA, SAMI and TIMER. An incomplete list of notable tools used for processing data from large surveys includes Pipe3D (Sánchez et al., 2016a,b), the MaNGA data analysis pipeline (Belfiore et al., 2019; Westfall et al., 2019), LZIFU (Ho et al., 2016) and `gist` (Bittner et al., 2019).

In order to analyse the PHANGS-MUSE data we sought a software framework, which

would:

- integrate an adaptive spatial binning scheme, leading to a robust measurement of the targeted observable quantities;
- perform a well-tested and robust extraction of physical quantities, including gas and stellar kinematics, and stellar population properties;
- parallelize the spectral fitting step over multiple cores, in order to allow for efficient processing of $\sim 10^6$ spectra (possibly several times, when iterating over subsequent data releases);
- be sufficiently modular to allow us to implement changes and/or replace individual modules, without affecting the structure of the code;
- support the analysis of IFU data sets from other instruments and surveys, in order to allow direct comparisons with publicly available high-level products, and therefore benchmark the output of our code against best practices in the field.

We judged these requirements to correspond closely to the philosophy behind the `gist` code[10] (Bittner et al., 2019), which has a module-based structure and supports parallelization for the fitting stages. We therefore adopted `gist` as the starting point for our pipeline environment.

The modular structure of `gist` allowed us to easily replace several of its constituent modules with algorithms more closely aligned to our goals with PHANGS-MUSE. In particular, with respect to the public implementation of `gist`, we have made changes to virtually every module, and replaced the emission line spectral fitting and the stellar population analysis routines with ones written by members of our team (F. Belfiore and I. Pessa). The version of the code used for the analysis of PHANG-MUSE has been made publicly available.[11]

Our pipeline implementation, which we refer to as `DAP` is described in detail in the next subsections. Several of these pipeline-level software tools share core pieces of software to perform spatial binning and spectral fitting. Two such modules stand out for their wide applicability: `vorbin` (Cappellari & Copin, 2003b), and `pPXF` (Cappellari & Emsellem, 2004b). These were originally developed for the pioneering IFU work performed as part of the SAURON/ATLAS^{3D} surveys (de Zeeuw et al., 2002; Cappellari et al., 2011), and subsequently updated and upgraded (Cappellari, 2017b). They address the key tasks of binning 2D data to reach a specific S/N level, and to fit the stellar continuum, and optionally, the gas emission lines, with a non-negative linear combination of templates. Below we briefly described these modules.

`vorbin` – This is a robust and broadly used package to adaptively bin datacubes along the two spatial dimensions. The method uses Voronoi tesselations (Cappellari & Copin, 2003b), an optimal solution being found via an iterative process constrained by a given parameter representing the targeted signal to noise. For the present data sets, we used the estimate of the signal-to-noise ratio in a given wavelength range per spaxel as direct input.

[10] https://abittner.gitlab.io/thegistpipeline
[11] https://gitlab.com/francbelf/ifu-pipeline

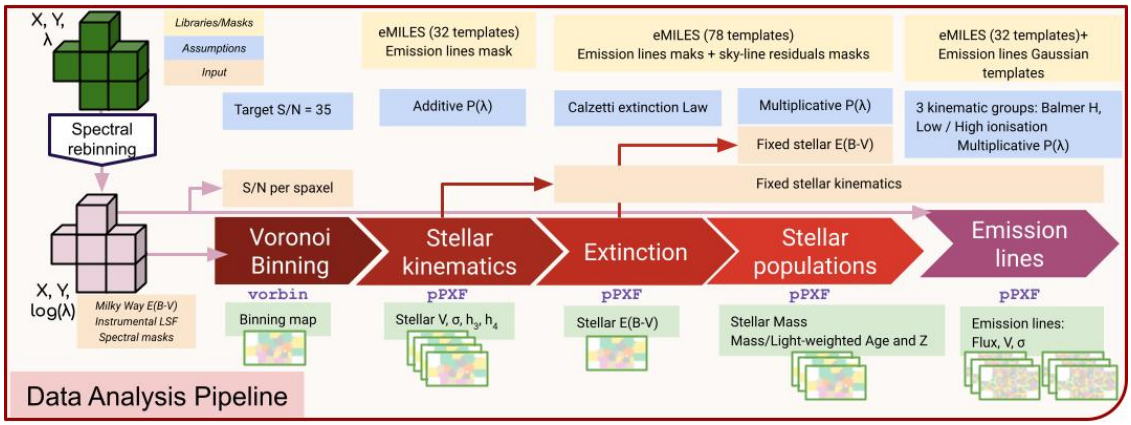

Figure 4.1: Analysis flow for the PHANGS Data Analysis Pipeline (DAP). After spectral rebinning using a ln(λ) prescription, the resulting mosaicked cubes are used to obtain stellar kinematics, stellar extinction, and stellar population maps, using an appropriate adaptive binning scheme, while the emission line maps (including the corresponding gas kinematics) are derived from the originally sampled cubes. The main information pertaining to the stellar libraries, spectral masks, assumptions and fixed input for each step are mentioned in the upper part of the figure, while the data products are illustrated in its lower part. See Sect. 4.2.1 for further details.

pPXF – The extraction of the stellar and gas kinematics, and information pertaining to the stellar population content of spectra, has been popularized via a set of excellent pieces of software which exploit spectral features in various ways. pPXF (Cappellari & Emsellem, 2004b; Cappellari, 2017b) is an intensively-tested and robust algorithm to perform direct pixel fitting of spectra making use of spectral template libraries. The generic fitting module of pPXF is extremely flexible and supports a wide range of applications, including the simultaneous fitting of absorption and emission lines and the extraction of non-parametric star formation histories, with the possibility to add multiple kinematic components and generic constraints (e.g., line flux ratios). The DAP consists of several modules wrapping pPXF for specific applications.

4.2.1 The data analysis flow

In this section, we describe the analysis flow developed within the DAP going from the preparatory to the main computational steps delivering specific data products. The DAP workflow consists of a set of modules running in series, some depending on the outcome of previous steps (e.g., derivation of the stellar kinematics is needed as input to the emission lines fitting module). Fig. 4.1 contains a schematic representation of DAP, including the main input and output parameters, libraries and constraints. Each of the individual DAP modules writes to disk a set of intermediate output files, which can be useful to re-run specific modules in case of a failure, and also contains a more extensive set of outputs which may be of interest for specialized analysis. The key set of physical parameters produced by the DAP are then consolidated into a main output file, described in Sec. 4.2.1.

Preparatory steps

The DAP requires as input a configuration file, which specifies certain pipeline parameters, the location of the input IFU data, the galaxy's redshift (or systemic velocity), and the Galactic extinction at its position.

The data are read via a bespoke input module, which is instrument-specific (tailored to MUSE in our case), but may be replaced in order to process data from different instruments. By appropriately changing the parameters in the configuration files and writing a new input module, users can easily process data from other surveys. For PHANGS-MUSE, we utilize a common data input model for both the WFM-NOAO and WFM-AO observations. The wavelength range corresponding to the AO gap is automatically masked in the case of AO observations. This mask is propagated by the DAP. We assume the line-spread function (LSF) given by a Gaussian profile whose FWHM changes as a function of wavelength, following Bacon et al. (2017). The systemic velocity of each galaxy is taken from Lang et al. (2020), who derived these from an analysis of the PHANGS-ALMA CO(2–1) kinematic maps. The MUSE data is corrected for foreground Galactic extinction, using the Cardelli et al. (1989) extinction law and the $E(B-V)$ values from Schlafly & Finkbeiner (2011).

Since we chose to produce fully-reduced MUSE datacubes on a linear wavelength axis,[12] we perform a resampling of the data on a logarithmic (natural log) wavelength axis, as required for input to DAP using a channel size of 50 km s^{-1}. This channel size is sufficient to Nyquist sample the LSF of the MUSE data with more than two pixels for $\lambda < 7000$ Å, but inevitably oversamples it at the blue edge of the MUSE wavelength range. As discussed further below, we fit the wavelength range 4850−7000 Å in order to avoid strong sky residuals in the redder part of the MUSE wavelength range.

Spatial binning

As extensively discussed in the literature, an accurate and unbiased determination of the stellar kinematics and stellar population properties from full spectral fitting requires a minimum signal-to-noise (S/N) ratio (Johansson et al., 2012; Westfall et al., 2019). In the DAP the continuum S/N is computed in the 5300−5500 Å wavelength range, using the noise vector provided by the reduction pipeline.

The data are then Voronoi binned to a target S/N of 35 making use of `vorbin`. This S/N level is used to determine both the stellar kinematics and the stellar population properties. The value of 35 was chosen to ensure that the relative uncertainty in the stellar mass measurement, which we estimated via Monte Carlo realizations of the errors (see Sect. 4.2.1 below), stays below 15%. For comparison, the MaNGA data is rebinned to a S/N = 10 to determine the stellar kinematics by the publicly-available run of the data analysis pipeline (Westfall et al., 2019). We opted for a higher S/N threshold for two reasons: a) we aimed to keep the same Voronoi bins for both the stellar kinematics analysis and the determination of stellar population properties via full spectral fitting, which generally require higher S/N, b) a S/N target of 35 still generated bins which are generally of small size, comparable with

[12] Note that the MUSE DRS allows one to reduce the data on a logarithmically-sampled wavelength axis when needed, which would save one rebinning step in the spectral fitting process. Our team, however, decided to maintain the default linear sampling which has been used for most existing MUSE data published in the literature to this date.

the scale of the PSF, except for the edges of the maps where bins can be significantly larger.

The large size of our MUSE mosaics, well beyond the size of images intended for use with the `vorbin` package by their authors, meant that we had to limit the size of an optimization loop in the `vorbin` code in order to ensure convergence. When calculating the errors for the binned spectra, we assume the MUSE spaxels to be independent. This is not strictly correct, because of the inevitable resampling of the raw data in the datacube-generation process. In short, spaxels nearly congruent with a single detector pixel will have almost no covariance, while spaxels whose flux originates from several pixels at the detector level will have errors which are strongly correlated with their nearest neighbours (see Sec. 4.6 of Weilbacher et al., 2020). In our native datacubes, this effect is visible as weak horizontal and vertical bands (the two orientations are due to the set of 90 deg rotations we perform) in the noise maps. An example map of the average noise vector and the resulting S/N distribution in the 5300−5500 Å wavelength range are shown in Fig. 4.2. The striping pattern we are referring to should not be confused with the much more evident change in the noise properties of the data in the overlap region of the different MUSE pointings, which corresponds to a real reduction in the noise due to longer effective exposure times. Within mosaics where one pointing consists of fewer than the nominal four exposures (e.g., because one exposure was discarded for quality control reasons) the noise is also consequently higher.

In Fig. 4.2, we also show the resulting Voronoi binning map, demonstrating that the small-scale noise striping pattern does not have a visible effect on the resulting Voronoi bins. In this work, we therefore neglect the issue of small-scale spatial covariance in the MUSE data.

The `DAP` supports the determination of emission line properties for two different binning schemes: either the same Voronoi bins as the stellar kinematics, or for single spaxels. For the PHANGS-MUSE data release, the emission line properties are derived for single spaxels because the Hα emission is detected at the single-spaxel level across most maps.

We have also tested the pipeline with different binning schemes. Two such implementations, optimized for the study of H II regions and the diffuse ionized gas respectively, are discussed in Santoro et al. (2022) and Belfiore et al. (2022).

Stellar kinematics

The stellar kinematics are derived using `pPXF`, following the same procedure as implemented by Bittner et al. (2019) in `gist`. Briefly, to fit the stellar continuum we use E-MILES simple stellar population models (Vazdekis et al., 2016), generated with a Chabrier (2003) initial mass function, BaSTI isochrones (Pietrinferni et al., 2004), eight ages (0.15−14 Gyr, logarithmically spaced in steps of 0.22 dex) and four metallicities ($[\mathbf{Z/H}] = [-1.5, -0.35, 0.06, 0.4]$), for a total of 32 templates. We fit the wavelength range 4850−7000 Å in order to avoid strong sky residuals in the redder part of the MUSE wavelength range. The regions around the expected positions of ionized gas emission lines are masked. The mask width is taken to be ±400 kms of the systemic velocity of the galaxy. This mask width is found to be appropriate for the range of velocities and dispersions present in the PHANGS data. In MUSE-NOAO observations the region around the Na I D absorption doublet is also masked, because of the potential ISM contribution. Finally, we mask the region around the bright sky lines at the observed wavelengths of 5577, 6300 and 6363 Å.

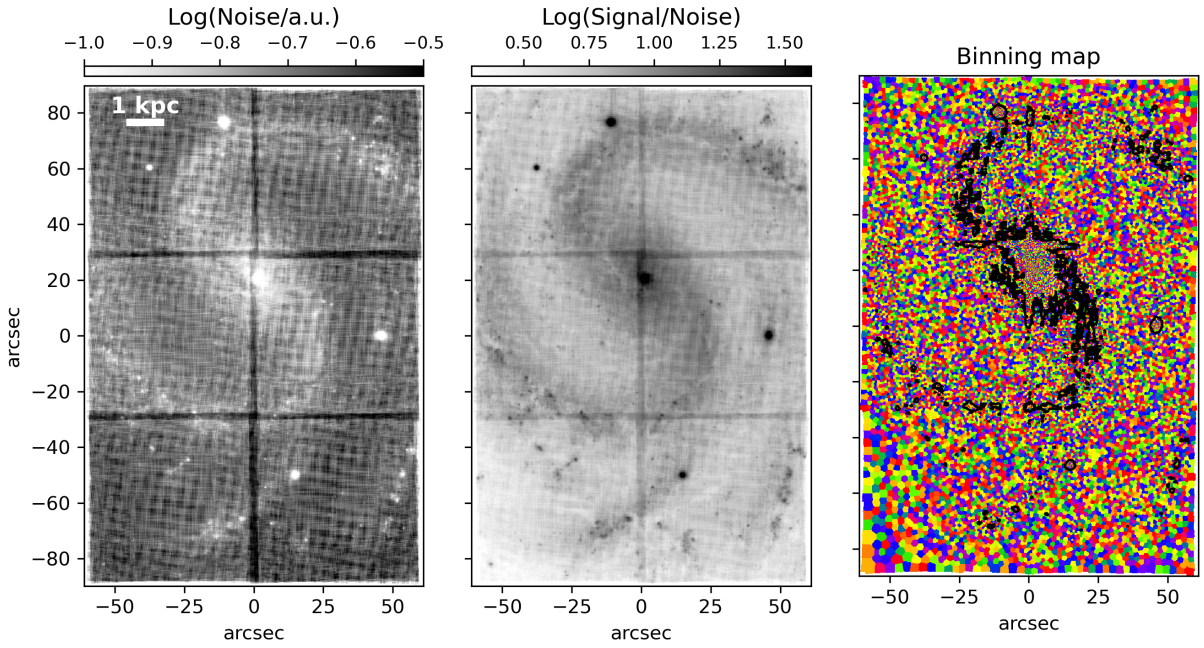

Figure 4.2: Maps of the average noise (left panel), Signal/Noise (middle panel) and binning map (right panel) for NGC 4535. The noise and signal/noise maps are computed by averaging the pipeline noise and flux over the 5300−5500 Å wavelength range. The stripes dividing the surveyed area into six squared subregions correspond to the overlap regions of the six MUSE pointings obtained for this galaxy. The noise map also shows an evident cross-hatch pattern within individual pointings, due to the cube-generating resampling step in the MUSE data reduction pipeline when combining exposures with different rotation angles. This behaviour is also visible in the S/N map, but does not significantly affect the results of the binning process. The binning map shows the result of the Voronoi binning procedure with target S/N = 35. The black contour shows the S/N = 12 level on individual spaxels. In this target only the galaxy center (and a few foreground stars) have S/N > 35 in individual spaxels, which are therefore left unbinned.

The spectral resolution of E-MILES[13] is higher than that of the MUSE data within the wavelength range we are considering, although at ∼7000 Å E-MILES is expected to have virtually the same spectral resolution as MUSE. The templates are therefore convolved to the spectral resolution of the data, using an appropriate wavelength-dependent kernel. No convolution of the data is performed where the E-MILES resolution is worse than or comparable to that of the MUSE data (beyond about 7000 Å). Velocities are computed with respect to the systemic velocity of the galaxy. We fitted four moments of the line-of-sight velocity distribution (i.e., velocity, velocity dispersion, $h3$ and $h4$). To derive the stellar kinematics we make use of additive Legendre polynomials (12^{th} order, in the spectral direction), and no multiplicative polynomials. Polynomials are found to be advantageous in the derivation of stellar kinematics with `pPXF` (Westfall et al., 2019); the choice between additive and multiplicative is purely dictated by computing efficiency in this step.

[13]Taken from
http://www.iac.es/proyecto/miles/pages/spectral-energy-distributions-seds/e-miles.php

The code is able to perform an MCMC-based error estimate for kinematic parameters (a feature inherited from `gist`), but this step was not performed for the current data release. The errors reported for the kinematic parameters are therefore formal errors, as given by `pPXF`.

Stellar populations

The stellar population module also employs `pPXF` in a sequence of steps optimized for use with our MUSE data. We do not use the original `gist` code for this module, because we moved away from 'regularization', as explained below. The stellar population analysis is performed on the Voronoi-binned data, i.e., the same spectra used for the stellar kinematics determination.

As in the derivation of stellar kinematics, we used E-MILES stellar population models, but we increased the number of templates to 78, with ages = [0.03, 0.05, 0.08, 0.15, 0.25, 0.40, 0.60, 1.0, 1.75, 3.0, 5.0, 8.5, 13.5] Gyr and [Z/H] = [−1.49, −0.96, −0.35, +0.06, +0.26, +0.4]. We fit the same wavelength range as used for the stellar kinematics determination. We retain the previously-derived stellar kinematics parameters by fixing them in the `pPXF` fit, and mask the regions around emission lines, as in Sec. 4.2.1. Additionally, we mask further regions of the spectrum particularly affected by sky line residuals (wavelengths within ranges [5861.08−5911.74], [6528.80−6585.08] and [6820.00−6990.90] Å).

The fit is performed in two stages. In the first stage we determine the extinction of the stellar continuum, as parametrized by a Calzetti (2001) extinction curve. In the second iteration the stellar extinction is kept fixed, and multiplicative polynomials of 12^{th} order, with a mean of one, are used to correct for residual inaccuracies in the relative flux calibration. This two-tiered procedure was demonstrated to be necessary to overcome inaccuracies in the sky continuum subtraction, which can cause subtle changes in the spectral shape. To the best of our knowledge, such residuals do not have a large effect on the derived stellar population properties, except for the $E(B-V)$ of the stellar component, as discussed in Sec. 4.3.1. Additive polynomials cannot be used as they both modify the absorption line equivalent widths and affect our measurements of stellar mass surface density.

Given the degeneracy that exists in spectral fitting (i.e., between attenuation, metallicity, and age), the use of regularization (i.e., along metallicity and age axes) when trying to recover star formation histories has been promoted for certain situations (e.g., Cappellari, 2017b). Given the average spatial resolution of ∼50 pc, our data resolve individual star-forming regions with significant contributions from very young stars, resulting in strong variations in the spatial distribution of stellar ages across the galactic disks. Extensive tests showed that forcing a fixed level of regularization on our data set leads to star formation histories with strong biases, that themselves vary strongly from region to region and are difficult to control. While we could envision a scheme to provide a more controlled bias, this is beyond the scope of the present release. We therefore decided to rely on Monte Carlo simulations to estimate the uncertainty in the recovered stellar population parameters, and use unregularized fitting. For each spectrum, we performed 20 Monte Carlo iterations. In each iteration, we add to the input spectrum Gaussian noise with a mean of zero and a standard deviation corresponding to the error vector at each wavelength bin. The uncertainties of stellar population parameters are calculated as the standard deviation of their distributions produced by the Monte Carlo realizations. This is meant as a first-order estimate of the true

uncertainties. We only run Monte Carlo realizations during the second step of the fitting procedure, once the stellar extinction has been fixed. Hence, no error is computed for the stellar $E(B-V)$. The output of `pPXF` is a vector with the weights of the templates that, when linearly combined, best reproduce the observed spectrum. These weights represent the fraction of the total stellar mass born with a given age and metallicity, and they can be used to produce the final maps, including stellar mass surface densities, and both light- or mass-weighted ages and metallicities. The stellar mass surface density maps include both, the contributions from live stars and remnants. For each pixel, the average age and metallicity are computed as:

$$\langle \log \mathrm{age} \rangle = \frac{\Sigma_i \log(\mathrm{age}_i)\, w_i}{\Sigma_i\, w_i} \tag{4.1}$$

and

$$\langle [\mathrm{Z/H}] \rangle = \frac{\Sigma_i\, [\mathrm{Z/H}]_i\, w_i}{\Sigma_i\, w_i} \ , \tag{4.2}$$

where age_i and $[\mathrm{Z/H}]_i$ correspond to the age and metallicity of each template, and w_i is its corresponding weight in the linear combination. To convert mass-weighted quantities to light-weighted quantities, we use the mass-to-light ratio of each template in the V-band. We compute luminosity-fraction weights as:

$$w_i^{\mathrm{LW}} = \frac{w_i}{(M/L_V)_i} \ , \tag{4.3}$$

where w_i^{LW} corresponds to the luminosity-fraction weight of a given template, w_i its mass-fraction weight, and $(M/L_V)_i$ correspond to its mass-to-light ratio in the V-band. We can use these luminosity-fraction weights to calculate light-weighted properties, following Equations 5.1 and 5.2. It is possible to use the stellar population weights we derive to produce maps of, e.g., stellar mass in different age ranges (e.g., young, intermediate and old stars), or to study the age/metallicity relation within individual regions.

Emission lines

Emission lines are fitted by performing an independent call to `pPXF`, where emission lines are treated as additional Gaussian templates, and the stellar continuum is fitted simultaneously. We do not use the module provided with `gist`, based on the `gandalf` implementation (Sarzi et al., 2006). This choice mirrors the philosophy of the MaNGA data analysis pipeline, and is motivated by the greater flexibility of the `pPXF` implementation and the extensive testing and experience documented in Belfiore et al. (2019) and Westfall et al. (2019). Some of the code we use to interface with `pPXF` in this fitting stage was adapted directly from the MaNGA data analysis pipeline, and makes use of the analytical Fourier transform implemented in version higher than 6 of `pPXF` (Cappellari, 2017b).

The fits are performed on individual spaxels, fixing the stellar velocity moments to the values obtained during the stellar kinematics fitting step within the associated Voronoi bin (Sec. 4.2.1). We have tested the effect of leaving the stellar kinematics free and find largely identical results for spaxels with large S/N in the continuum. We use the same set of 32

stellar templates as in Sec. 4.2.1.

The kinematic parameters of the emission lines (velocity and velocity dispersion) are tied in three groups, as follows:

1. Hydrogen Balmer lines: Hα, Hβ;
2. Low-ionization lines: [O I]$\lambda\lambda$6300,64, [N I]$\lambda\lambda$5197,5200, [N II]$\lambda\lambda$6548,84, [N II]λ5754, [S II]$\lambda\lambda$6717,31;
3. High-ionization lines: [He I]λ5875, [O III]$\lambda\lambda$4959,5007, [S III]λ6312.

We tie the intrinsic (astrophysical) velocity dispersion within each kinematic group, prior to convolution with the instrumental LSF. The measured velocity dispersion of lines belonging to the same kinematic group is therefore different, but the difference is that required to bring the intrinsic velocity dispersion into agreement, given the assumed LSF. Because the MUSE LSF changes with wavelength, this is an important effect to take into account.

Initial testing showed that the kinematics of the [O III] line is sufficiently different from that of the Balmer lines to require an independent kinematic component. On the other hand, we found that leaving the kinematics of the Hβ line free generates a large number of nonphysical Balmer decrements (Hα/Hβ) at low S/N ratios. The definition of a third group of low-ionization metal lines may support specific science cases focusing on the diffuse ionized gas, where such low-ionization lines are prevalent with respect to the hydrogen Balmer lines. Alternative tying strategies can be trivially implemented by changing simple keywords in a configuration file of the `DAP`.

During the emission lines fit, `pPXF` is run with 8$^{\text{th}}$ order multiplicative Legendre polynomials, but no additive polynomials (polynomials are only applied to the stellar continuum templates). The use of additive polynomials would be inappropriate in this fitting stage as they modify the equivalent width of the Balmer absorption lines, and therefore potentially introduce non-physical corrections to the hydrogen Balmer line fluxes. The use of a different set of polynomials for this fitting stage with respect to the stellar kinematics fitting stage, in addition to the different S/N of the continuum (going from bins to single spaxels) and the absence of a mask in the wavelength regions around emission lines contribute to creating subtle differences in the best-fit continua generated in the two, complementary fitting stages. The effects of the different polynomials treatment and of masking versus simultaneous fitting of the emission lines are discussed in detail in Belfiore et al. (2019, their Sec. 5.2), who find that the effect of polynomials can be large ($\sim$10% of the emission line flux), especially for the high-order Balmer lines (not present, however, in the MUSE spectral range). They find moreover, that the effects of masking versus simultaneous fitting of the emission lines are only evident in the regions of Balmer absorption, causing small systematic changes in the fluxes of hydrogen Balmer lines ($< 2\%$ for Hα). In light of these findings we prefer to refit the continuum in the emission lines fitting stage.

We note that alternative approaches to this problem are possible. In the Pipe3d CALIFA analysis, for example, the best-fit continuum from the bins used for the stellar kinematics extraction is simply rescaled according to the median flux in the constituent spaxels, so that the spectrum which is subtracted at the spaxel level is left unchanged (Sánchez et al., 2016a). In the SAMI public data release, a new fit is performed at the spaxel level, as done here, but to limit the impact of degeneracies only those stellar templates with non-zero weights in

the parent Voronoi bin are retained in the fit of the individual spaxels (Croom et al., 2012). In general, the effect of restricting the template library in this way are small if the stellar populations are reasonably uniform within the Voronoi bin (Westfall et al., 2019, specifically their Sec. 7.4.1). At the spatial resolution of PHANGS this may not be always the case, since the distribution of young stellar populations is stochastic on small scales. We prefer, therefore, not to restrict the range of templates used, also in light of the fact that we use a small set of templates to start with. Aside from the correction for foreground Milky Way extinction, applied by the `DAP` as part of its preliminary steps, no correction for dust is applied within the target galaxy.

Output files

The `DAP` output consists of 2D maps of parameters and physical properties of interest. These maps are consolidated in the so-called `maps` file. These maps employ the exact same pixel grid and world coordinate system as the mosaic datacubes produced by the reduction pipeline. The extensions include maps of stellar kinematics, ionized gas fluxes and kinematics, and stellar-population-related (stellar mass and age) measurements. The `DAP` also produces many intermediate products which are not part of the public data release, but could be useful to expert users for specific science cases (e.g., the individual weights of the best-fit stellar templates, which can be used to compute the mass fraction within specified age bins).

4.3 Quality assessment of the stellar population-related products

To validate our final data products of the PHANGS-MUSE sample we derive several statistical measures within the million spectra of our large program, and also cross-compare with existing data on our galaxies. In this section we present quality tests performed both on the final mosaicked cubes, and the high-level data products of the data analysis pipelines, focusing specifically on the products related to the stellar population analysis.

Stellar masses

We now compare the values of stellar mass surface density derived from our stellar population analysis (Sec. 4.2.1) with those derived by Querejeta et al. (2015) using the 3.6 μm and 4.5 μm IRAC bands from the *Spitzer* Survey of Stellar structure in Galaxies (S^{4}G; Sheth et al., 2010). The S^{4}G work uses an independent component analysis (ICA) presented in Meidt et al. (2014) to separate the contributions of the stellar and the dust emission to the IRAC fluxes, and derive a relation that allows to obtain the mass-to-light ratio (M/L) using the [3.6]$-$[4.5] colour, assuming that the contribution to the stellar light at those wavelengths is dominated by an old population with an almost constant M/L ratio.

We convolved the MUSE maps to an angular resolution of 1.5 arcsec, consistent with that from the S^{4}G maps, and computed, for each pixel, the ratio $M_{\rm MUSE}/M_{\rm S^4G}$, where $M_{\rm MUSE}$ and $M_{\rm S^4G}$ correspond to the stellar mass derived from our MUSE data and S^{4}G data, respectively. On average, we found that $M_{\rm MUSE}$ values are about 30% smaller than $M_{\rm S^4G}$,

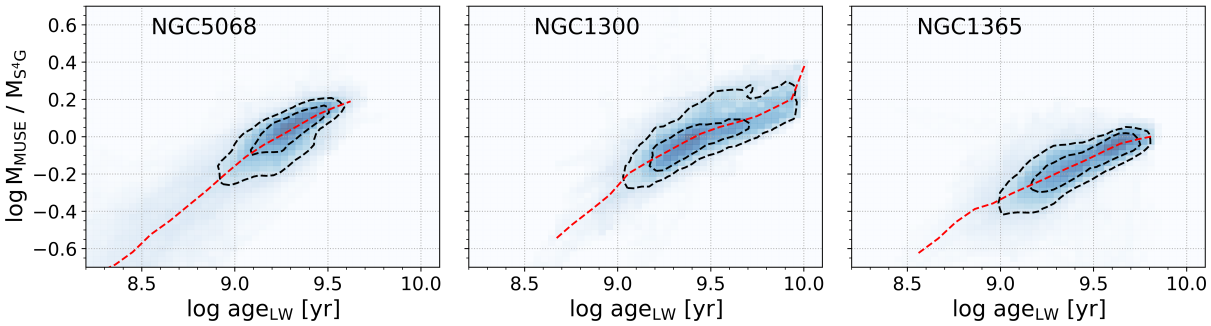

Figure 4.3: 2D histogram of the ratio between the stellar mass surface density derived from full spectral fitting from MUSE (Sec. 4.2.1) and archival stellar mass maps from S^{4}G, based on *Spitzer* IRAC maps (Querejeta et al., 2015), as a function of the light-weighted age of the underlying stellar population in each pixel, derived from the full spectral fitting. We show three galaxies in our sample, spanning the stellar mass range of the PHANGS-MUSE sample (in ascending order from left to right). The figure shows good agreement between the MUSE and the S^{4}G mass maps in pixels dominated by stellar populations older than ∼4 Gyr. However, in regions hosting younger populations, the masses derived from the near-IR data are systematically larger, possibly due to the contribution of AGB stars to the near-IR flux. The contours mark the iso-probability curves where the probability density drops below 40% and 10% of the maximum. The red dashed line shows the median mass ratio at a given luminosity weighted age.

but the differences are strongly dependent on the age of the underlying stellar population estimated from the full spectral fitting.

This can be seen in Fig. 4.3, where we show galaxies spanning the stellar mass range probed by PHANGS-MUSE, NGC 5068 being the least massive object in our sample, NGC 1300 close to the median mass, and NGC 1365 being the most massive galaxy. We show $\log(M_{\rm MUSE}/M_{\rm S^4G})$ as a function of the light-weighted age of each pixel. As can be seen, both methods agree when the light is dominated by old stars, but start to diverge when the mean light-weighted age is lower than ∼4 Gyr. A similar trend was reported by de Amorim et al. (2017) using CALIFA data. This is not surprising, as the S^{4}G calibration assumes that the stellar flux in the near-IR is dominated by old stars. However, in stellar populations with ages of 1−2 Gyr, the contribution of AGB stars to the near-IR flux can be dominant (leading to a different M/L than that appropriate for an old population) and all the pixels with a mean light-weighted age below ∼4 Gyr have a contribution of stars in this age range. It is worth mentioning that the age dependence of the mass difference is much stronger when a constant M/L ratio is applied to the original 3.6 μm image, i.e., the ICA has some effect in compensating the excess of light in regions hosting young stellar populations, but does not completely remove the age trend.

Figure 4.4 shows the median $\rm M/L_{3.6\,\mu m}$ ratio of a pixel, at a given light-weighted age, calculated as the ratio $\rm M_{MUSE}/L_{3.6\,\mu m}$, where $\rm L_{3.6\mu m}$ corresponds to the luminosity of a pixel in the original IRAC 3.6 μm image (not the ICA version from S^{4}G), in solar units. Each line represents a galaxy, coloured by its total stellar mass. The typical dispersion in the M/L ratio measurement at a given age across galaxies is ∼0.03. The figure shows little variations of this trend among galaxies, with no obvious correlation with total stellar mass. The horizontal

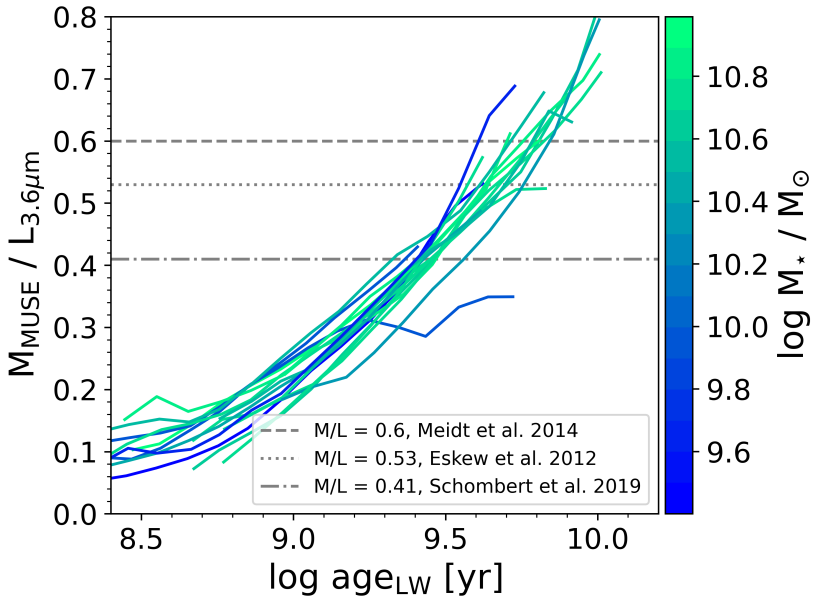

Figure 4.4: Age dependency of the $\mathrm{M_{MUSE}/L_{3.6\,\mu m}}$ ratio for the galaxies in our sample, where $\mathrm{L_{3.6\,\mu m}}$ corresponds to the luminosity of a pixel in the original IRAC 3.6 μm image (not the ICA version from S^{4}G). Each line represents a galaxy, coloured by its total stellar mass. The figure shows a positive trend, with pixels hosting older stellar populations having larger M/L ratios. The horizontal lines mark different values adopted in the literature (dot-dashed line $\mathrm{M/L} = 0.41$, Schombert et al. 2019; dotted line, $\mathrm{M/L} = 0.53$ Eskew et al. 2012; dashed line $\mathrm{M/L} = 0.6$, Meidt et al. 2014).

lines in Figure 4.4 correspond to M/L values commonly adopted in the literature. The value of Meidt et al. (2014) was intended to be applied to the dust-corrected images (i.e., after applying the ICA to remove dust emission), and is therefore higher than the other values from the literature and closer to the value expected for a very old stellar population.

Leroy et al. (2021a) compare the MUSE mass maps presented here with their *GALEX* + *WISE* version from z0MGS (following Leroy et al., 2019). As an alternative to the ICA procedure, they use a M/L that scales with *GALEX* + *WISE* colours to compensate for the impact of specific SFR on the 3.6 μm or 3.4 μm flux, in the range of $0.2 < \mathrm{M/L} < 0.5$. Our mass maps agree well with this range of values. However, they also find an offset of 0.08 dex between their masses inferred from *GALEX* + *WISE* imaging and our MUSE-derived mass maps. The offset is found to be roughly independent of specific star formation rate, which can be understood as a proxy for stellar age, and is therefore likely associated with other systematic differences in the stellar population modelling (e.g., differences in the SSP models etc.).

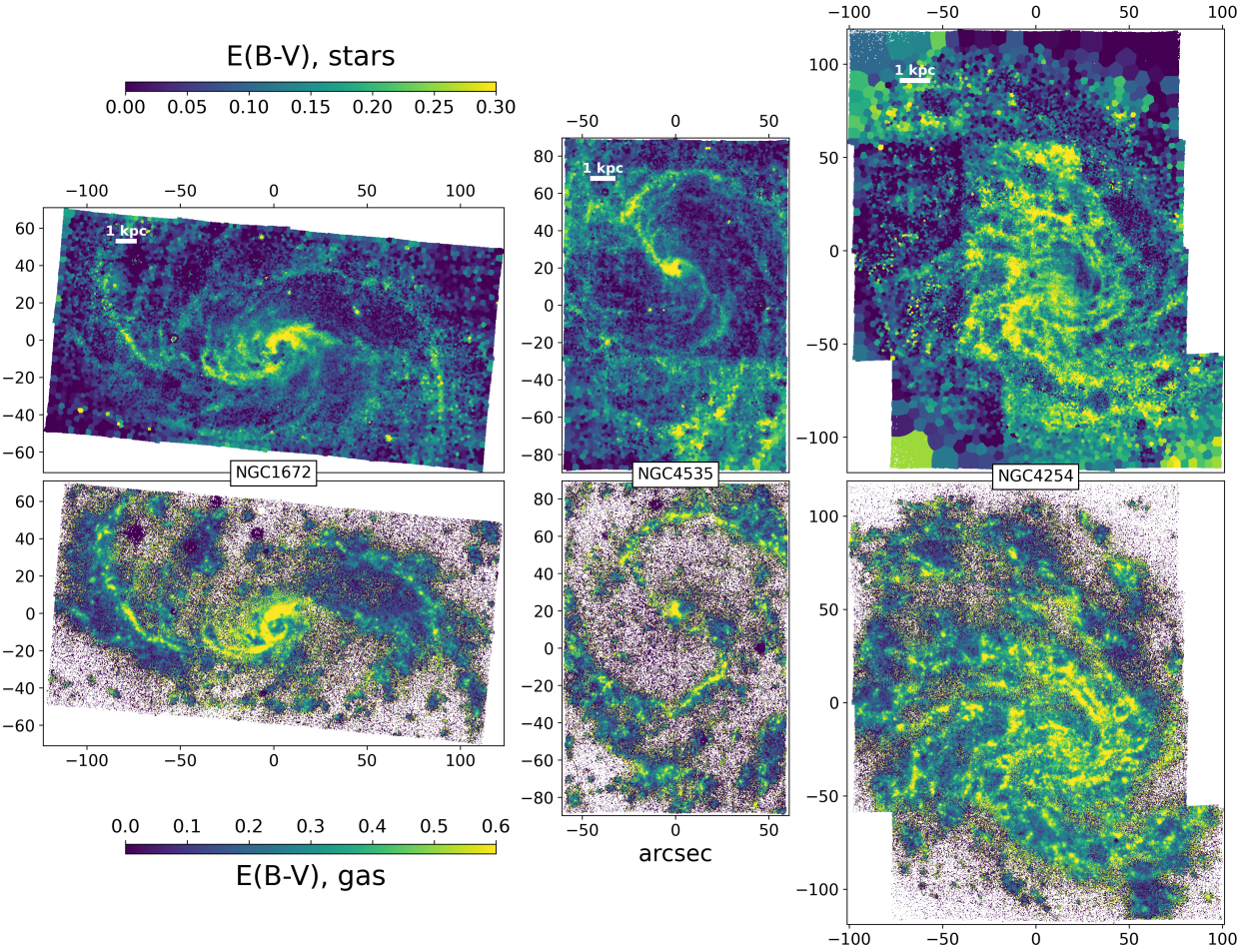

Figure 4.5: Stellar and gas $E(B-V)$ for three example galaxies. The stellar $E(B-V)_{\rm stars}$ is determined from the Voronoi binned datacubes used for stellar population analysis, while the gas $E(B-V)_{\rm gas}$ is computed from the Balmer decrement, derived from the spaxel-level analysis of the ionized gas emission lines (only regions with $\mathrm{S/N} > 4$ in the line emission are considered). The colour bars for the gaseous $E(B-V)$ is stretched by a factor of two, to account for the average ratio $E(B-V)_{\rm stars} \sim 0.5\,E(B-V)_{\rm gas}$. $E(B-V)_{\rm stars}$ traces similar structures as $E(B-V)_{\rm gas}$, although jumps are evident when comparing the average level of some MUSE pointings to that of their neighbours (e.g., the bottom-right pointing in NGC 4535 and the three left-most pointings in NGC 4254).

4.3.1 Known systematic errors in the stellar population maps

Imperfect sky subtraction: effect on stellar extinction

As discussed earlier, the stellar $E(B-V)$ map shows clear systematic jumps between different MUSE pointings. These jumps are caused by spectral differences in the sky continuum subtraction across adjacent pointings in the mosaic. We use the overlap regions among adjacent MUSE pointings to quantify the impact of the different continuum levels on the recovered stellar extinction. We computed the stellar $E(B-V)$ for this set of 2×249 spectra (two per overlap region), extracted from the individual overlap regions. For each pair of spectra, we calculated $\Delta E(B-V)$, as the absolute difference in the extinction between the two. We therefore measured 249 values of $\Delta E(B-V)$ across our full sample obtaining a median value (as well as the 68, 95 and 99.7$^{\text{th}}$ percentiles, respectively) of $\Delta E(B-V)=0.037$ (0.058, 0.133 and 0.261, resp.). This test implies that, although most of the pointings are relatively homogeneous with respect to their neighbours, with $\Delta E(B-V)<0.04$, a fraction of them show larger spectral differences that lead to systematic offsets in the derived stellar extinction, up to $\Delta E(B-V)\approx0.3$, in agreement with the pointing-to-pointing jumps visible in Fig. 4.5. Fixing such an issue would require the usage of different sky continuum reference spectra for individual exposures, something that is envisioned for future data releases.

Systematic errors in the stellar population fits at young ages

While examining the maps associated with the stellar population fitting (see Sect. 4.2.1), we noticed the presence of low metallicity values (**LW** $[\mathrm{Z/H}]<-1.3$) in a few regions encompassing very young stellar clusters (**LW age** <400 Myr). Such low metallicity values would be inconsistent with an internal and progressive chemical enrichment of the interstellar medium (e.g., Ho et al., 2017). This suggests that the fitting process converges towards a misleading local minimum, the bluest available stellar template, constrained by the youngest age bin (30 Myr) of the implemented template library. These low metallicity regions usually coincide with strong Hα emission, indicating that these young clusters are indeed actively forming stars. In addition to the lack of younger templates (due to the low number of young and metal-poor stars in the E-MILES library), contributions from nebular emission as well as unmasked emission lines are expected to further impact the χ^2 minimization in such 'young' regions. A visual inspection of the spectral fits for some associated spaxels revealed a systematic overestimation of the stellar continuum at wavelengths bluer than $\sim$5100 Å. We therefore deem these age and metallicity measurements (as well as $E(B-V)$) unreliable. This issue has already been reported in several studies (e.g., Carrillo et al., 2020; Bittner et al., 2020), who similarly reported unexpected low metallicities in young regions.

We have explored whether adding younger templates to our age-metallicity grid is sufficient or not to overcome this issue. To this end, we used SSP models from the Bruzual & Charlot evolutionary population synthesis database (Charlot and Bruzual 2007, private communication; CB07), computed assuming a Padova 1994 isochrone and a Chabrier (2003) IMF. In order to account for differences driven by using a different stellar library, we have defined two sets of CB07 templates: CB07-A, with five metallicity bins ($[\mathrm{Z/H}]=[-1.7, -0.7, -0.4, 0, 0.4]$) and 16 age bins, log-spaced from 30 Myr to 20 Gyr, i.e., with the same low-age limit than E-MILES, and CB07-B, with the same metallicity bins, but with a larger

age coverage, including 25 age bins ranging from 1 Myr to 20 Gyr.

Figure 4.6 presents the output LW age, LW [Z/H] and stellar $E(B-V)$, obtained with each different set of templates (E-MILES, CB07-A, and CB07-B) for the nuclear star-forming ring of NGC 3351. As expected, adding younger templates has an impact, in the sense that the young clusters are younger and mildly less metal-poor. However, the improvement is marginal, the derived metallicities for the above-mentioned regions being still significantly lower than for their surrounding spaxels. The associated low measured $E(B-V)$ is also likely driven by the same mechanism, biasing the blue end of the best fit spectrum. We conclude here that including templates younger than 30 Myr unfortunately does not solve the problem. A robust solution would require a broader consideration, examining a combined set of factors such as nebular emission (continuum and lines), template mismatch due to the currently poor observational constraints in the young and metal-poor regime, and potential sky-subtraction residuals. The impact of some of these factors in the SSP fitting of young regions is presented in Sec. 4.4

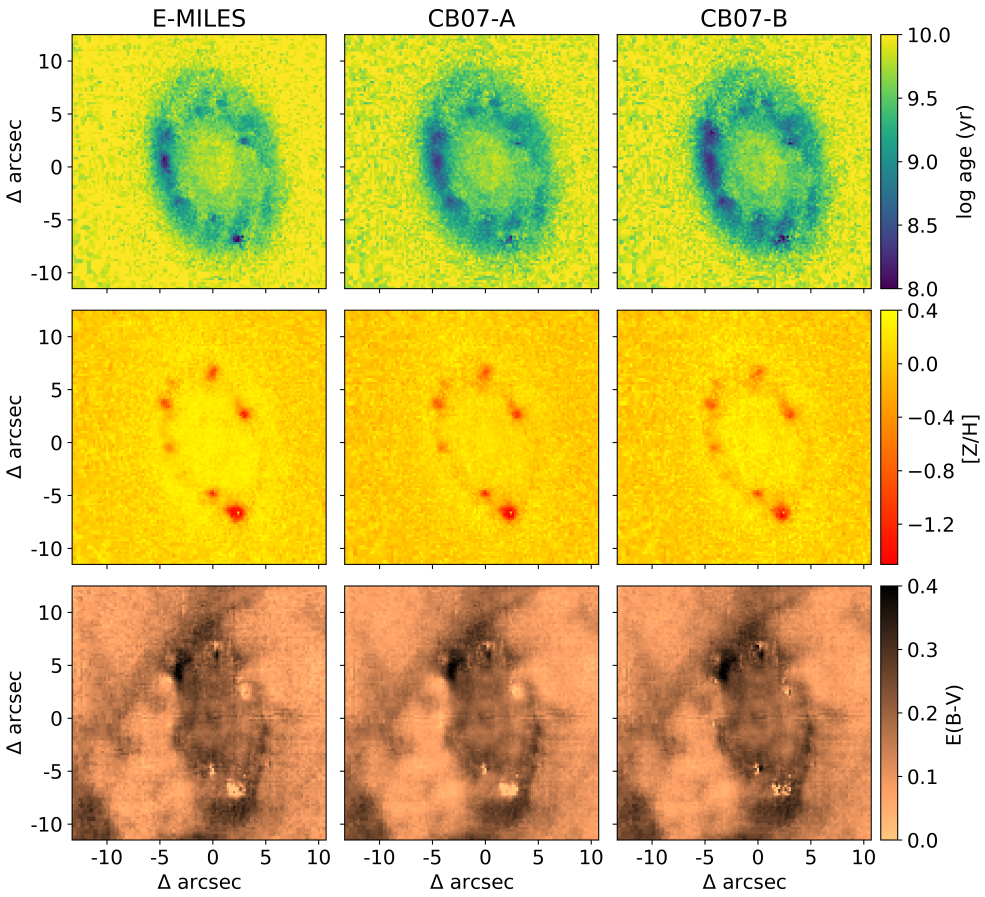

Figure 4.6: Age (top row), metallicity (middle row), and extinction (bottom row) of the inner star-forming ring of NGC 3351 obtained using three different sets of templates; E-MILES (left column), CB07, excluding templates younger than 30 Myr (CB07-A; central column), and CB07 including young templates (CB07-B; right column). Adding younger templates to our template grid slightly alleviates the problem of extremely metal poor and young regions, in the sense that the young clusters are younger and mildly less metal-poor. However, the improvement is marginal, and these regions are still significantly more metal-poor than the surrounding pixels. Panels in the last row show, additionally, an abnormally low extinction in the young and metal-poor regions. This is likely a consequence of the same issue, as it is partially improved when younger templates are included. Overall, adding templates younger than 30 Myr to our age-metallicity grid does not provide a solution to the issue of young and extremely metal poor regions.

4.4 Improving the fitting of young stellar populations

As described in the previous section, the maps associated with the stellar population fitting show low metallicity values (LW [Z/H] < -1.3) in regions consistent with very young star-forming stellar clusters. These low metallicity values are unphysical, and not consistent with the scenario in which new stars form from an interstellar medium that has been progressively metal-enriched by previous generations of stars (e.g., Ho et al., 2017)

In this section, we perform a broader exploration of the parameter space, aiming to define a better approach to fit the spectra of these problematic regions and reduce the artifacts in their derived stellar population properties. This exploration includes the usage of different libraries of templates (Sec.4.4.1), the subtraction of the stellar continuum before fitting the observed spectra (Sec. 4.4.2), accounting for nebular emission (Sec. 4.4.3), and varying the metallicity grid of the templates (Sec. 4.4.4).

4.4.1 Impact of different sets of templates

The stellar library, together with the initial mass function, and stellar evolution models (isochrones) are the basic ingredients to generate the spectra of SSPs. Variations in these three ingredients will lead to differences in the resulting SSPs, that ultimately can produce systematic differences in the measured properties of a galaxy, or galactic region, from its integrated spectrum (see, e.g., Ge et al., 2019). In this section, we explore how our results vary as a function of the set of SSP templates used to fit our data. In addition to our fiducial E-MILES templates, for these tests we consider the following set of templates:

- Charlot & Bruzual (2007, priv. comm.) - updated version 2016, to which we will refer as 'CB07'. These templates include five [Z/H] bins: [-1.7, -0.7, -0.4, 0, 0.4], and 25 age bins ranging from 1 Myr to 20 Gyr, of which 9 are younger than our fiducial age limit of 30 Myr.

- E-MILES + young extension presented in González Delgado et al. (2005, 2014b), to which we will refer as 'E-MILES + G-D'. This combined set of templates consists of our fiducial grid, plus six extra age bins, ranging from 1 Myr to 20 Myr, with four [Z/H] bins: [-0.71, -0.4, 0, 0.22]. These younger templates are only available at a spectral resolution of ~ 6 Å, lower than our fiducial E-MILES templates (FWHM ~ 2.51Å)

- E-MILES + newly computed young MILES SSP models, presented in Asa'd et al. (2017), to which we will refer as 'E-MILES young'. These templates are an extension of the MILES library towards younger ages, available for a Padova isochrone. The combined library consist of 18 age bins, ranging from 6.3 Myr to 14 Gyr, and five [Z/H] bins, ranging from -1.33 to 0.22 for templates older than 60 Myr, and from -1.33 to 0.41 for templates younger than 60 Myr.

Finally, the tests are performed in the central region of NGC 3351, which shows a prominent star-forming ring, and provides a perfect testing sample to evaluate the impact of the different templates/setting on the resultant fitting of young stellar populations. The quantities that we consider to evaluate the improvement of the quality of the solution are LW age, LW metallicity, E(B-V), and stellar mass surface density (Σ_*).

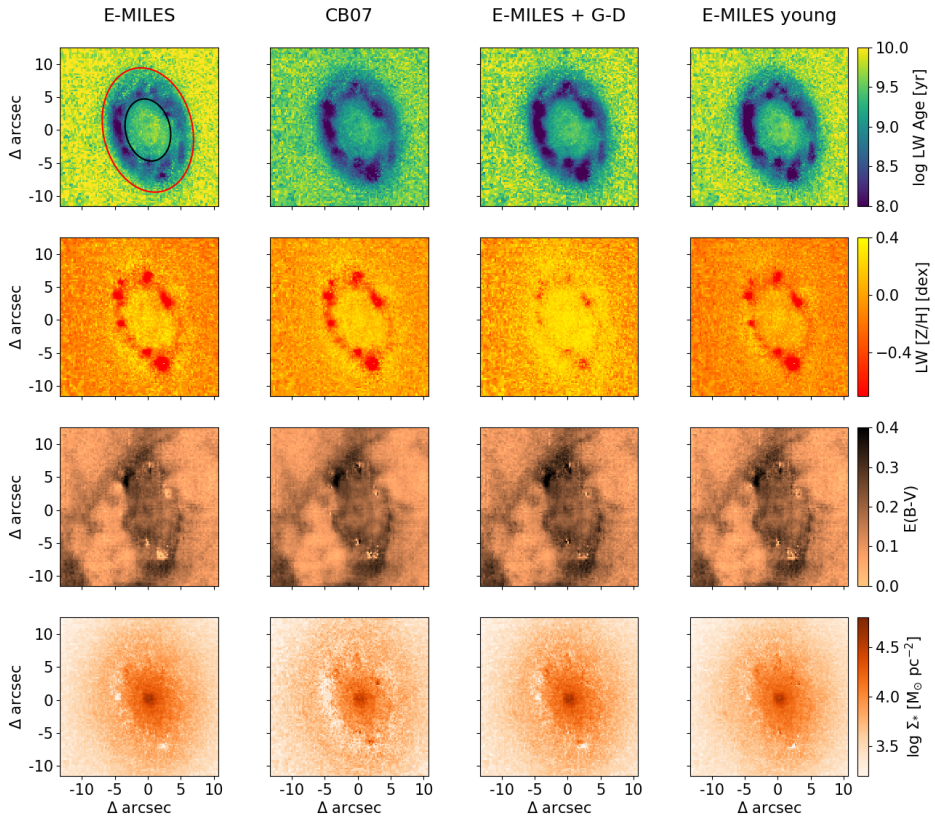

Figure 4.7: Light-weighted age (top row), light-weighted [Z/H] (second row), stellar E(B-V) (third row), and stellar mass surface density (bottom row) maps derived for the central star-forming ring of NGC 3351. Each column shows the maps obtained using the set of templates indicated at the top of each column. The maps obtained using our fiducial set of templates are shown in the left column. The area outside the red ellipse in the top-left panel is used to probe disk stellar population properties, and the area between the red and the black ellipses is used to probe stellar population properties of the young star-forming ring (see text).

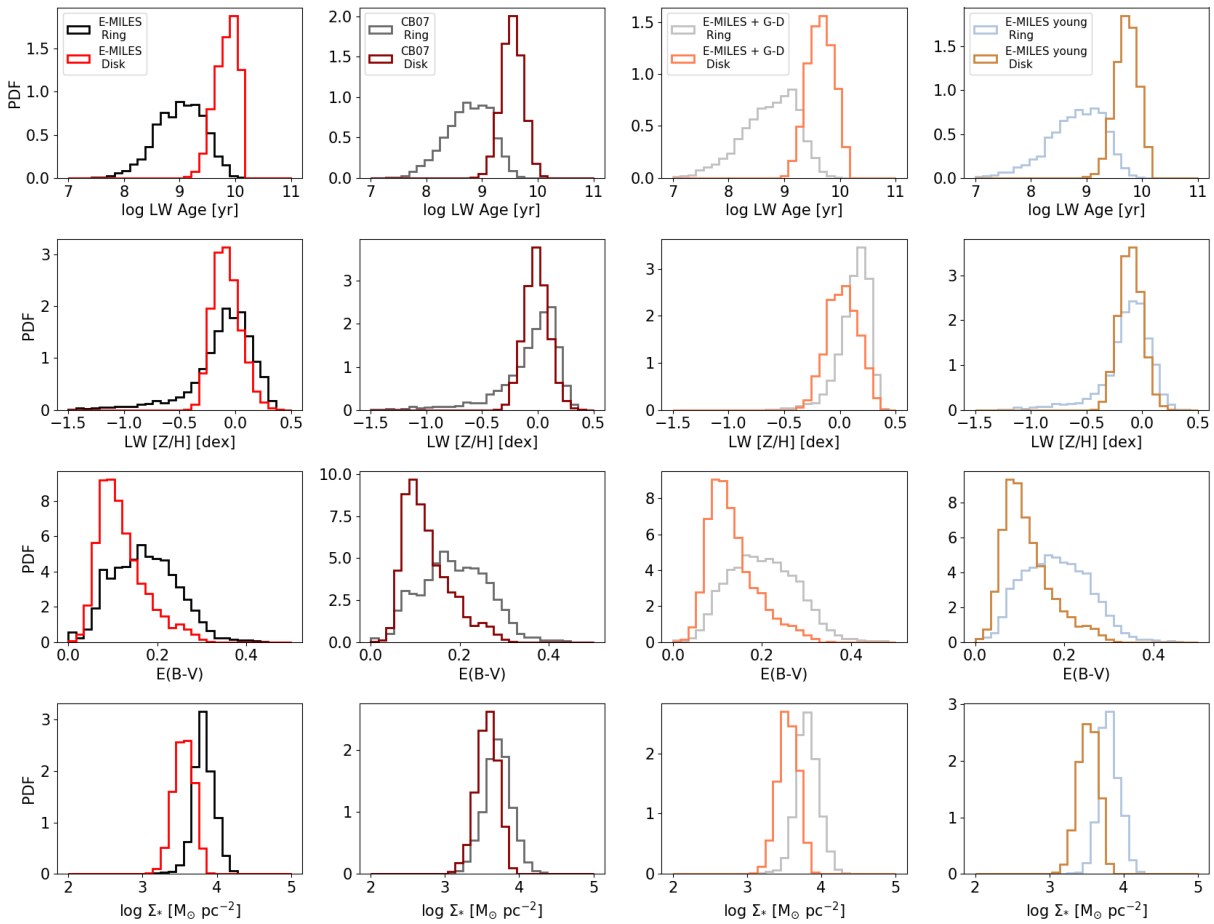

Figure 4.8: Light-weighted age (top row), light-weighted [Z/H] (second row), stellar E(B-V) (third row), and stellar mass surface density (bottom row) normalized distributions for the star-forming ring (black) and disk (red), delimitated in the top-left panel of Fig. 4.7. Each column shows the distributions obtained using the set of templates indicated in the legends of the top-row panels. The distributions obtained using our fiducial set of templates are shown in the left column.

Figure 4.7 shows the maps of these four quantities, for each one of the set of templates tested here. It is clear that the addition of younger templates to the age grid is not sufficient to overcome the issue of extremely metal-poor young regions, as the low metallicity values in the inner ring of NGC3351 persist for all SSP templates. To quantify variations, in terms of these four quantities, we consider their distributions within the ring (between the black and red ellipses in the top-right panel of Fig. 4.7), and at radii larger than the ring (i.e., disk, outside the red ellipse). Specifically, we compare the 5^{th} percentile of the ring distribution, with the median of the disk distribution. The reason for this difference is that young clusters within the ring are young, often 'erroneously' characterized by low metallicity, low extinction, and low stellar masses. Therefore, the low-value tail of these ring distributions encodes information about these problematic regions. On the other hand, the distribution beyond the ring is relatively smooth, and its median is a robust metric for characterizing it.

Figure 4.8 shows the ring and disk distributions for each of these four quantities, for each

set of templates used to produce Fig. 4.7. We define:

$$\Delta \mathrm{X} = \mathrm{X}_{p5}^{\mathrm{Ring}} - \mathrm{X}_{p50}^{\mathrm{Disk}} \tag{4.4}$$

for X in [log age, [Z/H], E(B-V), log Σ_*], where $\mathrm{X}_{p5}^{\mathrm{Ring}}$ stands for the 5$^{\mathrm{th}}$ percentile of the ring distribution for the quantity X, and $\mathrm{X}_{p50}^{\mathrm{Disk}}$ stands for the 50$^{\mathrm{th}}$ percentile (median) of the disk distribution for the same quantity.

Hence, in terms of these four quantities, a good solution should yield to: (i) lower (negative) Δlog age, i.e. star-forming clusters are expected to be younger than the surrounding disk, (ii) higher (positive or $\sim$0) Δ[Z/H], i.e. young clusters should not be associated with very metal-poor metallicities, compared to the disk, (iii) not strongly negative ΔE(B-V) values, i.e. holes in the E(B-V) map associated with these young regions are unphysical, and finally, (iv) positive (or ~ 0) $\Delta \log \Sigma_*$, due to the expected smooth underlying stellar mass surface density gradient.

In the following, we will show the output maps generated with these four set of templates, under different considerations, and at the end of the section, we will present the final comparison in terms of Δlog age, Δ[Z/H], ΔE(B-V), and $\Delta \log \Sigma_*$.

4.4.2 Is the stellar continuum shape driving the low-metallicity feature?

Low-metallicity SSPs have a continuum bluer than their high-metallicity counterparts, at a fixed stellar age. Thus, a natural feature to explore the origin of this problem is the stellar continuum shape. One possible explanation for the young and metal-poor feature is that the solution is being driven by the continuum shape, as the software might be struggling to find blue enough templates to reproduce the observed spectra of these young regions. To test if the shape of the stellar continuum is responsible for the metal-poor feature, we have repeated our measurements after subtracting the continuum of both, the templates and the observed spectra of each Voronoi bin. We have used the `specutils`[14] python package to calculate the continuum shape for a given spectrum, iteratively fitting a 5$^{\mathrm{th}}$ order polynomial to account for the stellar continuum, removing outlier absorption and emission features in each iteration. This step is repeated until no more pixels are identified as outliers and rejected from the fit.

Figure 4.9 shows the maps obtained with the four template sets under study when the stellar continuum is subtracted before performing the fit. The extinction is calculated before subtracting the continuum, therefore this presents no change with respect to the fiducial case. The stellar mass surface density maps can not be computed once the continuum is subtracted, and hence, the last row has been omitted from the figure. We highlight two aspects from Fig. 4.9. First, the solution in age and metallicity is much noisier, compared to the fiducial case. This is because the unsupervised continuum subtraction is not perfect, and creates artifacts in the spectra, often associated with absorption features or residual emission lines perturbing the definition of the continuum level. Nevertheless, the ring is still recovered as a young and metal-poor feature for 3 out of the 4 libraries investigated, and we

[14] https://specutils.readthedocs.io/en/stable/

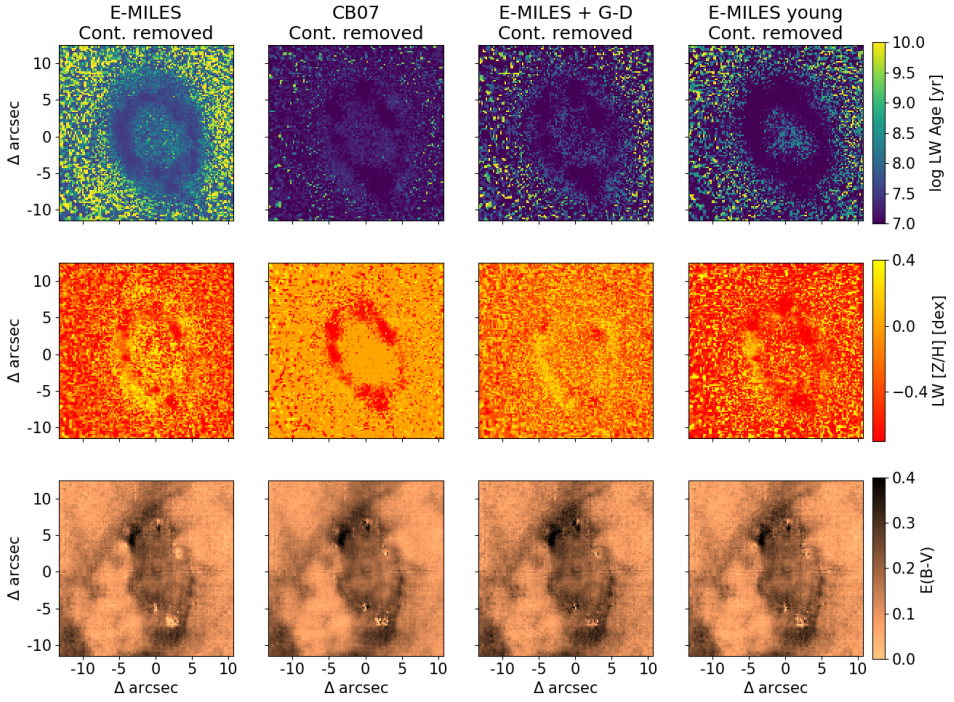

Figure 4.9: Light-weighted age (top row), light-weighted [Z/H] (middle row), and stellar E(B-V) (bottom row) maps derived for the central star-forming ring of NGC 3351, once the stellar continuum has been removed from the observed spectra and the templates. Each column shows the maps obtained using the set of templates indicated at the top of each column. The maps obtained using our fiducial set of templates (after removing the stellar continuum) are shown in the left column. Note that the E(B-V) maps are identical to those in Fig. 4.8, as the stellar extinction is measured before subtracting the stellar continuum.

conclude that the shape of the continuum is not the primary driver of the low metallicity solutions for young regions.

4.4.3 Could nebular emission be the responsible?

High-energy ultraviolet photons emitted from nearby hot (and young) stars can ionize the surrounding interstellar medium, leading to nebular emission. Nebular emission is composed of nebular line emission and nebular continuum. While the former is primarily produced by radiative recombination processes and emission from specific line transitions, the latter is a continuous emission spectrum that consists of free-free (Bremsstrahlung), free-bound (recombination continuum), and two-photon emission (Byler et al., 2017)

The strength of emission from these two components depends on both the ionizing radiation field and the metallicity of the gas. The amount of nebular emission thus varies from galaxy to galaxy, and can evolve with cosmic time. As stated in Sec. 4.2, for our analysis we have masked emission lines, as they make measurements of the underlying absorption features unreliable. However, nebular continuum emission might also have a pronounced

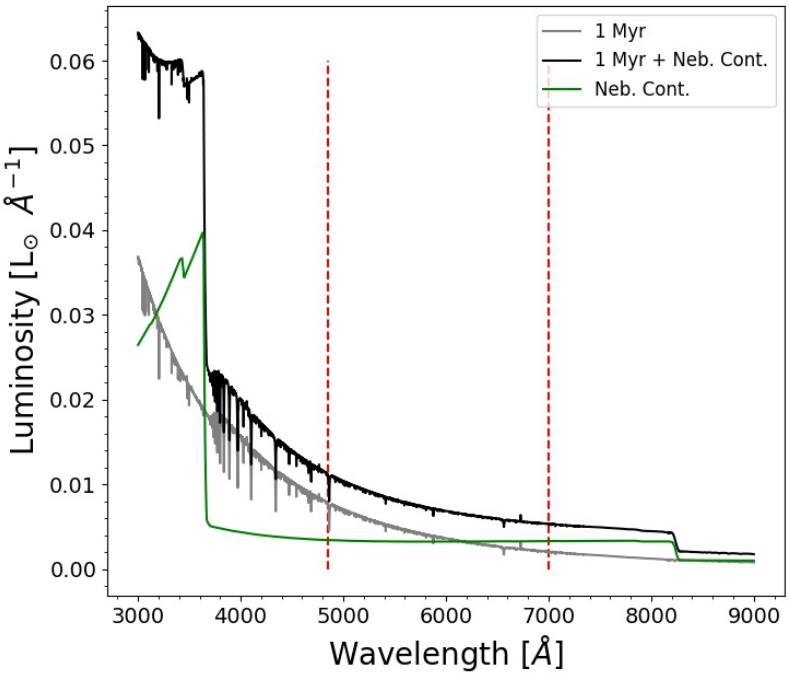

Figure 4.10: Example of the impact of nebular continuum emission on the SED of a 1 Myr old solar metallicity SSP. The sudden decrease of nebular emission (green line) at $\sim$ 3646Å and $\sim$ 8207Å correspond to the Balmer and Paschen breaks, respectively. The vertical red dashed lines enclose the wavelength range considered for the full spectral fitting [4850,7000] Å.

impact on the SSP fitting.

Figure 4.10 shows the spectrum of a solar metallicity SSP at an age of 1 Myr, with and without the inclusion of nebular emission. The nebular component is computed with `FSPS` (Flexible Stellar Population Synthesis; Conroy et al., 2009; Conroy & Gunn, 2010), a python package that generates spectra and photometric predictions for arbitrary stellar populations, using Cloudy (Ferland et al., 2013; Byler et al., 2017; Byler, 2018) to calculate the emission produced by ionized gas.

In order to test the influence of nebular continuum emission in our fitting, we first choose two representative regions within the young ring in the center of NGC 3351, one of them is found to be extremely metal-poor, while the other is relatively metal-rich in our fiducial fitting. For each region, we extract a high-SN spectrum, and we use these spectra for further tests. We will refer to these two young regions as MR (metal-rich) and MP (metal-poor). Figure 4.11 shows these regions, and the stellar metallicity map determined with E-MILES templates as background. The MR and MP regions are indicated with an orange circle and a blue ellipse, respectively.

We use `FADO` (Fitting Analysis using Differential evolution Optimization; Gomes & Papaderos, 2017), a SED-fitting software (similar to pPXF) that aims for recovering the best-fitting SFH, while consistently accounting for the observed nebular emission characteristics of a star-forming (SF) galaxy, to fit the spectra of these two regions, and quantify the

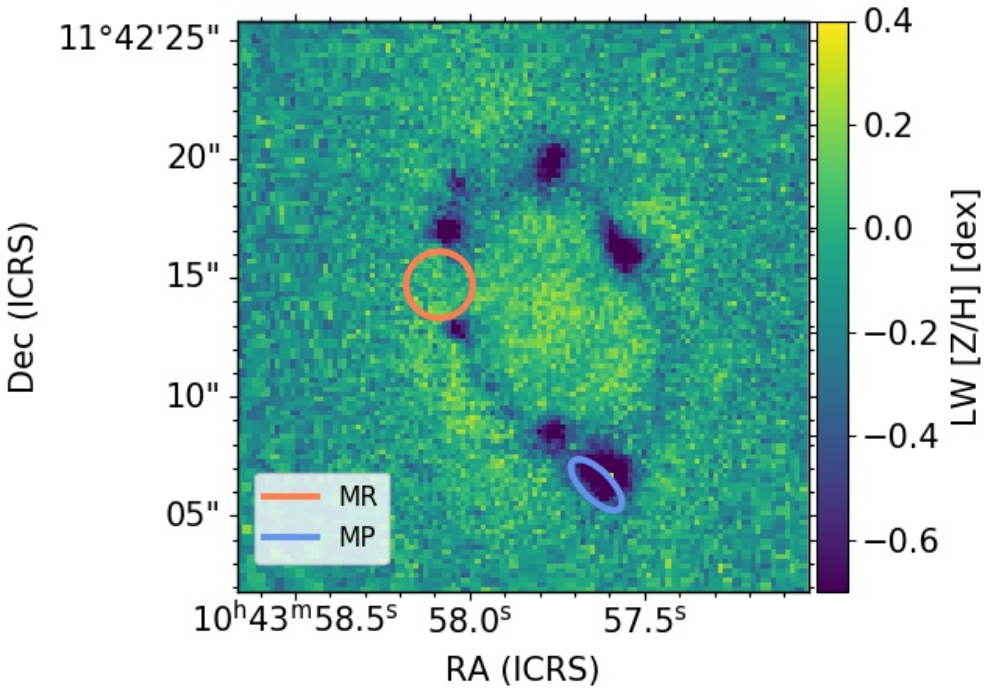

Figure 4.11: Two very young regions within the central star-forming ring of NGC 3351 with different inferred metallicity values. The orange circle encloses the metal-rich (MR) region, and the blue ellipse encloses the metal-poor (MP) region. The background map shows the light-weighted stellar metallicity in the central region .

contribution expected from nebular emission.

Figure 4.12 shows that both spectra contain some degree of nebular continuum emission contribution. This is expected, as both of them correspond to young SF regions. However, region MP hosts a much larger nebular continuum contribution than MR, while also being much younger. Moreover, the metal-poor peaks in Fig. 4.11 spatially correlate well with peaks in the Hα flux surface density map. This suggests that not accounting properly for nebular continuum contribution in the spectra of the youngest regions could be responsible for the low metallicity obtained for the MP spectrum. Indeed, in the wavelength range of interest, the nebular continuum can be represented, to zero$^{\text{th}}$ order, as a flat spectrum (see Fig. 4.10). This boost of the continuum yields weaker absorption features (i.e. shallower relative to the continuum level). This effect can be further quantified by measuring different line-strength indices for different contributions of nebular continuum emission.

Figure 4.13 shows a set of line-strength indices (Burstein et al., 1984; Faber et al., 1985) as a function of stellar metallicity measured for the CB07 templates, at a fixed age of 1 Myr. It also shows the measurement at solar metallicity obtained under different assumptions for the nebular continuum contribution, from an escape fraction of 1 (i.e., no nebular continuum), to an escape fraction of 0 (i.e., the full contribution of nebular emission as computed using `FSPS`).

For most line-strength indices that correlate with stellar metallicity (neglecting the most metal-poor bin), the contribution of nebular emission causes a shift in the index, consistent

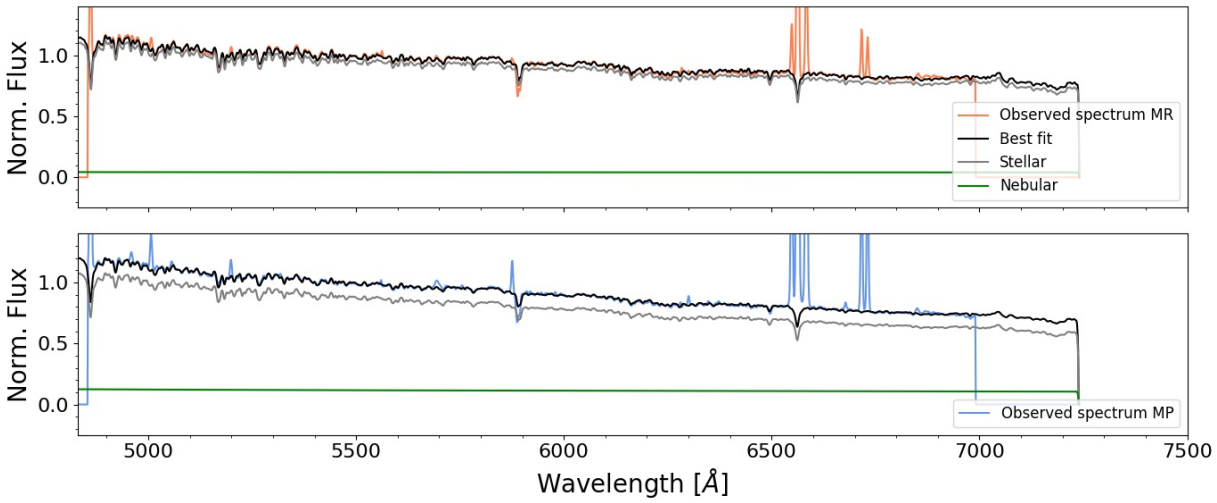

Figure 4.12: Best SED-fitting obtained with FADO for the MR and MP regions, defined in Fig. 4.11. The orange and blue lines represent the MR and MP observed spectra, respectively. The black line show the best-fitting model, and the grey and green curves show separately the stellar and nebular continuum contribution, respectively. It is clear that the MP region (bottom) requires a more significant contribution of nebular continuum than the MR (top) region.

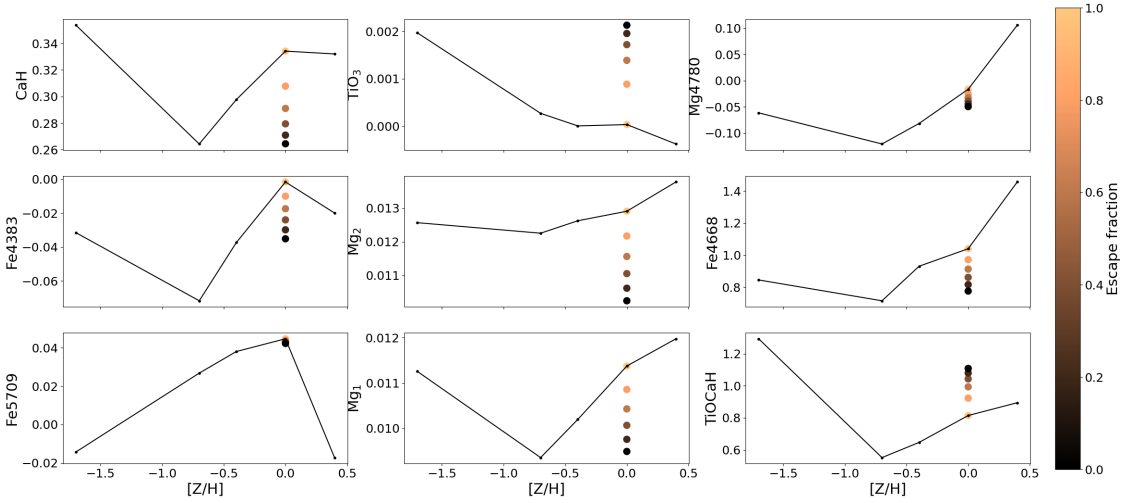

Figure 4.13: Set of line-strength indices commonly used as stellar metallicity tracers, measured for the SED of a 1 Myr SSP model from the CB07 library, for the full range of metallicity values available. For solar metallicity, we show the measurement for different levels of nebular continuum contribution. It is clear that a stronger nebular continuum contribution (lower escape fraction) yields a line-strength index measurement consistent with lower metallicities (with TiOCaH being the only exception, bottom right panel). Also, we note that the most metal-poor metallicity bin often appears as a strong outlier in the line-strength-[Z/H] relation.

with a more metal-poor metallicity. Therefore, in the next tests, we explore the impact that including nebular continuum emission in the SSP fitting has in the output maps.

It is worth noting that although `FADO` does account for nebular emission, it is currently not implemented in python, and thus, we opt for different approaches to account for this contribution using pPXF. To include nebular emission in the fitting, we investigate two different options:

- Include nebular contribution in the templates, as computed by `FSPS`: this approach has the advantage of including an accurate description of the nebular emission in the fitting. However, it has the drawback that it is only useful for libraries that already include very young templates (i.e. $\lesssim 5$ Myr). We will refer to this approach as 'Neb. A' in the following text.

- Tie the nebular continuum contribution to the emission line measurement: as they are originating from the same source, it is expected that the amount of nebular continuum scales with the flux of emission lines (e.g. Byler et al., 2017). Specifically, we model the nebular continuum emission as a flat spectrum with its flux equal to 0.5% of the Hβ flux, and we subtract this contribution before proceeding with the SSP fit. As this is a very simplistic representation of the nebular contribution, we do not perform additional corrections (i.e., we do not correct by extinction), which could, in principle, lead to an underestimation of the nebular continuum emission. Despite the simplicity of this approach, it offers the advantage of being applicable to any of the libraries of templates used. We will refer to this approach as 'Neb. B' in the following text.

Impact of neglecting nebular continuum contribution in synthetic spectra

Here we use a set of mock spectra built from the CB07 library to assess how problematic it can be to not account for existing nebular emission during the full spectrum fitting. To evaluate this, we define our mock-spectra library to harbor a fixed contribution of 100 solar masses of an old ($\sim$ 10 Gyr) and metal-poor ([Z/H] = -0.7) component, a fixed contribution of 20 solar masses of a medium age ($\sim$ 1 Gyr) and medium metallicity ([Z/H] = -0.4) component, and a variable contribution (30 values covering the range from 0 to 1.5 solar masses) of a young (2 Myr) and solar metallicity component. We have chosen such a configuration aiming for a realistic representation of the combination of multiple stellar populations, in which most of the mass is contributed by old and metal-poor stars (formed from unprocessed gas), and subsequent stellar generations formed from a recycled (and thus, metal-enriched) interstellar medium. Finally, young stars are sub-dominant in terms of mass, but their light strongly influences the spectrum of the combined population. We build this mock library using young templates that include nebular continuum contribution (computed using FSPS), and then we fit them to recover their original SFH, removing the nebular contribution from the templates used in the fitting. Since we want to explore exclusively the impact of neglecting the contribution of existing nebular emission in the mock spectra, we assume an infinite S/N regime, in order to remove noise-driven differences.

Figure 4.14 shows the real light-weighted mean age, light-weighted mean metallicity, total mass, and extinction values as a function of their recovered values, accounting for nebular emission (left column) and neglecting nebular emission (right column) in the fitting. It is

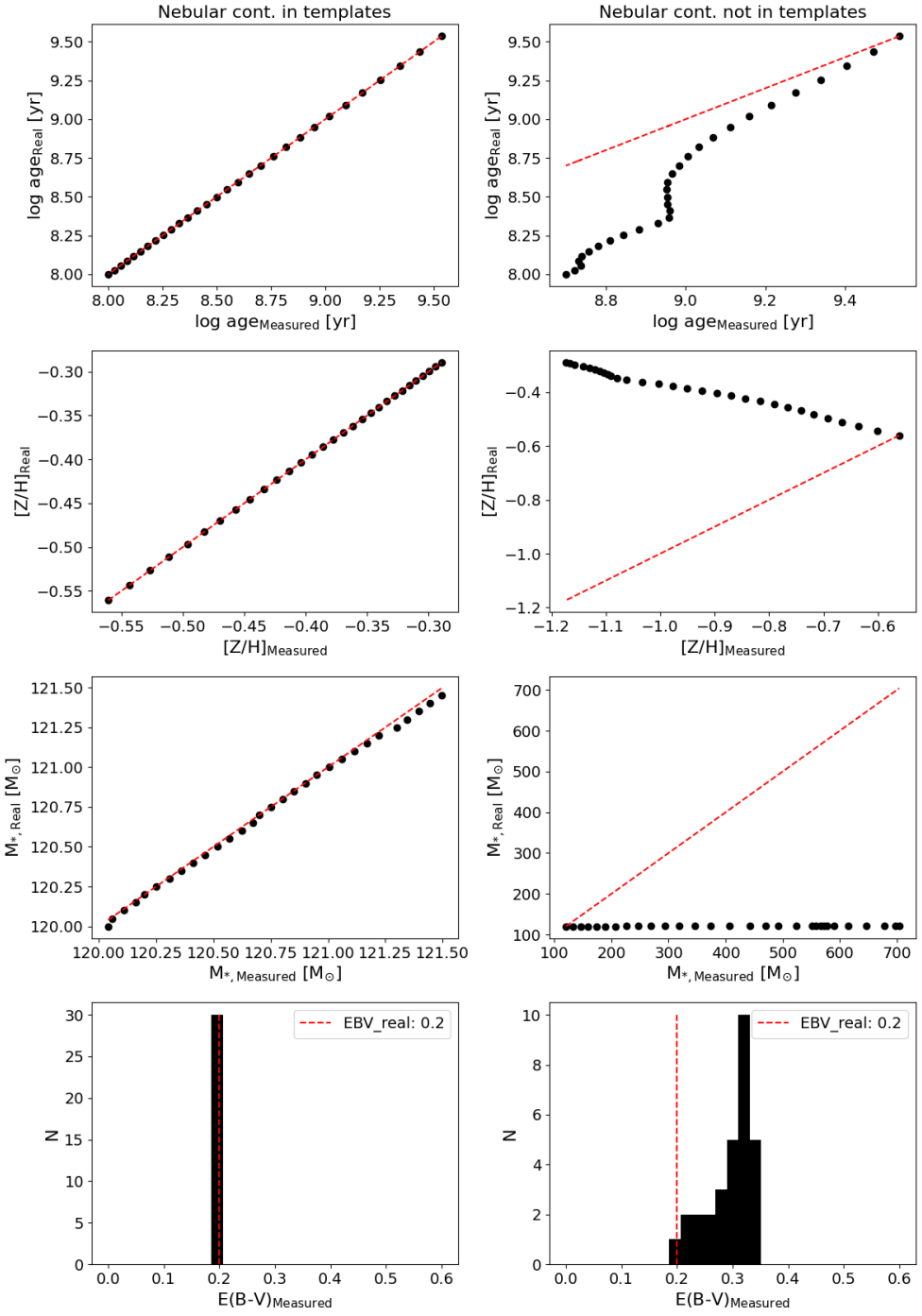

Figure 4.14: Mock-spectra test designed to investigate the impact on the outcome of the SSP fitting when nebular continuum emission is present in the data, but neglected in the analysis. We created a synthetic sample of 30 linear combinations of SSP, with a constant contribution of old (metal-poor), and intermediate age (intermediate metallicity) SSPs, and a varying contribution of a young (metal-rich) SSP that include nebular continuum contribution (computed using FSPS, i.e., Neb. A approach). Both columns show the real age (top row), metallicity (second row), and stellar mass (third row) of each mock spectra in the y-axis, and the recovered value in the x-axis. The bottom panels show an histogram of the recoved E(B-V) values, and the vertical dashed red line shows the real E(B-V) applied to the mock spectra (0.2). The left column shows the results obtained when nebular continuum emission is accounted for in the templates used to fit the data, and the right column shows the same results when nebular continuum emission is neglected from the fitting. It is remarkable that when existing nebular emission is neglected in the fitting, we obtain an anti-correlation between the real metallicity and its recovered values.

remarkable that when existing nebular emission is neglected in the fitting, we recover an anti-correlation between the real metallicity and its measured values. This effect is similar to the trend revealed by the line-strength indices; the nebular continuum contribution reduces the equivalent width of absorption features, mimicking lower metallicities. Another interesting effect is that the stronger continuum is interpreted as a higher total stellar mass, when the templates lack this contribution. This is a direct consequence of the higher level of the continuum due to the nebular continuum emission. However, in our data, we see that the stellar mass surface density is underestimated in the young regions (see, e.g., Fig. 4.7), i.e., the observed bias in stellar mass in regions expected to have a strong nebular continuum emission contribution is in the opposite direction than that found in this test. A higher extinction is not surprising, as the recovered low-metallicity of the young templates will lead to a bluer spectrum. Thus, a higher extinction value is needed to match the spectral shape of the observed spectrum.

Effect of accounting for nebular continuum contribution in the output maps

Figures 4.15 and 4.16 show the output maps obtained when nebular emission is included in the SSP fitting using the two approaches described earlier (Neb. A and Neb. B, respectively). Despite the impact that nebular continuum emission is expected to have on the spectra of SSPs, particularly in young populations, its addition to the fitting does not lead to a visually significant improvement of the low-metallicity feature.

4.4.4 Do we trust our full metallicity grid?

In the previous paragraphs, it has become clear that the issue of the young metal-poor feature issue persists, even when we add younger templates to the age grid, remove the stellar continuum of the spectra, or account for nebular continuum emission.

In the next set of tests, we explore if this metal-poor feature could be due to the lack of many hot stars in the stellar libraries used to build the models, that makes the predictions uncertain (Villaume et al., 2017; Conroy et al., 2018). A hint for potential a mismatch between the metal-poor templates and the true galaxy spectra is provided by Fig. 4.13, which shows that the most metal-poor bin is often an outlier in the line-strength index vs. [Z/H] correlation. Furthermore, metallicity values such as -1.49 (MILES), -1.7 (CB07) and -1.33 (MILES young extensions) are extremely low, and unlikely to be significantly present in the stellar disk of massive star-forming galaxies, where the interstellar medium is being constantly recycled and enriched by star formation and its subsequent feedback (see, e.g., Ho et al., 2017). Thus, we repeat our measurements, removing these extremely low metallicity bins from our grid. Note that the MILES+G-D library already lacks metallicities lower than -1.0 for ages younger than 30 Myr. We will refer to the libraries lacking their most metal-poor metallicity bin as NoMP.

Figure 4.17 shows the output maps after removing the most metal-poor metallicity bin from each stellar library. The young metal-poor feature is drastically improved after implementing this change in the metallicity prior, meaning that the most metal-poor values get a significant weight in the fitting of the spectra of the young regions, when they are present.

With this in mind, and for completeness, we explore once again if the inclusion of nebular contribution has a positive impact on the fitting, after removing the most metal-poor bin of

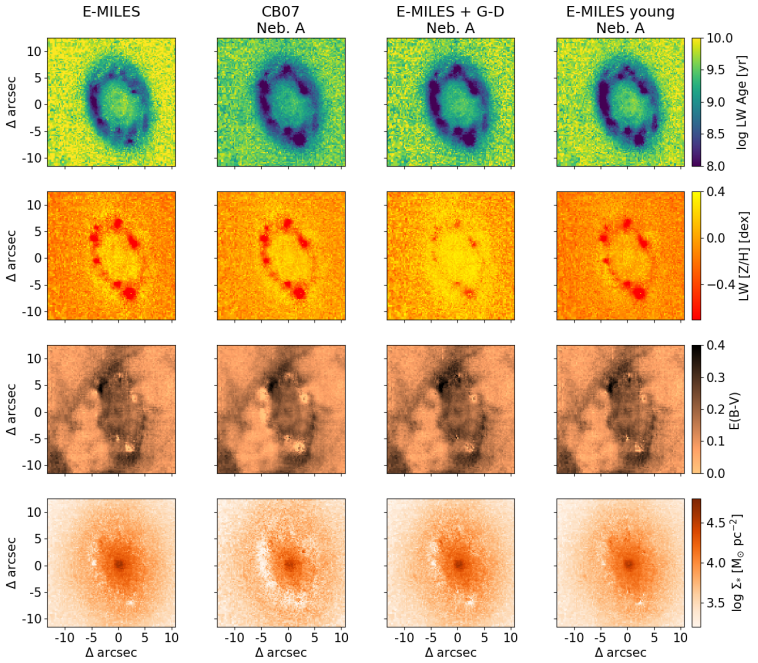

Figure 4.15: Light-weighted age (top row), light-weighted [Z/H] (second row), stellar E(B-V) (third row), and stellar mass surface density (bottom row) maps derived for the central star-forming ring of NGC 3351. Each column shows the maps obtained using the set of templates indicated at the top of each column, accounting for nebular continuum emission using the approach Neb. A (see main text). The maps obtained using our fiducial set of templates are shown in the left column.

each library, by examining the output maps obtained under this combination of settings.

Figures 4.18 and 4.19 show the maps obtained when nebular emission is included in the fit, together with the removal of low-metallicity templates, using the Neb. A and Neb. B descriptions, respectively. The metallicity maps show weaker low-metallicity features under the Neb. B + NoMP approach, compared to the Neb. A + NoMP one. Nevertheless, none of these tests exhibit a visually significant improvement compared to the NoMP scenario. Thus, it seems that the inclusion of nebular continuum emission does not significantly improve the quality of the output maps, even when the most metal-poor templates have been removed.

4.4.5 Deciding on best fitting results

In the previous sections, we have shown the output LW log age, LW [Z/H], E(B-V), and log Σ_* maps obtained using different spectral libraries and approaches to fit our data in order to obtain a visualization of the resulting maps that these different approaches yield. We parametrize quantitatively the quality of these results, in terms of Δ log age, Δ[Z/H], ΔE(B-V), and $\Delta \log \Sigma_*$, introduced earlier.

Figure 4.20 shows the values calculated for these quantities, for each one of the sets of templates used, under each different approach. The fiducial case for the four libraries is

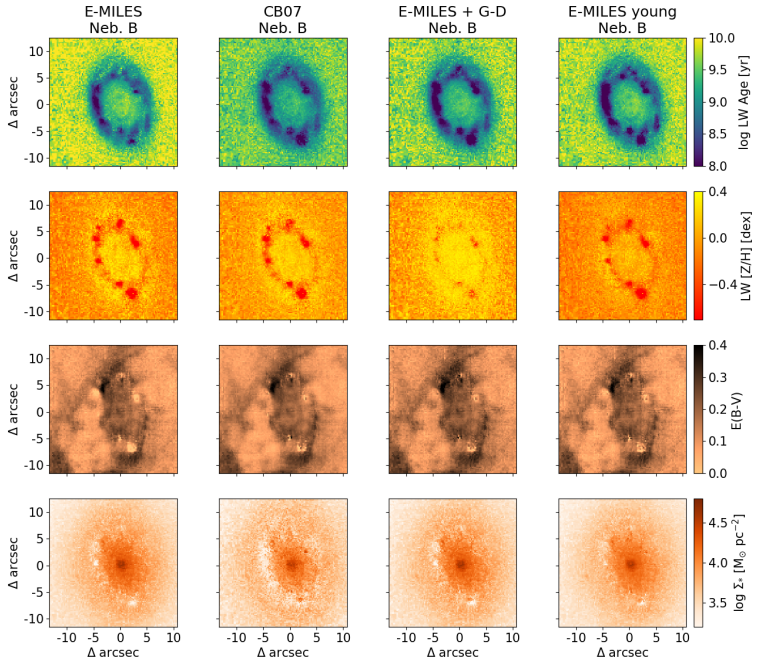

Figure 4.16: Light-weighted age (top row), light-weighted [Z/H] (second row), stellar E(B-V) (third row), and stellar mass surface density (bottom row) maps derived for the central star-forming ring of NGC 3351. Each column shows the maps obtained using the set of templates indicated at the top of each column, accounting for nebular continuum emission using the approach Neb. B (see main text). The maps obtained using our fiducial set of templates (with the modifications described) are shown in the left column.

indicated in grey. The two implementations of nebular emission are marked in red and blue. The tests removing the most metal-poor templates are marked in yellow, and finally, the tests that include a combination of including nebular emission, and removing the most metal-poor templates are indicated with green and pink backgrounds.

The figure clearly shows that the highest (closest to zero) Δ[Z/H] values (2nd row) are achieved when the most metal-poor templates are removed from the metallicity grid (yellow, green, and pink background). In particular, the CB07 templates yield the highest Δ[Z/H] value among the set of templates tested. This is visually consistent with what can be seen in Fig. 4.17. However, the last row shows that the CB07 templates also yield low stellar mass surface density values in the young regions (i.e., low $\Delta \log \Sigma_*$). This low-mass feature is also clearly visible in Fig. 4.17. Furthermore, in some cases, the CB07 templates also yield particularly low E(B-V) values in the young regions. Out of the remaining set of templates (MILES + G-D and MILES young, with metal-poor metallicity bins removed), both show similarly low Δlog age, and high Δ[Z/H], without any noticeable artifacts neither in E(B-V) nor in stellar mass surface density. Since the MILES + G-D templates suffer from a low spectral resolution in the youngest ages, and this different spectral resolution is not properly treated by the DAP in its current state, we finally choose the MILES young templates for future analysis of the stellar populations.

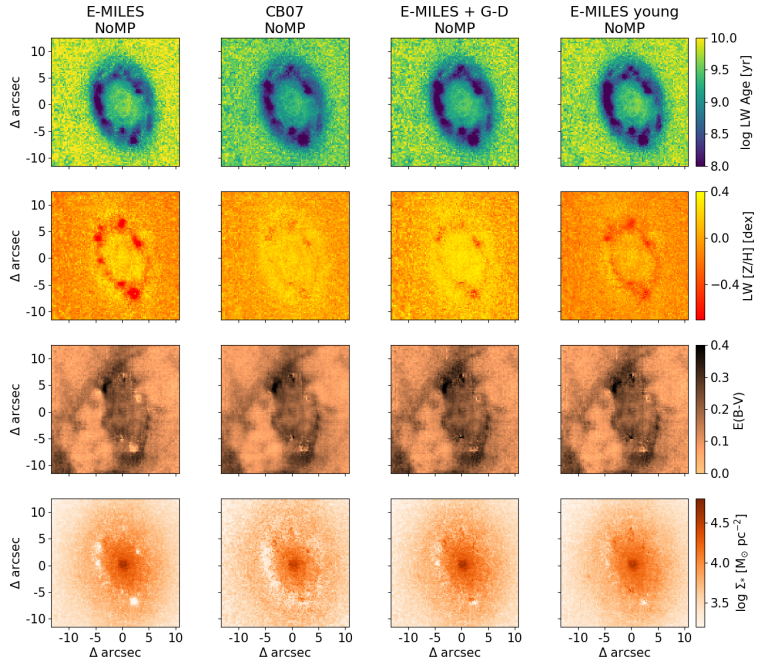

Figure 4.17: Light-weighted age (top row), light-weighted [Z/H] (second row), stellar E(B-V) (third row), and stellar mass surface density (bottom row) maps derived for the central star-forming ring of NGC 3351. Each column shows the maps obtained using the set of templates indicated at the top of each column, removing the lowest metallicity bins from the metallicity grid (see main text). The maps obtained using our fiducial set of templates (with the modifications described) are shown in the left column.

Despite choosing the best set of templates according to our criteria, among those libraries tested, we acknowledge that the fitting of the youngest regions is still sub-optimal, as the metal-poor metallicities persist for these regions. We consider these metallicities unreliably, and therefore mask them in further analysis. We have tested and adopted an extinction-corrected Hα [15] surface density emission threshold for our masking scheme, as it traces ongoing star-formation and thus, the presence of young stellar populations. Specifically, we masked those pixels in which we measure $\log \mathrm{H}\alpha_{\mathrm{corr}} > 35$ erg s^{-1} pc^{-2}[16]. We find that this value successfully identifies the youngest and most problematic regions. Figure 4.21 shows the LW age and LW [Z/H] maps of the central region of NGC 3351 after applying our masking scheme. The youngest pixels with low metallicities are thus removed from our sample.

There are ongoing efforts to further improve the SSP fitting in the regions dominated by young stellar populations. It is known that stellar populations of different ages are also characterized by different kinematic conditions, with older stars being dynamically hotter

[15] We de-reddend the Hα fluxes, assuming that under the absence of dust, Hα/Hβ = 2.86, as appropriate for a case B recombination, temperature T = 10^4 K, and density n_e = 100 cm^{-2}, adopting a O'Donnell (1994) extinction law.

[16] or log SFR $\gtrsim$ 0.16 M$_\odot$ yr^{-1} pc^{-2}, following Calzetti (2013)

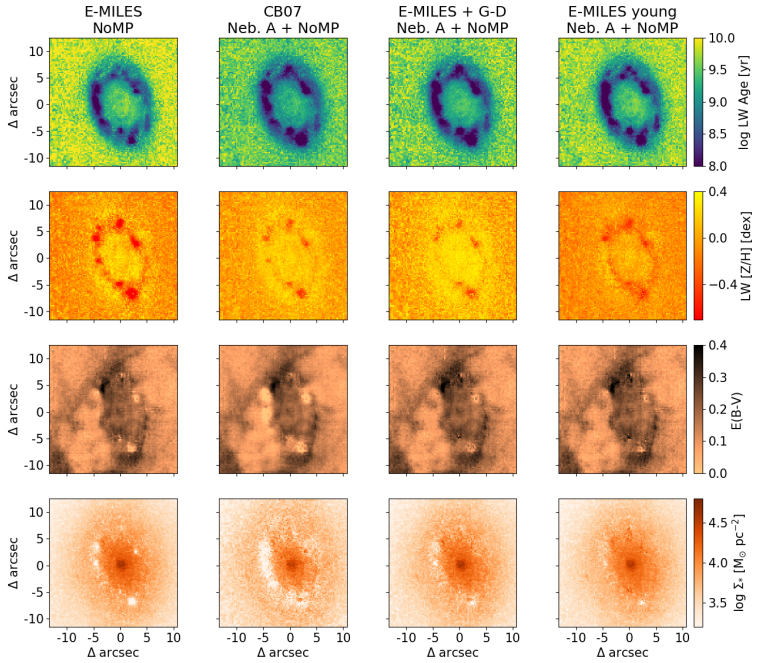

Figure 4.18: Light-weighted age (top row), light-weighted [Z/H] (second row), stellar E(B-V) (third row), and stellar mass surface density (bottom row) maps derived for the central star-forming ring of NGC 3351. Each column shows the maps obtained using the set of templates indicated at the top of each column, accounting for nebular continuum emission using the approach Neb. A, and removing the lowest metallicity bins from the metallicity grid (see main text). The maps obtained using our fiducial set of templates (with the modifications described) are shown in the left column.

than younger stars (see, e.g., Tarricq et al., 2021). In this regard, Zhang et al. (in prep.) will present a detailed exploration on how these differences in the kinematic conditions across different stellar populations can bias the recovered SFHs. This will potentially lead to improvements in the methodology currently employed in the PHANGS-MUSE pipeline, by including multiple stellar kinematic components to reproduce the observed spectra. An additional possibility to significantly improve our SSP fitting is using available photometric data from the PHANGS-HST survey to constrain bluer wavelength ranges, valuable to shed light on the properties of young stellar populations (see, e.g., González Delgado et al., 2005). However, the inclusion of additional photometric data to the spectral fitting technique is not trivial. It requires further development of the currently available tools, and thus, it is beyond the scope of the analysis presented here.

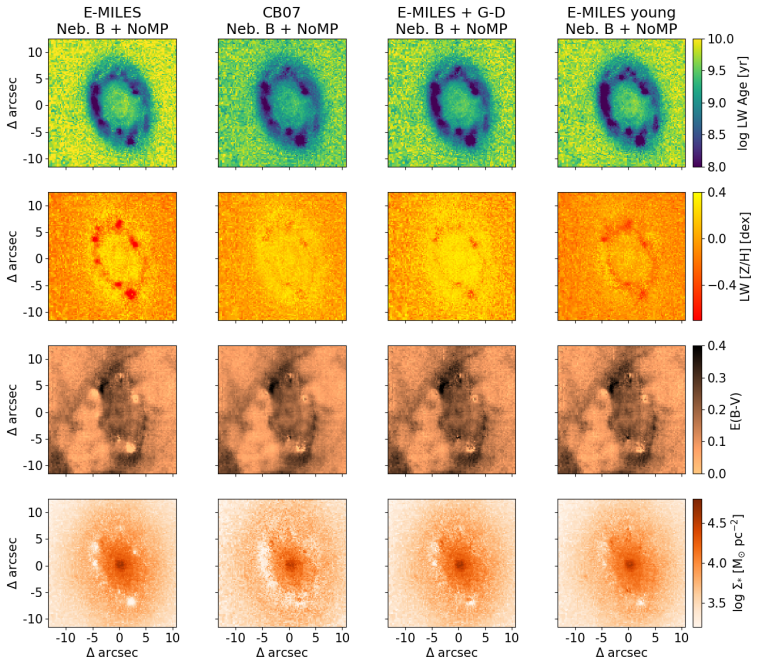

Figure 4.19: Light-weighted age (top row), light-weighted [Z/H] (second row), stellar E(B-V) (third row), and stellar mass surface density (bottom row) maps derived for the central star-forming ring of NGC 3351. Each column shows the maps obtained using the set of templates indicated at the top of each column, accounting for nebular continuum emission using the approach Neb. B, and removing the lowest metallicity bins from the metallicity grid (see text). The maps obtained using our fiducial set of templates (with the modifications described) are shown in the left column.

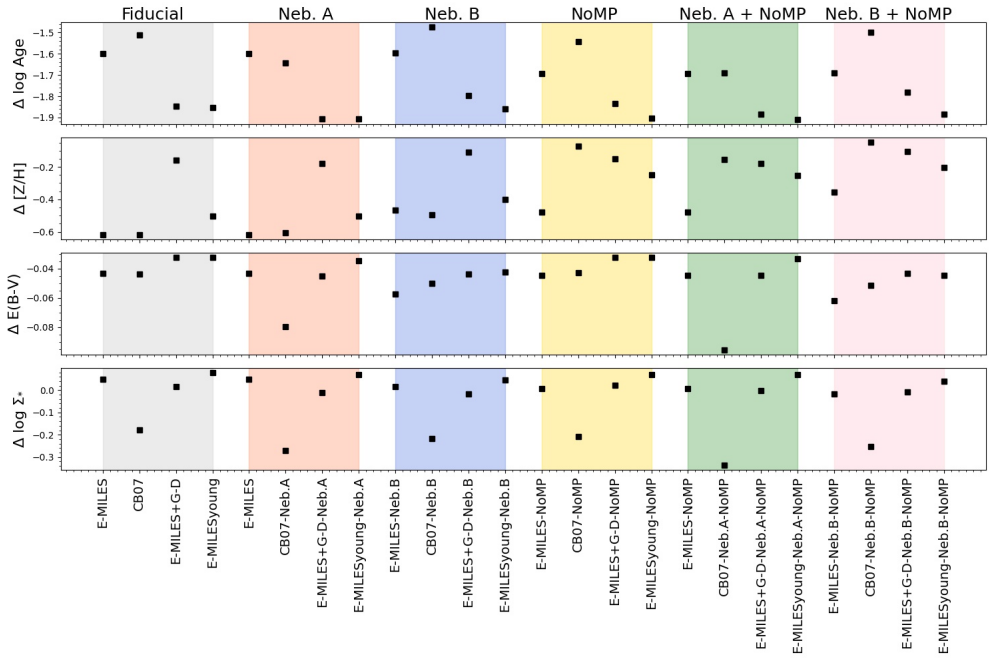

Figure 4.20: Values measured for Δlog age, Δ[Z/H], ΔE(B-V), and $\Delta \log \Sigma_*$, following Eq. 4.4, from the distribution of each one of these four quantities within the star-forming ring of NGC 3351, and in its surrounding disk, using each one of the sets of templates described in Sec. 4.4. We find that the MILES young templates, with the most metal-poor metallicity bin removed from the grid offers a good compromise between improving the young and metal-poor feature, reaching younger ages than our fiducial set of templates, and not leading to noticeable additional artifacts neither in the stellar mass surface density, nor in the stellar extinction map. See discussion in Sec. 4.4.5.

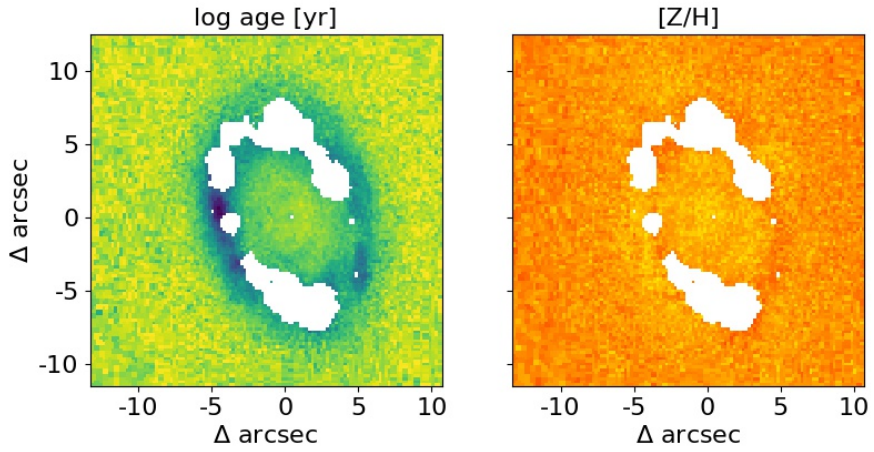

Figure 4.21: Stellar age (left) and metallicity (right) maps of the center of NGC 3351, after masking pixels with an extinction-corrected Hα surface density emission higher than 3×10^{-20} erg s^{-1} cm^{-2} pc^{-2}. This value successfully characterizes the youngest and most problematic regions.

4.5 Summary and conclusions

In this chapter, we have described in detail how to measure meaningful physical quantities such as stellar and gas kinematics, emission lines fluxes, and stellar populations properties from the MUSE mosaics of the PHANGS-MUSE galaxies, and we have also presented a quality assessment of some of the produced data products.

We have further described our efforts to improve the fitting of the spectra of regions dominated by young (< 30 Myr) stellar populations, where with our fiducial approach, we obtain unrealistically low ([Z/H] $<$ -1) stellar metallicities, which are unphysical given a scenario in which new stars are formed from gas that has been enriched by the previous generation of stars. These efforts include the usage of different libraries of templates, the subtraction of the stellar continuum before fitting the observed spectra, accounting for nebular emission, and varying the metallicity grid of the templates.

After an extensive set of tests, we find that the best outcome is obtained when we use a set of templates that includes SSP of ages as young as 6.5 Myr (namely MILES young, different from our fiducial set of templates) and when we remove extremely metal-poor values ([Z/H] = -1.33) from our metallicity grid, due to poorly constrained physics of the most metal-poor stars by the semi-empirical spectral libraries, and because such low metallicity values are also unlikely to be significantly present in the stellar disk of massive star-forming galaxies.

Nevertheless, we acknowledge that the fitting of the youngest regions is still sub-optimal, and we deem these metallicities as unreliable, masking them in further analysis presented in this thesis. Specifically, we have masked pixels with extinction-corrected Hα surface density emission higher than 3×10^{-20} erg s^{-1} cm^{-2} pc^{-2}.

Ongoing efforts to further improve the SSP fitting in the regions dominated by young stellar populations include a characterization of how different kinematic properties and dust-extinction of young stellar populations, with respect to older stars, can bias the computed SFHs. Similarly, including available photometric data from the PHANGS-HST survey to constrain bluer wavelength ranges would be a natural next step in the direction of improving the SSP fitting in these problematic regions. These refinements are, however, beyond the scope of this thesis.

5 Spatially resolved star-formation histories in PHANGS galaxies

This chapter will be published in a future refereed article (Pessa 2022, in prep.), which is still in progress.

5.1 Introduction

Understanding the process by which galaxies assemble their stellar mass through cosmic time is a crucial aspect of galaxy evolution. This process can be modulated either by external (e.g., merger of galaxies) or internal (e.g., secular evolution) mechanisms (Kormendy, 2013). These different mechanisms ultimately lead to the wide variety of galaxy properties that we see in the present-day Universe, such as morphologies and stellar populations. The study of stellar populations through the fossil method (Tinsley, 1968), which consists in reproducing the observed spectra with a linear combination of single stellar populations (SSPs) of known ages and metallicities, has demonstrated to be a powerful tool to unveil the assembly history of galaxies (e.g., Wilkinson et al., 2015; López Fernández et al., 2018; Zhuang et al., 2019; Neumann et al., 2020). Although the investigation of stellar populations has been used as an approach to address the evolution of galaxies for many years (Sarzi et al., 2005; Rogers et al., 2007), large Integral Field Spectroscopy (IFS or IFU) surveys, such as CALIFA (Sánchez et al., 2012) MaNGA (Bundy et al., 2015), and SAMI (Croom et al., 2012), have taken these studies to the next level, enabling the extraction of spectra from different regions of nearby galaxies simultaneously, with typical spatial resolutions of $\sim$1 kpc, and thus, resolving stellar populations and ionized gas properties in different regions and morphological components. This acknowledges the fact that galaxies are extended and complex objects whose stellar population and gas properties might change drastically from one specific region to another.

One of the most studied features in the context of spatially resolved stellar populations is the radial distribution of the properties (age and metallicity) of the underlying stellar populations (see, e.g., Sánchez-Blázquez et al., 2014; González Delgado et al., 2014b, 2016; Ibarra-Medel et al., 2016; Zheng et al., 2017; García-Benito et al., 2017; López Fernández et al., 2018; Zhuang et al., 2019; Parikh et al., 2021). These studies have revealed that radial gradients of age and metallicity is primarily connected with the Hubble type of the galaxy (Goddard et al., 2017; Parikh et al., 2021), with late-type galaxies (LTGs) showing negative age and metallicity gradients (i.e., centers are older and more metal-rich), and early-type galaxies (ETGs) showing a nearly flat age gradient, and a negative metallicity

gradient (albeit flatter than that found for LTGs). These works also report a dependency of the gradients on total stellar mass, where more massive galaxies exhibit steeper gradients.

In terms of galaxy evolution, negative age gradients point to an inside-out growth of galaxies, where the inner regions assembled their stellar mass earlier than outer regions. In this regard, Ibarra-Medel et al. (2016) found that LTGs would have a more pronounced inside-out formation mode, compared to ETGs (i.e., a more obvious difference between the formation times of inner and outer regions), and that low-mass galaxies ($M_* < 5 \times 10^9$) show a large diversity in their radial assembly history.

With respect to the origin of the metallicity gradients, Zhuang et al. (2019) find that they are a reflection of the local stellar mass surface density-metallicity relation (González Delgado et al., 2014a), and conclude that the spatial distribution of stellar populations within a galaxy is primarily the result of the in-situ local star formation history, rather than being shaped by radial migration. However, Neumann et al. (2021) report that the local correlation between stellar metallicity and stellar mass surface density (Σ_*) shows an increased scatter towards the outer part of galaxies, suggesting that something else, besides Σ_*, drives chemical enrichment at larger galactocentric distances (e.g., gas accretion, outflows). Zhuang et al. (2019) also find that low-mass LTGs show more commonly positive metallicity gradients, consistent with stellar feedback being more efficient in regulating the baryon cycle in the central regions of these galaxies.

Beyond radial gradients of stellar age and metallicity, recent studies have aimed at studying the assembly history of the galactic disk in a 2D manner (Peterken et al., 2019, 2020), by 'time-slicing' galaxies across their lifetime. However, the limited spatial resolutions of large IFU surveys place limitations on this kind of study. At a spatial resolution of ~ 1 kpc, much of the galactic structure is not resolved (spiral arms typically have widths of a few hundred parsecs; Querejeta et al., 2021).

In this chapter, we will present what we can learn from spatially resolved SFHs of a sample of LTGs, measured at spatial scales of ~ 100 pc, at which different morphological components are clearly resolved and can be studied separately. Thus, we can address how the properties of stellar populations vary as a function of local galactic environment and assess the importance/role of galactic structure in the assembly history of galaxies.

This chapter is structured as follows. In Sec. 5.2 we present the data and data products used in our analysis. In Sec. 5.3 we show our results and discussions. Finally, we present a summary and the conclusions of our analysis in Sec. 5.4.

5.2 Data

We use a sample of 19 star-forming galaxies, all of them are close to the star-forming main sequence of galaxies (SFMS; e.g., Brinchmann et al., 2004; Daddi et al., 2007; Noeske et al., 2007). These galaxies represent a subsample of the Physics at High Angular resolution in Nearby GalaxieS (PHANGS[17]) survey (Leroy et al., 2021a). The PHANGS galaxies have been chosen to be a representative set of galaxies where most of the star formation is occurring in the local Universe. They have been selected to have a distance smaller than 20 Mpc to resolve the typical scale of star-forming regions (50−100 pc) and to be moderately

[17] http://phangs.org/

inclined ($i < 60°$) to limit the effect of extinction and allow the identification of individual star-forming regions.

Table 5.1 summarizes our sample. We use the global parameters reported by Leroy et al. (2021a) and we use the distance compilation of Anand et al. (2021). The inclination values adopted are those reported by Lang et al. (2020).

5.2.1 VLT/MUSE

We make use of the PHANGS-MUSE survey (PI: E. Schinnerer; Emsellem et al., 2022). This survey employs the Multi-Unit Spectroscopic Explorer (MUSE; Bacon et al., 2014) optical integral field unit (IFU) mounted on the VLT UT4 to mosaic the star-forming disk of 19 galaxies from the PHANGS sample. These galaxies correspond to a subset of the 90 galaxies from the PHANGS-ALMA survey (PI: E. Schinnerer; Leroy et al., 2021a). The target selection for the PHANGS-MUSE sample focused on galaxies from the PHANGS parent sample that had already available ALMA data, as part of the ALMA pilot project, or from the ALMA archive.

The mosaics consist of 3 to 15 individual MUSE pointings. Each pointing provides a $1' \times 1'$ field of view sampled at 0.2 arcsecond per pixel, with a typical spectral resolution of $\sim$2.5 Å FWHM ($\sim$100 km s^{-1}) covering the wavelength range of 4800−9300 Å, and with spatial resolutions ranging from $\sim$0.5 to $\sim$1.0 arcsecond for the targets with and without AO, respectively. The nine galaxies observed with AO are marked with a black dot in the first column of Table 5.1. The total on-source exposure time per pointing for galaxies in the PHANGS-MUSE Large Program is 43 min. Observations were reduced using a pipeline built on `esorex` and developed by the PHANGS team[18] (Emsellem et al., 2022). The total area surveyed by each mosaic ranges from 23 to 441 kpc^2. Once the data have been reduced, we have used the PHANGS data analysis pipeline (DAP) to derive various physical quantities. The DAP is described in detail in Emsellem et al. (2022). It consists of a series of modules that perform single stellar population (SSP) fitting and emission line measurements to the full MUSE mosaic. Some of these outputs are described in Sec. 5.2.3.

5.2.2 Environmental masks

We employ the environmental masks described in Querejeta et al. (2021) to morphologically classify the different environments of each galaxy and label them as disk, spiral arms, rings, bars and centers. This classification was done using photometric data, mostly from the Spitzer Survey of Stellar structure in Galaxies (S^{4}G; Sheth et al., 2010). We refer the reader to that paper for a detailed explanation on how the masks are defined.

In brief, disks and centers are identified via 2D photometric decomposition of 3.6 μm images (see, e.g., Salo et al., 2015). A central excess of light is labeled as center, independently of its surface brightness profile. The size and orientation of bars and rings are defined visually on the NIR images, following Herrera-Endoqui et al. (2015) for S^{4}G galaxies. We define spiral arms by fitting a log-spiral function to bright regions along the arms on the NIR images, only when the spiral arms are clear features across the galaxy. The width of the spiral

[18] https://github.com/emsellem/pymusepipe

arms is determined empirically based on CO emission. We use these environmental mask to probe the properties of stellar populations separately across different galactic environments.

5.2.3 Stellar population properties maps

The PHANGS-MUSE DAP (Emsellem et al., 2022) includes a stellar population fitting module, a technique where a linear combination of SSP templates of known ages, metallicities, and mass-to-light ratios is used to reproduce the observed spectrum. This permits us to infer stellar population properties from an integrated spectrum, such as mass- or light-weighted ages, metallicities, and total stellar masses, together with the underlying star formation history.

Before doing the SSP fitting, we correct the full mosaic for Milky Way extinction assuming a Cardelli et al. (1989) extinction law and the $E(B-V)$ values obtained from the NASA/IPAC Infrared Science Archive[19] (Schlafly & Finkbeiner, 2011). In detail, our spectral fitting pipeline performs the following steps: First, we apply a Voronoi tessellation (Cappellari & Copin, 2003a) to bin our MUSE data to a minimum signal-to-noise ratio (S/N) of ∼35, computed at the wavelength range of 5300−5500 Å. This value is chosen in order to keep the relative uncertainty in our mass measurements below 15%, even for pixels dominated by a younger stellar population. To do this, we tried different S/N levels to bin a fixed region in our sample, and we bootstrapped our data to have an estimate of the uncertainties at each S/N level.

We use then the Penalized Pixel-Fitting (pPXF) code (Cappellari & Emsellem, 2004a; Cappellari, 2017a) to fit the spectrum of each Voronoi bin. We fit our data with a grid of templates consisting of 18 ages, ranging from 6.3 Myr to 14 Gyr, logarithmically-spaced, and four metallicity bins $[\mathbf{Z/H}] = [-0.7, -0.4, 0, 0.22]$. The templates are from the MILES (Vazdekis et al., 2010, 2012) database, assuming a Chabrier (2003) IMF and Padova isochrone (Girardi et al., 2000). The MILES templates originally were computed for a minimum age of 63 Myr (for the Padova isochrone). We have complemented this original set of templates with the young extension to the MILES SSP models presented in Asa'd et al. (2017), adding five additional age bins, from 6.3 Myr to ~ 40 Myr. These young templates have been computed for the same metallicity bins, except for the most metal-rich one, which for the young-extension templates is 0.41 (instead of 0.22). We fit the wavelength range 4850−7000 Å, in order to avoid spectral regions strongly affected by sky residuals.

We implemented a two-steps SSP fitting. First, we fitted our data assuming a Calzetti et al. (2000) extinction law to correct for internal extinction. We then corrected the observed spectrum using the measured extinction value before fitting it a second time, including a 12 degree multiplicative polynomial in this iteration. This two-step fitting process accounts for offsets between individual MUSE pointings. These offsets arise because different MUSE pointings are not necessarily observed under identical weather conditions, and variations in the sky continuum levels might lead to subtle differences in the flux calibration of individual neighboring MUSE pointing. An analysis of the regions of the mosaic where different pointings overlap revealed that these variations yield differences in the measured stellar extinction levels of the order of ΔE(B-V) ~ 0.04 (see Emsellem et al., 2022, for a detaled description of this issue). Therefore, in the first iteration of the SSP fitting, we measure a

[19] https://irsa.ipac.caltech.edu/applications/DUST/

reddening value, and correct the observed spectra accordingly, and in the second iteration, we use a high-degree multiplicative polynomial to correct for those nonphysical features and homogenize the outcome of the different pointings. To recover the kinematic properties of the observed spectra, the templates are shifted in the velocity space and convolved to match observed spectral features. We fit the first two velocity moments (v, σ), using a single stellar kinematic component, i.e., the same velocity and velocity dispersion is applied to all the templates used for the SSP fitting.

The output of `pPXF` consists of a vector with the weights of the templates that best reproduce the observed spectrum. Physically, these weights represent the fraction of the total stellar mass born with a given metallicity, at a given lookback time, and they are used to produce the final maps, including stellar mass surface densities, and both light- or mass-weighted ages and metallicities. The stellar mass surface density maps include both, contributions from live stars and remnants. The total weight for a given age bin, integrating for the different metallicity values, also represent the SFH of a given spectrum. For each pixel, the average age and metallicity are computed as:

$$\langle \log \mathrm{age} \rangle = \frac{\Sigma_i \log(\mathrm{age}_i)\, w_i}{\Sigma_i\, w_i} \tag{5.1}$$

and

$$\langle [\mathrm{Z/H}] \rangle = \frac{\Sigma_i\, [\mathrm{Z/H}]_i\, w_i}{\Sigma_i\, w_i}\ , \tag{5.2}$$

where age_i and $[\mathrm{Z/H}]_i$ correspond to the age and metallicity of each template, and w_i is its corresponding weight in the linear combination. To convert mass-weighted quantities to light-weighted quantities, we use the mass-to-light ratio of each template in the V-band. We compute luminosity-fraction weights as:

$$w_i^{\mathrm{LW}} = \frac{w_i}{(M/L_V)_i}\ , \tag{5.3}$$

where w_i^{LW} corresponds to the luminosity-fraction weight of a given template, w_i its mass-fraction weight, and $(M/L_V)_i$ correspond to its mass-to-light ratio in the V-band. We can use these luminosity-fraction weights to calculate light-weighted properties, following Equations 5.1 and 5.2.

We use Monte Carlo simulations to estimate the uncertainty in the recovered stellar population parameters. For each spectrum, we performed 20 Monte Carlo iterations, where in each iteration, we perturb the input spectrum assuming a Gaussian noise with a mean of zero and a standard deviation corresponding to the error vector at each wavelength bin. The uncertainties of stellar population parameters are calculated as the standard deviation of their distributions produced by the Monte Carlo realizations. This is meant as a first-order estimate of the true uncertainties. We only run Monte Carlo realizations for the second step of the fitting procedure, once the stellar extinction has been fixed. Hence, no error is computed for the stellar $E(B-V)$. Finally, we have identified foreground stars as velocity outliers in the SSP fitting, and we have masked those pixels for the analysis carried out in this chapter.

Target	RA	DEC	$\log_{10}(M_*)$	$\log_{10}(M_{H_2})$	$\log_{10}(M_{H_I})$	$\log_{10}(SFR)$	ΔMS	Distance	Inclination	Mapped area
	(degrees)	(degrees)	($M_\odot$)	($M_\odot$)	($M_\odot$)	($M_\odot\, yr^{-1}$)	(dex)	(Mpc)	(degrees)	(kpc^2)
(1)	(2)	(3)	(4)	(5)	(6)	(7)	(8)	(9)	(10)	(11)
NGC0628	24.1739	15.7836	10.3	9.4	9.7	0.24	0.18	9.84±0.61	8.9	98
NGC1087	41.6049	−0.4987	9.9	9.2	9.1	0.12	0.33	15.85±2.08	42.9	128
NGC1300•	49.9208	−19.4111	10.6	9.4	9.4	0.07	-0.18	18.99±2.67	31.8	366
NGC1365	53.4015	−36.1404	11.0	10.3	9.9	1.23	0.72	19.57±0.77	55.4	421
NGC1385•	54.3690	−24.5012	10.0	9.2	9.2	0.32	0.50	17.22±2.42	44.0	100
NGC1433•	55.5062	−47.2219	10.9	9.3	9.4	0.05	-0.36	18.63±1.76	28.6	441
NGC1512	60.9756	−43.3487	10.7	9.1	9.9	0.11	-0.21	18.83±1.78	42.5	270
NGC1566•	65.0016	−54.9380	10.8	9.7	9.8	0.66	0.29	17.69±1.91	29.5	212
NGC1672	71.4270	−59.2473	10.7	9.9	10.2	0.88	0.56	19.4±2.72	42.6	255
NGC2835	139.4704	−22.3547	10.0	8.8	9.5	0.09	0.26	12.22±0.9	41.3	88
NGC3351	160.9906	11.7037	10.4	9.1	8.9	0.12	0.05	9.96±0.32	45.1	76
NGC3627	170.0625	12.9915	10.8	9.8	9.1	0.58	0.19	11.32±0.47	57.3	87
NGC4254•	184.7068	14.4164	10.4	9.9	9.5	0.49	0.37	13.1±1.87	34.4	174
NGC4303•	185.4789	4.4737	10.5	9.9	9.7	0.73	0.54	16.99±2.78	23.5	220
NGC4321•	185.7289	15.8223	10.7	9.9	9.4	0.55	0.21	15.21±0.49	38.5	196
NGC4535•	188.5846	8.1980	10.5	9.6	9.6	0.33	0.14	15.77±0.36	44.7	126
NGC5068	199.7281	−21.0387	9.4	8.4	8.8	−0.56	0.02	5.2±0.22	35.7	23
NGC7496•	347.4470	−43.4278	10.0	9.3	9.1	0.35	0.53	18.72±2.63	35.9	89
IC5332	353.6145	−36.1011	9.7	–	9.3	−0.39	0.01	9.01±0.39	26.9	34

Table 5.1: Summary of the galactic parameters of our sample adopted through this work. •: Galaxies observed with MUSE WFM-AO mode. Values in columns (4), (5), (6), and (7) correspond to those presented in Leroy et al. (2021a). Column (8) provides the vertical offset of the galaxy from the integrated main sequence of galaxies, as defined in Leroy et al. (2019). Distance measurements are taken from Anand et al. (2021) and inclinations from Lang et al. (2020). Uncertainties for the values in columns (4), (5), (6), (7), and (8) are on the order of 0.1 dex. Column (11) lists the area mapped by MUSE.

5.3 Results

In Chapter 4 of this thesis, we have described in detail the methodology adopted to fit the spectra of galaxies in our sample with a linear combination of SSPs to derive their SFHs, in a spatially resolved manner. In the following sections, we will show how we can use them to gain insights into galaxy assembly and evolution.

5.3.1 Radial structure of stellar population properties

The radial distribution of the mean stellar populations across the galactic disk, such as age and metallicity, has been widely studied thanks to integral field spectroscopy surveys, such as CALIFA (Sánchez et al., 2012), MaNGA (Bundy et al., 2015) and SAMI (Croom et al., 2012), as it is intimately related to the galaxy's assembly process (e.g., Sánchez-Blázquez et al., 2014; González Delgado et al., 2014b, 2016; García-Benito et al., 2017; Zhuang et al., 2019; Parikh et al., 2021). However, these studies have typically been performed a spatial resolutions on the order of ~ 1 kpc. Late-type galaxies often exhibit non-axisymmetric morphological features, such as bars, or spiral arms that can not be resolved at these spatial scales, and their peculiarities would not be captured in an azimuthally averaged radial profile either.

In this section, we show the radial distribution of the light- and mass-weighted mean age

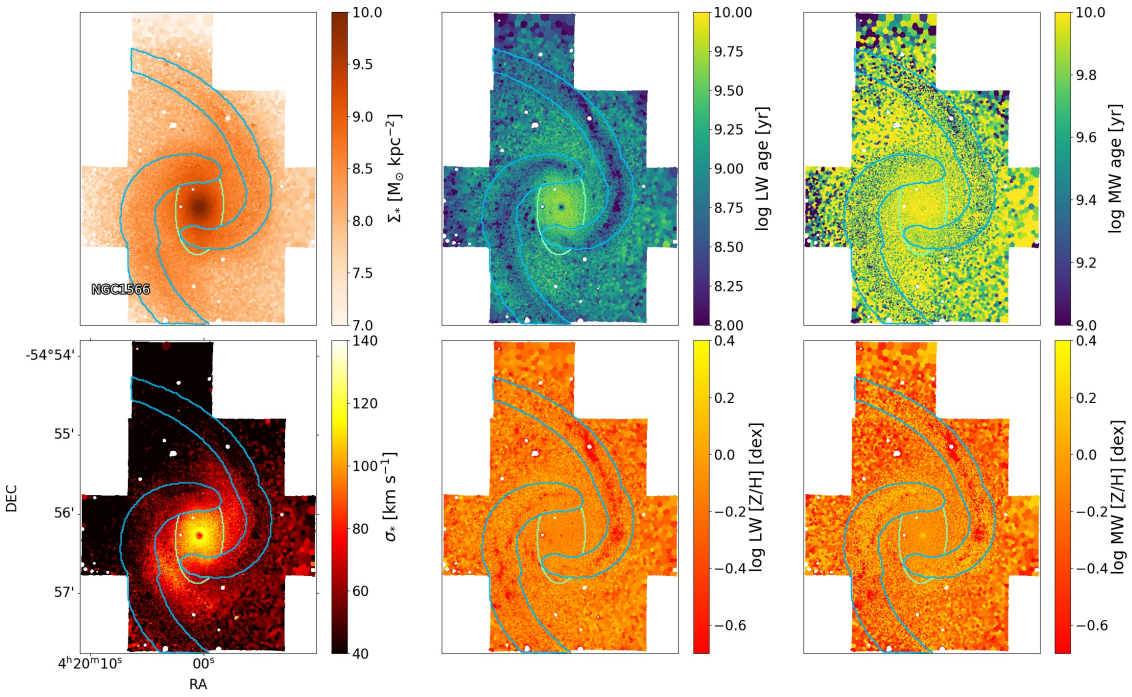

Figure 5.1: Example of some of the DAP outputs obtained for the mosaic of NGC 1566. Stellar mass surface density (top-left), light-weighted age (top-center), mass-weighted age (top-right), stellar velocity dispersion (bottom-left), light-weighted [Z/H] (bottom-center), and mass-weighted [Z/H] (bottom-right). The spiral arms and bar of the galaxy are marked with blue and green contours, respectively.

and metallicity of the stellar populations of PHANGS galaxies, at a resolution of ~ 100 pc, thus, clearly resolving their different morphological components. While light-weighted quantities are very sensitive to recent star formation events, and thus, encode information about the ongoing galaxy evolution, mass-weighted quantities trace the properties of long-lived low-mass stars that dominate the stellar mass budget, and thus, encode information about the mass growth and secular redistribution history of galaxies. Fig. 5.1 show the stellar mass surface density, velocity dispersion, mean light- and mass-weighted age, and mean light- and mass-weighted metallicity for a galaxy in our sample (NGC 1566), as an example of our mean stellar population properties maps. Overplotted contours delimit the spiral structure and the bar.

We derive the radial variation of these parameters, averaging the quantities azimuthally in concentric rings. The size of the radial bins is defined according to the size of each galaxy, parametrized using the R_{25} radius. Each radial bin has a width of $0.03\,R_{25}$, corresponding to a physical size of about 0.4 ± 0.2 kpc for the galaxies in our sample. For each radial bin, ages and metallicities of the stellar populations are azimuthally averaged. To define the radial bins consistently, we use the galactic inclinations reported in Lang et al. (2020), measured from CO(2-1) data. Only those radial bins in which at least one-third of the ring is covered by the MUSE mosaic are considered valid for the radial profiles.

Age radial profiles

Figure 5.2 shows the light-weighted (LW) age profiles for the 19 galaxies in our sample, for the full field of view (FoV), and each morphological component separately. LW quantities are strongly biased towards young populations (e.g., Zibetti et al., 2017). Therefore, sudden declines in these profiles are associated with recent star formation.

The first obvious feature here is the overall decreasing trend with radius present for most of the galaxies in our sample. Negative age gradients have been reported in previous studies (e.g., Sánchez-Blázquez et al., 2014; González Delgado et al., 2014b). The only exceptions are NGC 1087 and NGC 1385, which are both on the low-mass end of our sample (log M_* of 9.9 and 10.0, respectively). This is consistent with previous findings of a larger diversity in the radial structure of low-mass galaxies (Ibarra-Medel et al., 2016). This trend can be more clearly appreciated in the last panel of Fig. 5.2, where low-mass galaxies (blue) show either flat or negative gradients, while higher mass galaxies (green) show mostly negative gradients. This panel also reveals a clear trend of the normalization of the LW age radial profile with total stellar mass of the galaxies, where more massive galaxies are in general older than lower mass galaxies.

Now we look at specific galactic strucutures. Some galaxies show evidence of recent star formation in their inner-most region. Althought our sample suggest that this rejuvenation occurs preferentially in the central region of barred galaxies, the low number of non-barred galaxies in our sample, makes it hard to determine exactly the impact of the bar on this phenomenon. Spiral arms show up usually as younger structures at any given radius, compared to the disk, indicating that star formation is occurring preferentially in spiral arms. On the other hand, bars show also a very clear negative profile. Some galaxies show a sharp drop in LW age at the outer radius of the bar (NGC 1300, NGC 1365, NGC 1672, NGC 7496), consistent with a scenario where the oldest populations dominate in the inner and rounder part of the bar, while young population are located on more elongated orbits, populating the

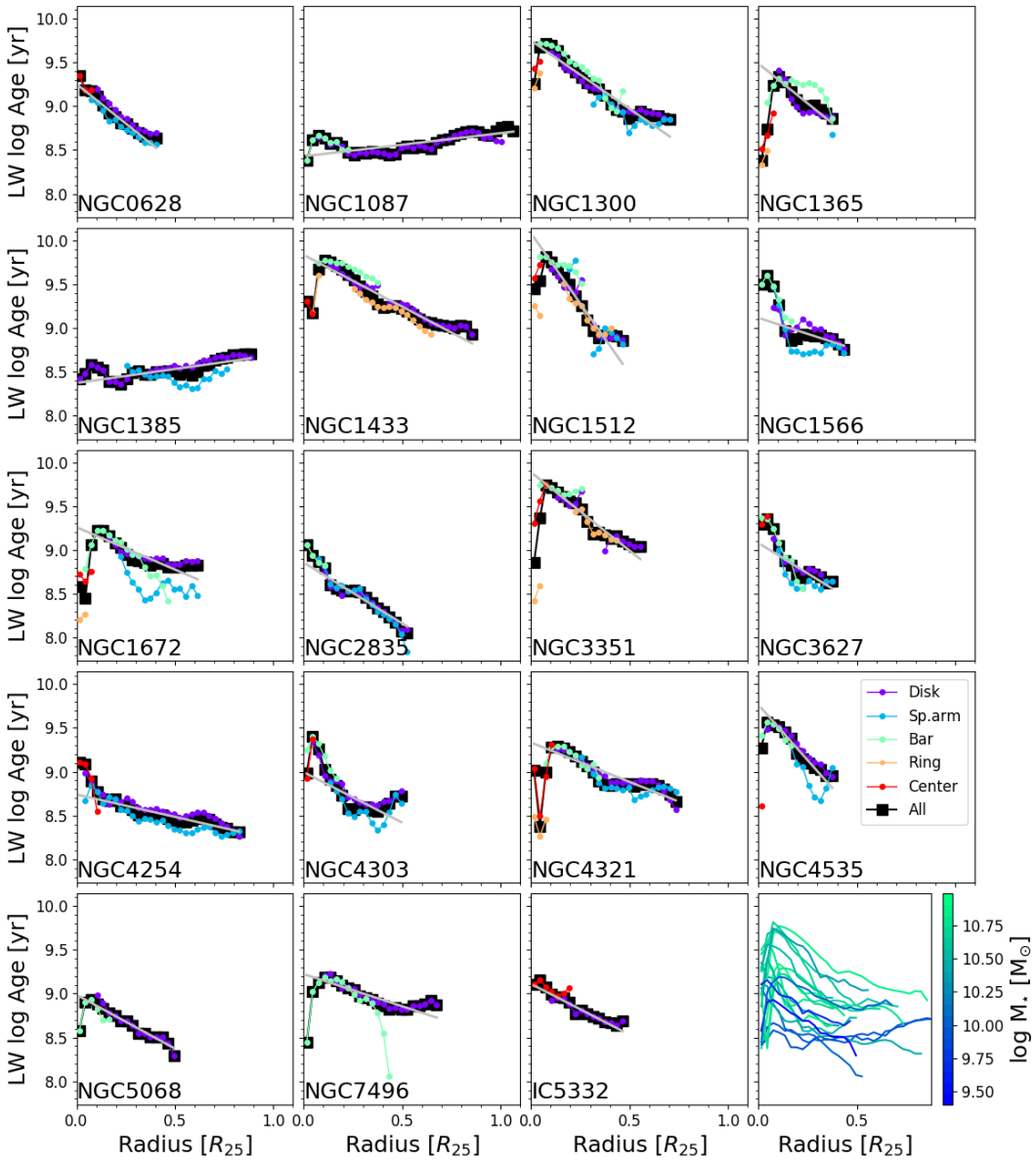

Figure 5.2: Light-weighted stellar age radial profiles for the galaxies in our sample. Different colors indicate the radial gradient measured across different environments, as indicated in the legend of the last panel (from left to right) of the fourth row. The black line shows the gradient measured for the entire FoV (i.e., all environments together). The galactocentric distance is measured in units of R_{25}, in order to measure radial distance homogeneously across our sample. The dashed line shows the best-fit gradient for each galaxy. The bottom-right panel displays the entire FoV trends for all galaxies, color-coded by total stellar mass.

bar ends (Wozniak, 2007; Neumann et al., 2020). It is also worth noting that many galaxies exhibit a clear flattening of their radial gradients towards larger radii. This break in the radial gradient roughly coincides with the bar radius, when a bar is present.

Figure 5.3 shows the mass-weighted (MW) age profiles for the galaxies in our sample. Mass-weighted quantities are dominated by faint, but much more numerous low-mass stars, which comprise the bulk of the total mass of galaxies. Hence, mass-weighted quantities trace much better the assembly history of galaxies, as they are not biased by recent star-formation events (Conroy, 2013). As a consequence, MW ages are older than their LW counterpart, as the bulk of the mass of a galaxy is dominated by old stellar populations (see, e.g., Cook et al., 2020).

The most evident feature in the radial MW age profiles is that environmental differences are basically absent, and that the dynamic range in age is drastically reduced, typically confined to values older than log (age/yr) ≈ 9.5 (~ 3 Gyr). This implies that the distribution of older stellar populations is significantly more homogeneous across the galactic structure than for younger populations. Clear negative trends persist in the MW profile (although they are shallower, consistent with findings from Parikh et al. (2021) and Neumann et al. (2020)), meaning that inner regions assembled the bulk of their stellar mass earlier in cosmic history than outer regions. These age gradients have been interpreted as a spatially resolved imprint of the inside-out (Mo et al., 1998) growth of galaxies by several studies (e.g., González Delgado et al., 2014b; Goddard et al., 2017; Parikh et al., 2021). The bottom-right panel of Fig. 5.3 also shows a clear gradient of the normalization of the MW age profile with the total stellar mass of galaxies, where more massive galaxies show older MW ages, which can be interpreted as an imprint of the downsizing in galaxy evolution (Heavens et al., 2004; Pérez-González et al., 2008, see also Sec. 5.3.4). Finally, it is worth noting that the break of the age gradient at approximately the bar radius discussed earlier persists for the MW age gradients, although it is more subtle, due to the smaller dynamical range of the MW ages. The sharp decrease of age in the central region also persists in the MW age profile of some galaxies, indicating that these centers have formed a substantial amount of stellar mass in relatively recent times. In Sec. 5.3.3, we investigate this further.

Finally, the slope of both, LW- and MW-age radial gradients span a wide range of values. We measured these gradients using an ordinary least-squares (OLS) fitting routine to fit a linear model to the radial profiles of the full FoV (i.e., all environments together), but dropping the inner-most radial bins (r $< 0.06\ R_{25}$), that are often outliers in the radial trend. The linear models are indicated with a grey line in Figs. 5.2 and 5.3. We investigated if these gradients correlate with global galaxy properties. We acknowledge the caveat that although the linear models generally capture well the observed radial trend, some galaxies show gradients that are intrinsically hard to capture with a simple linear model (e.g., LW log age radial profile of NGC 1566 or NGC 3627). In these galaxies, a single slope is not sufficient to describe the observed gradients, and a more appropriate representation of the data would be provided by a compound model with two different slopes. However, a more sophisticated modeling is beyond the scope of the analyses presented here.

Figure 5.4 shows the slope of the LW-age gradients, as a function of total stellar mass (log M_*), total SFR (log SFR), offset from the global main sequence of galaxies as defined in Leroy et al. (2019) (ΔMS), total molecular gas mass-to-stellar mass ratio (M_{mol} / M_*), total atomic gas mass-to-stellar mass ratio (M_{HI}), total gas (molecular + atomic)-to-stellar

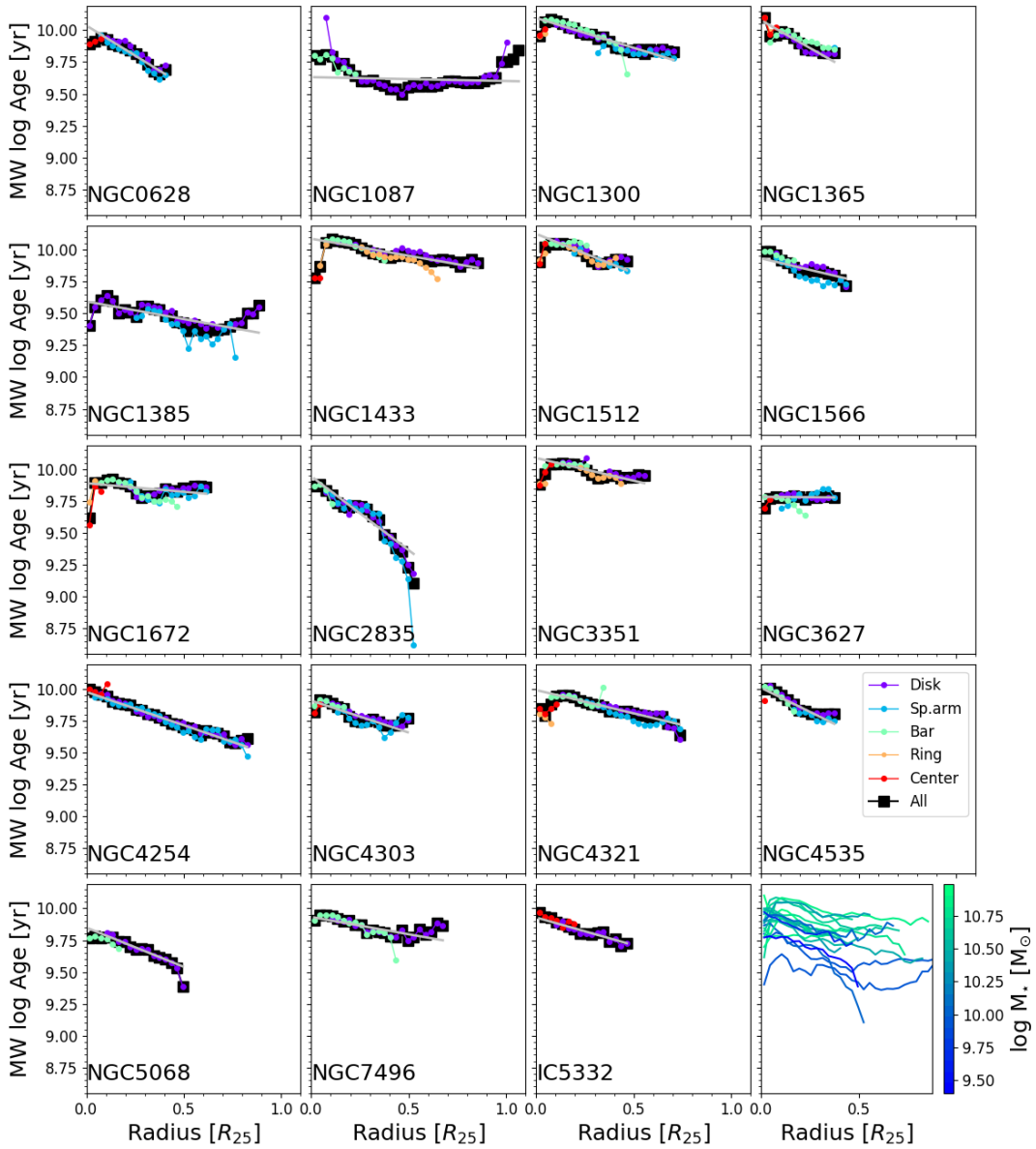

Figure 5.3: Mass-weighted stellar age radial profiles for the galaxies in our sample. Different colors indicate the radial gradient measured across different environments, as indicated in the legend of the last panel (from left to right) of the fourth row. The black line shows the gradient measured for the entire FoV (i.e., all environments together). The galactocentric distance is measured in units of R_{25}, in order to measure radial distance homogeneously across our sample. The dashed line shows the best-fit gradient for each galaxy. The bottom-right panel displays the entire FoV trends for all galaxies, color-coded by total stellar mass.

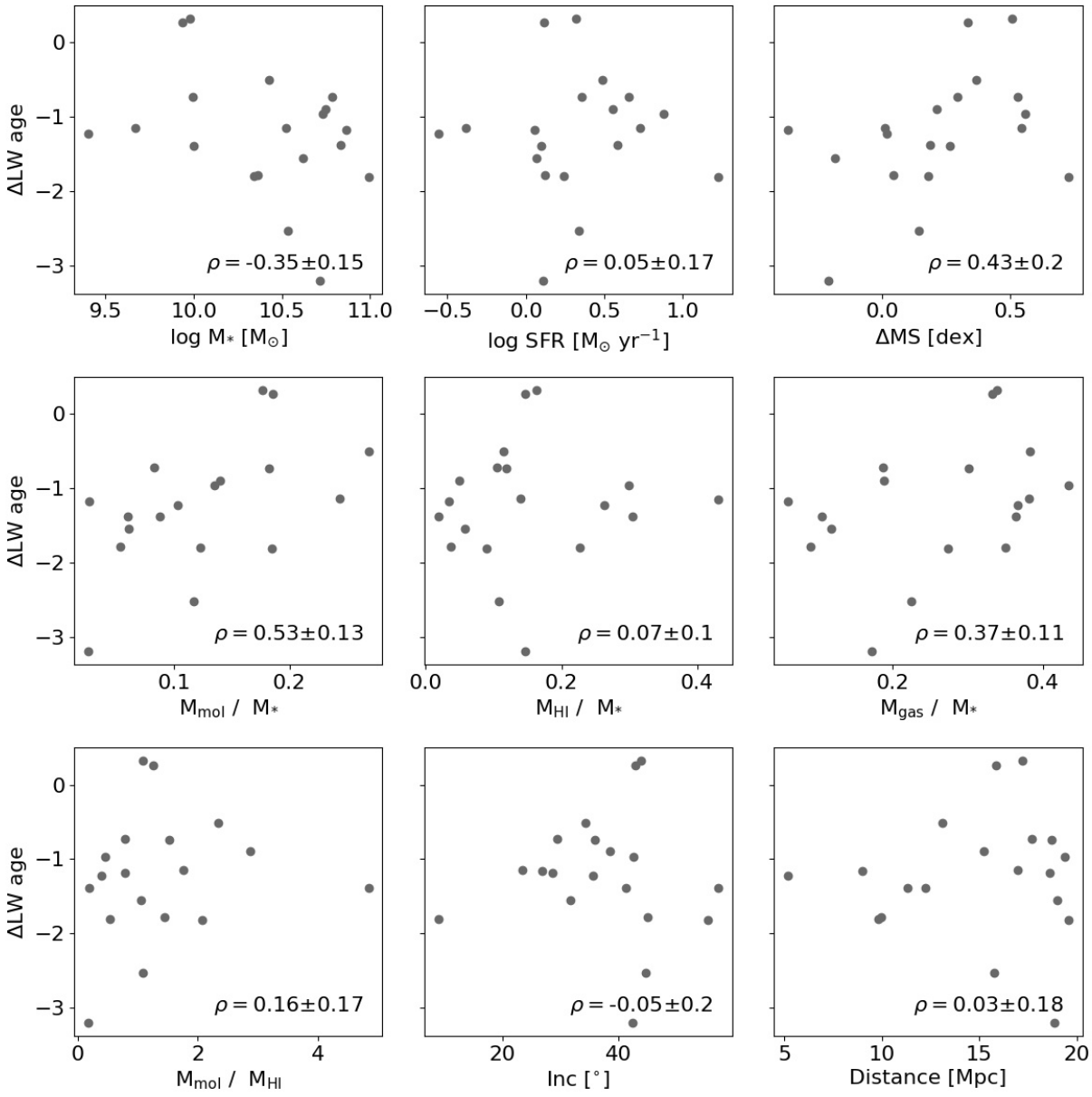

Figure 5.4: Slope of the LW-age gradient, as a function of (from left to right, and from top to bottom) total stellar mass (log M_*), total SFR (log SFR), offset from the global main sequence of galaxies (ΔMS), total molecular gas mass-to-stellar mass ratio (M_{mol} / M_*), total atomic gas mass-to-stellar mass ratio (M_{HI}), total gas (molecular + atomic)-to-stellar mass ratio M_{gas} / M_*, and molecular-to-atomic gas mass ratio (M_{mol} / M_{HI}), galaxy inclination and distance. The Pearson correlation coefficient for each parameter is indicated in the bottom-right corner of each panel.

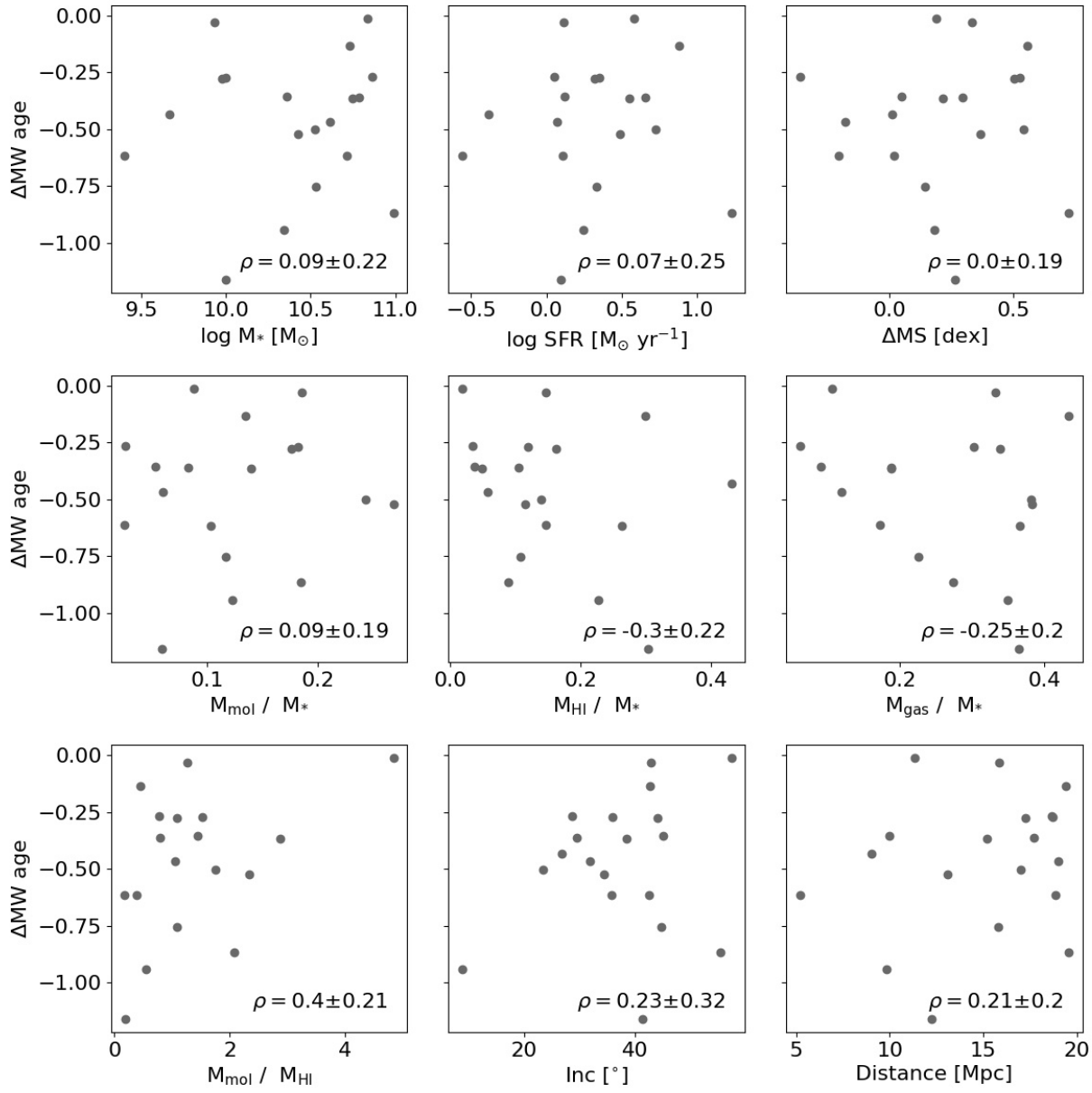

Figure 5.5: Slope of the MW-age gradient, as a function of (from left to right, and from top to bottom) total stellar mass (log M_*), total SFR (log SFR), offset from the global main sequence of galaxies (ΔMS), total molecular gas mass-to-stellar mass ratio (M_{mol} / M_*), total atomic gas mass-to-stellar mass ratio (M_{HI}), total gas (molecular + atomic)-to-stellar mass ratio M_{gas} / M_*, and molecular-to-atomic gas mass ratio (M_{mol} / M_{HI}), galaxy inclination and distance. The Pearson correlation coefficient for each parameter is indicated in the bottom-right corner of each panel.

mass ratio M_{gas} / M_*, and molecular-to-atomic gas mass ratio (M_{mol} / M_{HI}). We also include inclination and distance, to ensure that the different gradients are not related to these non-intrinsic properties.

The strongest correlation are with M_{mol} / M_* ($\rho = 0.53$) and ΔMS ($\rho = 0.43$) implying that galaxies with higher molecular gas content and a global enhancement of SFR also have a less negative (i.e. flatter) LW-age radial gradient. This is consistent with the findings from Ellison et al. (2018) and Pessa et al. (2021), where the authors find that a global enhancement of SFR is reflected primarily on the SFR of the inner galactic regions. In this case, since the LW-age is very sensitive to recent star-formation, a more negative gradient implies an older and less star-forming central region, with respect to the outer radii.

Figure 5.5 shows the same set of correlations for the MW-age gradients. The slopes of the MW-age gradients do not correlate strongly neither with ΔMS, M_{mol} / M_*, nor with any of the parameters explored. However, we see a trend in which galaxies with a high total gas content span a wide range of gradients, while galaxies with a low gas content exhibit exclusively flatter gradients. This trend could indicate that galaxies with a low gas content have consumed their gas supply to fuel star formation, leading to younger populations in their centers, hence, flatter MW-age profiles. Even though the level of correlation of M_{mol} / M_* with LW-age is not particularly high ($\rho = 0.37$), the trend seems to be opposite to the one with MW-age. This is not in contradiction with the scenario suggested for the origin of the trend between the MW-age gradient and M_{mol} / M_*, since a low total gas content could certainly imply a lower total present-day SFR (and hence, less SFR in the central region), but it does not imply a lack of SFR on longer time-scales, to which MW-age is sensitive (as opposite to LW-age, that is strongly biased toward recent SFR).

In summary, we find generally negative age radial gradients, with LW profiles being steeper than the MW ones. We also see a flattening of the age profiles towards the outer radii. More massive galaxies are overall older than less massive galaxies. Galaxies with higher total-gas content and that are experiencing a global enhancement of SFR exhibit flatter LW age profiles. Morphological features can be distinguished in the LW gradients. Spiral arms host young populations than the disk at a given radius, and bars often show a sharp decrease towards the bar ends, indicating that younger stellar populations are located preferentially on more elongated orbits. However, MW age profiles do not exhibit obvious differences across the different galactic morphological features, indicating that older stellar populations are homogeneously distributed across the galaxy.

Metallicity radial profiles

Regarding stellar metallicity, Figs. 5.6 and 5.7 show the LW and MW stellar metallicity profiles measured for our sample galaxies. The figures show flatter, generally slightly negative profiles, with the exception of the same two low-mass galaxies mentioned earlier (NGC 1087, NGC 1385). Overall, negative trends are consistent with results reported previously in the literature (Goddard et al., 2017; Coenda et al., 2020). On the other hand, NGC 1385 shows a strongly positive metallicity gradient. This is consistent with the findings from Zhuang et al. (2019), who reported that low-mass and late morphological types commonly show positive metallicity profiles, which can be explained due to stellar feedback more efficiently modifying the baryon cycle in these galaxies. In some galaxies, spiral arms show up with a slightly lower metallicity than the disk at a given radius. This is likely an artifact arising

from the SSP fitting, and the imperfect masking of the youngest regions (see Chapter 4 of this thesis).

Zhuang et al. (2019) also show that these metallicity gradients are a consequence of the local [Z/H]-stellar mass surface density (Σ_*) relation, and that they are expected to arise primarily due to the in-situ local star formation history. Indeed, Neumann et al. (2021) report a tight correlation between [Z/H] and Σ_*, with a higher scatter towards larger galactocentric radii, implying that in the outer regions of galaxies, additional mechanisms such as gas accretion or outflows might become relevant in determining the chemical enrichment.

The bottom-right panels of Figs. 5.6 and 5.7 show a clear dependency of the normalization of the stellar metallicity gradients on total stellar mass. This trend is expected from the well studied mass-metallicity relation of galaxies (Foster et al., 2012; Ma et al., 2016), which is thought to arise because more massive galaxies are more likely to retain a larger fraction of their metals due to their stronger gravitational potential, as opposed to low-mass galaxies, in which stellar feedback is able to remove metals more efficiently (see, e.g., Ma et al., 2016).

Finally, there are some peculiarities in the metallicity gradients that are worth mentioning. NGC 3351 exhibits an 'S' shape LW metallicity gradient, which originates from recent star formation occurring in the central region and in the outer ring, leading to enhanced metallicities at these radii. NGC 4535 also has strong star formation at the ends of its bar and in the spiral arms, leading to enhanced metallicities in these environments. NGC 7496 shows a sharp decrease in metallicity in the bar profile, which is likely an artifact from the SSP fitting (see Chapter 4 of this thesis). The LW metallicity gradient of NGC 1433 shows a strange discontinuous pattern that is likely an artifact originated due to subtle systematic differences between the MUSE pointings of the mosaic.

Figures 5.8 and 5.9 show the LW- and MW- stellar metallicity gradients, as a function of the same global properties that we explored for the age gradients. We do not see any obvious trends between metallicity gradients and these global properties. Goddard et al. (2017) report steeper negative metallicity profiles for more massive galaxies. In our sample, we find that the highest ρ values are indeed obtained with total stellar mass and total SFR, however, possibly due to our low-number statistics, we can not robustly confirm such a trend, but in general, it seems that low-mass galaxies ($\log(M_*/M_\odot) \lesssim 10$) span a more diverse range of gradients, while higher mass galaxies exhibit stellar metallicity gradients that correlate better with total mass.

In summary, we find negative stellar metallicity radial profiles, with more massive galaxies exhibiting overall higher metallicities and steeper gradients. Lower-mass galaxies, on the other hand, show a larger variety in their gradients. Some specific features in the LW metallicity gradients correlate with recent star formation episodes yielding higher stellar metallicities in specific environments, such as rings, spiral arms, or bar ends.

5.3.2 Evidence for radial mixing in bars?

Interaction of stars or gas with non-axisymmetric structures can lead to gain or loss of angular momentum, ultimately causing their radial migration towards inner or outer orbits. Different mechanisms, such as the exchange of angular momentum at the corotation resonance of spiral arms (Sellwood & Binney, 2002), or induced by the bar-spiral arms resonance overlap (Minchev et al., 2011) are thought to drive the migration of stars. Radial migration of

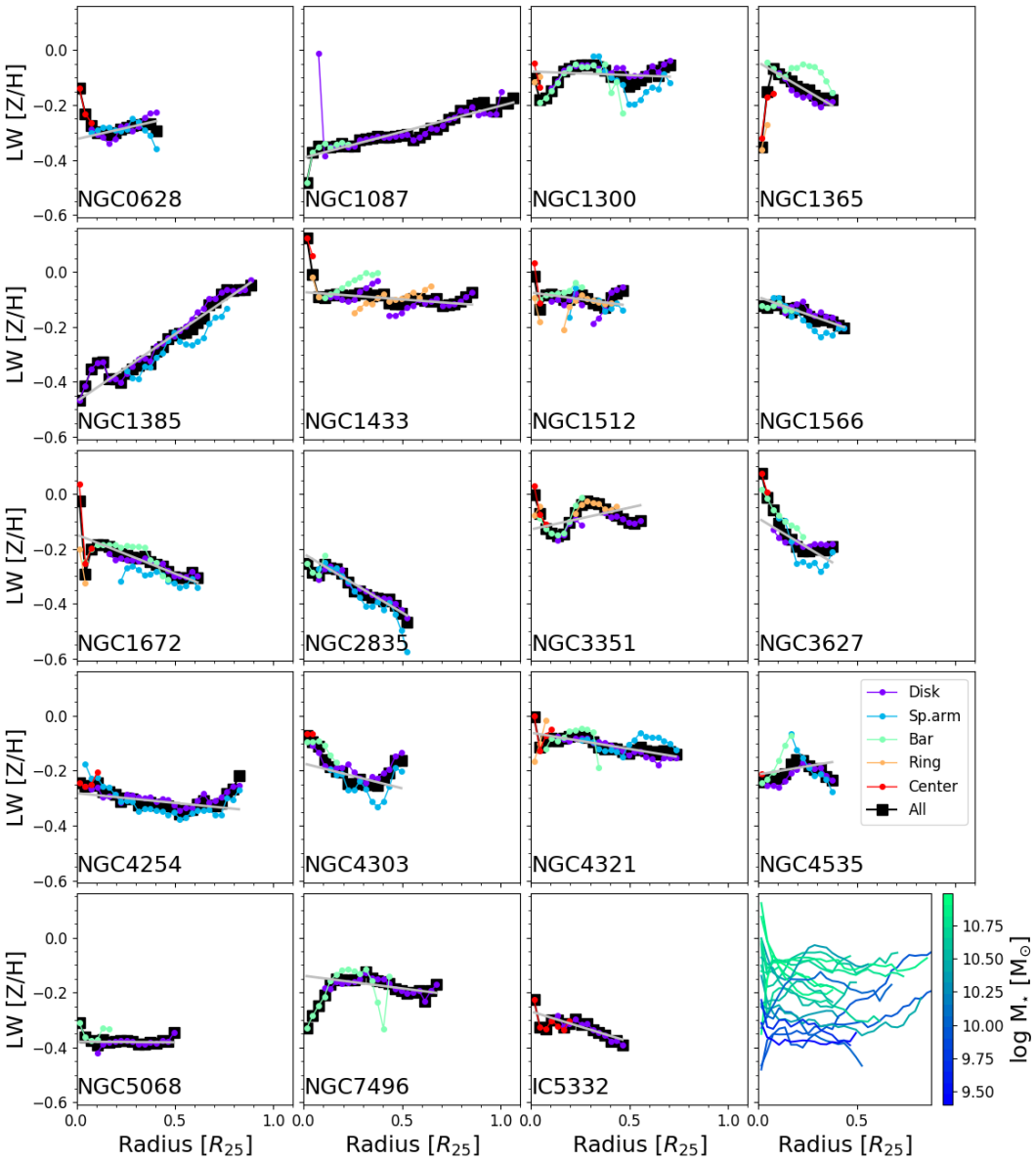

Figure 5.6: Light-weighted stellar [Z/H] radial profiles for the galaxies in our sample. Different colors indicate the radial gradient measured across different environments, as indicated in the legend of the last panel (from left to right) of the fourth row. The black line shows the gradient measured for the entire FoV (i.e., all environments together). The galactocentric distance is measured in units of R_{25}, in order to measure radial distance homogeneously across our sample. The dashed line shows the best-fit gradient for each galaxy. The bottom-right panel displays the entire FoV trends for all galaxies, color-coded by total stellar mass.

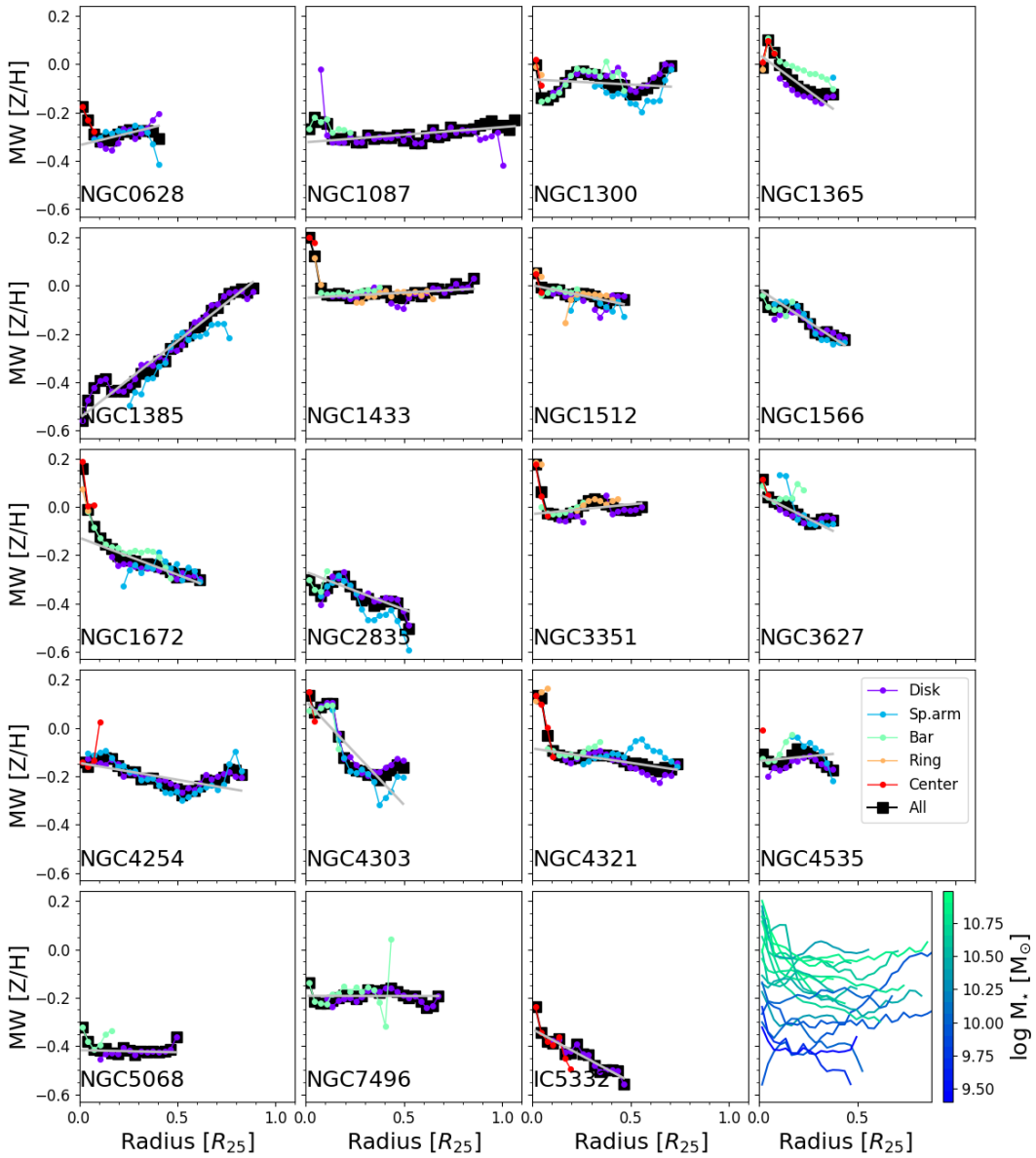

Figure 5.7: Mass-weighted stellar [Z/H] radial profiles for the galaxies in our sample. Different colors indicate the radial gradient measured across different environments, as indicated in the legend of the last panel (from left to right) of the fourth row. The black line shows the gradient measured for the entire FoV (i.e., all environments together). The galactocentric distance is measured in units of R_{25}, in order to measure radial distance homogeneously across our sample. The dashed line shows the best-fit gradient for each galaxy. The bottom-right panel displays the entire FoV trends for all galaxies, color-coded by total stellar mass.

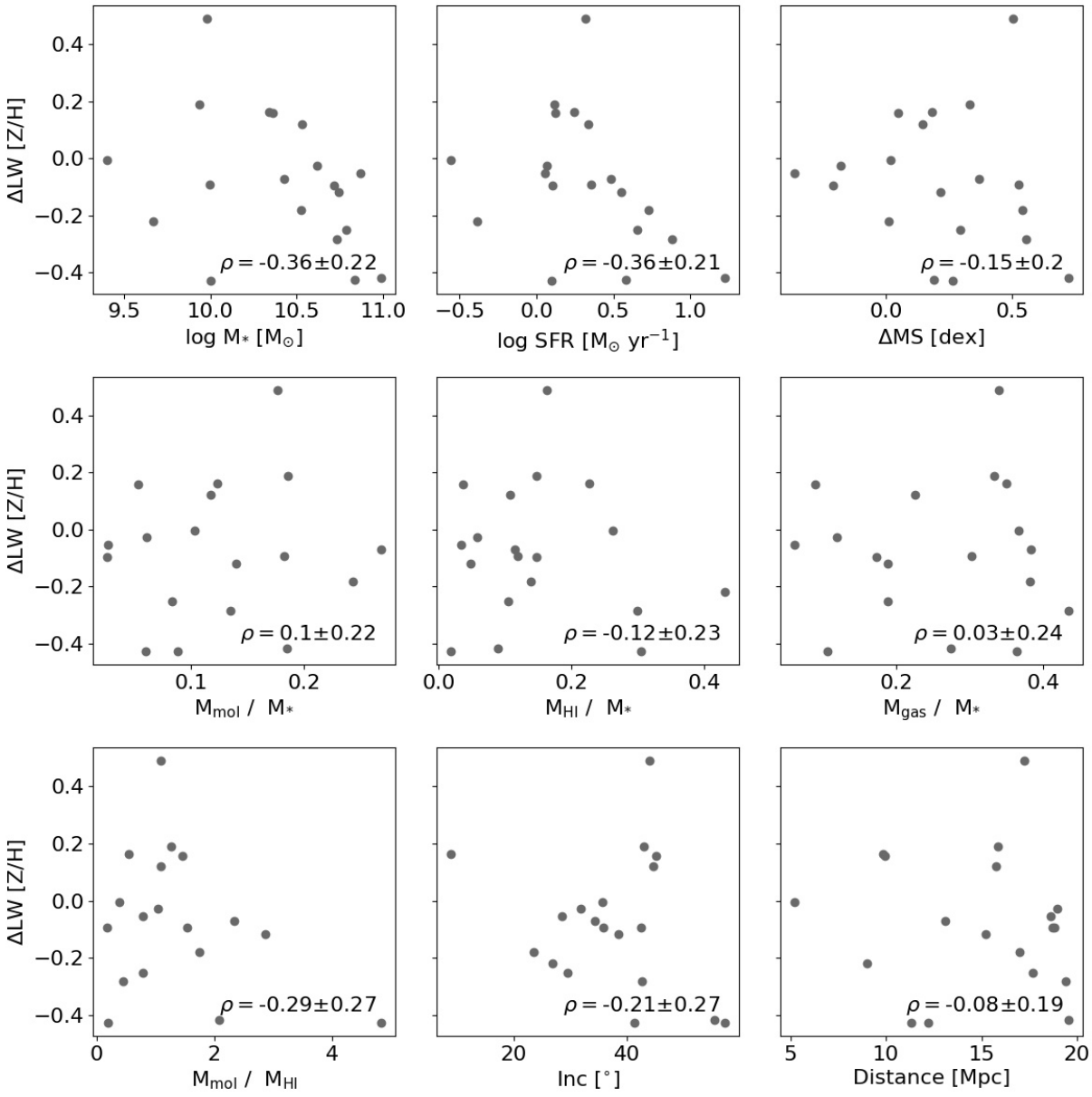

Figure 5.8: Slope of the LW-[Z/H] gradient, as a function of (from left to right, and from top to bottom) total stellar mass (log M_*), total SFR (log SFR), offset from the global main sequence of galaxies (ΔMS), total molecular gas mass-to-stellar mass ratio (M_{mol} / M_*), total atomic gas mass-to-stellar mass ratio (M_{HI}), total gas (molecular + atomic)-to-stellar mass ratio M_{gas} / M_*, and molecular-to-atomic gas mass ratio (M_{mol} / M_{HI}), galaxy inclination and distance. The Pearson correlation coefficient for each parameter is indicated in the bottom-right corner of each panel.

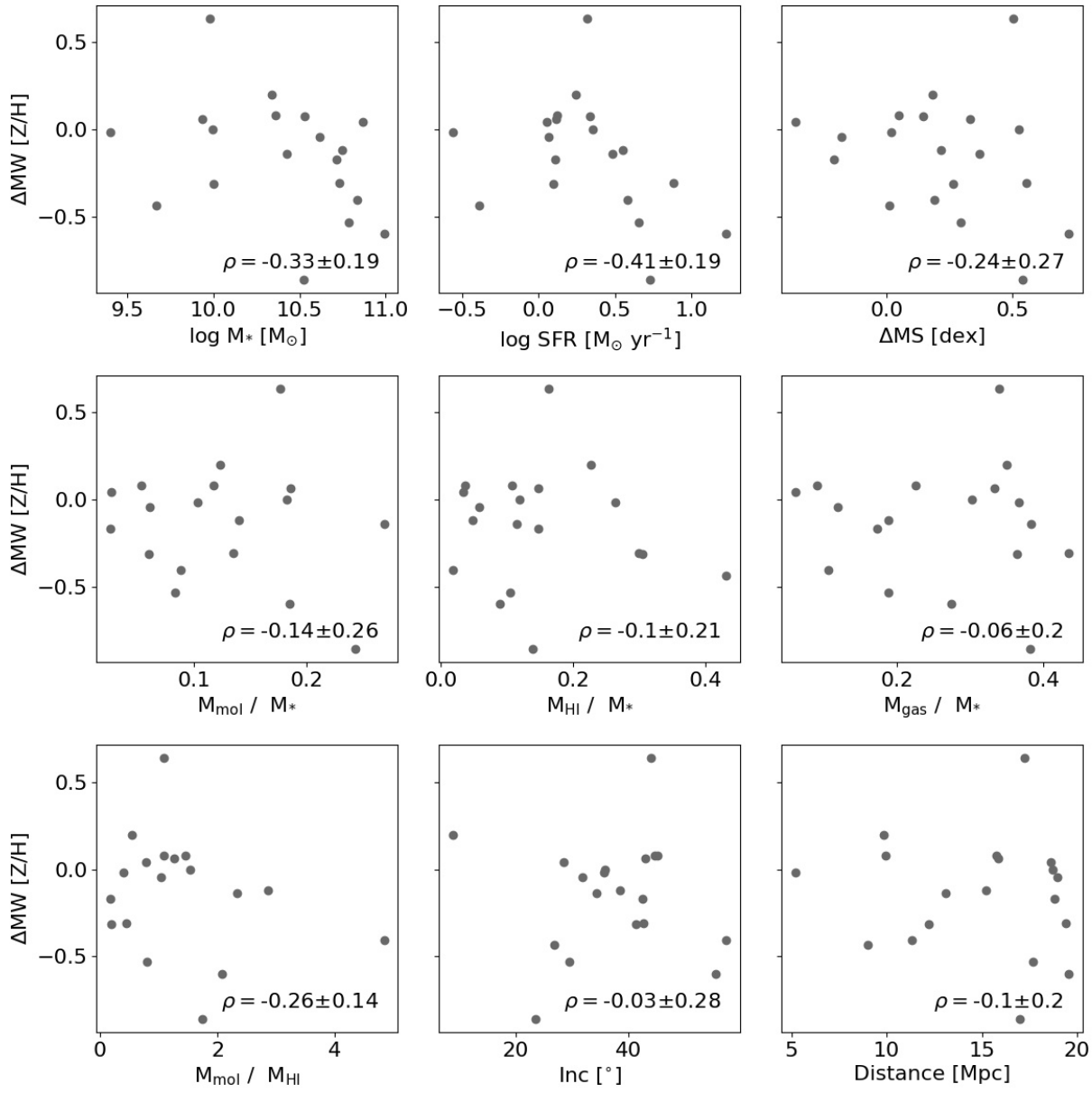

Figure 5.9: Slope of the MW-[Z/H] gradient, as a function of (from left to right, and from top to bottom) total stellar mass (log M_*), total SFR (log SFR), offset from the global main sequence of galaxies (ΔMS), total molecular gas mass-to-stellar mass ratio (M_{mol} / M_*), total atomic gas mass-to-stellar mass ratio (M_{HI}), total gas (molecular + atomic)-to-stellar mass ratio M_{gas} / M_*, and molecular-to-atomic gas mass ratio (M_{mol} / M_{HI}), galaxy inclination and distance. The Pearson correlation coefficient for each parameter is indicated in the bottom-right corner of each panel.

stars yields a radial mixing of material, and it is expected to produce a flattening of the stellar population properties radial gradients, especially for older stellar populations (e.g., Di Matteo et al., 2013).

Simulations show that bars provide very efficient mechanisms for the radial redistribution of gas and angular momentum (Brunetti et al., 2011; Spinoso et al., 2017); hence, radial gradients of stellar population properties along the bar are expected to be flatter than along the galactic disk. A number of studies have tested this prediction using nearby galaxies (Sánchez-Blázquez et al., 2014; Seidel et al., 2016; Fraser-McKelvie et al., 2019; Neumann et al., 2020), obtaining a variety of results. Sánchez-Blázquez et al. (2014) see no significant differences between the radial profiles of stellar age and metallicity of barred and unbarred galaxies from the CALIFA sample. Seidel et al. (2016) use data from the BaLROG project (Seidel et al., 2015), and find that stellar metallicity gradients along the bar major axis are considerable flatter than along its minor axis. Fraser-McKelvie et al. (2019) measure flatter stellar age and metallicity gradients along bars, compared to disks in galaxies from the MaNGA sample. Neumann et al. (2020) used data from the TIMER project (Gadotti et al., 2019), and find flatter MW age radial profiles along bars, compared to the disk, but no significant differences in the MW metallicity radial profiles, and in general mild differences between the gradients along the major and minor axis, with significant scatter, and no clear trend with bar strength.

Here, we measure MW age and metallicity radial gradients along pseudo-slits placed across the bar major axis and perpendicular to it. Figure 5.10 shows the position of the pseudo-slits overplotted on the stellar mass surface density map of NGC 1433. We have measured radial gradients along each of these two pseudo-slits (excluding centers). The radial profiles (and the best-fit gradients, measured using an OLS fitting routine) of MW age and metallicity measured along each one of these pseudo-slits for NGC 1433 are shown in Fig. 5.11. We excluded the innermost and outermost radial bins when measuring the radial gradients, in order to avoid potential deviations from the radial trend driven by these extreme values. The gradients along the bar major axis, and their perpendicular counterparts, are calculated as the mean gradient of the two possible directions along each axis from the center (i.e., mean gradient between dark-green (black) and pale-green (gray) pseudo-slits in Fig. 5.10). The difference between both measurements span a wide range of values, from ~ 0, to more than 1 dex, and it is interpreted as the uncertainty in the galaxy gradient (along a given axis).

Figures 5.12 and 5.13 show the slopes of the MW age and metallicity gradients measured along the bar axis (green), and its perpendicular direction (black), for the 14 barred galaxies in our sample. NGC 2835 was excluded because the small size of its bar makes the measurement of the gradients unreliable. The slopes of the gradients are shown as a function of bar length (in units kpc and R_{25}), total stellar mass, and offset from the main sequence of galaxies (ΔMS).

The red line is defined as the difference of the absolute value of the gradient measured along the bar and its perpendicular direction, i.e.,

$$\Delta\mathrm{MWage}_{\mathrm{disk-bar}} = |\Delta\mathrm{MWage}_{\mathrm{disk}}| - |\Delta\mathrm{MWage}_{\mathrm{bar}}| \tag{5.4}$$

and

$$\Delta\mathrm{MW[Z/H]}_{\mathrm{disk-bar}} = |\Delta\mathrm{MW[Z/H]}_{\mathrm{disk}}| - |\Delta\mathrm{MW[Z/H]}_{\mathrm{bar}}| \tag{5.5}$$

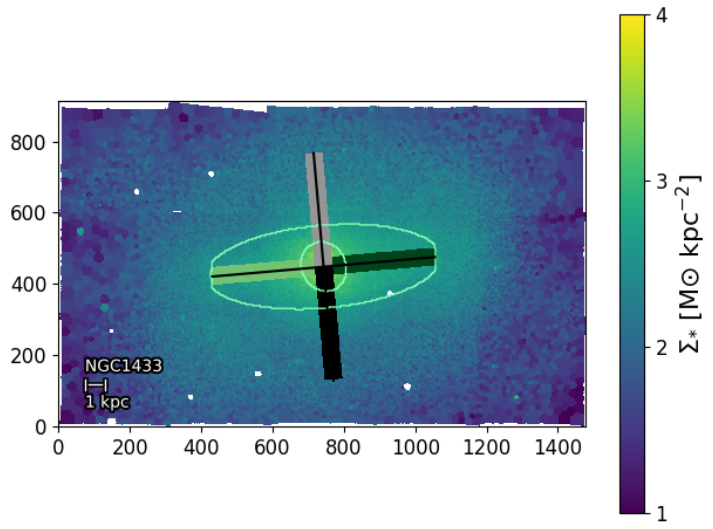

Figure 5.10: Representation of the location of the pseudo-slits along the bar of NGC 1433 (pale and dark green rectangles), and perpendicular to the bar axis (grey and black rectangles). The position of the bar is indicated by the light-green ellipses. The background shows the stellar mass surface density map of the galaxy.

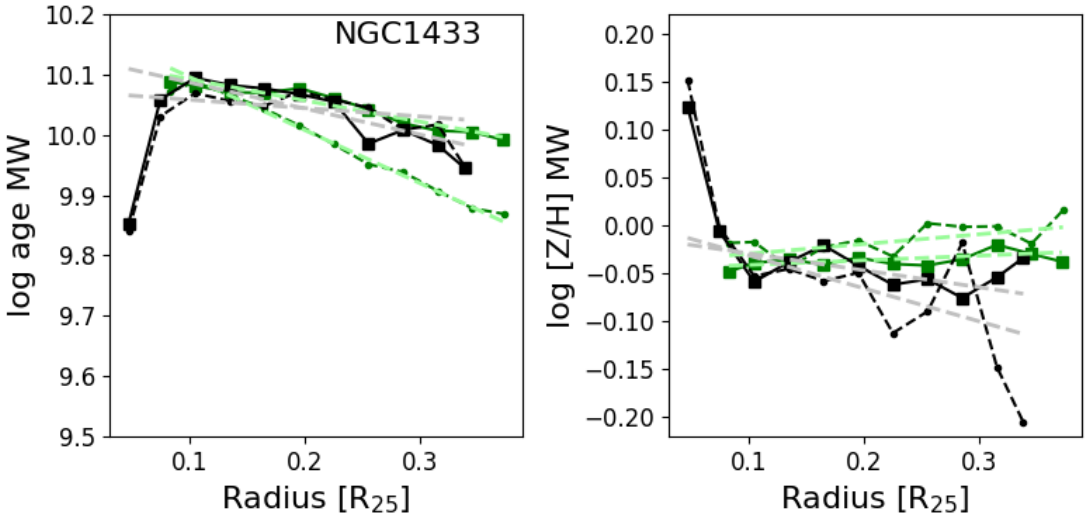

Figure 5.11: Mass-weighted age (left) and [Z/H] (right) radial profiles along the bar major axis (dark green), and along its perpendicular direction (black), for NGC 1433. The solid and dashed dark green and black lines represent the gradient measured towards each possible direction from the center. The pale green dashed lines show the best-fitting linear model to the bar major axis gradient (dark green lines), and the silver dashed lines show the best-fitting to the gradients measured in the direction perpendicular to the bar.

implying that positive values correspond to a flatter profile along the bar, compared to the perpendicular direction, and negative values otherwise.

For ΔMW age, we do not see evidence of flatter profiles along the bar. Indeed, we find that, on average, MW age gradients are steeper along the bar (-0.59 ± 0.33), than along its perpendicular direction (-0.38 ± 0.50), and less than half of the galaxies (6) show a flatter MW age gradient along the bar. We do not find any trend between flatter profiles, and bar length, total stellar mass, or ΔMS.

On the other hand, we observe flatter MW [Z/H] gradients for bars. We calculate a mean gradient of 0.08 ± 0.31 along bars, and -0.30 ± 0.48 in the perpendicular direction. In terms of individual galaxies, 10 out of the 14 barred galaxies in our sample show a flatter metallicity profile along the bar, without any obvious trend with bar length, total stellar mass, or ΔMS.

Finding more negative age profiles along the bar is not surprising. Seidel et al. (2016) also find that age profiles are more negative along the bar semi-major axis, than along its semi-minor axis. This is consistent with chemodynamic simulations (Wozniak, 2007) that predict that younger stellar populations will be confined to more elongated orbits, populating the edges of the bar. Neumann et al. (2020) report a similar spatial distribution of stellar populations within the bar of nearby galaxies, with old (>8 Gyr) stars shaping the inner and rounder part of the bar, intermediate age (2-6 Gyr) stars trapped on more elongated orbits, and an accumulation of young (<2 Gyr) stars in the bar edges.

In the case of metallicity, we find considerable flatter profiles along bars, compared to their perpendicular direction. This result is consistent with simulations that investigate the bar-driven secular evolution of galaxies, and predict flatter metallicity gradients in barred galaxies (Di Matteo et al., 2013), and that have been observationally confirmed (e.g., Seidel et al., 2016).

In conclusion, we find steeper age gradients, but flatter metallicity gradients along bars, compared to their semi-minor axis. The natural explanation for flatter [Z/H] gradients is orbital mixing of gas along the bar, as gas is more susceptible to non-axisymmetric structure than stars. Hence, gas from which stars form is homogeneized along the bar. However, we acknowledge that due to the limited size of our sample, our results are also consistent with similar metallicity gradients along bars, and perpendicular to them.

5.3.3 Further insights on the inside-out growth of galaxies

In this section, we explore in more detail what we can learn about the radial structure of the stellar mass assembly of PHANGS galaxies, beyond the mean age radial gradients.

Figure 5.14 shows the age of the Universe at which each radial ring formed 80% of its current total stellar mass (neglectic the impact of stellar migration, whose contribution in shaping the radial structure of stellar populations is expected to be of second order; see e.g., Zhuang et al., 2019). A positive trend in these plots implies that outer regions assembled their stellar mass later in cosmic time than inner regions. The figure shows that most galaxies show an overall well-defined positive trend, a direct imprint of the inside-out growth of galaxies. The most remarkable exception is NGC 1385, that shows an almost perfectly flat trend. This, together with positive age and metallicity radial trend make NGC 1385 a very peculiar system. Another exception is NGC 3627, which also shows a nearly flat MW age radial profile. NGC 3627 is a member of the interacting group Leo Triplet (Zhang et al.,

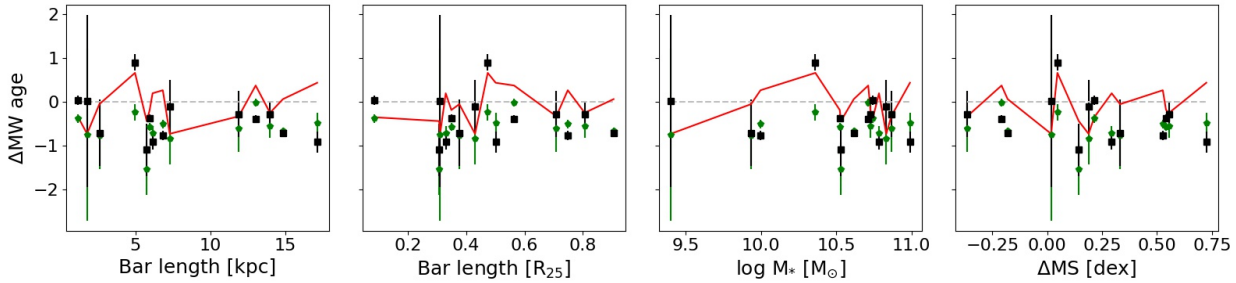

Figure 5.12: Mass-weighted age gradients measured along bar major axis (green pentagons), and along its perpendicular direction (black squares), as a function of the bar length (in units kpc and R_{25}), total stellar mass, and offset from the global main sequence of galaxies (ΔMS), for 14 barred galaxies in our sample. The red line is calculated following Eq. 5.4. It is defined to be positive in galaxies that show a flatter gradient along their bar major axes, compared to the bar perpendicular direction, and negative values otherwise.

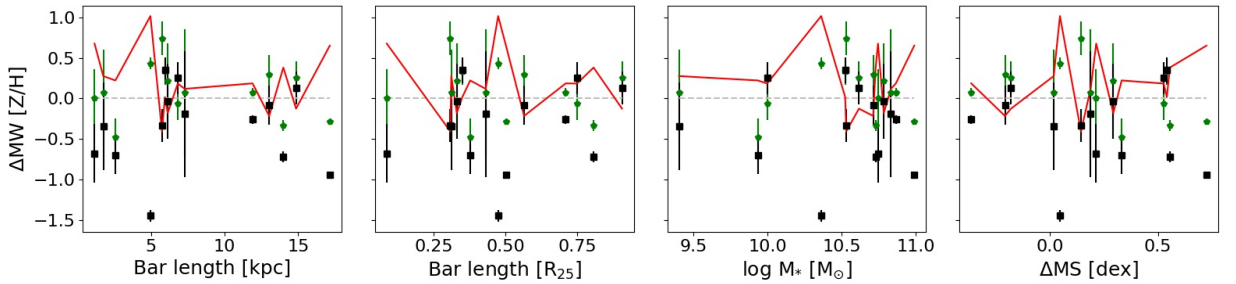

Figure 5.13: Mass-weighted [Z/H] gradients measured along bar major axis (green pentagons), and along its perpendicular direction (black squares), as a function of the bar length (in units kpc and R_{25}), total stellar mass, and offset from the global main sequence of galaxies (ΔMS), for 14 barred galaxies in our sample. The red line is calculated following Eq. 5.5. It is defined to be positive in galaxies that show a flatter gradient along their bar major axis, compared to the bar perpendicular direction, and negative values otherwise.

1993), interactions with nearby galaxies could have triggered episodes of star formation (e.g., Renaud et al., 2019) that might explain its peculiar radial assembly of stellar mass.

Other galaxies, such as NGC 1672 or NGC 1300 show a positive trend across parts of their stellar disk, and then a negative trend in the outer radii. Such a negative trend suggest that in these galaxies, the outer regions have remained relatively quiescent for long periods of time, compared to the inner radii. This does not imply that they lack current star formation, but it means they have not formed a substantial amount of stellar mass in the last ~ 5 Gyr. Indeed, Fig 5.2 shows that these galaxies do not show older LW ages in their outer radii.

The bottom-right panel of Fig. 5.14 displays the trends for the entire FoV of all galaxies, colored by total stellar mass. There is a trend such that the radial assembly profiles of more massive galaxies (green) are steeper, with values at smaller radii being preferentially located at younger ages, this is, in the earlier Universe, while less massive galaxies (blue) show flatter gradients, with their inner regions preferentially showing formation times at older ages of the Universe.

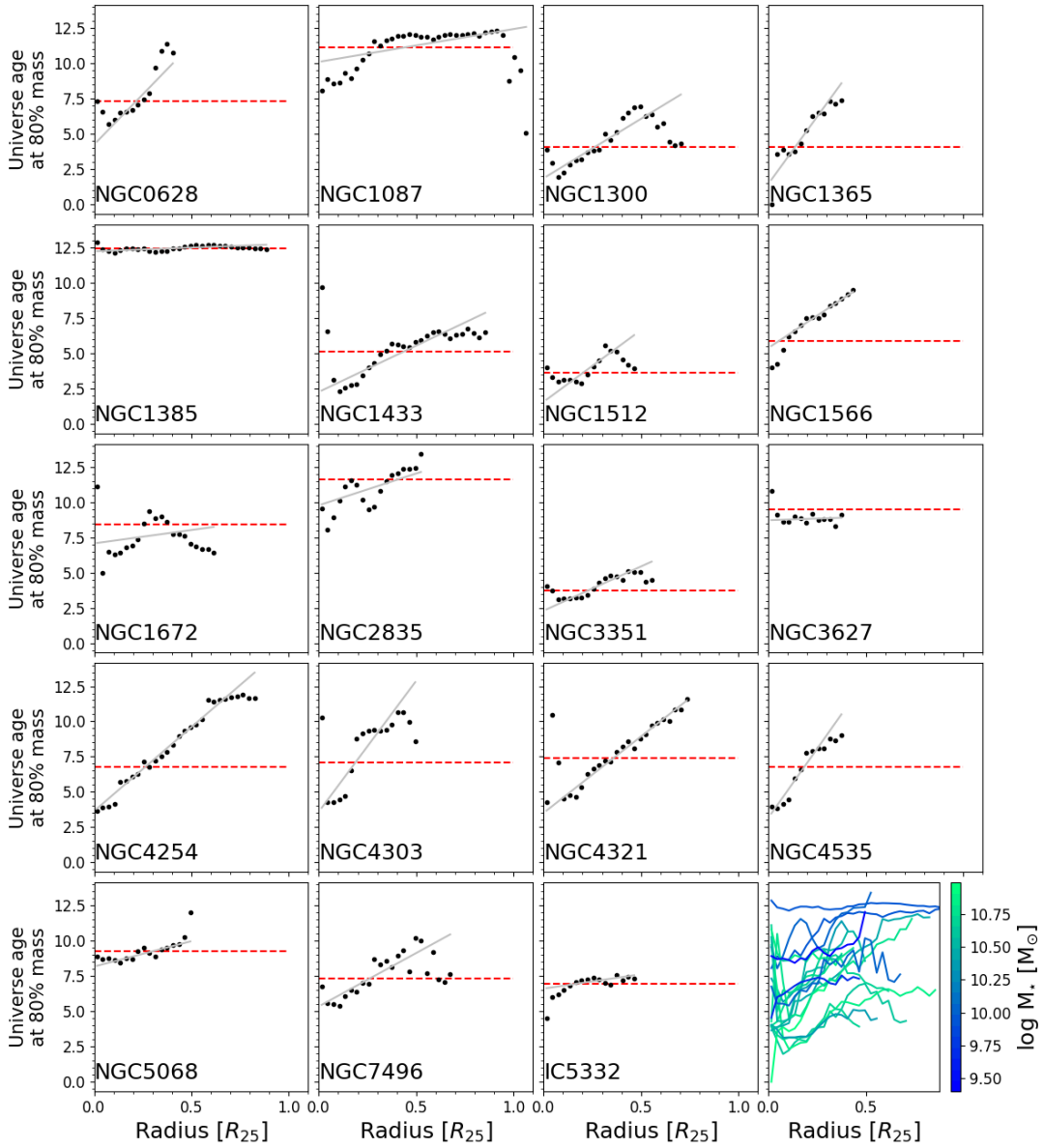

Figure 5.14: Radial assembly history of PHANGS galaxies. The y-axis shows the age of the Universe at which each radial bin assembled 80% of its total current stellar mass. A positive trend in these plots implies that outer regions assembled their stellar mass later in cosmic history than inner regions. The grey dashed lines show the best-fit linear model to each galaxy. The bottom-right panel displays the trends for all galaxies, color-coded by total stellar mass.

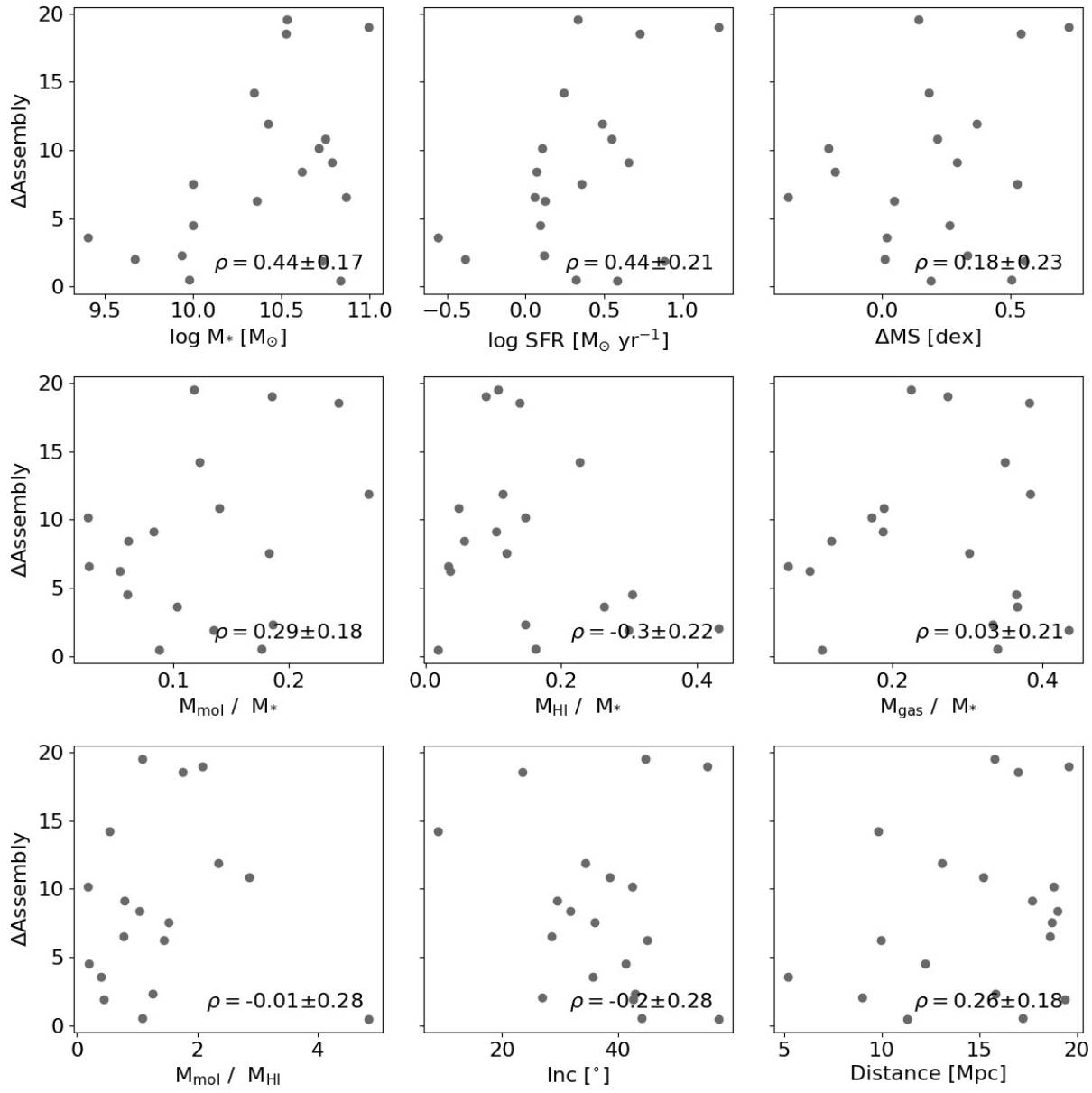

Figure 5.15: Slope of the radial assembly history gradients (i.e., grey dashed lines in Fig. 5.14), as a function of (from left to right, and from top to bottom) total stellar mass (log M_*), total SFR (log SFR), offset from the global main sequence of galaxies (ΔMS), total molecular gas mass-to-stellar mass ratio (M_{mol} / M_*), total atomic gas mass-to-stellar mass ratio (M_{HI}), total gas (molecular + atomic)-to-stellar mass ratio M_{gas} / M_*, and molecular-to-atomic gas mass ratio (M_{mol} / M_{HI}), galaxy inclination and distance. The Pearson correlation coefficient for each parameter is indicated in the bottom-right corner of each panel.

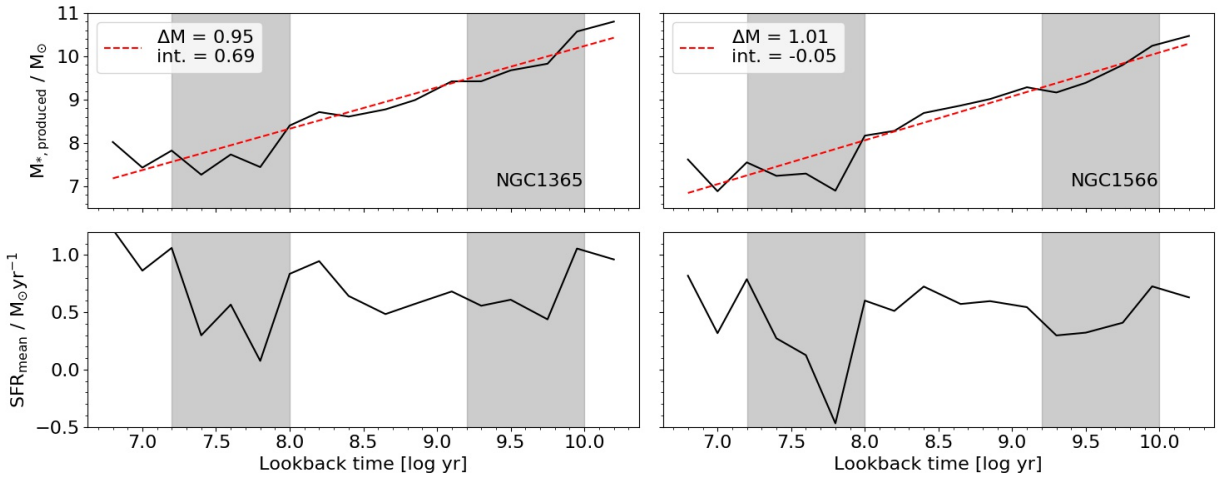

Figure 5.16: Star formation history (top) and star formation rate history (bottom) derived for NGC 1365 (left) and NGC 1566 (right). The best-fitting linear model for the SFH curve of each galaxy is shown as a red dashed line, and its slope and intercept are plotted in the corner of the top panels. The shaded areas mark sudden decreases in the SFR at ages log (age/yr) ~ 7.7 and log (age/yr) ~ 9.5, found to exist in all galaxies in some degree, deemed as an artifact of the computed SFHs.

In Fig. 5.15 we show the correlations beween the gradient of the radial assembly of galaxies (ΔAssembly), measured using an OLS fitting routine, as a function of the same global properties probed in the previous sections. We do not see any strong correlation of ΔAssembly with global galactic properties. The highest correlation coefficients are obtained for total mass and total SFR ($\rho = 0.44$). Although ρ is not particularly high, we see a trend in which low-mass galaxies show preferentially flatter gradients, while high-mass galaxies exhibit preferentially steeper gradients, albeit with higher scatter. This implies that although the total mass might play a role in setting the radial assembly history, there might be other factors such as gas accretion, or interactions introducing scatter in the relation.

In summary, galaxies show a generally well-defined inside-out stellar mass assembly history, meaning that inner regions assembled their current stellar mass earlier in cosmic history than outer regions. The inside-out growth signal shows a clear dependency on stellar mass, where more massive galaxies show, on average, a more obvious difference in the assembling time of inner vs. outer regions than less massive galaxies.

5.3.4 Downsizing in galaxy evolution

Another interesting topic that we can probe within our sample is the downsizing paradigm of galaxy evolution (see, e.g., Cowie et al., 1996; Heavens et al., 2004; Pérez-González et al., 2008). This phenomenon describes how more massive galaxies assembled their stellar mass earlier in cosmic history than less massive galaxies.

Figure 5.16 shows the SFH and SFR-history for two galaxies in our sample (NGC 1365 and NGC 1566). The figure show, in the top panels, the total stellar mass formed in a given age bin, and in the bottom panels, the average SFR in a given age bin, defined as the total stellar mass formed, divided by the time-separation between each bin, and the previous one.

In the case of the first bin, the time-separation is calculated with respect to the present time (lookback time = 0).

The SFHs (and time-averaged SFRs) of most of the galaxies in our sample show a sudden decrease in the formation of stars at ages log (age/yr) ~ 7.7 and log (age/yr) ~ 9.5 (indicated as the shaded area in Fig. 5.16). We acknowledge that this is very likely an artifact of the derivation of the SFH. This decrease occurs everywhere in the galaxy, and we have been not able to identify a clear cause for it. Similar systematic problems at these ages have been identified in the literature. Peterken et al. (2020) report a correlation between the weights assigned for two similar age bins, finding evidence that it is related to the 'UV upturn' in old stellar populations (Yi, 2008). Although we do not report here an identical problem (we do not see a sudden increment in the SFH, as they do), SFH derivations are subject to systematics that depend on the spectral library (e.g, Walcher et al., 2011; Martins, 2021), and the code used to derive it (San Roman et al., 2019, e.g.,). Finding the exact cause of this artifact is beyond the scope of this paper, but we exclude it from the interpretation of our results.

The SFHs derived are well represented by almost perfectly linear power-laws (see top panels of Fig. 5.16). This is partially by construction, as we designed our age grid to be log-spaced, and the time-averaged SFR is nearly flat across cosmic time (neglecting the artifacts described above). However, deviations from this linearity reflect real features of the mass assembly process of these galaxies. Galaxies that assembled most of their stellar mass earlier in cosmic history show steeper power-laws (i.e., higher ΔM). On the other hand, galaxies that have assembled a substantial amount of their current stellar mass later in cosmic history are characterized by flatter SFHs (i.e., lower ΔM)

Figure 5.17 shows the slope of the SFH (ΔM), measured using an OLS fitting routine, as a function of the same global parameters explored in the previous sections. We find clear correlations between ΔM and several of the global properties, including total stellar mass ($\rho = 0.61$), atomic gas fraction ($\rho = -0.56$), and total gas fraction ($\rho = -0.64$).

Despite the artifacts present in our SFHs, we believe that trends in the assembly history of galaxies are robust, where more massive galaxies, with lower gas content assembled their stellar mass earlier in cosmic history, than galaxies with lower stellar masses, and higher gas content.

This reflects clearly the downsizing effect in galaxy evolution, and is consistent with findings from previous works (e.g., Ibarra-Medel et al., 2016; Peterken et al., 2019). Thus, we conclude that the derived SFHs tell a consistent story of the stellar mass assembly of the galaxies in our sample, with strong imprints of an inside-out formation, and an overall downsizing in galaxy evolution.

5.3.5 Kinematic imprints of different stellar populations across the galactic disk

The dynamical evolution of galactic disks is encoded in present-day observations of the kinematics properties of its different stellar populations. It has long been known that older populations of solar neighborhood stars have larger velocity dispersions, compared to younger stars (Roman, 1954; Wielen, 1977; Freeman, 1987). The trend of increasing velocity dispersions with age is known as the age-velocity relation (AVR). Binney et al. (2000) used

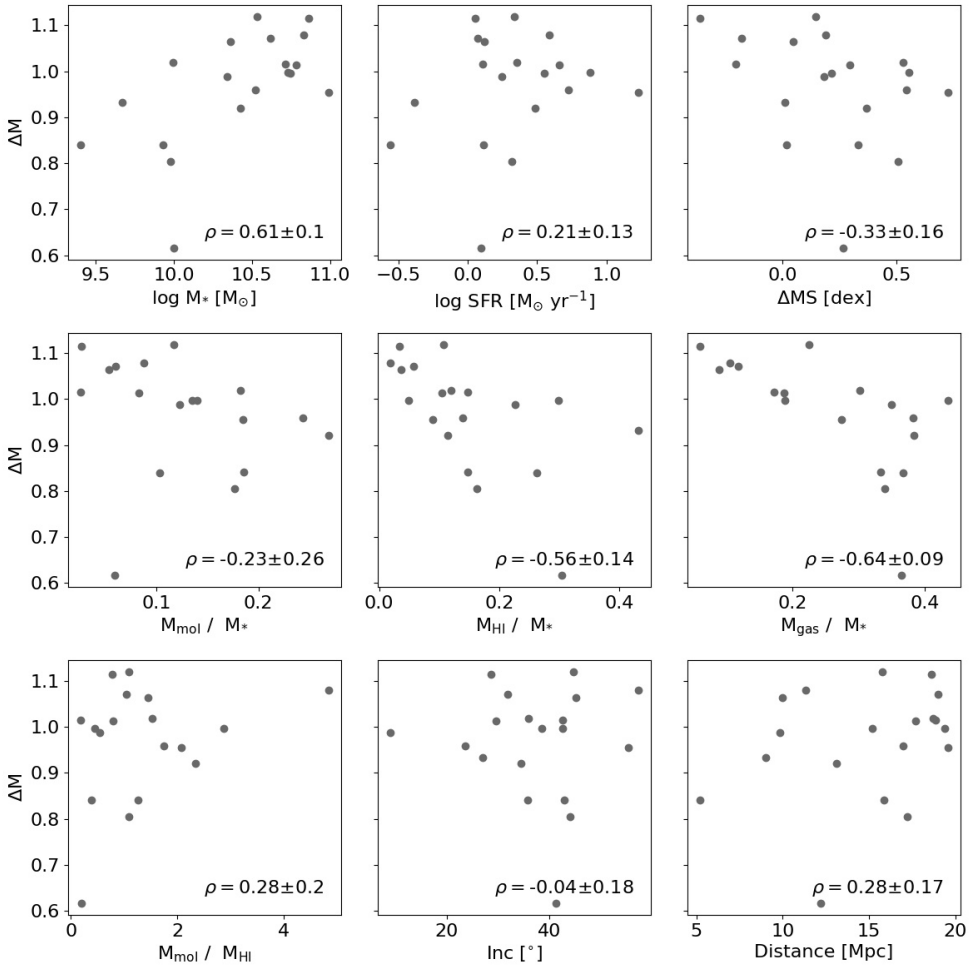

Figure 5.17: Slope of the SFH of PHANGS galaxies, as a function of (from left to right, and from top to bottom) total stellar mass (log M_*), total SFR (log SFR), offset from the global main sequence of galaxies (ΔMS), total molecular gas mass-to-stellar mass ratio (M_{mol} / M_*), total atomic gas mass-to-stellar mass ratio (M_{HI}), total gas (molecular + atomic)-to-stellar mass ratio M_{gas} / M_*, and molecular-to-atomic gas mass ratio (M_{mol} / M_{HI}), galaxy inclination and distance. The Pearson correlation coefficient for each parameter is indicated in the bottom-right corner of each panel.

Hipparcos (Perryman et al., 1997) data to quantify the rate at which the velocity dispersion of a coeval group of stars increases with time, and found that it scales with age as $\tau^{0.33}$, with τ in Gyr. Recent works (Yu & Liu, 2018; Mackereth et al., 2019; Tarricq et al., 2021) have performed similar measurements for open clusters and field stars in our Galaxy, using data from Gaia DR2 (Gaia Collaboration et al., 2018).

An alternative explanation to the AVR is that the interstellar medium at high redshift was more turbulent, and thus, older stars retain larger velocity dispersion to present day (Stott et al., 2016). Along this line, Leaman et al. (2017) find that observation of galaxies from the Local Group are consistent with a model in which stars are born with a velocity dispersion close to that of the gas from which they formed, and are then dynamically heated with an efficiency that depends on the galaxy mass.

Different mechanisms can contribute to the progressive dynamical heating of stars that lead to the AVR, such as interaction with giant molecular clouds (Spitzer & Schwarzschild, 1953), interaction with spiral arms (Barbanis & Woltjer, 1967; Sellwood & Carlberg, 1984; Mackereth et al., 2019), bars (Grand et al., 2016), or even external sources of perturbation (Grand et al., 2016). However, measuring the relative importance of these different mechanisms is not straightforward, as studies of the AVR are confined to the Local Group, where individual stars can be resolved, and thus, the parameter space of factors that could contribute to the diffusion of stars (e.g., galactic structure) is poorly covered.

In this section, we present an exploration of the AVR measured in nearby galaxies from the PHANGS sample, using the LW age and velocity dispersion maps derived as explained in Sec. 5.2. Although the spatial resolution of ~ 100pc is far from being sufficient to resolve individual stars, it is possible to resolve young star-forming regions, and more generally, regions dominated by stellar populations of distinguishable ages. Furthermore, since at this spatial scale the structural components of the galaxy (namely bars, spiral arms, centers, rings, and disks) are clearly resolved, we can also search for changes in dynamical heating of stars as a function of local environment.

Figure 5.18 show the AVR (using LW age) as 2D histograms for two sample galaxies (NGC 1566 and NGC 3627). These two galaxies are good examples of the general trend that we see in our sample; spiral arms and disk share similar stellar velocity dispersion (σ_*) values, with the former located preferentially at younger ages, and centers and bars dominated by older stellar populations, with higher σ_* values. These positive correlations could, at first glance, be naively interpreted as the AVR. However, in order to properly interpret these trends, it is important to take into account the overall negative σ_* radial gradient set by the underlying stellar mass distribution, following the virial theorem (see, e.g., Bittner et al., 2020). The overall negative σ_* radial profile is clearly visible in the bottom left panel of Fig. 5.1. The σ_* trend, in combination with the negative LW age profiles discussed in Sec. 5.3.1, result in the positive trends seen in Fig. 5.18.

Therefore, in order to explore the trend between σ_* and LW age in a meaningful way, we investigate the radial gradients of σ_* for three different LW age bins; young (log LW age < 100 Myr), intermediate (100 Myr $<$ log LW age < 600 Myr), and old (log LW age > 3 Gyr). This choice is motivated by the results from Tarricq et al. (2021), that find that the increase in σ_* occurs more rapidly within the first Gyr after stars form, following a much slower increase from this point. To do this measurement, we take the square root of the azimuthally averaged square of the σ_* values in a given radial bin, considering separately

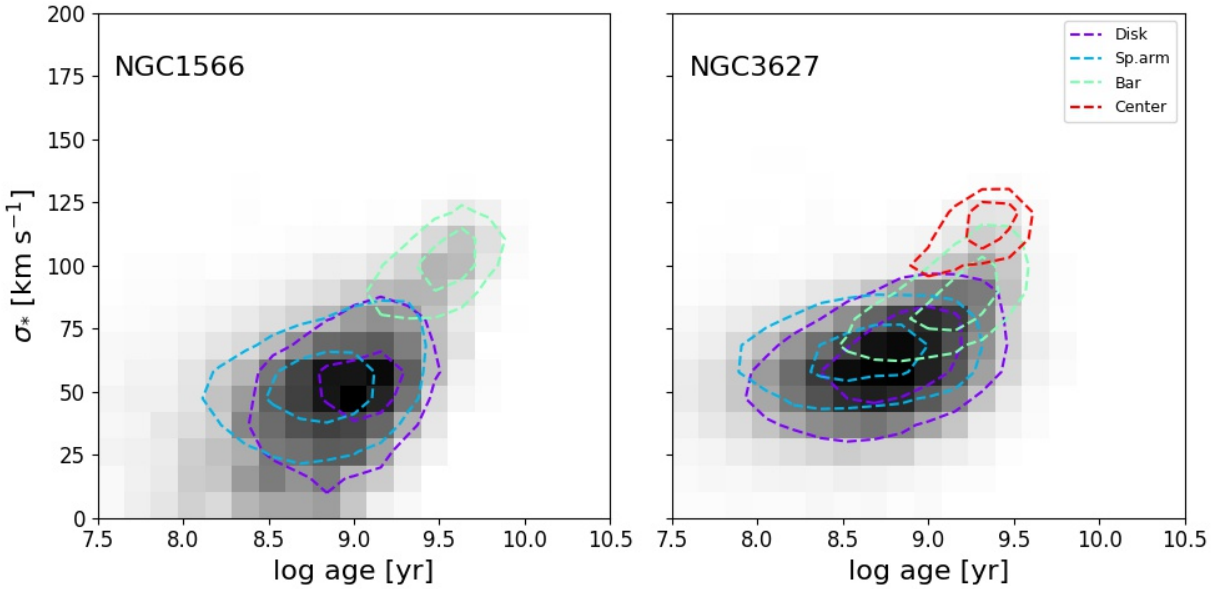

Figure 5.18: 2D histogram that shows the distribution of stellar velocity dispersion (σ_*) and log age (light-weighted), for NGC 1566 (left) and NGC 3627 (right). The color of each [log age, σ_*] bin scales with the number of pixels within that bin. The contours show the one- and two-sigma limits of the distribution of each individual galactic environment, following the color code indicated in the top-right corner of the right of the panel.

spaxels with LW ages in each one of the three age bins defined.

Figure 5.19 show the σ_* radial profiles for the same two galaxies, and also for NGC 1365, separately for the three age bins defined, and across for different galactic environments. For reference, we also display the molecular gas $\sigma_{\rm mol}$ profile, measured from the CO(2-1) PHANGS-ALMA data.

The figures show a clear age gradient in the σ_* value at a given galactocentric distance, with younger populations having lower velocity dispersions than older ones. This effect is very clear across disk and spiral arms in general, but the age gradient is generally inexistent in bars. Out of the 14 barred galaxies in our sample, the only noticeable exceptions are NGC 1365 and NGC 5068, with a very clear age gradient present also in the bar. It is interesting to note that these two galaxies represent the high- and low-stellar mass extremes of our sample (logM_* = 10.99 and 9.40, respectively). Therefore, this similarity is likely not connected to their total stellar mass. On the other hand, we do not observe meaningful differences between spiral arms and disks, at any given radius. Finally, the molecular gas from which young stars form shows a nearly flat radial $\sigma_{\rm mol}$ profile, with very low ($\lesssim 20$ km s^{-1}) velocity dispersion values, and a rapid increase towards the inner radii. Overall, these findings suggest that (i) the dynamical heating of stellar populations occurs at any given radius, increasing the velocity dispersion from $\lesssim 20$ km s^{-1}, up to $\gtrsim 50$km s^{-1} on timescales of hundreds of Myr; (ii) assuming that molecular gas traces the velocity dispersion of stars at birth (Leaman et al., 2017), the dynamical heating takes place in shorter timescales within the bar, as we do not see clear difference in the σ_* of the different populations in bars of most galaxies. However, we acknowledge that this result could be driven by the lack of

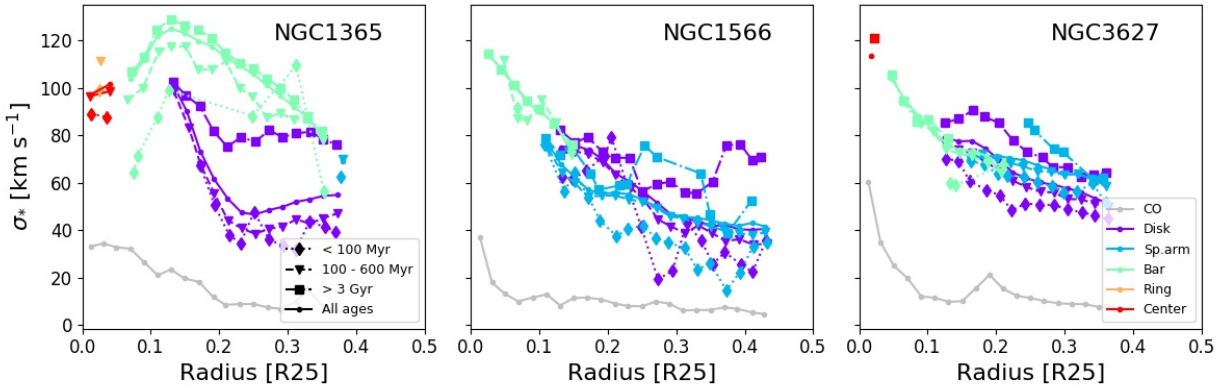

Figure 5.19: Radial profile of stellar velocity dispersion (σ_*) for NGC 1365 (left), NGC 1566 (center), and NGC 3627 (right), splited as a function of galactic structure (colors) and LW age of the underlying stellar populations. Stellar populations younger than 100 Myr are indicated by diamonds (dotted line). Stellar populations of ages in the range of 100 Myr $<$ log LW age $<$ 600 Myr are marked with triangles (dashed line). Stars older than 3 Gyr are represented by squares (dashdotted line). Circles (solid line) show the radial profile considering all stellar populations. The gray line shows the radial velocity dispersion gradient measured for the molecular gas, from the PHANGS-ALMA CO(2-1) data.

young stellar populations in the bar not enabling measuring a clear age gradient. (iii) Spiral arms do not play a primary role in the heating of stellar populations, as we observe this phenomenon across the entire disks, including galaxies that do not present spiral arms.

To illustrate these trends across our full sample, Fig. 5.20 shows the σ_* values measured for stellar populations within the three different age bins defined at a fixed radius (0.25 - 0.30 R_{25}) for the disk environment. For those few galaxies that do not show these three stellar ages present within the previously defined radius range (NGC 1087, NGC 1433, NGC 1512, NGC 3351, NGC 4303), we opted by choosing a different radial bin of the same length (0.05 R_{25}), located at the minimum possible radius in which the three populations are present. The figure makes clear that a positive trend between σ_* and LW age of the underlying stellar populations exist for most of the galaxies in our sample. However, the differences in σ_* between different age bins are often comparable or even smaller than the standard deviation of the distribution of σ_* values within a given age bin (shown as the error bars in Fig. 5.20). Although this could, in principle, imply that the measured σ_* differences are not statistically significant, the fact that we find them to be nearly ubiquitous in our sample and that error bars within a given age bin are intrinsically overestimated due to the underlying gradient gradients points to that these differences in σ_* across stellar populations of different ages are indeed a real feature in our data. Furthermore, while it is true that the light (and thus, measurement of σ_*) in the pixels with young LW ages is dominated by the spectra of young stars, these pixels also have a subdominant (in light) old component with higher velocity dispersion, that would bias the σ_* measurements towards higher values, reducing the measured differences. This effect would become stronger in pixels with relatively higher light contributions from old stars. Finally, the bottom right panel of Fig. 5.20) shows that there is not any clear trend between differences in the velocity dispersion of stellar populations and total stellar mass of the galaxies.

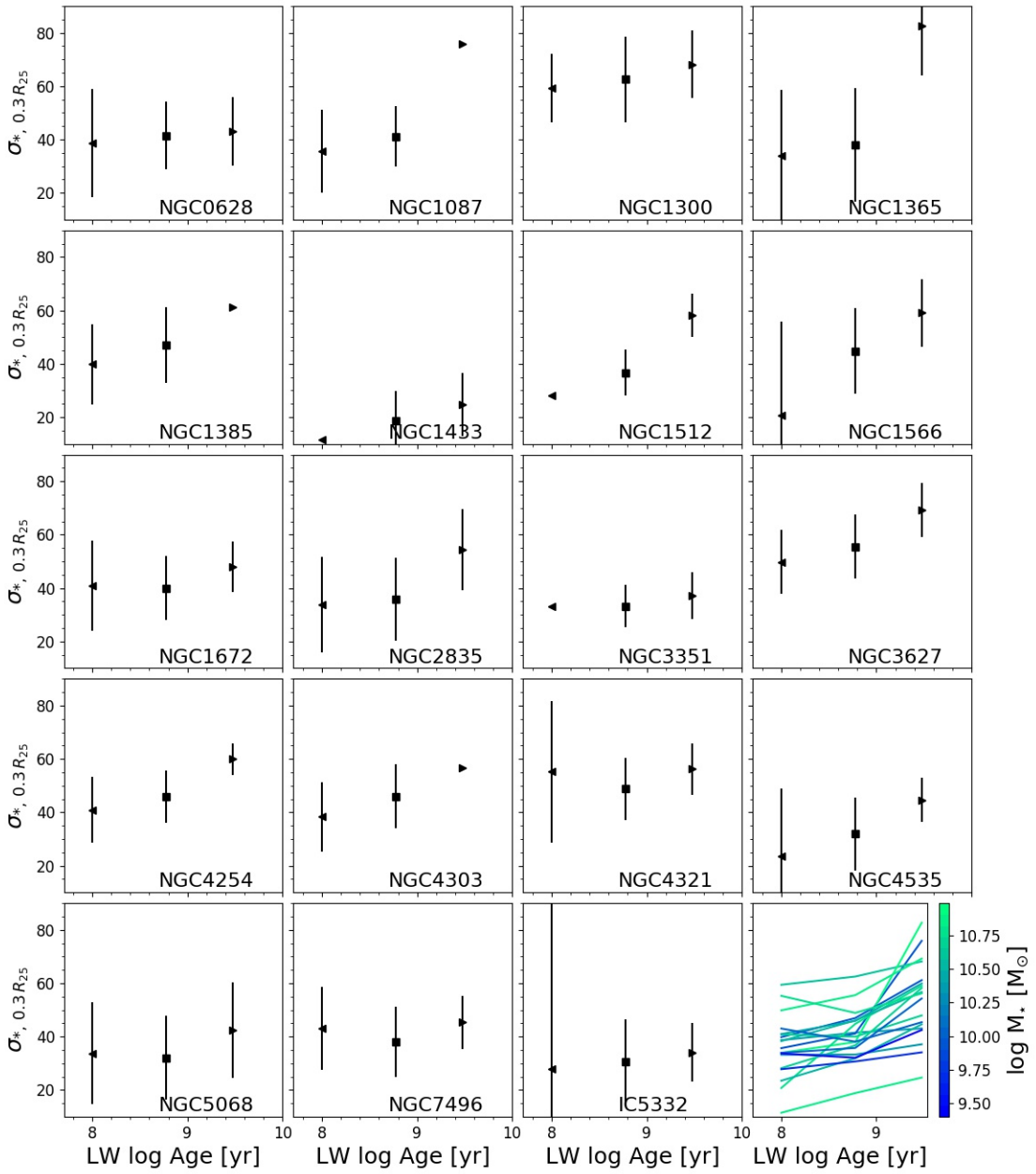

Figure 5.20: Mean stellar velocity dispersion (σ_*) measured at a galactocentric radius of 0.25-0.30 R_{25} in the disk environment of all our sample galaxies for stellar populations with light-weighted ages within the three different age bins defined in the main text. Note that for visualization purposes, the x-axis position of each data point is located at the edge of the age bin it represents. In each panel, the leftmost triangle represents the mean (area-weighted) velocity dispersion of all populations younger than 100 Myr. The central square marks the mean velocity dispersion of populations with 100 Myr $<$ LW age $<$ 300 Myr, and the rightmost triangle shows the same quantity for populations older than 3 Gyr. The errorbar indicates the standard deviation of the σ_* values of the pixels within a given age bin. The bottom right panel shows the trend for all galaxies, colored by total stellar mass.

The scenario in which young stellar populations diffuse progressively towards higher vertical heights (i.e., increasing $\sigma_{*,z}$), producing a continuous gradient between age and $\sigma_{*,z}$ (at a given radius), is also consistent with the results from Bovy et al. (2012), where the authors report that the vertical mass distribution of the disk of our Galaxy is consistent with a single structural component, rather than a combination of a 'thin' and a 'thick' disk. This diffusion would also naturally lead to higher galactic latitudes being populated exclusively by old stars, while galactic latitudes closer to the galactic plane could be populated by a wider variety of stellar populations, a trend that has been indeed observed in our Galaxy (Casagrande et al., 2016).

It is worth noting that because of the generally low inclination of the galaxies in our sample ($< 60°$), our setting allows us to measure the velocity dispersion in the vertical direction primarily (i.e., $\sigma_{*,z}$). Although different works have shown that the diffusion of stars occurs similarly in all directions (Yu & Liu, 2018; Mackereth et al., 2019; Tarricq et al., 2021), there is debate in the literature about the relative strength of the diffusion towards different directions. Yu & Liu (2018), Mackereth et al. (2019) and Sharma et al. (2021) find that the diffusion in the vertical direction is stronger than in the angular and radial directions. More recently, Tarricq et al. (2021) found that the diffusion in the radial and angular directions are stronger than in the vertical direction. In these works, the rate at which the velocity dispersion of young stars increase with time is quantified by the index of the power law (β) between age and σ_*, such that $\sigma_* \propto \tau^{\beta}$, following Binney et al. (2000). A similar quantification scheme is not applicable to our data. This is because we define age bins significantly broader than the time-resolution of the measured SFH in order to maximize the radial coverage at a given age, and decrease the statistical uncertainty in our measurements. The exact offset between the young, intermediate, and old populations depends on the definition of the bins, the galactocentric distance, local galactic environment, as well as systematic uncertainties associated with our SSP fitting. Nevertheless, our analysis provides useful insights on the impact of galactic structure on the progressive dynamical heating of young stellar populations, and the speed at which it occurs in star-forming galaxies beyond our Local Group.

Finally, these findings are also encouraging to refine our SSP fitting methodology currently implemented in the PHANGS-MUSE DAP, to include two independent kinematic components rather than just one. Zhang et al. (in prep.) will present an exploration of this dimension in more detail, characterizing the bias in the derived stellar population parameters yielded by the different kinematic conditions of young stellar populations.

5.3.6 Star formation histories across the galactic disks

In this section, we present how different galactic regions have formed stars through the lifetime of a galaxy. Interpreting the present-day spatially resolved SFHs as the real assembly history of a given galactic region neglects the impact of mechanisms that could cause stars travel far away from their birthplace. However, the negative age and metallicity profiles, and the general inside-out formation found for these galaxies point to an evolution dominated primarily by in-situ star formation, with radial migration having a second-order effect (Ibarra-Medel et al., 2016; Zhuang et al., 2019; Neumann et al., 2021).

Figures 5.21 and 5.22 show the time-averaged SFR in five time bins, calculated as the total

stellar mass formed within that time window (according to the derived SFH), divided by the length of the time-bin, for NGC 1566, and NGC 3627. There are a number of interesting features worth noting. The most obvious one is the lack of SFR in the second-youngest age bin (25 Myr - 100 Myr). The low SFR in this time bin is a consequence of the artifact in the SFHs described in Sec. 5.3.4, i.e., the dip in the SFH at log age ~ 7.7 Myr. Hence, we avoid physically interpreting this feature.

The central region of NGC 1566 seems to have been quenched (i.e., stopped forming stars) after the oldest age bin, and restarting star formation activity only very recently. A possibility could be that bar-driven secular evolution has enabled star formation in the center, by supplying gas to the inner region. However, as discussed in Sec. 5.3.3, the lack of nonbarred galaxies in our sample makes it difficult to quantify the role of the bar in the reactivation of star formation in centers. On the other hand, NGC 3627 seems to have been forming stars in its center continuously (this is also reflected in its inner radial bin, in Fig. 5.14). In our sample, we see a variety of behaviors, such as a drastic decrease of star formation in the inner regions, from early times to present day (e.g., NGC4254), a continuous star formation activity, or a reactivation of star formation in recent times.

Another clear feature is how galactic structure is evident in the youngest age bins, but it is progressively less prominent towards older ages, to become essentially non-existent for old stars. This is expected, as the dynamical heating discussed in Sec. 5.3.5 would eventually disrupt substructure, leading to a smooth distribution. Along this line, Neumann et al. (2020) use magneto-hydrodynamical cosmological simulations and find that while older stars (> 8 Gyr) follow a smooth distribution with a central concentration, younger stars (< 4 Gyr) are strongly coupled to the galactic structure.

The dynamical heating of young stellar populations, and the subsequent diffusion of galactic structure can be clearly appreciated in the time-averaged SFR maps of NGC 1566, particularly for its spiral arms. While in the youngest bin, stars are located preferentially along the spiral arms (marked in blue), in the third age bin (150 - 700 Myr), the spiral pattern is still clearly visible, although due to the diffusion of stars, the spiral arms are considerably broader. It is worth mentioning that while in Sec. 5.3.5 we presented evidence for dynamical heating in the vertical direction (i.e., increase of $\sigma_{*,z}$ with time), it is the dynamical heating in the perpendicular directions (i.e., radial and angular directions) that is responsible of the broader spiral arms we see in the third age bin, compared to the youngest bin. We also note that the diffusion of stars occurs everywhere across the galactic disk, not only across the spiral arms. However, the existence of a clear spiral pattern provides the opportunity of observing the process of stellar diffusion, and the subsequent 'washing out' of galactic structure across discrete age bins. A quantification of this diffusion from these SFR maps is challenging, due to the generally low spiral arm-disk contrast in the third age bin map, and due to artifacts in the maps (pointing-to-pointing jumps, or 'holes' in the maps). A sophisticated approach to quantify the time-scales of this broadening is thus, beyond the scope of this paper.

In order to visually identify this difussion phenomenon in the time-averaged SFR maps, we require the galaxy to have clear spiral arms, and that the spiral arms had been persisting in time, not formed recently by, e.g., a local instability sheared by differential rotation (Goldreich & Lynden-Bell, 1965). Thus, it is not surprusing that this effect is more prominent in some galaxies than in other. In the particular case of NGC 3627, the spiral arms-disk

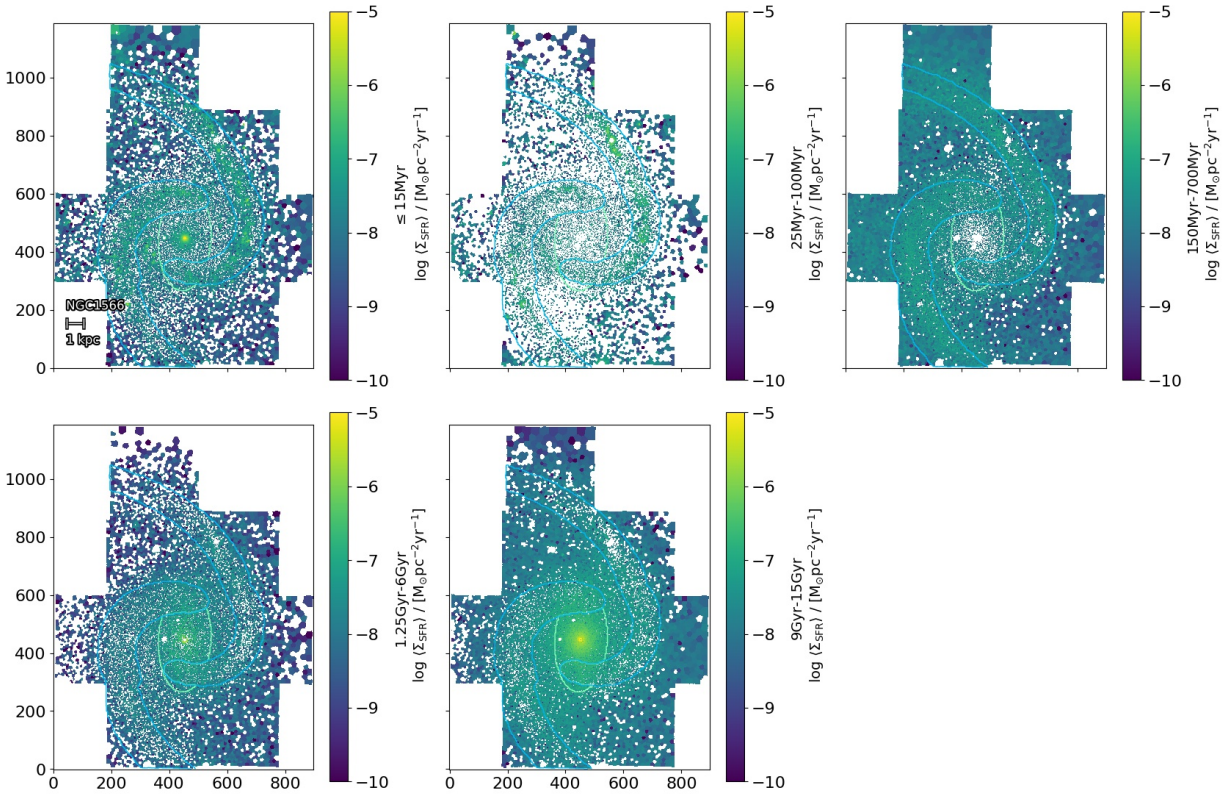

Figure 5.21: Time-averaged SFR in five different time bins, calculated fro the spatially resolved SFH, for NGC 1566. The panels show how different regions of the galactic disk have assembled their stellar mass in different moments of cosmic history. The blue and green contours mark the position of the spiral arms and the bar, respectively.

constrast is very low in the third age bin, which could be indicating a more recent origin of its spiral arms, possibly connected to a disruption driven by interactions with other galaxies from the Leo triplet (NGC 3623, and NGC 3628). Thus, this approach can provide a powerful tool to study the nature and prevalence of spiral arms across time.

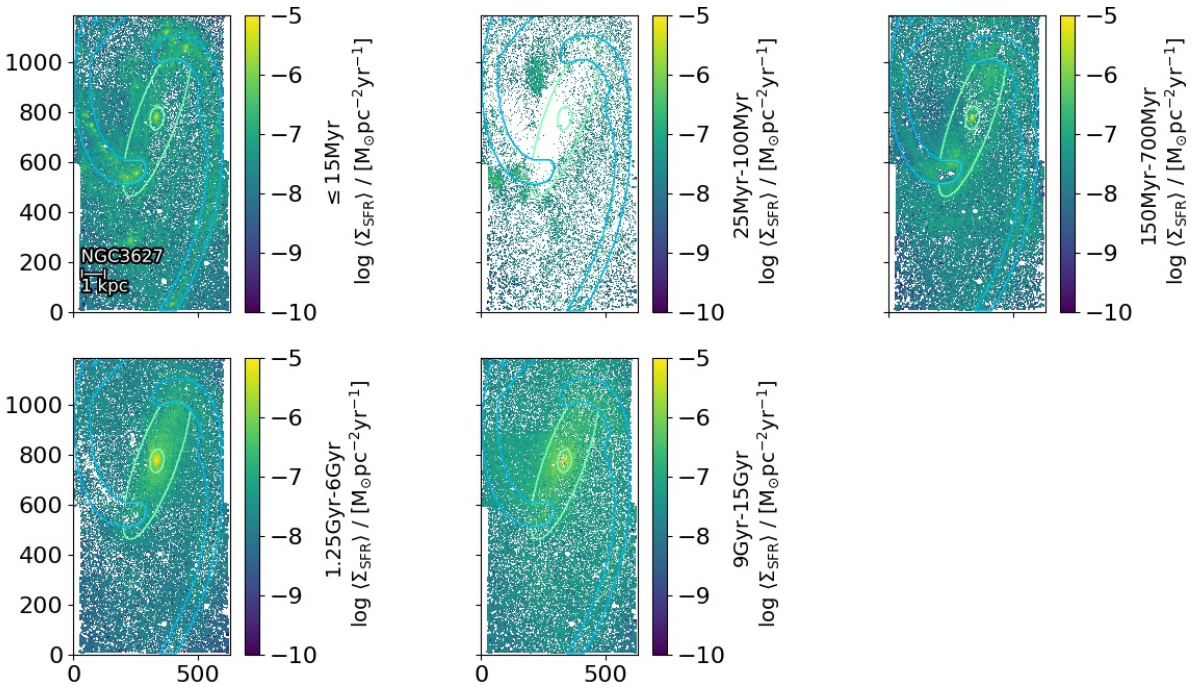

Figure 5.22: Time-averaged SFR in five different time bins, calculated fro the spatially resolved SFH, for NGC 3627. The panels show how different regions of the galactic disk have assembled their stellar mass in different moments of cosmic history. The blue and green contours mark the position of the spiral arms and the bar, respectively.

5.4 Summary and conclusions

In this chapter, we have presented a detailed analysis of the stellar populations properties of PHANGS-MUSE galaxies, including investigating the radial structure of age and metallicity, radial assembly history, dynamical heating of young stellar populations, and time-averaged SFRs across the galactic disks of 19 massive star-forming galaxies, and our main conclusions are the following:

- We find generally negative mass-weighted (MW) and light-weighted (LW) age profiles. Low-mass galaxies NGC 1385 and NGC 1087 are exceptions, showing nearly flat profiles. We find that the slope of the radial gradients correlates reasonably well with global quantities, such that galaxies with higher offset from the main sequence or molecular gas content show flatter LW age profiles. Spiral arms host younger (lower LW ages) populations than other galactic environments at any given radius.

- Galaxies have mostly negative metallicity profiles and show some degree of correlation of the slope of the metallicity gradient with total stellar mass and SFR, such that more massive (and star-forming) galaxies exhibit steeper metallicity gradients.

- We find flatter metallicity gradients along galactic bars, compared to the bar's perpendicular direction. This is consistent with the expectation from bar-driven secular

evolution inducing radial migration within bars. However, we can not robustly establish that metallicity gradients are flatter along bars due to our small sample size.

- We measure an overall well-defined radial assembly history, in which inner regions assembled their stellar mass earlier than outer regions, pointing to an 'inside-out' growth. This is consistent with previous findings in the literature, where late-type galaxies have been found to show a clear inside-out growth mode.

- Galaxies in our sample preserve the signal of 'downsizing' in galaxy evolution, where more massive galaxies, with lower total gas content, assembled their stellar mass earlier in cosmic history than less massive galaxies.

- We investigated the progressive increase of velocity dispersion of young stellar populations, and we find a clear gradient in velocity dispersion with age, such that at any given radius, younger stellar populations (< 100 Myr) have in general lower velocity dispersion than intermediate age [100 Myr, 600 Myr] and old (> 3 Gyr) populations. This gradient is an imprint of the mechanisms dynamically heating young stellar populations, such as interactions with molecular clouds or non-axisymmetric galactic substructure. We find this process to occur regardless of the presence of spiral arms. The age gradient in velocity dispersion is not present in bars, and we interpret this as dynamical heating being more efficient in the bar region.

- We have used the spatially resolved SFHs to reconstruct time-averaged SFR maps and study how different regions of galaxies assembled their mass. We find a wide variety of features, such as centers continuously forming stars, or quenched early in the galaxy lifetime. Younger populations are coupled to galactic structural components, but older stars follow a much more homogeneous and centrally concentrated distribution. Finally, in some galaxies we see a clear increase in the width of spiral arms with increasing age of the stellar populations probed, and interpret this as a sign of the diffusion of young stellar populations in the radial and angular directions.

Overall, the derived SFHs tell us a story in which galaxies assembled their stellar in an 'inside-out' mode, leading to negative age and metallicity profiles, and were more massive galaxies assembled their stellar mass earlier in cosmic history than less massive galaxies, consistent with the expectation from previous studies. Furthermore, thanks to the high spatial resolution achieved by PHANGS-MUSE, for the first time, we have been able to investigate the properties of stellar populations across multiple galactic environments separately, covering a significant part of the stellar disk of nearby star-forming galaxies.

6 Summary and Outlook

"One can begin to reshape the landscape with a single flower"

by Spock

6.1 Summary and conclusions

The evolution of galaxies through cosmic times has led to the large variety of shapes and colors in galaxies that we see today. In-situ formation of stars is a major driver of galaxy evolution, especially in disky late-type galaxies, progressively enriching the interstellar medium with metals through feedback from massive stars. The evolution of a galaxy driven by star formation through its lifetime is encoded in its star formation history (SFH), while the ongoing evolution is encoded in its current star-formation activity. Together, these two metrics offer a comprehensive picture of galaxy evolution.

However, galaxies are extended and complex objects whose properties can change drastically from one region to another. Moreover, the formation of stars and stellar population properties, and hence, the characteristics of the overall evolutionary process, are known to depend on local properties, such as physical conditions of the interstellar medium (Sun et al., 2020a) or local galactic structure (Querejeta et al., 2021), besides global conditions such as galactic potential.

Studies in our Galaxy offer the advantage of performing very accurate measurements of star formation and stellar populations properties, as we can resolve and measure the properties of individual stars through large photometric and spectroscopic surveys. However, they are biased, as a single galaxy is not sufficient to understand how star formation modulates the evolution of galaxies across different mass ranges or Hubble types. Moreover, since our Solar system is embedded within the disk of our Galaxy, we are able to observe only specific Galactic regions and not our Galaxy as a whole entity.

In this regard, nearby galaxies provide us with the amazing opportunity of studying galaxies in a holistic manner, allowing the study of galactic properties on sub-galactic scales for representative samples. Large Integral Field Spectroscopic (IFS or IFU) surveys, such as CALIFA (Sánchez et al., 2012), MaNGA (Bundy et al., 2015), or SAMI (Croom et al.,

2012), have taken these studies to the next level, enabling measurements of stellar and gas properties of different regions of the galactic disk simultaneously, at spatial scales of the order of ~ 1 kpc. While these surveys represented a revolution in the study of nearby galaxies, spatial scales of ~ 1 kpc are still too coarse to investigate the interplay of star formation and the local conditions of the interstellar gas, or between properties of stellar populations and galactic structure. For such endeavors, it is necessary to resolve individual star-forming regions with typical sizes on the order of $\sim 50-100$ pc (Heyer & Dame, 2015). There exist other relevant IFU surveys that reach these spatial resolutions, such as TIMER, or MAD, but they were designed to address specific (and different) scientific questions, and thus, they lack a representative sample to carry out comprehensive studies on galactic evolution.

The PHANGS surveys provide, for the first time, a representative sample of nearby galaxies to study star formation, its interplay with properties of the interstellar medium, and galactic evolution in general, at spatial scales comparable to the size of individual star-forming regions. The combination of its three main pillars (PHANGS-ALMA, PHANGS-HST, and PHANGS-MUSE) enables the study of the chemical and kinematic properties of ionized gas, molecular gas, young stellar clusters, and underlying stellar populations.

In this thesis, we have shown how to exploit data from the PHANGS-ALMA and PHANGS-MUSE survey to address questions such as: what are the main mechanisms regulating the formation of stars across the galactic disks of late-type galaxies, and how the star-forming process depends on local galactic environment. We also detail how to derive stellar population properties from the MUSE mosaics, and present an exhaustive study of how these properties vary across galactic disks, and correlate with the morphological structure of galaxies. In the following, we will highlight the key results from each specific chapter of this thesis.

6.1.1 Star-formation scaling relations at a resolution of ∼100 pc

The complexity of star formation at the physical scale of molecular clouds is not yet fully understood. To gain insights into the physics that regulate the formation of stars, in Chapter 2, we explore the existence of the resolved star formation main sequence (Σ_* versus $\Sigma_{\rm SFR}$), resolved Kennicutt-Schmidt relation ($\Sigma_{\rm mol}$ versus $\Sigma_{\rm SFR}$), and resolved molecular gas main sequence (Σ_* versus $\Sigma_{\rm mol}$), characterizing their slope and scatter at spatial resolutions of ~ 100 pc, and investigating the impact of spatial resolution on our measurements. We employed data from the PHANGS-MUSE survey to probe the ionized gas properties, using it as our SFR tracer, as well as to measure the underlying stellar mass surface density from the stellar continuum, and data from the PHANGS-ALMA survey to probe molecular gas properties. We recover the three scaling relations at a spatial scale of ~ 100 pc for the first time in nearby galaxies, although with a significantly enhanced scatter, compared to lower resolution measurements. This is because, at a spatial scale of ~ 100 pc, each spatial resolution element is likely dominated by either a star-forming cloud with an excess of molecular gas (i.e., early in the star-forming process), or with an excess of ionized gas (i.e., later in the star-forming process), rather than stochastically sampling the different stages of the star-forming cycle and measure a representative averaged molecular gas (or SFR) surface density value. Furthermore, at these spatial scales, the distribution of both, molecular and ionized gas is highly inhomogeneous, strongly coupled with galactic structure, and hence,

the treatment of non-detections has a systematic impact on the inferred slope, as a function of the spatial scale.

Overall, we find that at a spatial scale comparable to the size of star-forming clouds, the resolved Kennicutt-Schmidt relation shows a much homogeneous behavior, not only between different individual galaxies but also across individual galactic environments, and we conclude that the availability of molecular gas is the main factor regulating the formation of stars. We have also investigated if variations in the slope of these relations correlate with global galaxy properties, and found that galaxies experiencing a global enhancement of SFR are also more likely to show a steeper resolved star formation main sequence, pointing to a scenario in which the enhancement of SFR is occurring preferentially in the inner and denser regions.

Studying the star-forming scaling relations in nearby galaxies at this high spatial resolution is a powerful tool to connect extragalactic observations with measurements in our own Galaxy, and quantifying systematic variations in these relations across galaxies and/or galactic environments provides valuable insights into how galaxies grow and evolve in the local universe.

6.1.2 Variations in the interplay between stellar mass, molecular gas mass, and star formation rate surface densities across galactic environments

There exists some consensus that Σ_* and $\Sigma_{\rm mol}$ are the main quantities responsible for locally setting the star formation rate. This regulating role is inferred from the existence of the locally resolved scaling relations between these two quantities and $\Sigma_{\rm SFR}$, studied in Chapter 2, as well as in several recent works based on lower resolution data. However, the universality of these relations is debated. While some authors have reported that the scatter of these relations is fully dominated by random uncertainties (Sánchez et al., 2021), others (e.g., Ellison et al., 2021), including our analyses in Chapter 2, find strong indications of galaxy-to-galaxy variations contributing to the scatter of these relations. Furthermore, thanks to the high resolution of our data, we have also been able to measure systematic variations in these scaling relations across galactic environments. In Chapter 3, we investigated in detail the interplay between these three quantities across different galactic environments at a spatial resolution of 150 pc, aiming at quantifying robust differences that correlate with local environments.

To do this, we performed a hierarchical Bayesian linear regression to find the best set of parameters $C_\star$, $C_{\rm mol}$, and $C_{\rm norm}$ that describe the star-forming plane conformed by $\Sigma_\star$, $\Sigma_{\rm mol}$, and $\Sigma_{\rm SFR}$, such that $\log\Sigma_{\rm SFR} = C_\star \log\Sigma_\star + C_{\rm mol}\log\Sigma_{\rm mol} + C_{\rm norm}$. If the SFR in a given region is primarily driven by these two quantities, then, this 'star-forming plane' should not change significantly between individual galaxies or among different galactic environments. On the other hand, significant variations in the best-fit star-forming plane among different locations would indicate that such a relationship offers an incomplete description of the data and hint at additional quantities or functional forms that are key to regulating star formation in galaxies.

The analysis carried out in Chapter 3 shows signs of evidence for variations in the posterior distributions of $C_\star$ and $C_{\rm mol}$ across different galactic environments. The dependence of $\Sigma_{\rm SFR}$

on $\Sigma_\star$ spans a wide range of slopes, with negative and positive values, while the dependence of $\Sigma_{\rm SFR}$ on $\Sigma_{\rm mol}$ is always positive. Bars show the most negative value of $C_\star$ (-0.41), which is a sign of longer depletion times, while spiral arms show the highest $C_\star$ among all environments (0.45). Variations in $C_{\rm mol}$ are also present, although they are more subtle than those found for $C_\star$.

From this analysis, we conclude that systematic variations in the interplay of $\Sigma_\star$, $\Sigma_{\rm mol}$, and $\Sigma_{\rm SFR}$ across different galactic environments exist at a spatial resolution of 150 pc, and we interpret these variations to be produced by an additional mechanism regulating the formation of stars that is not captured by either $\Sigma_\star$ or $\Sigma_{\rm mol}$. By studying environmental variations in single galaxies, we find that these variations correlate with changes in the star formation efficiency across environments, which could be linked to the dynamical state of the gas that prevents it from collapsing and forming stars, or to changes in the molecular gas fraction.

However, although these results are consistent with the existence of additional physics being at play in the regulation of star formation, a significantly larger sample of galaxies where we can simultaneously probe different galactic environments is required to confirm the correlations explored in Chapter 3, and thus, to provide a definitive answer to what is (or are) the additional parameter(s) modulating the formation of stars.

6.1.3 Modeling the spectral energy distribution of galaxies

The integrated spectral energy distribution (SED) of galaxies is our main source of information to reveal the physical processes occurring in galaxies. However, in order to infer the physical properties of galaxies from their emitted light, proper SED modeling is required. In particular, in the wavelengths where the SED is dominated by stellar light, the spectra of galaxies can be represented as a dust-attenuated linear combination of the spectra of single stellar populations (SSPs). The technique of inferring the properties of different stellar populations from an integrated spectrum is known as full-spectrum fitting or fossil record method. This technique has been refined during the past two decades, with the development of a number of stellar libraries and codes to implement it.

In Chapter 4, we describe in detail our adopted methodology to derive physical quantities from our MUSE mosaics (mainly through the full-spectrum fitting technique), including stellar population properties such as age and metallicity, stellar mass maps, emission line fluxes, stellar extinction, and kinematic properties of gas and stars. This work is framed in the context of the PHANGS-MUSE data analysis pipeline (DAP), of which I am one of the main contributors, developed to process data from the PHANGS-MUSE survey and provide science-ready data products to be used by members from the full PHANGS collaboration, as well as the rest of the scientific community.

We also present a quality assessment of the data products related to the stellar population fitting module of the DAP. We cross-compare our stellar mass surface density maps with those obtained using near infra-red (NIR) data from the S^{4}G survey, finding a generally good agreement between both data sets. However, in regions where stellar populations with ages younger than 1$-$2 Gyr are present, masses derived from the near-IR data are systematically larger. This is because the contribution of AGB stars to the near-IR flux can be dominant, leading to a different M/L than that appropriate for an old population.

A visual examination of the stellar age and metallicity maps produced by the DAP revealed unrealistically low metallicities (**LW** $[\mathbf{Z/H}] < -1.3$) in a few regions encompassing very young stellar clusters (**LW age** < 400 Myr). Such low metallicity values would be inconsistent with an internal and progressive chemical enrichment of the interstellar medium, suggesting that these metallicities are an artifact produced by the fitting process converging towards a misleading local χ^2 minimum. These low metallicity regions usually coincide with strong Hα emission, indicating that these young clusters coincide with active star formation. This is likely driven by a combination of different factors, including the lack of younger templates (due to the low number of young and metal-poor stars in the E-MILES library), contributions from nebular emission as unmasked emission lines, and the particular physical conditions in which young stars are embedded.

Finally, we present our efforts to improve the fitting of the spectra of these young regions. To achieve this, we perform a broader exploration of the parameter space, including the usage of different libraries of templates, the subtraction of the stellar continuum before fitting the observed spectra, accounting for nebular emission, and varying the metallicity grid of the templates. These efforts converged to using a specific set of templates that reaches ages as young as 6.5 Myr, and whose lowest metallicity bin ($[Z/H] = -1.33$) has been removed from the metallicity grid.

6.1.4 Spatially resolved stellar population properties and assembly histories of PHANGS-MUSE galaxies

The stellar populations present in different regions of a galactic disk provide extremely valuable information on how a galaxy assembled its current stellar mass through its lifetime. Although previous work has revealed common features in the stellar mass build-up of galaxies, their limited spatial resolution does not allow resolving the smaller scale structure of the stellar populations properties and how does it correlates with galactic morphological features.

In Chapter 5, we presented a detailed analysis of the spatially resolved stellar populations and star formation histories of PHANGS-MUSE galaxies, at a spatial resolution of ~ 100 pc. We show that our galaxies exhibit generally negative stellar age and metallicity profiles, a radial structure that is consistent with being the result of in-situ local star formation history primarily, and which are interpreted as a sign for inside-out growth of galaxies (age gradient), and as Σ_* being the main driver of chemical enrichment (metallicity gradient). We also find flatter stellar metallicity gradients along the bar major axes in barred galaxies, than along the bar minor axes, a feature expected from radial mixing of material occurring along the bar. In general, the derived assembly histories of the galaxies in our sample tell us a consistent story in which galaxies assembled the stellar mass residing in their inner regions earlier in cosmic history than that in outer regions (i.e., inside-out growth), and low mass galaxies assembled the bulk of their stellar mass later in cosmic history than higher mass galaxies (i.e., downsizing in galaxy evolution).

Besides star formation histories, we also show how stellar populations of different ages are characterized by different kinematic conditions. Specifically, we find that younger stellar populations have lower velocity dispersions than older stellar populations at similar galactocentric distances. This is an imprint of the progressive dynamical heating of young stellar

populations through interactions with molecular clouds or non-axisymmetric galactic substructure. Finally, we explore how the time-averaged SFR has evolved with time, and how it varies across galactic disks. This analysis reveals a wide variety in the SFH of centers and the diffusion of galactic structure with lookback time, consistent with our findings on the dynamical heating of young stars.

6.2 Future perspective

In this section, we outline future research directions to extend the research presented in this thesis. These lines of research are grouped into three main categories: (i) Confirming our results and carrying out more robust analyses, using a larger sample of galaxies, (ii) further refinements to our SSP fitting technique to improve the fitting of regions where young stellar populations are present, and (iii) development of a new research avenue, suitable for our dataset.

6.2.1 Confirmation of environmental variations in the star-formation plane and assessment of the role of bars in galaxy evolution using a larger sample of galaxies

The research projects outlined in this section aim to further explore and confirm the existence (as well as determining the drivers) of the environmental variations in the interplay between stellar mass, molecular gas mass, and star formation rate surface densities reported in this thesis (see Chapter 3), and to a robust assessment of the impact of bars in the evolution of the inner galactic regions (see Chapter 5).

Measure the origin of variations in the star-forming plane across galactic environments, using a larger sample of galaxies

In Chapter 3, we find significant variations in the star-forming plane across different galactic environments. However, our small sample of 18 galaxies does not allow us neither performing a robust measurement in the smaller (hence, lower number of pixels) environments, nor robustly determining which is (or are) the main parameter(s) driving the observed variations across environments. A recently submitted VLT/MUSE proposal (PI: Kathryn Kreckel) aims to more than double the PHANGS-MUSE sample with 30 additional galaxies that already have at least one existing VLT/MUSE pointing in the archival data. These galaxies have been selected in order to fully sample a representative range of the main parameters driving galaxy evolution, such as stellar masses, stellar environments, and gas fractions. This increased sample is also essential for more rigorous studies of the origin of the variations in the interplay between Σ_*, $\Sigma_{\rm mol}$, and $\Sigma_{\rm SFR}$, and ultimately will shed light on the unknown additional physics playing a relevant role in regulating the formation of stars.

Use larger, lower-resolution dataset to explore environmental-driven galaxy-to-galaxy variations in the star-forming plane

An alternative (and totally independent) approach to robustly establish the existence of environment-driven variations in the star-forming plane of galaxies would be using a larger optical+sub-mm dataset with lower spatial resolution (e.g., ALMaQUEST; Lin et al., 2019), and group galaxies based on the relative contribution of different galactic environments. If the galaxy-to-galaxy variations are significantly stronger among galaxies from different environment-categories, than among galaxies within the same group, it would be a clear indicator that galaxy-to-galaxy variations correlate with morphological features. On the

other hand, not detecting clear differences between these groups would imply that the strong galaxy-to-galaxy variations reported for this same dataset by Ellison et al. (2020a) do not correlate with the presence of different galactic environments, thus, entering in conflict with our results.

Determine the role of bars in the evolution of stellar population in the inner regions of galaxies

It is known that bars modulate the inflow of material towards the central regions of galaxies (Catalán-Torrecilla et al., 2017), thus, being responsible for an increase in the star formation activity in centers. In Chapter 3, we find that centers show less constrained values of the coefficients that define their star-forming plane (partly due to low number statistics, but also because centers show a wider variety of behaviors, consistent with results from Querejeta et al. (2021), that show that centers of PHANGS galaxies show a very broad distribution of depletion times). Furthermore, in Chapter 5 we show how in some galaxies, the central region deviates strongly from the radial assembly history, implying that in those galaxies, centers formed a substantial fraction of their current stellar mass in relatively recent cosmic times. However, studying the impact of bars in the evolution of centers with the current PHANGS-MUSE sample is difficult due to a lack of unbarred galaxies (only 4 out of 19). If the proposal to extend the PHANGS-MUSE sample mentioned above is accepted, it will enable quantifying the impact of bars in the SFHs and present-day SFR of centers as a function of global galactic parameters. A robust understanding of the impact bars have on the evolution of their galaxy would eventually lead to assessing which galaxies might have had bars in the past or which galaxies have developed their bars only in recent times.

6.2.2 Deriving more reliable SFHs by improving the SSP fitting of young stellar populations

As described in Chapter 4, there is plenty of room for improvement in the SSP fitting of the spectra of regions dominated by young ($\lesssim 30$ Myr) stellar populations. Here we propose several promising directions to achieve this goal. Firstly, we propose the usage of recently developed synthetic stellar libraries, which offer several advantages with respect to the empirical stellar libraries, such as unlimited spectral resolution and wide coverage of the parameter space. Other possibilities to improve our derived SFHs are (i) accounting for the different kinematic properties of young and old stellar populations in the fit (see Chapter 5), i.e., using more than one kinematic component in the SSP fitting, (ii) including available photometric data from the PHANGS-HST survey in the SSP fitting, to constrain bluer wavelength ranges, and (iii) acknowledge that young stellar populations are often subject to higher dust-extinction values, and modify our SSP fitting routine accordingly.

Explore the usage of synthetic stellar libraries to improve the SSP fitting of young clusters

Single stellar population (SSP) models are one of the most powerful tools developed over the last few decades in astrophysics and are hugely useful to interpret the observed spectral energy distribution of astronomical objects. SSP models fundamentally rely on a set of

ingredients from which they are constructed (i.e., stellar evolutionary track, stellar flux library, and initial mass function; see review by Conroy, 2013). In particular, a given stellar flux library (or stellar spectral library) consists of a homogeneous compilation of stellar spectra covering a broad range of the parameter space (e.g., surface gravity, metallicity, etc). A spectral library can be either empirical (i.e., based on the observed spectra of real stars), or theoretical (i.e., based on theoretical prediction for the SED of stars).

While empirical libraries offer the advantage of reproducing spectral features accurately, they have the drawback of not being able to fully sample the parameter space. On the other hand, theoretical libraries can sample the full parameter space, without any S/N or wavelength coverage constraints, at the cost of a limited ability to reproduce observations accurately due to our current limitations in the knowledge of the physics of stellar atmospheres (see discussion in Coelho et al., 2020).

Due to this limitation of the synthetic stellar libraries, we have focused our exploration on improving the SSP fitting for young regions (see Chapter 4) exclusively on empirical libraries. However, preliminary explorations using synthetic libraries to derive the star formation histories of galaxies from our sample offer promising first results in terms of improving the problematic young-metal-poor persisting feature in the derived metallicity maps. In particular, SSP templates from the recently published HR-PYPOPSTAR (Millán-Irigoyen et al., 2021) synthetic stellar library seem like a viable option to further improve our SSP fitting. More testing and exploration are needed in order to assess limitations and potential biases yielded by these newly developed templates before using them to carry out a rigorous analysis. Nevertheless, its characteristics (high spectral resolution, uniform, and higher than MUSE across the full wavelength range, a proper sampling of the parameter space, and a seemingly good capability to reproduce observed spectral features) make them a potential addition to future improvements and subsequent releases of PHANGS-MUSE data products.

Refine the fitting methodology currently implemented in our PHANGS-MUSE data analysis pipeline

Observation in our Galaxy have longly shown that older stellar populations are subject to higher velocity dispersion values than younger stellar populations. In Chapter 5, we report an equivalent trend across the full galactic disk of nearby star-forming galaxies. These different kinematic conditions between young and old populations could potentially be problematic to recover SFHs from the integrated spectrum, as young stars (when present) dominate the light of a given region, but older (low-mass) stars dominate the stellar mass budget. The exact impact of this effect on the measured SFHs has not been characterized. Zhang et al. (in prep.) will present a detailed exploration of the influence of these different kinematic conditions on the recovered SFHs. These findings could potentially motivate an upgrade in the SSP fitting methodology currently implemented in the PHANGS-MUSE pipeline, to include more than one kinematic stellar component to reproduce the observed spectra, aiming to recover less biased and more reliable SFHs, especially in the regions where young stars are present.

An additional possibility to greatly improve our SSP fitting is using the photometric data from the PHANGS-HST survey to constrain bluer wavelength ranges, which we can not access using MUSE. These bluer wavelengths are extremely valuable to constrain the properties of young stellar populations (see, e.g., González Delgado et al., 2005). In this

line, upcoming data from the PHANGS-JWST Treasure programme could also be used to constrain dust properties, and remove potential degeneracies between stellar extinction and stellar population properties. However, the inclusion of additional photometric data to the spectral fitting technique is not trivial, and requires further development of the currently available tools. Recently developed algorithms, such as `piXedfit` (Abdurro'uf et al., 2021) include this feature, and there are ongoing efforts to include it in pPXF.

Assess how the different physical conditions in which young stars are embedded bias the results of our SSP fitting

Young stellar populations are embedded in deeper layers of gas and dust, remnants of the cloud from which they formed, than old stellar populations. In this work, we have assumed a single extinction value for all the stellar populations present in a given region, parametrized by a Calzetti et al. (2000) extinction law. Although young stars disperse molecular clouds on relatively short time scales of a few Myr (Chevance et al., 2020b), young stellar populations in star-forming regions are likely affected by greater extinction values than their older counterparts. The impact of this different extinction across co-existing stellar populations on the measured SFHs has not been determined yet, although preliminary tests with mock data show that this effect can yield severely biased values of stellar age, metallicity, and mass surface density. Addressing this open issue and quantifying the impact of this effect in different regions of the parameter space (i.e., as a function of age, metallicity, gas fraction, etc.) would imply an important contribution to the scientific community, besides representing an opportunity to modify our SSP fitting routine to account for this effect, and obtain more reliably SFHs.

6.2.3 New research avenues suitable for our dataset

Investigate variations in the initial mass function of late-type galaxies

The initial mass function (IMF) encodes information on the relative number of stars that are born from a giant molecular gas cloud, after it fragments. Thus, it is a key tool that connects the light that a galaxy emits with its underlying stellar (and stellar remnant) mass, allowing astronomical measurements to be interpreted in terms of astrophysical models. As a result, many measurements, such as stellar masses, or star formation rates, rely on the assumption of an IMF. The IMF is also responsible for the modulation of the chemical enrichment of a galaxy, as it determines the number of massive stars that will explode as supernovae, and the amount of gas locked in low-mass stars. While there is evidence that supports the idea of a unique IMF in our Galaxy (Chabrier, 2003), the lack of theoretical understanding of the star formation process and cloud fragmentation make measurements of the IMF outside the Milky Way very valuable. Measurements of the IMF in early-type galaxies have been carried out recently (see, e.g., Martín-Navarro et al., 2019; Smith, 2020; Martín-Navarro et al., 2021), and while early-type galaxies have likely simpler SFHs that can be well represented by a single stellar population making constraints on the IMF easier, they have the drawback of offering a very limited mass range to probe the IMF (< 1 $M_{\odot}$), as they lack more massive stars due to their low levels of star formation. Despite these limitations, evidence suggests that more massive galaxies have an IMF steeper than that of the Milky Way (Sonnenfeld

et al., 2019; Martín-Navarro et al., 2019), i.e. a relative excess of low mass stars, leading to higher mass-to-light ratios (M/L). PHANGS provides the perfect data to extend this research to late-type galaxies similar to our Galaxy. With detailed spectroscopic information from the stellar populations, as measured by MUSE, and a powerful description of the gravitational potential, traced by the molecular gas, we have the information needed to place constraints on the IMF of nearby late-type galaxies. This would be a very interesting research direction to follow up on the research presented in this thesis, particularly after further refinement of our SSP fitting methodology. Specifically, measure the IMF of PHANGS galaxies, and provide, for the first time, a systematic study of the IMF slope in late-type galaxies, and how this IMF depends on local or global conditions. To carry out such project, it would be relevant to perform an exhaustive exploration of IMF-sensitive tracers using the integrated spectra of individual galactic regions, as well as testing the full-spectrum fitting approach. Similar approaches have been successfully applied to early-type galaxies (van Dokkum & Conroy, 2021; Martín-Navarro et al., 2021). However, the current lack of knowledge of the universality of the IMF in late-type galaxies makes this measurement necessary, as most of our current assumptions are based on measurements done in our Galaxy.

List of publications

These scientific publications have been submitted and published during my studies, or are in preparation for publication within this year.

1st AUTHOR PUBLICATIONS

1. **Pessa, I.**, Schinnerer, E., Belfiore, F., Emsellem, E., et al. 2021, A&A, 650, A134;
   "Star formation scaling relations at $\sim$100 pc from PHANGS: Impact of completeness and spatial scale"

   [Chapter 2 in this PhD Thesis]

2. **Pessa, I.**, Schinnerer, E., Leroy, A., Koch, E., Rosolowsky, E., et al. 2022, A&A, accepted for publication;
   "Variations in the $\Sigma_{\rm SFR}$–$\Sigma_{\rm mol}$–Σ_{*} plane across galactic environments in PHANGS galaxies"

   [Chapter 3, in this PhD Thesis]

3. **Pessa, I.**, Schinnerer, E., Belfiore, F., Groves, B., Sánchez-Blázquez, P., et al., in preparation
   "Spatially resolved star-formation histories in PHANGS galaxies"

   [Chapters 4 and 5 in this PhD Thesis]

4. **Pessa, I.**, Tejos, N., Barrientos, L. F., Werk, J., et al. 2018, MNRAS, 477, 2991;
   "A VLT/MUSE galaxy survey towards QSO Q1410: looking for a WHIM traced by BLAs in inter-cluster filaments"

   [Not included in this PhD Thesis]

CONTRIBUTIONS TO PUBLICATIONS INCLUDED IN THIS THESIS

1. Emsellem, E., Schinnerer, E., Santoro, F., Belfiore, F., **Pessa, I.**, et al. 2021, A&A, 659, A191;
   "The PHANGS-MUSE survey. Probing the chemo-dynamical evolution of disc galaxies"

   [Parts included in Chapter 4]

CONTRIBUTIONS TO PUBLICATIONS NOT INCLUDED IN THIS THESIS

1. Galbany, L., Smith, M., Duarte Puertas, S., González-Gaitán, S., **Pessa, I.**, et al. 2022, A&A, 659, A89.;
   "Aperture-corrected spectroscopic type Ia supernova host galaxy properties".

2. Belfiore, F., Santoro, F., Groves, B., Schinnerer, E., ..., **Pessa, I.**, et al. 2022, A&A, 659, A26;
   "A tale of two DIGs: The relative role of H II regions and low-mass hot evolved stars in powering the diffuse ionised gas (DIG) in PHANGS-MUSE galaxies"

3. Santoro, F., Kreckel, K., Belfiore, F., ..., **Pessa, I.**, et al. 2022, A&A, 658, A188;
   "PHANGS-MUSE: The H II region luminosity function of local star-forming galaxies"

4. Leroy, A., Schinnerer, E., Hughes, A., ..., **Pessa, I.**, et al. 2021, ApJS, 257, 43;
   "PHANGS-ALMA: Arcsecond CO(2-1) Imaging of Nearby Star-forming Galaxies"

5. Bešlić, I., Barnes, A. T., Bigiel, F., ..., **Pessa, I.**, et al. 2021, MNRAS, 506, 963;
   "Dense molecular gas properties on 100 pc scales across the disc of NGC 3627"

6. Williams, T., Schinnerer, E., Emsellem, E., ..., **Pessa, I.**, et al. 2021, AJ, 161, 185;
   "Applying the Tremaine-Weinberg Method to Nearby Galaxies: Stellar-mass-based Pattern Speeds and Comparisons with ISM Kinematics"

7. Kreckel, K, Ho, I., Blanc, G., ..., **Pessa, I.**, et al. 2020, MNRAS, 499, 193;
   "Measuring the mixing scale of the ISM within nearby spiral galaxies"

8. Lang, P., Meidt, S., Rosolowsky, E., ..., **Pessa, I.**, et al. 2020, ApJ, 897, 122;
   "PHANGS CO Kinematics: Disk Orientations and Rotation Curves at 150 pc Resolution"

9. Herrera, C., Pety, J., Hughes, A., ..., **Pessa, I.**, et al. 2020, A&A, 634, A121;
   "The headlight cloud in NGC 628: An extreme giant molecular cloud in a typical galaxy disk"

10. Lopez, S., Tejos, N., Barrientos, L. F., ..., **Pessa, I.**, et al. 2020, MNRAS, 491, 4442;
    "Slicing the cool circumgalactic medium along the major axis of a star-forming galaxy at z = 0.7"

11. Lopez, S., Tejos, N., Ledoux, C., ..., **Pessa, I.**, et al. 2018, Natur, 554, 493;
    "A clumpy and anisotropic galaxy halo at redshift 1 from gravitational-arc tomography"

Bibliography

Abazajian, K. N., Adelman-McCarthy, J. K., Agüeros, M. A., et al. 2009, ApJS, 182, 543 16, 44

Abdurro'uf, & Akiyama, M. 2017, MNRAS, 469, 2806 29, 48, 62, 100

Abdurro'uf, Lin, Y.-T., Wu, P.-F., & Akiyama, M. 2021, ApJS, 254, 15 220

Accurso, G., Saintonge, A., Catinella, B., et al. 2017, MNRAS, 470, 4750 21, 50, 103

Aharonian, F., Bykov, A., Parizot, E., Ptuskin, V., & Watson, A. 2012, Space Sci.Rev., 166, 97 25

Anand, G. S., Lee, J. C., Van Dyk, S. D., et al. 2021, MNRAS, 501, 3621 49, 51, 102, 103, 175, 178

Andersson, B. G., Lazarian, A., & Vaillancourt, J. E. 2015, ARA&A, 53, 501 25

Asa'd, R. S., Vazdekis, A., Cerviño, M., et al. 2017, MNRAS, 471, 3599 154, 176

Bacchini, C., Fraternali, F., Iorio, G., & Pezzulli, G. 2019a, A&A, 622, A64 48, 83, 112

Bacchini, C., Fraternali, F., Pezzulli, G., & Marasco, A. 2020, A&A, 644, A125 48, 83, 112

Bacchini, C., Fraternali, F., Pezzulli, G., et al. 2019b, A&A, 632, A127 83

Bacon, R., Vernet, J., Borisova, E., et al. 2014, The Messenger, 157, 13 50, 102, 175

Bacon, R., Conseil, S., Mary, D., et al. 2017, A&A, 608, A1 141

Bagetakos, I., Brinks, E., Walter, F., et al. 2011, AJ, 141, 23 20

Baker, W. M., Maiolino, R., Bluck, A. F. L., et al. 2022, MNRAS, 510, 3622 30

Baldwin, J. A., Phillips, M. M., & Terlevich, R. 1981, PASP, 93, 5 22, 53, 105

Barbanis, B., & Woltjer, L. 1967, ApJ, 150, 461 201

Barrera-Ballesteros, J. K., Utomo, D., Bolatto, A. D., et al. 2020, MNRAS, 492, 2651 24

Barrera-Ballesteros, J. K., Heckman, T., Sánchez, S. F., et al. 2021a, ApJ, 909, 131 49, 62, 76, 82, 83, 87, 100, 121

Barrera-Ballesteros, J. K., Sánchez, S. F., Heckman, T., et al. 2021b, MNRAS, 503, 3643 83, 122

Beck, R. 2003, arXiv e-prints, astro 25

Beck, R. 2009, in Cosmic Magnetic Fields: From Planets, to Stars and Galaxies, ed. K. G. Strassmeier, A. G. Kosovichev, & J. E. Beckman, Vol. 259, 3–14 25

—. 2015, A&A Rev., 24, 4 25

Beck, R., Berkhuijsen, E. M., Gießübel, R., & Mulcahy, D. D. 2020, A&A, 633, A5 25

Beck, R., Chamandy, L., Elson, E., & Blackman, E. G. 2019, Galaxies, 8, 4 25

Belfiore, F., Maiolino, R., Bundy, K., et al. 2015, MNRAS, 449, 867 53, 105

Belfiore, F., Westfall, K. B., Schaefer, A., et al. 2019, AJ, 158, 160 138, 145, 146

Belfiore, F., Santoro, F., Groves, B., et al. 2022, A&A, 659, A26 22, 53, 105, 142

Biernacki, P., & Teyssier, R. 2018, MNRAS, 475, 5688 26

Bigiel, F., Leroy, A., Walter, F., et al. 2008, AJ, 136, 2846 29, 48, 62, 64, 74, 100, 122

Bigiel, F., Leroy, A. K., Walter, F., et al. 2011, ApJ, 730, L13 48, 100

Binney, J., Dehnen, W., & Bertelli, G. 2000, MNRAS, 318, 658 199, 205

Bittner, A., Falcón-Barroso, J., Nedelchev, B., et al. 2019, A&A, 628, A117 102, 138, 139, 142

Bittner, A., Sánchez-Blázquez, P., Gadotti, D. A., et al. 2020, A&A, 643, A65 36, 138, 151, 201

Bittner, A., de Lorenzo-Cáceres, A., Gadotti, D. A., et al. 2021, A&A, 646, A42 36

Blanc, G. A., Heiderman, A., Gebhardt, K., Evans, Neal J., I., & Adams, J. 2009, ApJ, 704, 842 22, 53, 62, 100, 105

Blanton, M. R., & Moustakas, J. 2009, ARA&A, 47, 159 14

Bohlin, R. C. 1975, ApJ, 200, 402 23

Bolatto, A. D., Leroy, A. K., Rosolowsky, E., Walter, F., & Blitz, L. 2008, ApJ, 686, 948 28, 39

Bolatto, A. D., Wolfire, M., & Leroy, A. K. 2013, ARA&A, 51, 207 21, 51, 84, 103, 125

Bolatto, A. D., Wong, T., Utomo, D., et al. 2017, ApJ, 846, 159 43, 116

Boomsma, R., Oosterloo, T. A., Fraternali, F., van der Hulst, J. M., & Sancisi, R. 2008, A&A, 490, 555 20

Boselli, A., Cortese, L., Boquien, M., et al. 2014, A&A, 564, A67 21

Bosma, A. 1981, AJ, 86, 1825 20

Bovy, J., Rix, H.-W., & Hogg, D. W. 2012, ApJ, 751, 131 205

Bradley, L., Sipőcz, B., Robitaille, T., et al. 2020, astropy/photutils: 1.0.1, doi:10.5281/zenodo.596036 83

Brammer, G. B., Whitaker, K. E., van Dokkum, P. G., et al. 2009, ApJ, 706, L173 16

Breda, I., Papaderos, P., Gomes, J. M., et al. 2020, A&A, 635, A177 34

Brinchmann, J., Charlot, S., White, S. D. M., et al. 2004, MNRAS, 351, 1151 17, 48, 100, 174

Brinks, E. 1990, in Astrophysics and Space Science Library, Vol. 161, The Interstellar Medium in Galaxies, ed. J. Thronson, Harley A. & J. M. Shull, 39–65 20

Brook, C. B., Kawata, D., Martel, H., Gibson, B. K., & Bailin, J. 2006, ApJ, 639, 126 34

Brook, C. B., Stinson, G., Gibson, B. K., et al. 2012, MNRAS, 419, 771 34

Brunetti, M., Chiappini, C., & Pfenniger, D. 2011, A&A, 534, A75 192

Bundy, K., Bershady, M. A., Law, D. R., et al. 2015, ApJ, 798, 7 33, 74, 173, 179, 211

Burstein, D., Faber, S. M., Gaskell, C. M., & Krumm, N. 1984, ApJ, 287, 586 160

Burton, W. B. 1988, The structure of our Galaxy derived from observations of neutral hydrogen., ed. K. I. Kellermann & G. L. Verschuur, 295–358 20

Burton, W. B., Gordon, M. A., Bania, T. M., & Lockman, F. J. 1975, ApJ, 202, 30 21

Byler, N. 2018, Nell-Byler/Cloudyfsps: Initial Release Of Cloudyfsps, Zenodo, doi:10.5281/zenodo.1156412 159

Byler, N., Dalcanton, J. J., Conroy, C., & Johnson, B. D. 2017, ApJ, 840, 44 158, 159, 162

Calzetti, D. 2001, PASP, 113, 1449 144

—. 2013, Star Formation Rate Indicators, ed. J. Falcón-Barroso & J. H. Knapen, 419 24, 54, 73, 86, 105, 167

Calzetti, D., Armus, L., Bohlin, R. C., et al. 2000, ApJ, 533, 682 52, 104, 176, 220

Calzetti, D., Liu, G., & Koda, J. 2012, ApJ, 752, 98 48, 75

Cano-Díaz, M., Ávila-Reese, V., Sánchez, S. F., et al. 2019, MNRAS, 488, 3929 76

Cano-Díaz, M., Sánchez, S. F., Zibetti, S., et al. 2016, ApJ, 821, L26 28, 29, 48, 62, 100

Cappellari, M. 2017a, MNRAS, 466, 798 52, 104, 176

—. 2017b, MNRAS, 466, 798 139, 140, 144, 145

Cappellari, M., & Copin, Y. 2003a, MNRAS, 342, 345 52, 104, 176

—. 2003b, MNRAS, 342, 345 139

Cappellari, M., & Emsellem, E. 2004a, PASP, 116, 138 52, 104, 137, 176

—. 2004b, PASP, 116, 138 139, 140

Cappellari, M., Emsellem, E., Krajnović, D., et al. 2011, MNRAS, 416, 1680 139

Caputi, K. I., Deshmukh, S., Ashby, M. L. N., et al. 2017, ApJ, 849, 45 19

Cardelli, J. A., Clayton, G. C., & Mathis, J. S. 1989, ApJ, 345, 245 52, 104, 141, 176

Carrillo, A., Jogee, S., Drory, N., et al. 2020, MNRAS, 493, 4094 138, 151

Casagrande, L., Silva Aguirre, V., Schlesinger, K. J., et al. 2016, MNRAS, 455, 987 205

Catalán-Torrecilla, C., Gil de Paz, A., Castillo-Morales, A., et al. 2015, A&A, 584, A87 73, 86

—. 2017, ApJ, 848, 87 218

Catinella, B., Schiminovich, D., Kauffmann, G., et al. 2010, MNRAS, 403, 683 20

Catinella, B., Saintonge, A., Janowiecki, S., et al. 2018, MNRAS, 476, 875 21

Cazaux, S., & Spaans, M. 2009, A&A, 496, 365 24

Cazaux, S., & Tielens, A. G. G. M. 2004, ApJ, 604, 222 24

Chabrier, G. 2003, PASP, 115, 763 32, 52, 104, 142, 151, 176, 220

Chevance, M., Kruijssen, J. M. D., Hygate, A. P. S., et al. 2020a, MNRAS, 493, 2872 21, 27, 32, 74, 84, 116, 117

Chevance, M., Kruijssen, J. M. D., Vazquez-Semadeni, E., et al. 2020b, Space Sci.Rev., 216, 50 48, 116, 220

Ching, T. C., Li, D., Heiles, C., et al. 2022, Nature, 601, 49 25

Christlein, D., & Zabludoff, A. I. 2004, ApJ, 616, 192 14

Cid Fernandes, R., Mateus, A., Sodré, L., Stasińska, G., & Gomes, J. M. 2005, MNRAS, 358, 363 137

Clark, P. C., Glover, S. C. O., Klessen, R. S., & Bonnell, I. A. 2012, MNRAS, 424, 2599 27

Coelho, P. R. T., Bruzual, G., & Charlot, S. 2020, MNRAS, 491, 2025 219

Coenda, V., Mast, D., Muriel, H., & Martínez, H. J. 2020, A&A, 642, A132 186

Colombo, D., Hughes, A., Schinnerer, E., et al. 2014, ApJ, 784, 3 21, 101, 117

Combes, F., & Sanders, R. H. 1981, A&A, 96, 164 14

Conroy, C. 2013, ARA&A, 51, 393 182, 219

Conroy, C., & Gunn, J. E. 2010, ApJ, 712, 833 159

Conroy, C., Gunn, J. E., & White, M. 2009, ApJ, 699, 486 159

Conroy, C., Villaume, A., van Dokkum, P. G., & Lind, K. 2018, ApJ, 854, 139 164

Conselice, C. J. 2014, ARA&A, 52, 291 14

Cook, B. A., Conroy, C., & van Dokkum, P. 2020, ApJ, 893, 160 182

Cowie, L. L., Songaila, A., Hu, E. M., & Cohen, J. G. 1996, AJ, 112, 839 34, 198

Cronin, J. W., Gaisser, T. K., & Swordy, S. P. 1997, Scientific American, 276, 32 25

Croom, S. M., Lawrence, J. S., Bland-Hawthorn, J., et al. 2012, MNRAS, 421, 872 33, 43, 147, 173, 179, 211

Cui, W., Davé, R., Peacock, J. A., Anglés-Alcázar, D., & Yang, X. 2021, Nature Astronomy, 5, 1069 16

Daddi, E., Dickinson, M., Morrison, G., et al. 2007, ApJ, 670, 156 17, 19, 48, 100, 174

Das, A., Pandey, B., & Sarkar, S. 2021, Journal of Cosmology and Astroparticle Physics, 2021, 045 18

Das, M., McGaugh, S. S., Ianjamasimanana, R., Schombert, J., & Dwarakanath, K. S. 2020, ApJ, 889, 10 20

Davé, R., Cen, R., Ostriker, J. P., et al. 2001, ApJ, 552, 473 26

Davies, J. I., Baes, M., Bianchi, S., et al. 2017, PASP, 129, 044102 30

Davis, T. A., Greene, J. E., Ma, C.-P., et al. 2019, MNRAS, 486, 1404 21

de Amorim, A. L., García-Benito, R., Cid Fernandes, R., et al. 2017, MNRAS, 471, 3727 148

de Blok, W. J. G., Walter, F., Brinks, E., et al. 2008, AJ, 136, 2648 20

de Boer, T. J. L., Tolstoy, E., Hill, V., et al. 2012, A&A, 544, A73 32

de los Reyes, M. A. C., & Kennicutt, Robert C., J. 2019, ApJ, 872, 16 32, 48

de Meulenaer, P., Narbutis, D., Mineikis, T., & Vansevičius, V. 2013, A&A, 550, A20 17, 24, 138

de Vaucouleurs, G. 1948, Annales d'Astrophysique, 11, 247 15

De Vis, P., Jones, A., Viaene, S., et al. 2019, A&A, 623, A5 24

de Zeeuw, P. T., Bureau, M., Emsellem, E., et al. 2002, \mnras, 329, 513 139

den Brok, J. S., Chatzigiannakis, D., Bigiel, F., et al. 2021, MNRAS, 504, 3221 50, 103

Dey, B., Rosolowsky, E., Cao, Y., et al. 2019, MNRAS, 488, 1926 29, 48, 49, 62, 82, 100, 123

Di Matteo, P., Haywood, M., Combes, F., Semelin, B., & Snaith, O. N. 2013, A&A, 553, A102 192, 194

Dib, S., Hony, S., & Blanc, G. 2017, MNRAS, 469, 1521 49, 82, 100

Dib, S., Braine, J., Gopinathan, M., et al. 2021, A&A, 655, A101 20

Dickey, J. M. 1991, in Astronomical Society of the Pacific Conference Series, Vol. 18, The Interpretation of Modern Synthesis Observations of Spiral Galaxies, ed. N. Duric & P. C. Crane, 163–173 20

Djorgovski, S., & Davis, M. 1987, ApJ, 313, 59 14

Dobbs, C. L., Krumholz, M. R., Ballesteros-Paredes, J., et al. 2014, in Protostars and Planets VI, ed. H. Beuther, R. S. Klessen, C. P. Dullemond, & T. Henning, 3 21

Druard, C., Braine, J., Schuster, K. F., et al. 2014, A&A, 567, A118 41

Dwek, E., Staguhn, J., Arendt, R. G., et al. 2014, ApJ, 788, L30 23

Ellison, S. L., Lin, L., Thorp, M. D., et al. 2020a, arXiv e-prints, arXiv:2012.04771 29, 30, 31, 48, 62, 73, 88, 218

—. 2021, MNRAS, 501, 4777 100, 101, 113, 213

Ellison, S. L., Sánchez, S. F., Ibarra-Medel, H., et al. 2018, MNRAS, 474, 2039 73, 186

Ellison, S. L., Thorp, M. D., Lin, L., et al. 2020b, MNRAS, 493, L39 30, 75

Elmegreen, B. G. 1989, ApJ, 338, 178 122

Emsellem, E., Schinnerer, E., Santoro, F., et al. 2022, A&A, 659, A191 38, 40, 42, 44, 50, 52, 53, 101, 102, 104, 123, 138, 175, 176

Erroz-Ferrer, S., Carollo, C. M., den Brok, M., et al. 2019, MNRAS, 484, 5009 43

Eskew, M., Zaritsky, D., & Meidt, S. 2012, AJ, 143, 139 149

Evans, Neal J., I., Heiderman, A., & Vutisalchavakul, N. 2014, ApJ, 782, 114 74

Evans, Neal J., I., Dunham, M. M., Jørgensen, J. K., et al. 2009, ApJS, 181, 321 74

Ewen, H. I., & Purcell, E. M. 1951, Nature, 168, 356 20

Faber, S. M., Friel, E. D., Burstein, D., & Gaskell, C. M. 1985, ApJS, 57, 711 160

Fathi, K., & Peletier, R. F. 2003, A&A, 407, 61 14

Feldmann, R., Gnedin, N. Y., & Kravtsov, A. V. 2011, ApJ, 732, 115 32, 48, 75, 100, 116

Ferland, G. J., Porter, R. L., van Hoof, P. A. M., et al. 2013, Rev. Mexicana Astron. Astrofis., 49, 137 159

Fletcher, A. 2010, in Astronomical Society of the Pacific Conference Series, Vol. 438, The Dynamic Interstellar Medium: A Celebration of the Canadian Galactic Plane Survey, ed. R. Kothes, T. L. Landecker, & A. G. Willis, 197 25

Fletcher, A., Beck, R., Shukurov, A., Berkhuijsen, E. M., & Horellou, C. 2011, MNRAS, 412, 2396 25

Flores-Fajardo, N., Morisset, C., Stasińska, G., & Binette, L. 2011, MNRAS, 415, 2182 53, 105

Ford, G. P., Gear, W. K., Smith, M. W. L., et al. 2013, ApJ, 769, 55 48, 100

Förster Schreiber, N. M., & Wuyts, S. 2020, ARA&A, 58, 661 17

Foster, C., Hopkins, A. M., Gunawardhana, M., et al. 2012, A&A, 547, A79 187

Fraser-McKelvie, A., Merrifield, M., Aragón-Salamanca, A., et al. 2019, MNRAS, 488, L6 192

Freeman, K. C. 1987, ARA&A, 25, 603 199

Freeman, P., Rosolowsky, E., Kruijssen, J. M. D., Bastian, N., & Adamo, A. 2017, MNRAS, 468, 1769 28, 39

Gadotti, D. A., Sánchez-Blázquez, P., Falcón-Barroso, J., et al. 2019, MNRAS, 482, 506 36, 43, 192

Gaia Collaboration, Helmi, A., van Leeuwen, F., et al. 2018, A&A, 616, A12 201

Galli, D., & Padovani, M. 2015, arXiv e-prints, arXiv:1502.03380 25

García-Benito, R., González Delgado, R. M., Pérez, E., et al. 2017, A&A, 608, A27 33, 34, 173, 179

Garwood, R. W., & Dickey, J. M. 1989, ApJ, 338, 841 20

Ge, J., Mao, S., Lu, Y., Cappellari, M., & Yan, R. 2019, MNRAS, 485, 1675 154

Gehrz, R. 1989, in Interstellar Dust, ed. L. J. Allamandola & A. G. G. M. Tielens, Vol. 135, 445 23

Gelman, A., & Rubin, D. B. 1992, Statistical Science, 7, 457 110

Gensior, J., & Kruijssen, J. M. D. 2021, MNRAS, 500, 2000 108

Gensior, J., Kruijssen, J. M. D., & Keller, B. W. 2020, MNRAS, 495, 199 108

Genzel, R., Tacconi, L. J., Gracia-Carpio, J., et al. 2010, MNRAS, 407, 2091 28, 48, 100

Genzel, R., Tacconi, L. J., Combes, F., et al. 2012, ApJ, 746, 69 28, 48

Girardi, L., Bressan, A., Bertelli, G., & Chiosi, C. 2000, A&AS, 141, 371 176

Goddard, D., Thomas, D., Maraston, C., et al. 2017, MNRAS, 466, 4731 33, 173, 182, 186, 187

Goldreich, P., & Lynden-Bell, D. 1965, MNRAS, 130, 125 206

Goldsmith, P. F., & Langer, W. D. 1978, ApJ, 222, 881 25

Goldsmith, P. F., Li, D., & Krčo, M. 2007, ApJ, 654, 273 26

Gomes, J. M., & Papaderos, P. 2017, A&A, 603, A63 159

González Delgado, R. M., Cerviño, M., Martins, L. P., Leitherer, C., & Hauschildt, P. H. 2005, MNRAS, 357, 945 154, 168, 219

González Delgado, R. M., Cid Fernandes, R., García-Benito, R., et al. 2014a, ApJ, 791, L16 36, 174

González Delgado, R. M., Pérez, E., Cid Fernandes, R., et al. 2014b, A&A, 562, A47 33, 154, 173, 179, 180, 182

González Delgado, R. M., Cid Fernandes, R., Pérez, E., et al. 2016, A&A, 590, A44 33, 173, 179

Gould, R. J., Gold, T., & Salpeter, E. E. 1963, ApJ, 138, 408 27

Graham, A. W. 2013, Elliptical and Disk Galaxy Structure and Modern Scaling Laws, ed. T. D. Oswalt & W. C. Keel, Vol. 6, 91–140 14

Grand, R. J. J., Springel, V., Gómez, F. A., et al. 2016, MNRAS, 459, 199 201

Gutermuth, R. A., Pipher, J. L., Megeath, S. T., et al. 2011, ApJ, 739, 84 74

Haffner, L. M., Dettmar, R. J., Beckman, J. E., et al. 2009, Reviews of Modern Physics, 81, 969 53, 105

Hall, C., Courteau, S., Jarrett, T., et al. 2018, ApJ, 865, 154 73

Hani, M. H., Hayward, C. C., Orr, M. E., et al. 2020, MNRAS, 493, L87 75

Haydon, D. T., Kruijssen, J. M. D., Chevance, M., et al. 2020, MNRAS, 498, 235 73, 86

Heavens, A., Panter, B., Jimenez, R., & Dunlop, J. 2004, Nature, 428, 625 34, 182, 198

Heavens, A. F., Jimenez, R., & Lahav, O. 2000, MNRAS, 317, 965 137

Heiderman, A., Evans, Neal J., I., Allen, L. E., Huard, T., & Heyer, M. 2010, ApJ, 723, 1019 74

Henshaw, J. D., Kruijssen, J. M. D., Longmore, S. N., et al. 2020, Nature Astronomy, 4, 1064 117

Herbst, E. 1995, Annual Review of Physical Chemistry, 46, 27 19

Herrera-Endoqui, M., Díaz-García, S., Laurikainen, E., & Salo, H. 2015, A&A, 582, A86 52, 104, 175

Heyer, M., & Dame, T. M. 2015, ARA&A, 53, 583 21, 48, 212

Hirashita, H., & Ferrara, A. 2002, MNRAS, 337, 921 24

Ho, I. T., Kudritzki, R.-P., Kewley, L. J., et al. 2015, MNRAS, 448, 2030 85

Ho, I. T., Medling, A. M., Groves, B., et al. 2016, Ap&SS, 361, 280 138

Ho, I. T., Seibert, M., Meidt, S. E., et al. 2017, ApJ, 846, 39 22, 51, 103, 151, 154, 164

Homan, M. D., & Gelman, A. 2014, Journal of Machine Learning Research, 15, 1593 110

Hoyle, F. 1953, ApJ, 118, 513 100

Hsieh, B. C., Lin, L., Lin, J. H., et al. 2017, ApJ, 851, L24 29, 48, 62, 100

Hu, W., Cortese, L., Staveley-Smith, L., et al. 2021, MNRAS, 507, 5580 20

Hughes, A., Meidt, S. E., Colombo, D., et al. 2013, ApJ, 779, 46 41

Hunt, L. K., Tortora, C., Ginolfi, M., & Schneider, R. 2020, A&A, 643, A180 20, 21

Hunter, D. A., Elmegreen, B. G., & Baker, A. L. 1998, ApJ, 493, 595 108

Hygate, A. P. S., Kruijssen, J. M. D., Chevance, M., et al. 2019, MNRAS, 488, 2800 84

Ibarra-Medel, H. J., Sánchez, S. F., Avila-Reese, V., et al. 2016, MNRAS, 463, 2799 34, 173, 174, 180, 199, 205

James, P. A., & Percival, S. M. 2018, MNRAS, 474, 3101 73

Jeffreson, S. M. R., Kruijssen, J. M. D., Keller, B. W., Chevance, M., & Glover, S. C. O. 2020, MNRAS, 498, 385 101

Jenkins, E. B., & Savage, B. D. 1974, ApJ, 187, 243 23

Jian, H.-Y., Lin, L., Koyama, Y., et al. 2020, ApJ, 894, 125 18

Johansson, J., Thomas, D., & Maraston, C. 2012, MNRAS, 421, 1908 141

Kaplan, K. F., Jogee, S., Kewley, L., et al. 2016, MNRAS, 462, 1642 53, 105

Karim, A., Schinnerer, E., Martínez-Sansigre, A., et al. 2011, ApJ, 730, 61 19

Kennicutt, Robert C., J. 1989, ApJ, 344, 685 22

—. 1998, ApJ, 498, 541 28, 48, 74, 100

Kennicutt, R. C., & Evans, N. J. 2012, ARA&A, 50, 531 21, 48, 55, 105

Kewley, L. J., Groves, B., Kauffmann, G., & Heckman, T. 2006, MNRAS, 372, 961 23, 53, 83, 105

Khim, H.-g., Park, J., Seo, S.-W., et al. 2015, ApJS, 220, 3 14

Klessen, R. S., & Glover, S. C. O. 2016, Saas-Fee Advanced Course, 43, 85 27

Knapen, J. H., Pérez-Ramírez, D., & Laine, S. 2002, MNRAS, 337, 808 14

Koda, J., & Nearby Galaxies CO Survey Group. 2009, in American Astronomical Society Meeting Abstracts, Vol. 213, American Astronomical Society Meeting Abstracts #213, 485.04 41

Koleva, M., Prugniel, P., Bouchard, A., & Wu, Y. 2009, A&A, 501, 1269 137

Kormendy, J. 1979, ApJ, 227, 714 14

Kormendy, J. 1993, in Galactic Bulges, ed. H. Dejonghe & H. J. Habing, Vol. 153, 209 14, 33

—. 2013, Secular Evolution in Disk Galaxies, ed. J. Falcón-Barroso & J. H. Knapen, 1 14, 173

Kormendy, J., & Bender, R. 2012, ApJS, 198, 2 15

Kormendy, J., & Ho, L. C. 2013, ARA&A, 51, 511 26

Kormendy, J., & Kennicutt, Robert C., J. 2004, ARA&A, 42, 603 33

Kreckel, K., Faesi, C., Kruijssen, J. M. D., et al. 2018, ApJ, 863, L21 48, 64, 100

Kreckel, K., Ho, I. T., Blanc, G. A., et al. 2020, MNRAS, 499, 193 22, 50, 51, 101, 103

Kroupa, P. 2001, MNRAS, 322, 231 54, 105

Kruijssen, J. M. D., & Longmore, S. N. 2014, MNRAS, 439, 3239 32, 48, 64, 74, 86, 100, 116

Kruijssen, J. M. D., Schruba, A., Hygate, A. P. S., et al. 2018, MNRAS, 479, 1866 32, 48, 74, 86, 100, 116

Kruijssen, J. M. D., Schruba, A., Chevance, M., et al. 2019, Nature, 569, 519 48, 74, 116

Krumholz, M. R., Burkhart, B., Forbes, J. C., & Crocker, R. M. 2018, MNRAS, 477, 2716 108

Krumholz, M. R., McKee, C. F., & Bland-Hawthorn, J. 2019, ARA&A, 57, 227 48

Krumholz, M. R., Bate, M. R., Arce, H. G., et al. 2014, in Protostars and Planets VI, ed. H. Beuther, R. S. Klessen, C. P. Dullemond, & T. Henning, 243 21

Lang, P., Meidt, S. E., Rosolowsky, E., et al. 2020, ApJ, 897, 122 49, 51, 55, 102, 103, 106, 141, 175, 178, 180

Larson, R. B. 1976, MNRAS, 176, 31 34

Leaman, R., Mendel, J. T., Wisnioski, E., et al. 2017, MNRAS, 472, 1879 201, 202

Lee, H., Hoang, T., Le, N., & Cho, J. 2020, ApJ, 896, 44 24

Lee, J. C., Whitmore, B. C., Thilker, D. A., et al. 2022, ApJS, 258, 10 38, 101

Leitner, S. N., & Kravtsov, A. V. 2011, ApJ, 734, 48 26

Lelli, F., McGaugh, S. S., & Schombert, J. M. 2016, AJ, 152, 157 19

Lequeux, J. 2005, The Interstellar Medium, doi:10.1007/b137959 19, 32

Leroy, A., Bolatto, A., Walter, F., & Blitz, L. 2006, ApJ, 643, 825 41

Leroy, A. K., Walter, F., Brinks, E., et al. 2008, AJ, 136, 2782 48, 74, 82, 100

Leroy, A. K., Walter, F., Bigiel, F., et al. 2009, AJ, 137, 4670 41, 82

Leroy, A. K., Bigiel, F., de Blok, W. J. G., et al. 2012, AJ, 144, 3 73, 86

Leroy, A. K., Walter, F., Sandstrom, K., et al. 2013, AJ, 146, 19 29, 48, 50, 62, 64, 74, 75, 100, 103, 116

Leroy, A. K., Sandstrom, K. M., Lang, D., et al. 2019, ApJS, 244, 24 40, 51, 64, 103, 149, 178, 182

Leroy, A. K., Schinnerer, E., Hughes, A., et al. 2021a, ApJS, 257, 43 38, 41, 49, 50, 51, 101, 102, 103, 149, 174, 175, 178

Leroy, A. K., Hughes, A., Liu, D., et al. 2021b, ApJS, 255, 19 41, 50, 101, 102, 103, 122

Leroy, A. K., Rosolowsky, E., Usero, A., et al. 2022, ApJ, 927, 149 112

Li, A. 2004a, in Astronomical Society of the Pacific Conference Series, Vol. 309, Astrophysics of Dust, ed. A. N. Witt, G. C. Clayton, & B. T. Draine, 417 24

Li, A. 2004b, in Astrophysics and Space Science Library, Vol. 319, Penetrating Bars Through Masks of Cosmic Dust, ed. D. L. Block, I. Puerari, K. C. Freeman, R. Groess, & E. K. Block, 535 24

Li, A., & Greenberg, J. M. 2003, in Solid State Astrochemistry, ed. V. Pirronello, J. Krelowski, & G. Manicò, Vol. 120, 37–84 23

Li, Q., Narayanan, D., & Davé, R. 2019, MNRAS, 490, 1425 24

Lin, C. C., & Shu, F. H. 1964, ApJ, 140, 646 14

Lin, L., Dickinson, M., Jian, H.-Y., et al. 2012, ApJ, 756, 71 48, 100

Lin, L., Pan, H.-A., Ellison, S. L., et al. 2019, ApJ, 884, L33 29, 30, 48, 49, 62, 73, 82, 88, 100, 117, 119, 120, 121, 217

Lin, L., Ellison, S. L., Pan, H.-A., et al. 2020, ApJ, 903, 145 30, 43, 49, 101, 120

Lintott, C., Schawinski, K., Bamford, S., et al. 2011, MNRAS, 410, 166 16

Lintott, C. J., Schawinski, K., Slosar, A., et al. 2008, MNRAS, 389, 1179 16

Lisenfeld, U., Alatalo, K., Zucker, C., et al. 2017, A&A, 607, A110 21

Liszt, H. S., Braun, R., & Greisen, E. W. 1993, AJ, 106, 2349 20

Liu, Q., Wang, E., Lin, Z., et al. 2018, ApJ, 857, 17 29, 48, 73

López Fernández, R., González Delgado, R. M., Pérez, E., et al. 2018, A&A, 615, A27 33, 138, 173

Ma, X., Hopkins, P. F., Faucher-Giguère, C.-A., et al. 2016, MNRAS, 456, 2140 187

Mac Low, M.-M., & Klessen, R. S. 2004, Reviews of Modern Physics, 76, 125 100

Mackereth, J. T., Bovy, J., Leung, H. W., et al. 2019, MNRAS, 489, 176 201, 205

Madau, P., & Dickinson, M. 2014, ARA&A, 52, 415 18

Magris C., G., Mateu P., J., Mateu, C., et al. 2015, PASP, 127, 16 138

Marasco, A., Fraternali, F., Heald, G., et al. 2019, A&A, 631, A50 20

Márquez, I., Masegosa, J., González-Martin, O., et al. 2017, Frontiers in Astronomy and Space Sciences, 4, 34 22

Martig, M., Bournaud, F., Teyssier, R., & Dekel, A. 2009, ApJ, 707, 250 108

Martín-Navarro, I., Lyubenova, M., van de Ven, G., et al. 2019, A&A, 626, A124 220, 221

Martín-Navarro, I., Pinna, F., Coccato, L., et al. 2021, A&A, 654, A59 220, 221

Martins, L. P. 2021, in Galaxy Evolution and Feedback across Different Environments, ed. T. Storchi Bergmann, W. Forman, R. Overzier, & R. Riffel, Vol. 359, 386–390 33, 138, 199

Mateus, A., Sodré, L., Cid Fernandes, R., et al. 2006, MNRAS, 370, 721 16

Mathis, J. S. 1990, ARA&A, 28, 37 24

Mathis, J. S., Rumpl, W., & Nordsieck, K. H. 1977, ApJ, 217, 425 24

Matteucci, F., Franco, J., Francois, P., & Treyer, M.-A. 1989, Rev. Mexicana Astron. Astrofis., 18, 145 49, 82, 100

McKee, C. F., & Ostriker, E. C. 2007, ARA&A, 45, 565 25

Medling, A. M., Cortese, L., Croom, S. M., et al. 2018, MNRAS, 475, 5194 29, 48, 62

Meidt, S. E. 2016, ApJ, 818, 69 101

Meidt, S. E., Schinnerer, E., van de Ven, G., et al. 2014, ApJ, 788, 144 147, 149

Meidt, S. E., Hughes, A., Dobbs, C. L., et al. 2015, ApJ, 806, 72 41

Meidt, S. E., Leroy, A. K., Rosolowsky, E., et al. 2018, ApJ, 854, 100 101, 108

Meidt, S. E., Glover, S. C. O., Kruijssen, J. M. D., et al. 2020, ApJ, 892, 73 101, 108

Meidt, S. E., Leroy, A. K., Querejeta, M., et al. 2021, ApJ, 913, 113 21

Messa, M., Calzetti, D., Adamo, A., et al. 2021, ApJ, 909, 121 138

Millán-Irigoyen, I., Mollá, M., Cerviño, M., et al. 2021, MNRAS, 506, 4781 219

Minchev, I., Famaey, B., Combes, F., et al. 2011, A&A, 527, A147 187

Mo, H. J., Mao, S., & White, S. D. M. 1998, MNRAS, 295, 319 33, 182

Morselli, L., Popesso, P., Erfanianfar, G., & Concas, A. 2017, A&A, 597, A97 16

Morselli, L., Rodighiero, G., Enia, A., et al. 2020, MNRAS, 496, 4606 29, 30, 48, 62, 100

Muraoka, K., Sorai, K., Miyamoto, Y., et al. 2019, PASJ, 71, S15 112

Muxlow, T., Beswick, R. J., Richards, A. M. S., & Thrall, H. J. 2006, in Proceedings of the 8th European VLBI Network Symposium, ed. W. Baan, R. Bachiller, R. Booth, P. Charlot, P. Diamond, M. Garrett, X. Hong, J. Jonas, A. Kus, F. Mantovani, A. Marecki, H. Olofsson, W. Schlueter, M. Tornikoski, N. Wang, & A. Zensus, 31 19

Neumann, J., Fragkoudi, F., Pérez, I., et al. 2020, A&A, 637, A56 33, 36, 138, 173, 182, 192, 194, 206

Neumann, J., Thomas, D., Maraston, C., et al. 2021, MNRAS, 508, 4844 36, 174, 187, 205

Nicastro, F., Kaastra, J., Krongold, Y., et al. 2018, Nature, 558, 406 26

Nieten, C., Neininger, N., Guélin, M., et al. 2006, A&A, 453, 459 39

Noeske, K. G., Weiner, B. J., Faber, S. M., et al. 2007, ApJ, 660, L43 17, 48, 100, 174

Nozawa, T., & Fukugita, M. 2013, ApJ, 770, 27 24

Ocvirk, P., Pichon, C., Lançon, A., & Thiébaut, E. 2006, MNRAS, 365, 46 137

O'Donnell, J. E. 1994, ApJ, 422, 158 53, 105, 167

Oemler, Augustus, J., Abramson, L. E., Gladders, M. D., et al. 2017, ApJ, 844, 45 18

Okamoto, T. 2013, MNRAS, 428, 718 14

Omukai, K., Tsuribe, T., Schneider, R., & Ferrara, A. 2005, ApJ, 626, 627 24

Onodera, S., Kuno, N., Tosaki, T., et al. 2010, ApJ, 722, L127 48, 100

—. 2012, PASJ, 64, 133 41

Orellana, G., Nagar, N. M., Elbaz, D., et al. 2017, A&A, 602, A68 24

Osterbrock, D. E. 1989, Astrophysics of gaseous nebulae and active galactic nuclei 105

Ostriker, E. C., McKee, C. F., & Leroy, A. K. 2010, ApJ, 721, 975 29, 49, 82, 83

Ostriker, E. C., & Shetty, R. 2011, ApJ, 731, 41 29, 48, 49, 82

Ostriker, J. P., & Peebles, P. J. E. 1973, ApJ, 186, 467 14

Padoan, P., & Nordlund, Å. 2011, ApJ, 730, 40 25

Padovani, M., Galli, D., & Glassgold, A. E. 2009, A&A, 501, 619 25

Pan, H.-A., Schinnerer, E., Hughes, A., et al. 2022, ApJ, 927, 9 21, 32, 41, 76, 112, 116

Pannella, M., Carilli, C. L., Daddi, E., et al. 2009, ApJ, 698, L116 14, 19

Pannella, M., Elbaz, D., Daddi, E., et al. 2015, ApJ, 807, 141 17

Parikh, T., Thomas, D., Maraston, C., et al. 2021, MNRAS, 502, 5508 34, 35, 173, 179, 182

Parkash, V., Brown, M. J. I., Jarrett, T. H., & Bonne, N. J. 2018, ApJ, 864, 40 20

Pearson, W. J., Wang, L., Hurley, P. D., et al. 2018, A&A, 615, A146 17

Peng, Y.-j., Lilly, S. J., Kovač, K., et al. 2010, ApJ, 721, 193 18

Pérez, E., Cid Fernandes, R., González Delgado, R. M., et al. 2013, ApJ, 764, L1 33, 34

Pérez-González, P. G., Rieke, G. H., Villar, V., et al. 2008, ApJ, 675, 234 34, 182, 198

Perryman, M. A. C., Lindegren, L., Kovalevsky, J., et al. 1997, A&A, 500, 501 201

Pessa, I., Schinnerer, E., Belfiore, F., et al. 2021, A&A, 650, A134 100, 101, 105, 106, 107, 111, 113, 116, 186

Peterken, T., Merrifield, M., Aragón-Salamanca, A., et al. 2020, MNRAS, 495, 3387 38, 174, 199

Peterken, T., Fraser-McKelvie, A., Aragón-Salamanca, A., et al. 2019, MNRAS, 489, 1338 38, 174, 199

Pety, J., Schinnerer, E., Leroy, A. K., et al. 2013, ApJ, 779, 43 41

Pietrinferni, A., Cassisi, S., Salaris, M., & Castelli, F. 2004, ApJ, 612, 168 52, 104, 142

Planck Collaboration, Aghanim, N., Akrami, Y., et al. 2020, A&A, 641, A6 13, 26

Poggianti, B. M., Moretti, A., Gullieuszik, M., et al. 2017, ApJ, 844, 48 43

Popescu, C. C., Tuffs, R. J., Dopita, M. A., et al. 2011, A&A, 527, A109 24

Popesso, P., Morselli, L., Concas, A., et al. 2019, MNRAS, 490, 5285 17, 18, 48, 100

Popping, G., Somerville, R. S., & Trager, S. C. 2014, MNRAS, 442, 2398 20

Querejeta, M., Meidt, S. E., Schinnerer, E., et al. 2015, ApJS, 219, 5 147, 148

Querejeta, M., Schinnerer, E., Meidt, S., et al. 2021, A&A, 656, A133 21, 51, 63, 79, 101, 104, 107, 112, 116, 121, 138, 174, 175, 211, 218

Rahman, N., Bolatto, A. D., Wong, T., et al. 2011, ApJ, 730, 72 41

Reid, M. J., Menten, K. M., Brunthaler, A., et al. 2014, ApJ, 783, 130 116

Renaud, F., Bournaud, F., Agertz, O., et al. 2019, A&A, 625, A65 195

Renaud, F., Bournaud, F., Emsellem, E., et al. 2015, MNRAS, 454, 3299 21, 117

Renzini, A., & Peng, Y.-j. 2015, ApJ, 801, L29 19

Rinaldi, P., Caputi, K. I., van Mierlo, S., et al. 2021, arXiv e-prints, arXiv:2112.03935 19

Rogers, B., Ferreras, I., Lahav, O., et al. 2007, MNRAS, 382, 750 173

Roman, N. G. 1954, AJ, 59, 307 199

Rosado-Belza, D., Falcón-Barroso, J., Knapen, J. H., et al. 2020, A&A, 644, A116 36

Rosolowsky, E., Keto, E., Matsushita, S., & Willner, S. P. 2007, ApJ, 661, 830 41

Rosolowsky, E., Hughes, A., Leroy, A. K., et al. 2021, MNRAS, 502, 1218 39, 101, 117

Saintonge, A., Catinella, B., Cortese, L., et al. 2016, MNRAS, 462, 1749 48, 100

Salim, S., & Narayanan, D. 2020, ARA&A, 58, 529 23

Salim, S., Rich, R. M., Charlot, S., et al. 2007, ApJS, 173, 267 48, 76, 100

Salo, H., Laurikainen, E., Laine, J., et al. 2015, ApJS, 219, 4 52, 104, 175

Salvatier, J., Wiecki, T. V., & Fonnesbeck, C. 2016, PeerJ Computer Science, 2, e55 109

Sammut, C., & Webb, G. I. 2010, Encyclopedia of Machine Learning, doi:10.1007/978-0-387-30164-8 119

San Roman, I., Sánchez-Blázquez, P., Cenarro, A. J., et al. 2019, A&A, 622, A181 33, 138, 199

Sánchez, S. F. 2020, ARA&A, 58, 99 33, 137

Sánchez, S. F., Kennicutt, R. C., Gil de Paz, A., et al. 2012, A&A, 538, A8 28, 33, 101, 116, 173, 179, 211

Sánchez, S. F., Rosales-Ortega, F. F., Jungwiert, B., et al. 2013, A&A, 554, A58 28

Sánchez, S. F., Pérez, E., Sánchez-Blázquez, P., et al. 2016a, Rev. Mexicana Astron. Astrofis., 52, 21 138, 146

—. 2016b, Rev. Mexicana Astron. Astrofis., 52, 171 138

Sánchez, S. F., Barrera-Ballesteros, J. K., Colombo, D., et al. 2021, MNRAS, 503, 1615 29, 30, 31, 62, 82, 100, 116, 117, 121, 213

Sánchez-Blázquez, P., Rosales-Ortega, F. F., Méndez-Abreu, J., et al. 2014, A&A, 570, A6 33, 173, 179, 180, 192

Sancisi, R., Fraternali, F., Oosterloo, T., & van der Hulst, T. 2008, A&A Rev., 15, 189 20

Sandstrom, K. M., Leroy, A. K., Walter, F., et al. 2013, ApJ, 777, 5 26

Santoro, F., Kreckel, K., Belfiore, F., et al. 2022, A&A, 658, A188 83, 103, 142

Sarzi, M., Rix, H.-W., Shields, J. C., et al. 2005, ApJ, 628, 169 173

Sarzi, M., Falcón-Barroso, J., Davies, R. L., et al. 2006, MNRAS, 366, 1151 145

Satyapal, S., Abel, N. P., & Secrest, N. J. 2018, ApJ, 858, 38 17

Schawinski, K., Urry, C. M., Simmons, B. D., et al. 2014, MNRAS, 440, 889 16, 17

Schinnerer, E., Meidt, S. E., Pety, J., et al. 2013, ApJ, 779, 42 41, 117

Schinnerer, E., Meidt, S. E., Colombo, D., et al. 2017, ApJ, 836, 62 41

Schinnerer, E., Hughes, A., Leroy, A., et al. 2019a, ApJ, 887, 49 21, 27, 32, 76, 112, 116

Schinnerer, E., Leroy, A., Blanc, G., et al. 2019b, The Messenger, 177, 36 38

Schlafly, E. F., & Finkbeiner, D. P. 2011, ApJ, 737, 103 52, 104, 141, 176

Schmidt, M. 1959, ApJ, 129, 243 28, 48, 100

Schneider, R., Omukai, K., Inoue, A. K., & Ferrara, A. 2006, MNRAS, 369, 1437 24

Schombert, J., McGaugh, S., & Lelli, F. 2019, MNRAS, 483, 1496 149

Schreiber, C., Pannella, M., Elbaz, D., et al. 2015, A&A, 575, A74 18

Schruba, A., Kruijssen, J. M. D., & Leroy, A. K. 2019, ApJ, 883, 2 82, 122

Schruba, A., Leroy, A. K., Walter, F., Sandstrom, K., & Rosolowsky, E. 2010, ApJ, 722, 1699 32, 48, 64, 74, 100, 116

Schruba, A., Leroy, A. K., Walter, F., et al. 2011, AJ, 142, 37 41, 48, 62, 100

Schruba, A., Leroy, A. K., Kruijssen, J. M. D., et al. 2017, ApJ, 835, 278 74

Scoville, N. Z., & Solomon, P. M. 1975, ApJ, 199, L105 21

Seidel, M. K., Falcón-Barroso, J., Martínez-Valpuesta, I., et al. 2015, MNRAS, 451, 936 192

—. 2016, MNRAS, 460, 3784 192, 194

Sellwood, J. A., & Binney, J. J. 2002, MNRAS, 336, 785 187

Sellwood, J. A., & Carlberg, R. G. 1984, ApJ, 282, 61 201

Semenov, V. A., Kravtsov, A. V., & Gnedin, N. Y. 2017, ApJ, 845, 133 74, 116

Serra, P., Oosterloo, T., Morganti, R., et al. 2012, MNRAS, 422, 1835 20

Sérsic, J. L. 1963, Boletin de la Asociacion Argentina de Astronomia La Plata Argentina, 6, 41 15

Shah, H., & Seta, A. 2021, MNRAS, 508, 1371 25

Sharma, S., Hayden, M. R., Bland-Hawthorn, J., et al. 2021, MNRAS, 506, 1761 205

Shaw, G., Ferland, G. J., Henney, W. J., et al. 2009, ApJ, 701, 677 25

Sheth, K., Elmegreen, D. M., Elmegreen, B. G., et al. 2008, ApJ, 675, 1141 14

Sheth, K., Regan, M., Hinz, J. L., et al. 2010, PASP, 122, 1397 52, 104, 147, 175

Shetty, R., Clark, P. C., & Klessen, R. S. 2014, MNRAS, 442, 2208 29, 112

Shi, Y., Helou, G., Yan, L., et al. 2011, ApJ, 733, 87 49, 82, 100, 120

Shi, Y., Yan, L., Armus, L., et al. 2018, ApJ, 853, 149 49, 82, 100, 120

Shu, F. H., Adams, F. C., & Lizano, S. 1987, ARA&A, 25, 23 100

Shull, J. M., Smith, B. D., & Danforth, C. W. 2012, ApJ, 759, 23 26

Slavin, J. D., & Cox, D. P. 1993, ApJ, 417, 187 22

Smith, R. J. 2020, ARA&A, 58, 577 220

Solomon, P. M., Rivolo, A. R., Barrett, J., & Yahil, A. 1987, ApJ, 319, 730 39

Sonnenfeld, A., Jaelani, A. T., Chan, J., et al. 2019, A&A, 630, A71 220

Sorai, K., Kuno, N., Muraoka, K., et al. 2019, PASJ, 71, S14 41, 112

Speagle, J. S., Steinhardt, C. L., Capak, P. L., & Silverman, J. D. 2014, ApJS, 214, 15 48, 100

Spinoso, D., Bonoli, S., Dotti, M., et al. 2017, MNRAS, 465, 3729 192

Spitzer, Lyman, J., & Schwarzschild, M. 1953, ApJ, 118, 106 201

Stevens, A. R. H., Diemer, B., Lagos, C. d. P., et al. 2019, MNRAS, 483, 5334 20

Stott, J. P., Swinbank, A. M., Johnson, H. L., et al. 2016, MNRAS, 457, 1888 201

Su, Y., Sun, Y., Li, C., et al. 2016, ApJ, 828, 59 21

Sun, J., Leroy, A. K., Schruba, A., et al. 2018, ApJ, 860, 172 28, 117

Sun, J., Leroy, A. K., Ostriker, E. C., et al. 2020a, ApJ, 892, 148 29, 82, 101, 117, 122, 211

Sun, J., Leroy, A. K., Schinnerer, E., et al. 2020b, ApJ, 901, L8 21

—. 2020c, ApJ, 901, L8 50, 63, 83, 103, 117

Tacconi, L. J., Genzel, R., Neri, R., et al. 2010, Nature, 463, 781 28, 48, 100

Takagi, T., Vansevicius, V., & Arimoto, N. 2003, PASJ, 55, 385 23

Takezawa, S. 1970, J. Chem. Phys., 52, 5793 21

Tarricq, Y., Soubiran, C., Casamiquela, L., et al. 2021, A&A, 647, A19 168, 201, 205

Thilker, D. A., Braun, R., & Walterbos, R. A. M. 2000, AJ, 120, 3070 83

Tielens, A. G. G. M. 2005, The Physics and Chemistry of the Interstellar Medium 24

Tinsley, B. M. 1968, ApJ, 151, 547 32, 137, 173

—. 1980, Fund. Cosmic Phys., 5, 287 137

Tojeiro, R., Heavens, A. F., Jimenez, R., & Panter, B. 2007, MNRAS, 381, 1252 137

Tomczak, A. R., Quadri, R. F., Tran, K.-V. H., et al. 2014, ApJ, 783, 85 17

—. 2016, ApJ, 817, 118 17

Toomre, A. 1977, ARA&A, 15, 437 14

Trumpler, R. J. 1930, PASP, 42, 267 22

Tully, R. B., & Fisher, J. R. 1977, A&A, 500, 105 14

Tumlinson, J., Peeples, M. S., & Werk, J. K. 2017, ARA&A, 55, 389 26

Utomo, D., Sun, J., Leroy, A. K., et al. 2018, ApJ, 861, L18 122

Vale Asari, N., Couto, G. S., Cid Fernandes, R., et al. 2019, MNRAS, 489, 4721 22

van de Hulst, H. C. 1946, PhD thesis, - 20

van Dokkum, P., & Conroy, C. 2021, ApJ, 923, 43 221

Van Eck, C. L., Brown, J. C., Ordog, A., et al. 2021, ApJS, 253, 48 25

Vazdekis, A., Koleva, M., Ricciardelli, E., Röck, B., & Falcón-Barroso, J. 2016, MNRAS, 463, 3409 142

Vazdekis, A., Ricciardelli, E., Cenarro, A. J., et al. 2012, MNRAS, 424, 157 52, 104, 176

Vazdekis, A., Sánchez-Blázquez, P., Falcón-Barroso, J., et al. 2010, MNRAS, 404, 1639 52, 104, 176

Vehtari, A., Gelman, A., & Gabry, J. 2017, Statistics and Computing, 27, 1413 120

Villaume, A., Conroy, C., Johnson, B., et al. 2017, ApJS, 230, 23 164

Vulcani, B., Poggianti, B. M., Moretti, A., et al. 2019, MNRAS, 488, 1597 73

Walch, S., Girichidis, P., Naab, T., et al. 2015, MNRAS, 454, 238 27

Walcher, J., Groves, B., Budavári, T., & Dale, D. 2011, Ap&SS, 331, 1 33, 137, 138, 199

Walter, F., Brinks, E., de Blok, W. J. G., et al. 2008, AJ, 136, 2563 82, 120

Walter, F., Carilli, C., Neeleman, M., et al. 2020, ApJ, 902, 111 26, 27

Watson, A. A. 2011, Nuclear Physics B Proceedings Supplements, 212, 13 25

Weilbacher, P. M., Palsa, R., Streicher, O., et al. 2020, A&A, 641, A28 102, 142

Weinzirl, T., Jogee, S., Conselice, C. J., et al. 2011, ApJ, 743, 87 33

Werk, J. K., Prochaska, J. X., Tumlinson, J., et al. 2014, ApJ, 792, 8 26

Westfall, K. B., Cappellari, M., Bershady, M. A., et al. 2019, AJ, 158, 231 138, 141, 143, 145, 147

Whitaker, K. E., van Dokkum, P. G., Brammer, G., & Franx, M. 2012, ApJ, 754, L29 17, 19, 48, 100

Whitaker, K. E., Franx, M., Bezanson, R., et al. 2015, ApJ, 811, L12 28

Whitney, A., Ferreira, L., Conselice, C. J., & Duncan, K. 2021, ApJ, 919, 139 13

Widrow, L. M. 2002, Reviews of Modern Physics, 74, 775 25

Wiegert, T., de Mello, D. F., & Horellou, C. 2004, A&A, 426, 455 16

Wielebinski, R., & Beck, R. 2005, Cosmic Magnetic Fields, Vol. 664, doi:10.1007/b104621 25

Wielen, R. 1977, A&A, 60, 263 199

Wilkinson, D. M., Maraston, C., Thomas, D., et al. 2015, MNRAS, 449, 328 33, 34, 138, 173

Williams, R. J., Quadri, R. F., Franx, M., van Dokkum, P., & Labbé, I. 2009, ApJ, 691, 1879 19

Williams, T. G., Gear, W. K., & Smith, M. W. L. 2018, MNRAS, 479, 297 48, 100

Williams, T. G., Kreckel, K., Belfiore, F., et al. 2022a, MNRAS, 509, 1303 22, 103

—. 2022b, MNRAS, 509, 1303 122

Wisotzki, L., Bacon, R., Brinchmann, J., et al. 2018, Nature, 562, 229 26

Wolfire, M. G., McKee, C. F., Hollenbach, D., & Tielens, A. G. G. M. 2003, ApJ, 587, 278 20

Wong, T., Hughes, A., Ott, J., et al. 2011, ApJS, 197, 16 39

Wong, T., Xue, R., Bolatto, A. D., et al. 2013, ApJ, 777, L4 29

Wootten, A., & Thompson, A. R. 2009, IEEE Proceedings, 97, 1463 39

Wozniak, H. 2007, A&A, 465, L1 36, 182, 194

Wuyts, S., Förster Schreiber, N. M., van der Wel, A., et al. 2011, ApJ, 742, 96 18

Wyder, T. K., Martin, D. C., Barlow, T. A., et al. 2009, ApJ, 696, 1834 28, 48, 100

Yan, R., & Blanton, M. R. 2012, ApJ, 747, 61 22

Ye, T. 1992, MNRAS, 255, 32 28

Yi, S. K. 2008, in Astronomical Society of the Pacific Conference Series, Vol. 392, Hot Subdwarf Stars and Related Objects, ed. U. Heber, C. S. Jeffery, & R. Napiwotzki, 3 199

York, D. G., Adelman, J., Anderson, John E., J., et al. 2000, AJ, 120, 1579 16

Yu, J., & Liu, C. 2018, MNRAS, 475, 1093 201, 205

Zhang, H.-X., Hunter, D. A., Elmegreen, B. G., Gao, Y., & Schruba, A. 2012, AJ, 143, 47 19

Zhang, K., Yan, R., Bundy, K., et al. 2017, MNRAS, 466, 3217 53, 105

Zhang, X., Wright, M., & Alexander, P. 1993, ApJ, 418, 100 194

Zheng, Z., Wang, H., Ge, J., et al. 2017, MNRAS, 465, 4572 33, 173

Zhuang, Y., Leaman, R., van de Ven, G., et al. 2019, MNRAS, 483, 1862 33, 36, 138, 173, 174, 179, 186, 187, 194, 205

Zhukovska, S., Dobbs, C., Jenkins, E. B., & Klessen, R. S. 2016, ApJ, 831, 147 23

Zibetti, S., Gallazzi, A. R., Ascasibar, Y., et al. 2017, MNRAS, 468, 1902 32, 36, 37, 180

Acknowledgements

First and foremost, I would like to express my gratitude to my supervisor Dr. Eva Schinnerer for her mentoring and for always being available to provide useful feedback and advice on scientific, personal, and career development matters. The work presented here was only possible thanks to your permanent guidance during these four years, and I feel truly fortunate to have had the opportunity to carry out my Ph.D. studies in this awesome research group.

My sincere thanks also to Hans-Walter Rix, Simon Glover, Matthias Bartelmann, and Eva Grebel for agreeing to be examiners of this thesis.

I would like to thank Kathryn Kreckel, I-Ting Ho, Rebecca McElroy, Thomas Williams, and Hsi-An Pan, with whom I have worked closely during my Ph.D. studies at the MPIA and whose support has been truly valuable for this thesis. I would like to thank everyone in my research group (current and former members), with whom I have had many insightful, constructive, and also fun conversations during my stay at the institute: Francesco Santoro, Toshiki Saito, Christopher Faesi, Daizhong Liu, Neven **Tomičić**, Sarah Leslie, Sophia Stuber, Philip Lang, Bingqing Zhang, **Ugnė Dudzevičiūtė**, Olga Borodina, and Ilin Lazar.

I feel very grateful for being part of the PHANGS collaboration. It is an incredible group of people whose advice and feedback have been key during these years. I would like to thank every PHANGS member, especially Eric Emsellem, Francesco Belfiore, Adam Leroy, Brent Groves, Eric Koch, Erik Rosolowsky, Diederik Kruijssen, Patricia Sánchez-Blázquez, Miguel Querejeta, and Andreas Schruba, whose contribution has been crucial to the work presented in this thesis.

I wish to thank the support from the International Max Planck Research School in Heidelberg (IMPRS-HD) for giving me the opportunity of doing my Ph.D. studies in this amazing place. In particular, I would like to thank Christian Fendt and Huong Witte-Nguy, who have made my life easier since my first day in Heidelberg. I also acknowledge the support received from current and former MPIA staff members, particularly Uli Hiller and **Björn** Binroth from the IT department, and Ingrid Apfel, Daniela Scheerer, and Heide Seifert from the administration.

I have shared these four years with wonderful people, and I want to thank them for making my time in Heidelberg an amazing experience: Gustavo Medina, Marcelo Barraza, Nicolás Kurtovic, Lizxandra Flores, Samantha Brown, Bastián Reinoso, Raúl Domínguez, Bahar Bidaran, Giancarlo Mattia, Sebastián Marino, and Diego Sotillo. I also would like to render thanks to Tomás Salazar and Blas Cagliano for your friendship for so many years. Despite the distance, I know I can always count on both of you, and your unconditional trust that I could succeed in this process has been very important to me. Thanks also to Felipe Robles,

Pedro Concha, Pedro Olate, Esteban Montoya, Joaquin Aguilar, Natalia Hernández, Ramiro Pinto, and Cristóbal Morales, with whom I started this long path, and despite the years, are always present.

The support from my family has been invaluable, not only during my Ph.D. studies but throughout my entire life. Thank you very much for always being there and supporting each one of the decisions that have taken me to this point. This thesis is dedicated to my parents, Carmen Gutiérrez and Natalio Pessa, my sisters Alejandra and Natalia Pessa, and of course, my brothers-in-law Jaime Cárdenas and Gerardo Bluhm Ceballos, and my father in law Gerardo Bluhm Mandel. Finally, thank you very much to Paz Bluhm for being my partner in life and walking this path with me. Sharing my life with you has been an exciting adventure, and I am looking forward to facing all the upcoming challenges side by side with you in this new step we are both moving into.

Declaration of Originality

Declaration of Originality

I hereby declare that this thesis is my own work and that I have used no other than the stated sources and aids.

Declaration

Ich versichere, dass ich diese Arbeit selbstständig verfasst habe und keine anderen als die angegebenen Quellen und Hilfsmittel benutzt habe.

Heidelberg, der 16. Mai 2022

Ismael Alejandro Pessa Gutiérrez